

# A direct measurement of $P_{\mu}^{\pi\xi}$ from muon decay

by

James Bueno

M.Phys., The University of Oxford, 2005

A THESIS SUBMITTED IN PARTIAL FULFILMENT OF  
THE REQUIREMENTS FOR THE DEGREE OF

Doctor of Philosophy

in

The Faculty of Graduate Studies

(Physics)

The University Of British Columbia

(Vancouver)

August, 2009

© James Bueno 2009

# Table of Contents

<b>Abstract</b> . . . . .	ii
<b>Table of Contents</b> . . . . .	iii
<b>List of Tables</b> . . . . .	ix
<b>List of Figures</b> . . . . .	xi
<b>Acknowledgements</b> . . . . .	xiv
<b>1 Introduction</b> . . . . .	1
1.1 The standard model of particle physics . . . . .	1
1.2 Spin and polarisation . . . . .	4
1.3 Muon production . . . . .	4
1.4 Muon decay . . . . .	6
1.4.1 Decay modes . . . . .	6
1.4.2 Matrix element . . . . .	7
1.4.3 Muon decay parameters . . . . .	8
1.4.4 Differential decay rate . . . . .	9
1.4.5 Theoretical spectrum and radiative corrections . . . . .	9
1.5 Standard model extensions . . . . .	12
1.5.1 Right-handed muons . . . . .	12
1.5.2 Left-right symmetric electroweak models . . . . .	13
1.6 Muon depolarisation mechanisms . . . . .	15
1.6.1 Depolarisation in a magnetic field . . . . .	15
1.6.2 Depolarisation while decelerating . . . . .	16
1.6.3 Depolarisation after thermalisation . . . . .	17
1.7 Previous $P_{\mu}^{\pi} \xi$ measurements . . . . .	21
1.7.1 Measurements of $P_{\mu}^{\pi} \xi$ . . . . .	21
1.7.2 Measurements of $P_{\mu}^K \xi$ . . . . .	23

<b>2</b>	<b>Apparatus</b>	25
2.1	Overview	25
2.2	Muon production and delivery	25
2.2.1	Location	25
2.2.2	Muon production	25
2.2.3	M13 beam line	26
2.2.4	Beam line momentum calibration	27
2.2.5	Particles delivered	29
2.2.6	M13 configurations	29
2.3	Measuring the muon beam	30
2.4	Quadrupole steering	33
2.5	The detector	34
2.6	Coordinate system	35
2.7	Solenoid magnet	36
2.8	Wire chambers	39
2.9	The upstream “beam package”	41
2.10	Muon stopping target	42
2.11	Muon ranging	44
2.12	Electronics	44
2.13	Alignments	46
<b>3</b>	<b>Analysis</b>	48
3.1	Overview	48
3.2	Track reconstruction	50
3.2.1	“Unpacking”	50
3.2.2	Crosstalk removal	52
3.2.3	Windowing	52
3.2.4	Classification	52
3.2.5	Pattern recognition	53
3.2.6	Fitting the helical trajectory	56
3.2.7	Improved drift chamber space-time-relationship	58
3.2.8	Improved resolution function	60
3.3	Track selection and cuts	62
3.3.1	Trigger particle time-of-flight	63
3.3.2	Event classification cut	63
3.3.3	Muon cuts	64

*Table of Contents*

---

3.3.4	Decay particle trajectories . . . . .	66
3.3.5	Kinematic fiducial region . . . . .	67
3.4	Extraction of muon decay parameters . . . . .	70
3.5	Energy calibration . . . . .	73
3.6	Time dependence of depolarisation . . . . .	75
3.7	Muon beam average . . . . .	77
<b>4</b>	<b>Simulation . . . . .</b>	<b>80</b>
4.1	Introduction . . . . .	80
4.2	Overview of the simulation . . . . .	80
4.3	Primary particle generation . . . . .	81
4.4	Depolarisation . . . . .	82
4.4.1	Initial polarisation . . . . .	84
4.4.2	Electromagnetic field . . . . .	84
4.4.3	Time-dependent depolarisation . . . . .	85
4.4.4	Other depolarisation . . . . .	85
4.5	Muon decay . . . . .	85
4.6	Wire chamber response . . . . .	86
<b>5</b>	<b>Data . . . . .</b>	<b>87</b>
5.1	Overview . . . . .	87
5.2	Muon beam tuning . . . . .	87
5.3	Data sets . . . . .	88
5.4	Data quality checks . . . . .	91
5.4.1	Data acquisition system . . . . .	91
5.4.2	Chamber signals . . . . .	91
5.4.3	Rates . . . . .	92
5.4.4	Beam line stability . . . . .	92
5.4.5	Chamber foil bulging . . . . .	93
5.4.6	Muon stopping distribution . . . . .	93
5.4.7	Muon beam stability . . . . .	93
<b>6</b>	<b>Systematic Uncertainties . . . . .</b>	<b>96</b>
6.1	Introduction . . . . .	96
6.2	Overview . . . . .	96
6.3	Polarisation . . . . .	99

*Table of Contents*

---

6.3.1	Measures of polarisation . . . . .	99
6.3.2	Muon beam and fringe field . . . . .	100
6.3.3	Stopping material . . . . .	120
6.3.4	Production target . . . . .	126
6.3.5	Background muon contamination . . . . .	127
6.3.6	Beam intensity . . . . .	131
6.4	Chamber response . . . . .	133
6.4.1	Drift chamber space-time relationship . . . . .	133
6.4.2	Wire time offsets . . . . .	135
6.4.3	Upstream-downstream efficiency . . . . .	135
6.4.4	Dead zone . . . . .	136
6.4.5	Chamber foil bulge . . . . .	137
6.4.6	Cell asymmetry . . . . .	138
6.4.7	Density variations . . . . .	138
6.5	Detector alignment . . . . .	138
6.5.1	Magnetic field to axis . . . . .	139
6.6	Positron interactions . . . . .	139
6.6.1	$\delta$ -electron and Bremsstrahlung rates . . . . .	139
6.6.2	Outside material . . . . .	142
6.6.3	Multiple scattering . . . . .	143
6.7	Resolution . . . . .	145
6.8	Momentum calibration . . . . .	147
6.8.1	Magnetic field shape . . . . .	147
6.8.2	Use of kinematic endpoint . . . . .	148
6.9	External . . . . .	151
6.9.1	Radiative corrections . . . . .	151
6.9.2	$\eta$ correlation . . . . .	151
<b>7</b>	<b>Results . . . . .</b>	<b>152</b>
7.1	Blinded results . . . . .	152
7.2	White box consistency test . . . . .	154
7.3	Implications . . . . .	154
7.3.1	Global analysis of muon decay data . . . . .	154
7.3.2	Right-handed muon decay . . . . .	154
7.3.3	Left-right symmetric models . . . . .	154
7.4	Future experiments . . . . .	156

7.5 Conclusions . . . . .	157
<b>Bibliography</b> . . . . .	158
<b>Appendices</b>	
<b>A Personal contributions</b> . . . . .	167
<b>B History of the muon</b> . . . . .	169
<b>C Naming of the muon</b> . . . . .	171
<b>D Magnetic field mapping and simulation</b> . . . . .	174
<b>E New downstream trigger</b> . . . . .	177
<b>F Bias in <math>P_{\mu}^{\pi} \xi</math> extraction technique</b> . . . . .	179
<b>G Time expansion chambers analysis</b> . . . . .	180
G.1 Introduction . . . . .	180
G.2 Typical raw events . . . . .	180
G.3 Analysis . . . . .	182
G.3.1 Unpacking and wire time offsets . . . . .	182
G.3.2 Reject multiple trigger events . . . . .	182
G.3.3 Discriminator amplitude walk . . . . .	183
G.3.4 Track candidates . . . . .	183
G.3.5 Final multiple track removal . . . . .	185
G.3.6 Other algorithms . . . . .	185
G.4 Sense plane calibration . . . . .	186
G.4.1 Wire time offsets . . . . .	186
G.4.2 Discriminator amplitude walk . . . . .	187
G.4.3 Space-time relationship . . . . .	188
G.5 Performance . . . . .	189
G.5.1 Resolution . . . . .	189
G.5.2 Number of hits per event . . . . .	190
G.6 Summary . . . . .	190

<b>H</b>	<b>E1111: Subsidiary <math>\mu^+</math>SR experiment</b>	192
H.1	Introduction	192
H.2	Theory	192
H.3	$\mu^+$ SR Apparatus	194
H.3.1	M20 Beam line	194
H.3.2	Detector	194
H.3.3	Sample preparation	197
H.4	Data	197
H.5	Analysis	198
H.5.1	Rebinning	198
H.5.2	Calibration using spin glass	199
H.5.3	Metal samples	203
H.6	Correction due to scintillator stops	209
H.7	Other systematic uncertainties	212
H.8	Conclusions	212
H.9	Future experiments	213
<b>I</b>	<b><math>(g - 2)</math> and the M13 beam line</b>	214
<b>J</b>	<b>Estimating muon stops in PC6 gas</b>	216

# List of Tables

1.1	Fermions in the standard model . . . . .	2
1.2	Muon decay modes . . . . .	6
1.3	Weak coupling constants: experimental limits . . . . .	8
1.4	Right-handed muon decay probability . . . . .	13
2.1	Materials traversed by the muons . . . . .	45
3.1	Event types in the fiducial. . . . .	64
5.1	Data sets for this measurement. . . . .	90
6.1	Summary of uncertainties . . . . .	98
6.2	Summary of $\mu^+$ beam and fringe field uncertainties . . . . .	100
6.3	Beginning and end of set muon beam measurements . . . . .	104
6.4	Uncertainty from initial position/angle of beam . . . . .	107
6.5	Uncertainty from translational alignment of magnetic field . . . . .	110
6.6	Uncertainty from rotational alignment of magnetic field . . . . .	111
6.7	Validation of the magnetic field map . . . . .	112
6.8	$P_\mu(0)$ for different field maps . . . . .	113
6.9	Summary of $\mu^+$ beam and fringe field uncertainties . . . . .	118
6.10	Relaxation rate $\lambda$ for each data set . . . . .	122
6.11	Scale factors for beam intensity systematic uncertainty . . . . .	132
6.12	Resolution difference between data and simulation . . . . .	147
6.13	Magnetic field shape systematic: fit parameters . . . . .	147
6.14	Energy calibration uncertainties . . . . .	149
7.1	Blinded $\Delta P_\mu^\pi \xi$ results . . . . .	153
7.2	Right-handed muon decay probability: results . . . . .	154
A.1	Personal contributions: internal analysis reports. . . . .	168

*List of Tables*

---

H.1	$\mu^+$ SR data sets . . . . .	198
H.2	$\mu^+$ SR calibration : spin glass fit results . . . . .	200
H.3	$\mu^+$ SR scintillator contribution: fit results . . . . .	201
H.4	$\mu^+$ SR SRIM simulation results . . . . .	211

# List of Figures

1.1	Surface muon production . . . . .	5
1.2	Dominant muon decay mode . . . . .	6
1.3	Radiative corrections to the spectrum . . . . .	10
1.4	$P_\mu^\pi \xi$ effect on the decay spectra . . . . .	11
1.5	Previous measurements of $P_\mu^\pi \xi$ . . . . .	23
2.1	Graphite production target . . . . .	26
2.2	M13 beam line . . . . .	27
2.3	Momentum calibration of beam line . . . . .	28
2.4	Time expansion chambers: positioning . . . . .	31
2.5	Time expansion chambers: module location . . . . .	31
2.6	Cross section of a time expansion chamber module . . . . .	32
2.7	Principle of quadrupole steering . . . . .	34
2.8	Muon beam sensitivity to Q6 steering . . . . .	35
2.9	TWIST spectrometer . . . . .	36
2.10	Magnetic field lines . . . . .	38
2.11	Side view of TWIST spectrometer . . . . .	40
2.12	Schematic of a wire chamber . . . . .	40
2.13	Upstream “beam package” . . . . .	43
2.14	Muon stopping target . . . . .	43
2.15	Summary of alignments . . . . .	46
3.1	Analysis procedure . . . . .	49
3.2	Wire time offsets . . . . .	51
3.3	Determining helix fit parameters. . . . .	54
3.4	Determining the helix wavelength . . . . .	55
3.5	Event display . . . . .	57
3.6	GARFIELD and refined space-time-relationships . . . . .	59
3.7	Analysis using refined STRs . . . . .	60

3.8	Resolution function for helix fitting . . . . .	61
3.9	Events removed for each cut . . . . .	62
3.10	Time-of-flight selection . . . . .	63
3.11	Pulse widths in target proportional chambers . . . . .	65
3.12	Theoretical and reconstructed muon decay spectra . . . . .	69
3.13	Theoretical derivative spectra . . . . .	72
3.14	Kinematic endpoint in data and simulation . . . . .	73
3.15	Dependence of the endpoint position on $ 1/\cos\theta $ . . . . .	74
3.16	Theoretical predicted for muon decay asymmetry . . . . .	76
3.17	Exponential fit to the asymmetry . . . . .	77
3.18	Muon beam with large transverse momentum . . . . .	79
4.1	Dependence of range on $x$ position . . . . .	83
5.1	Tuned muon beam . . . . .	88
5.2	$\mu^+$ beam stability from time expansion chambers . . . . .	94
5.3	$\mu^+$ beam stability from wire chambers . . . . .	95
6.1	OPERA field components . . . . .	102
6.2	Muon beam envelopes . . . . .	103
6.3	Quadratic dependence of $P_\mu(0)$ . . . . .	106
6.4	OPERA+coils fringe field map . . . . .	108
6.5	$B_x$ for OPERA and OPERA+coils field maps . . . . .	114
6.6	Correlation between $A$ and $P_\mu(0)$ . . . . .	116
6.7	$P_\mu(0)$ sensitivity to multiple scattering correction . . . . .	117
6.8	Number of hits in final TEC track . . . . .	119
6.9	Muon pulse widths in PC5 and PC6 . . . . .	123
6.10	Asymmetry analysis applied to simulation . . . . .	125
6.11	Background muon contamination . . . . .	129
6.12	Muon stopping distribution in data and simulation . . . . .	130
6.13	Time residuals after refining the drift cell STR . . . . .	134
6.14	Inefficiency: dependence on $p$ and $\cos\theta$ . . . . .	137
6.15	Validation of $\delta$ -electron measurement . . . . .	140
6.16	Measure of the $\delta$ -electron rate . . . . .	141
6.17	Measure of the Bremsstrahlung rate . . . . .	142
6.18	Outside material systematic uncertainty . . . . .	144
6.19	Resolution in data and simulation . . . . .	146

6.20	Difference in kinematic endpoint for nominal data/simulation . . . . .	150
7.1	$\Delta P_{\mu}^{\pi\xi}$ consistency . . . . .	152
7.2	Weak coupling constants: improvement . . . . .	155
C.1	Muon naming: frequency in abstracts . . . . .	171
D.1	Field mapper device: schematic . . . . .	175
D.2	Field mapper device: photograph . . . . .	175
D.3	OPERA simulation components . . . . .	176
D.4	Difference between measured and OPERA map . . . . .	176
E.1	New downstream trigger: photograph . . . . .	177
E.2	New downstream trigger: front view . . . . .	178
G.1	Examples of TEC events . . . . .	181
G.2	Track candidate construction . . . . .	184
G.3	Collimator used to calibrate time expansion chambers . . . . .	186
G.4	Stability of wire time offsets for the time expansion chambers . . . . .	187
G.5	Correction parameters for TEC discriminator amplitude walk . . . . .	188
G.6	Single hit resolution for time expansion chambers . . . . .	189
G.7	Time expansion chambers: sense plane aging . . . . .	191
H.1	$\mu^+$ SR experimental setup . . . . .	196
H.2	Sensitivity of empirical asymmetry to binning . . . . .	199
H.3	Second exponential term for scintillator . . . . .	202
H.4	$\mu^+$ SR fit results for silver mask . . . . .	204
H.5	$\mu^+$ SR fit results for TWIST metal samples . . . . .	205
H.6	$\mu^+$ SR example fit to Al target . . . . .	207
H.7	$\mu^+$ SR example fit to Ag target . . . . .	208
H.8	SRIM simulation results . . . . .	210
H.9	Sensitivity of $\lambda$ to fraction of muons stopping in scintillator . . . . .	211
I.1	On-axis particle passing through the beam line . . . . .	214
I.2	Extreme trajectories through the M13 beam line . . . . .	215
J.1	Estimating of gas contamination in zone 1 . . . . .	217

# Chapter 1

## Introduction

This thesis describes the TWIST collaboration's final direct measurement of  $P_\mu^\pi \xi$ , where  $P_\mu^\pi$  is the polarisation of the muon from pion decay, and  $\xi$  describes the asymmetry of the positrons from muon decay. This measurement is a high precision test of the standard model of particle physics.

The current chapter will describe the physics under investigation and the previous measurements of  $P_\mu^\pi \xi$ . Chapter 2 describes the delivery of muons, the time expansion chambers that measured the muon beam, and the low mass spectrometer that was used to measure the positron tracks. Chapter 3 describes the analysis that identified the particles and reconstructed their trajectories. The analysis of the time expansion chambers can be found separately in Appendix G. The detailed simulation of the particles and the spectrometer is covered in Chapter 4. A subsidiary  $\mu^+$ SR experiment to determine  $P_\mu(t)$  is described in Appendix H; this project was part of the author's thesis proposal, but its results were not competitive with those from the TWIST detector. Chapter 5 describes the data accumulated in 2006 and 2007 that were analysed for this measurement. The uncertainties that dominated the  $P_\mu^\pi \xi$  measurement are described in Section 6. Lastly, the results and their physics implications are considered in Chapter 7.

Appendix A details the author's personal contributions to the experiment. Appendices B and C describe the discovery and naming of the muon.

### 1.1 The standard model of particle physics

The standard model (SM) describes the fundamental particles that make up all matter, and the interactions between these particles[1]. The model is very successful, but has known limitations; an extension is needed to accommodate neutrino oscillations, gravity is not included, and the fundamental interactions are not unified under a common symmetry. The SM uses arbitrary parameters (masses, couplings, mixing angles, *etc.*) that must be measured, rather than being predicted by the model itself.

In the SM, all matter is composed of fundamental spin-1/2 particles<sup>1</sup> called fermions.

---

<sup>1</sup>Spin is an intrinsic property, such as mass or charge. More detail will be given in Section 1.2.

There are six leptons, which exist as free particles, and six quarks, which have not been observed as free particles. They are grouped into three generations (I, II, III) of increasing mass scale; Table 1.1 lists the particles and their charges. The leptons are the electron ( $e^-$ ), muon ( $\mu^-$ ), and tau lepton ( $\tau^-$ ), all with charge -1 (in units of elementary charge), and their associated neutrinos that have no electric charge. The quark flavours are up ( $u$ ), down ( $d$ ), charm ( $c$ ), strange ( $s$ ), top ( $t$ ) and bottom ( $b$ ), and in each generation there is a quark of charge ( $+\frac{2}{3}$ ) and ( $-\frac{1}{3}$ ). Quarks have an extra degree of freedom, “colour charge”, which can be red, green or blue. For each fermion there is an associated antiparticle with the same mass but opposite charge. Antiparticles are denoted by their opposite charge (*e.g.*  $\mu^+$ ) or a bar (*e.g.*  $\bar{\nu}_\mu$ ).

Table 1.1: Fundamental fermions in the SM, in generations of increasing mass scale[2]. Charge,  $Q$ , is given in units of elementary charge ( $\approx 1.60 \times 10^{-19}$  C).

Particle	Generation			$Q/ e $
	I	II	III	
leptons	$e^-$	$\mu^-$	$\tau^-$	-1
	$\nu_e$	$\nu_\mu$	$\nu_\tau$	0
	$u$	$c$	$t$	+2/3
quarks	$d$	$s$	$b$	-1/3

The SM describes three of the four fundamental interactions between fermions, which are mediated by particles of integral spin, namely the bosons. The strong interaction binds quarks, and is mediated by spin-1 massless gluons that also carry a colour charge; the interactions are described by quantum chromodynamics (QCD). Leptons do not carry colour, and are therefore unaffected by the strong interaction. The electromagnetic interaction is mediated by massless photon exchange, and both quarks and charged leptons can interact. The weak interaction is mediated by three massive charged bosons, the  $W^\pm$  and  $Z_0$ , each with a mass of order 100 protons. Gravity is not included in the SM, but is supposedly mediated by a spin-2 boson called the graviton. Relative to the strong interaction, the strength of the force between two protons is  $10^{-2}$  for the electromagnetic interaction,  $10^{-7}$  for the weak interaction, and  $10^{-39}$  for gravity[2].

The charged weak interaction (WI) can convert charged leptons into neutral leptons, and vice-versa, but only within a single generation. The WI can convert quarks between generations, by defining WI eigenstates that are a mixture of mass eigenstates. The mixing

is then characterised by the Cabbibo-Kobayashi-Maskawa (CKM) matrix,  $V_{\text{CKM}}$ , defined by

$$\begin{pmatrix} d' \\ s' \\ b' \end{pmatrix} = V_{\text{CKM}} \begin{pmatrix} d \\ s \\ b \end{pmatrix} = \begin{pmatrix} V_{ud} & V_{us} & V_{ub} \\ V_{cd} & V_{cs} & V_{cb} \\ V_{td} & V_{ts} & V_{tb} \end{pmatrix} \begin{pmatrix} d \\ s \\ b \end{pmatrix}, \quad (1.1)$$

where  $(d', s', b')$  are the WI eigenstates and  $(d, s, b)$  are the mass eigenstates. The elements of  $V_{\text{CKM}}$  are determined experimentally, and  $V_{\text{CKM}}$  is found to be close to diagonal with the latest values[3]

$$V_{\text{CKM}} = \begin{pmatrix} 0.97419 \pm 0.00022 & 0.2257 \pm 0.0010 & 0.00359 \pm 0.00016 \\ 0.2256 \pm 0.0010 & 0.97334 \pm 0.00023 & 0.0415^{+0.0010}_{-0.0011} \\ 0.00874^{+0.00026}_{-0.00037} & 0.0407 \pm 0.0010 & 0.999133^{+0.000044}_{-0.000043} \end{pmatrix}, \quad (1.2)$$

under the assumption that only three generations exist.

The weak interaction has been experimentally determined to violate parity; this is the symmetry that physical laws are the same after an improper rotation ( $\vec{r} \rightarrow -\vec{r}$ ), which is a conserved quantity under the strong and electromagnetic interactions. The operator for the weak interaction was found to be vector minus axial-vector, or  $(V - A)$ . This combination resulted in maximal parity violation since  $(V - A)$  projects out the left-handed part of the wave function.  $(V - A)$  is called the SM prediction for the weak interaction since there is no experimental data to disfavour this combination of operators.

The SM includes the Glashow Weinberg Salam (GWS) model of electroweak interactions, which unifies the electromagnetic and weak interactions. At higher energies the interactions have the same strength, and the symmetry is only broken at lower energies. The GWS model addresses maximal parity violation by making left-handed particles (right-handed antiparticles) transform as doublets, and the right-handed particles (left-handed antiparticles) as singlets, so that in the first generation of fermions one has,

$$\begin{pmatrix} u \\ d \end{pmatrix}_L, \begin{pmatrix} \nu_e \\ e^- \end{pmatrix}_L, u_R, d_R, e_R^-. \quad (1.3)$$

The symmetries of the theory are weak isospin ( $I$ ) and hypercharge ( $Y$ ); the latter is defined as  $Y = Q - I_3$ , where  $Q$  is the electric charge and  $I_3$  is the third component of weak isospin. The weak isospin determines the behaviour under the weak interaction; the left-handed fermions have  $I_3 = \pm\frac{1}{2}$ , and these doublets behave the same under the weak interaction. The right-handed leptons have  $I = 0$ , and do not participate in the weak inter-

action.

Although the SM includes the unification of the electromagnetic and weak interactions through the GWS theory, it does not unify the electroweak and strong interactions. This is the subject of Grand Unified Theories (GUTs). For more detail on the SM, the reader is referred to Refs. [2, 4], which contain explanations that are accessible to the experimentalist.

## 1.2 Spin and polarisation

The spin of a lepton is an intrinsic property, such as its mass or charge. Spin has no classical analogue, and the spin operator cannot be defined in terms of physical observables, in contrast to the orbital angular momentum operator, which is  $(\vec{r} \times \vec{p})$ . However, the spin operators do obey the same commutation relations as the orbital angular momentum, and therefore spin is considered to be an “intrinsic angular momentum”, although nothing is actually “spinning”.

Spin is quantised, and the component along a direction can only take on the values  $\hbar m_i$ , where  $m_i = -s, -s + 1, \dots, s - 1, s$  and  $\hbar s$  is the total spin. Muons are leptons, which are spin-1/2, so that the spin in a given direction can be  $\pm \frac{\hbar}{2}$ .

A “spin vector” can be defined for a single particle, as the expectation of the spin along each axis. This is a useful concept since the spin vector can receive a torque in a magnetic field that results in classical precession about the field direction. For an ensemble of particles with spin, the “spin polarisation” can be introduced, which describes the degree to which the spins are aligned in a particular direction. This gives a space direction about which to define a probability distribution. From here on, the muon (spin) polarisation is denoted  $P_\mu$ , and this is always defined with respect to the magnetic field at the point of decay, which is equivalent to the  $z$ -axis in the experiment’s coordinate system.

## 1.3 Muon production

The muons in the experiment were produced in pion decay. A high energy proton beam incident on a stationary carbon target produced  $\pi^+$ , which then decayed with a branching ratio of  $> 99.98\%$ [3] into

$$\pi^+ \rightarrow \mu^+ \nu_\mu. \quad (1.4)$$

In the  $\pi^+$  rest frame, conservation of energy and momentum leads to a  $\mu^+$  momentum,

$$p_\mu = \frac{m_\pi^2 - m_\mu^2}{2m_\pi} \approx 29.79 \text{ MeV}/c, \quad (1.5)$$

where the neutrino mass is assumed to be zero. The neutrino has negative helicity<sup>2</sup> (it is “left-handed”), so that its polarisation and momentum vectors are opposite[5]. The  $\pi^+$  has spin-0 and the  $\nu_\mu$  and  $\mu^+$  are spin- $\frac{1}{2}$ ; therefore conservation of angular momentum ensures the muon also has negative helicity, as described in Fig. 1.1.

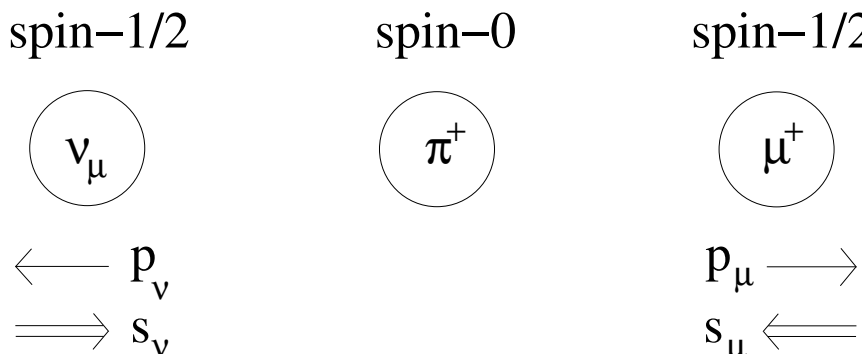


Figure 1.1: Neutrinos have their momentum ( $\vec{p}$ ) and spin ( $\vec{s}$ ) vectors in opposite directions (they are “left-handed”). Conservation of angular momentum requires the muon to also be left-handed.

Thus, the muons from  $\pi^+$  decay are 100% polarised, with the exception of the following mechanisms:

- Finite neutrino mass reduces the neutrino’s helicity by a factor  $(1 - p/E)$ . Even with a conservative upper mass limit<sup>3</sup> of 0.19 MeV, this changes the muon’s polarisation by just  $2 \times 10^{-5}$ , which is an order of magnitude below the experimental sensitivity. Note that cosmological data suggests the sum of the neutrino mass eigenstates is  $< 2.0$  eV[3].
- The  $\pi^+$  has a radiative decay mode with branching ratio 0.02%,

$$\pi^+ \rightarrow \mu^+ \nu_\mu \gamma. \quad (1.6)$$

In this mode, the muon’s longitudinal polarisation is a function of the photon and muon energies. The present experiment selects a limited range of muon momenta, and the branching ratio for this process is already at the  $10^{-4}$  level, so that the loss of polarisation due to the radiative decay mode is negligible.

---

<sup>2</sup>The neutrino has negative chirality. Under the assumption of massless neutrinos (which is adequate for this measurement),  $v = c$  so that the neutrino also has negative helicity.

<sup>3</sup>This is the 90% C.L. from muon based neutrino mass measurements[3].

- If the SM is incomplete, the weak interaction may allow for right-handed neutrinos in pion decay, which would force the muon to also be right-handed. The possibility of right-handed muons is part of the physics motivation for measuring  $P_\mu^\pi \xi$  at the level of  $10^{-4}$  (see Section 1.5.2).

There is also a pion decay mode with branching ratio 0.0123%,  $\pi^+ \rightarrow e^+ \nu_e$ , which is observable by the experiment; see Section 2.2.5 for more details.

## 1.4 Muon decay

### 1.4.1 Decay modes

The muon decays with a lifetime of  $2.197 \mu\text{s}$  into the three modes listed in Table 1.2, with the most probable mode shown in Fig. 1.2. The positron is emitted with a range of energies, up to a kinematic maximum of  $W_{e\mu} = (m_\mu^2 + m_e^2)/2m_\mu \approx 52.83 \text{ MeV}$ , which provides an energy reference feature.

Table 1.2: Muon decay modes, from the Particle Data Group[3].

Decay mode	Fraction ( $\Gamma_i/\Gamma$ )
$\mu^+ \rightarrow e^+ \nu_e \bar{\nu}_\mu$	$(98.6 \pm 0.4)\%$
$\mu^+ \rightarrow e^+ \nu_e \bar{\nu}_\mu \gamma$	$(1.4 \pm 0.4)\%$
$\mu^+ \rightarrow e^+ \nu_e \bar{\nu}_\mu e^+ e^-$	$(3.4 \pm 0.4) \times 10^{-5}$

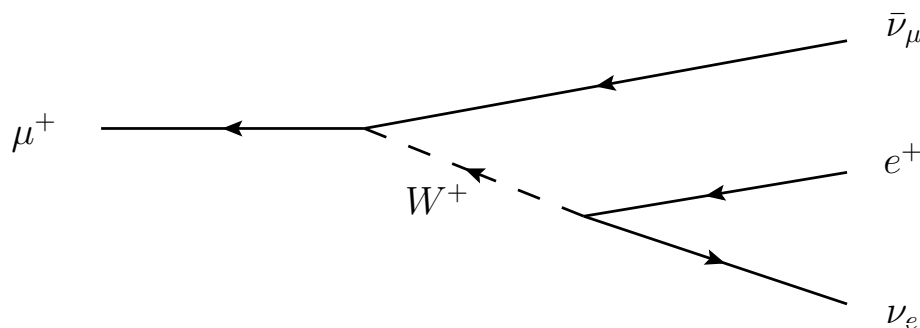


Figure 1.2: Feynman diagram for the most probable muon decay mode[6].

## 1.4.2 Matrix element

The Particle Data Group regularly reviews the theoretical form for muon decay[3]. For energies much less than  $m_W$ , muon decay can be considered a four-fermion point interaction. The most general, local<sup>4</sup>, Lorentz-invariant, derivative-free, lepton-number-conserving matrix element  $M$  can be written in terms of helicity-preserving amplitudes as

$$M = \frac{4G_F}{\sqrt{2}} \sum_{\substack{i=L,R \\ j=L,R \\ \kappa=S,V,T}} g_{ij}^\kappa \langle \bar{\psi}_{e_i} | \Gamma^\kappa | \psi_{\nu_e} \rangle \langle \bar{\psi}_{\nu_\mu} | \Gamma_\kappa | \psi_{\mu_j} \rangle, \quad (1.7)$$

where  $G_F$  is the Fermi coupling constant ( $1.17 \times 10^{-11} \text{ MeV}^{-2}$ ),  $i$  labels the electron and muon chiralities,  $j$  labels the neutrino chiralities,  $g_{ij}^\kappa$  are complex amplitudes, and  $\Gamma^\kappa$  are the possible interactions (scalar-pseudoscalar (S), vector-axialvector (V), tensor (T)), which are given by

$$\Gamma^S = 1, \quad \Gamma^V = \gamma^\mu, \quad \Gamma^T = \frac{1}{\sqrt{2}} \sigma^{\mu\nu} \equiv \frac{i}{2\sqrt{2}} (\gamma^\mu \gamma^\nu - \gamma^\nu \gamma^\mu). \quad (1.8)$$

The amplitudes  $g_{RR}^T$  and  $g_{LL}^T$  are both zero, leaving 10 complex values of  $g_{ij}^\kappa$ , one of which is constrained by normalisation[8],

$$\begin{aligned} \frac{1}{4} \left( |g_{RR}^S|^2 + |g_{LR}^S|^2 + |g_{RL}^S|^2 + |g_{LL}^S|^2 \right) + |g_{RR}^V|^2 + |g_{LR}^V|^2 + |g_{RL}^V|^2 + |g_{LL}^V|^2 \\ + 3 \left( |g_{LR}^T|^2 + |g_{RL}^T|^2 \right) = 1 \end{aligned} \quad (1.9)$$

Since these are complex amplitudes, there are 18 independent parameters to determine, in addition to  $G_F$ . In the SM, where the weak vertex factor has the operator combination (V - A), the amplitude  $g_{LL}^V = 1$  and all others are zero. The values of  $g_{ij}^\kappa$  are experimentally determined from a global analysis of several inputs:

- The muon lifetime to determine the Fermi coupling constant,  $G_F$ .
- The energy and angle of the  $e^+$  from  $\mu^+ \rightarrow e^+ \nu_e \bar{\nu}_\mu$ , such as the experiment described here.
- The longitudinal polarisation of the  $e^+$  from  $\mu^+ \rightarrow e^+ \nu_e \bar{\nu}_\mu$ . Note that this measurement also determines  $G_F$ .
- Inverse muon decay,  $\nu_\mu e \rightarrow \mu^- \nu_e$ , to place strict limits on the scalar terms.

---

<sup>4</sup>The range of the  $W^+$  makes the interaction non-local, but this contributes a negligible deviation  $O(m_\mu^2/m_W^2) \approx 2 \times 10^{-6}$ [7].

A recent global analysis is described in more detail in Ref. [7], where 11 parameters from the above experiments are used to set confidence limits on the magnitude of the coupling constants. Table 1.3 gives the results from the last two global analyses, showing the impact of the TWIST experiment's published results for  $\rho$  and  $\delta$ .

Table 1.3: 90% confidence limits on the weak coupling constants. Limits on  $|g_{LL}^S|$  and  $|g_{LL}^V|$  are from Ref. [3].

	Prior to TWIST[9]	First TWIST $\rho, \delta$ publication[7]	Recent TWIST results MacDonald[10]
$ g_{RR}^S $	$< 0.066$	$< 0.067$	$< 0.062$
$ g_{RR}^V $	$< 0.033$	$< 0.034$	$< 0.031$
$ g_{LR}^S $	$< 0.125$	$< 0.088$	$< 0.074$
$ g_{LR}^V $	$< 0.060$	$< 0.036$	$< 0.025$
$ g_{LR}^T $	$< 0.036$	$< 0.025$	$< 0.021$
$ g_{RL}^S $	$< 0.424$	$< 0.417$	$< 0.412$
$ g_{RL}^V $	$< 0.110$	$< 0.104$	$< 0.104$
$ g_{RL}^T $	$< 0.122$	$< 0.104$	$< 0.103$
$ g_{LL}^S $	$< 0.550$	$< 0.550$	$< 0.550$
$ g_{LL}^V $	$> 0.960$	$> 0.960$	$> 0.960$

### 1.4.3 Muon decay parameters

The muon decay parameters<sup>5</sup>, which describe the energy and angle of the  $e^+$  from  $\mu^+ \rightarrow e^+ \nu_e \bar{\nu}_\mu$ , are defined as

$$\rho = \frac{3}{4} - \frac{3}{4} [|g_{RL}^V|^2 + |g_{LR}^V|^2 + 2 |g_{RL}^T|^2 + 2 |g_{LR}^T|^2 + \text{Re}(g_{RL}^S g_{RL}^{T*} + g_{LR}^S g_{LR}^{T*})], \quad (1.10)$$

$$\eta = \frac{1}{2} \text{Re}[g_{RR}^V g_{LL}^{S*} + g_{LL}^V g_{RR}^{S*} + g_{RL}^V (g_{LR}^{S*} + 6g_{LR}^{T*}) + g_{LR}^V (g_{RL}^{S*} + 6g_{RL}^{T*})], \quad (1.11)$$

$$\xi = 1 - \frac{1}{2} |g_{LR}^S|^2 - \frac{1}{2} |g_{RR}^S|^2 - 4 |g_{RL}^V|^2 + 2 |g_{LR}^V|^2 - 2 |g_{RR}^V|^2 + 2 |g_{LR}^T|^2 - 8 |g_{RL}^T|^2 + 4 \text{Re}(g_{LR}^S g_{LR}^{T*} - g_{RL}^S g_{RL}^{T*}), \quad (1.12)$$

$$\xi\delta = \frac{3}{4} - \frac{3}{8} |g_{RR}^S|^2 - \frac{3}{8} |g_{LR}^S|^2 - \frac{3}{2} |g_{RR}^V|^2 - \frac{3}{4} |g_{RL}^V|^2 - \frac{3}{4} |g_{LR}^V|^2 - \frac{3}{2} |g_{RL}^T|^2 - 3 |g_{LR}^T|^2 + \frac{3}{4} \text{Re}(g_{LR}^S g_{LR}^{T*} - g_{RL}^S g_{RL}^{T*}). \quad (1.13)$$

<sup>5</sup>These are sometimes referred to as the ‘‘Michel parameters’’, after the late theoretical physicist Louis Michel. He introduced the  $\rho$  and probably the  $\eta$  parameter, but  $\delta$  and  $\xi$  were introduced by Alberto Sirlin[11].

Under the SM where  $g_{ij}^k = 0$ , except for  $g_{LL}^V = 1$ , the muon decay parameters are  $\rho = \xi\delta = 3/4$ ,  $\xi = 1$  and  $\eta = 0$ . The TWIST experiment fixes  $\eta$  to the result of a global analysis, and then measures  $\rho$ ,  $\delta$  and  $P_\mu^\pi \xi$  simultaneously.

#### 1.4.4 Differential decay rate

The differential decay rate is proportional to  $|M|^2$ , and for a detector insensitive to the  $e^+$  polarisation, the rate is given by

$$\frac{d^2\Gamma}{dx d\cos\theta} = k(x) \{F_{IS}(x) + P_\mu \cos\theta F_{AS}(x)\}, \quad (1.14)$$

where  $x$  is the reduced energy ( $= E_e/W_{e\mu}$ ),  $\theta$  is the angle between the muon spin and positron momentum vectors,  $P_\mu = |\vec{P}_\mu|$  (the degree of muon polarisation),  $k(x)$  is defined for convenience as

$$k(x) = \frac{m_\mu}{4\pi^3} W_{e\mu}^4 G_F^2 \sqrt{x^2 - x_0^2}, \quad (1.15)$$

$$W_{e\mu} = E_{\max} = \frac{m_\mu^2 + m_e^2}{2m_\mu}, \quad (1.16)$$

and separate terms for the isotropic and anisotropic contributions are written in terms of Eqs. (1.10) to (1.13) as

$$F_{IS}(x) = x(1-x) + \frac{2}{9}\rho(4x^2 - 3x - x_0^2) + \eta x_0(1-x) + F_{IS}^{RC}(x), \quad (1.17)$$

$$F_{AS}(x) = \frac{1}{3}\xi\sqrt{x^2 - x_0^2} \left[ 1 - x + \frac{2}{3}\delta \left( 4x - 3 + \left( \sqrt{1 - x_0^2} - 1 \right) \right) \right] + F_{AS}^{RC}(x). \quad (1.18)$$

The superscript ‘‘RC’’ refers to radiative corrections, which are described in the next section.

#### 1.4.5 Theoretical spectrum and radiative corrections

Radiative decays with internal and external lines are treated as spectrum corrections. These have a significant effect close to  $x = 1$ , where the rate is changed by up to 10% (see Fig. 1.3). The current analysis includes the following levels of correction: full first order  $[O(\alpha)]$ [12], leading-logarithmic second order  $[O(\alpha^2 L^2)]$ , where  $L = \ln(m_\mu^2/m_e^2) \approx 10.7$ [13], next-to-leading-logarithmic second order  $[O(\alpha^2 L)]$ [14, 15], and leading-logarithmic third order  $[O(\alpha^3 L^3)]$ [15]. These publications cite the TWIST experiment as significant motivation

for their calculations; radiative corrections for the total decay rate calculations have been in existence for a longer time to help with muon lifetime measurements, but these calculations are simpler since the electron mass can be neglected. The current analysis does not include  $O(\alpha^2 L^0)$  corrections, which only became available in 2007[16].

The radiative corrections assume the SM coupling for the weak interaction,  $(V - A)$ . If the muon decay parameters are found to be different from the SM values, the radiative corrections will have to be recalculated using a more general form.

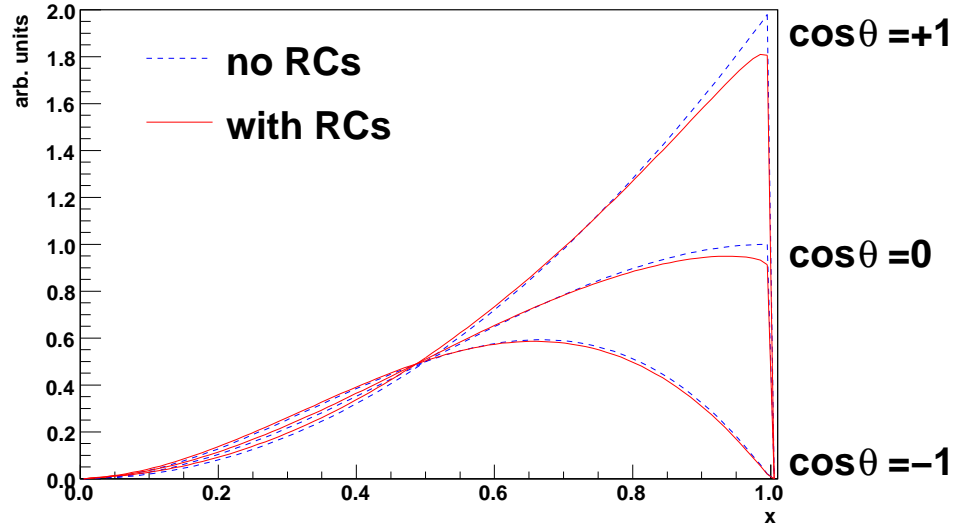


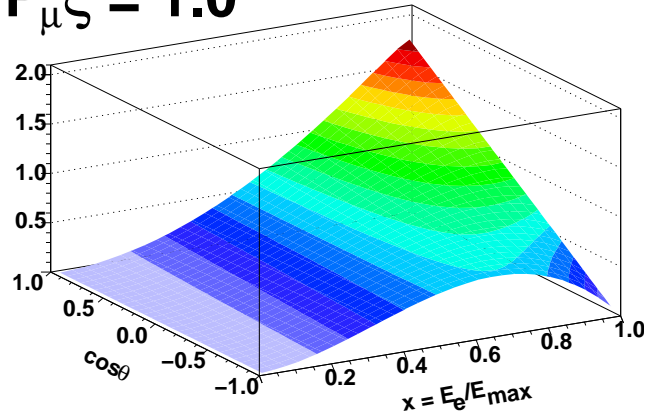
Figure 1.3: Slices of spectrum, demonstrating the effect of radiative corrections (RCs).

The change in spectrum shape due to  $P_\mu^\pi \xi$  is shown in Fig. 1.4, where the relative number of upstream and downstream counts are affected. The large  $|\cos \theta|$  and higher energy positrons have the most sensitivity to  $P_\mu^\pi \xi$ . TWIST simultaneously extracts  $\rho$ ,  $\delta$  and  $P_\mu^\pi \xi$ , which must satisfy  $P_\mu^\pi \xi \delta / \rho \leq 1$  to prevent an unphysical decay rate.

The TWIST experiment does not measure  $\eta$ , which has most sensitivity to lower energy  $e^+$ .  $\eta$  would have required  $\sim 2$  months of dedicated running with a reduced magnetic field, and careful validation of the hard scattering interactions ( $> 1$  MeV) in the simulation<sup>6</sup>. Even with these two improvements, the statistical uncertainty would have been uncompetitive with measurements derived from the  $e^+$  transverse polarisation, such as Ref. [17]. In practice, TWIST fixed  $\eta$  to the latest global analysis value of  $\eta = (-3.6 \pm 6.9) \times 10^{-3}$ [7], and included the correlation with  $\eta$  as a systematic uncertainty.

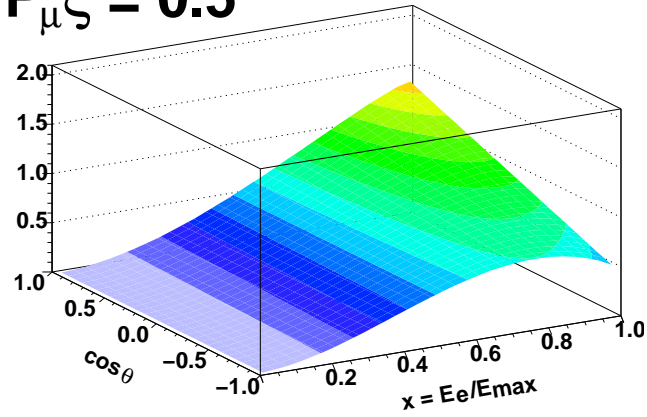
<sup>6</sup>The hard scattering is needed since a high energy positron may experience significant energy loss in the target (a few MeV), and end up being reconstructed at a lower energy; if the simulation does not behave in the same way, this would result in an incorrect  $\eta$  measurement.

**$P_{\mu}^{\xi} = 1.0$**



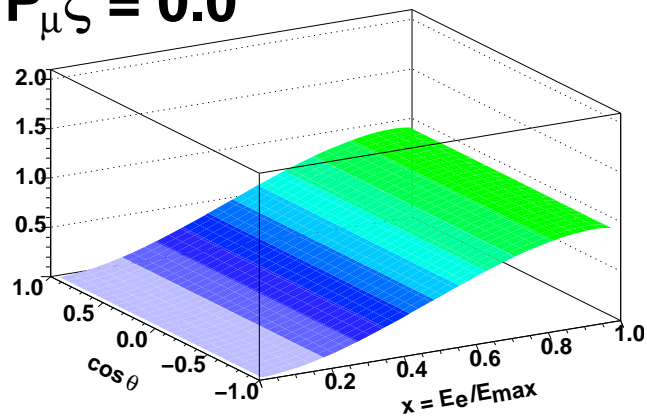
(a) Standard model,  $P_{\mu}^{\pi} \xi = 1$ .

**$P_{\mu}^{\xi} = 0.5$**



(b)  $P_{\mu}^{\pi} \xi = 0.5$

**$P_{\mu}^{\xi} = 0.0$**



(c)  $P_{\mu}^{\pi} \xi = 0$

Figure 1.4: Positron spectra (arbitrary units) for three different  $P_{\mu}^{\pi} \xi$  values.  $P_{\mu}^{\pi} \xi$  determines the relative number of upstream and downstream counts.

The asymmetry of the spectrum can be constructed from

$$A = \frac{N_F - N_B}{N_F + N_B}, \quad (1.19)$$

where  $N_F$  is the number of forward counts and  $N_B$  is the number of backward counts. After integration over  $x$ , this quantity depends only on  $P_\mu^\pi \xi$  and  $\eta$ , and for this reason  $P_\mu^\pi \xi$  is sometimes called “the integral asymmetry parameter”.

## 1.5 Standard model extensions

SM extensions with right-handed muons and left-right symmetry will now be described, since an improved  $P_\mu^\pi \xi$  measurement has sensitivity to these. There are other extensions such as supersymmetry, but the expected modifications to  $P_\mu^\pi \xi$  are beyond the current experimental precision.

### 1.5.1 Right-handed muons

Following the notation of Eq. (1.7), the total probability for a  $j$ -handed muon to decay into an  $i$ -handed electron,  $Q_{ij}$ , can be defined as[8]

$$Q_{RR} = \frac{1}{4} |g_{RR}^S|^2 + |g_{RR}^V|^2, \quad (1.20)$$

$$Q_{LR} = \frac{1}{4} |g_{LR}^S|^2 + |g_{LR}^V|^2 + 3 |g_{LR}^T|^2, \quad (1.21)$$

$$Q_{RL} = \frac{1}{4} |g_{RL}^S|^2 + |g_{RL}^V|^2 + 3 |g_{RL}^T|^2, \quad (1.22)$$

$$Q_{LL} = \frac{1}{4} |g_{LL}^S|^2 + |g_{LL}^V|^2. \quad (1.23)$$

The coefficients of  $g_{ij}^\kappa$  follow from the normalisation condition, Eq. (1.9). The total probability of a right-handed muon decaying into a left or right-handed electron is then

$$\begin{aligned} Q_R^\mu &= Q_{RR} + Q_{LR} \\ &= \frac{1}{4} |g_{LR}^S|^2 + \frac{1}{4} |g_{RR}^S|^2 + |g_{LR}^V|^2 + |g_{RR}^V|^2 + 3 |g_{LR}^T|^2, \\ &= \frac{1}{2} \left( 1 + \frac{1}{3} \xi - \frac{16}{9} \xi \delta \right). \end{aligned} \quad (1.24)$$

where the final step used Eqs. (1.12) and (1.13).  $Q_R^\mu = 0$  for the SM values of  $\xi = 1$  and  $\xi \delta = 3/4$ . The most precise experimental values are shown in Table 1.4, where the published

TWIST measurements of  $\rho$ ,  $\delta$  and  $P_\mu^\pi \xi$  have already improved the constraint on  $Q_R^\mu$  by a factor of six.

Table 1.4: Probability of a right-handed muon decaying into a positron of any handedness, 90% confidence limits.

Description	$Q_R^\mu$
Best result before TWIST[18].	1.4%
Global analysis using first TWIST $\rho$ , $\delta$ results[7].	0.31%
Global analysis using newest TWIST $\rho$ , $\delta$ , and $P_\mu^\pi \xi = 1.0003 \pm 0.0038$ [10].	0.23%

## 1.5.2 Left-right symmetric electroweak models

The electromagnetic and strong interactions conserve parity, yet the weak interaction has maximal parity violation. In left-right symmetric (LRS) electroweak models, a  $(V+A)$  current is introduced that couples right-handed wave functions, restoring parity conservation at high energies[19]. The gauge group is extended from  $SU(2)_L \times U(1)$  to  $SU(2)_L \times SU(2)_R \times U(1)$ , so that right-handed fermions also transform as doublets. The distinct vector-boson fields for the  $(V-A)$  and  $(V+A)$  currents are then mediated by a  $W_L$  and  $W_R$ , which are related to the mass eigenstates  $W_1$  and  $W_2$  by

$$\begin{aligned} W_L &= W_1 \cos \zeta + W_2 \sin \zeta, \\ W_R &= e^{i\omega} (-W_1 \sin \zeta + W_2 \cos \zeta) \end{aligned} \quad (1.25)$$

where  $\zeta$  is a mixing angle, and  $\omega$  is a CP violating phase<sup>7</sup>. The  $W_R$  is much heavier than the  $W_L$ , and parity violation at low energies is a result of this mass difference. The LRS models also introduce two additional massive neutral gauge bosons. The left and right-handed interactions have separate coupling constants  $g_R$  and  $g_L$ , which correspond to  $g_{RR}^V$  and  $g_{LL}^V$  in Eq. (1.7).

The relationship between the LRS parameters and muon decay parameters has been established[19]. Assuming that neutrinos are Dirac fermions (*i.e.* particle and antiparticle

---

<sup>7</sup>CP is the product of two transformations; charge conjugation (C), which converts a particle to its antiparticle, and parity (P), an improper rotation ( $\vec{r} \rightarrow -\vec{r}$ ). CP violation refers to a change of physical laws under the combined C and P transformations.

are different), and there is no mixing in the leptonic sector, then  $P_\mu$ ,  $\xi$ ,  $\rho$  have the relationships

$$P_\mu \simeq 1 - 2t_\theta^2 - 2\zeta_g^2 - 4t_\theta\zeta_g \cos(\alpha + \omega), \quad (1.26)$$

$$\xi \simeq 1 - 2(t^2 + \zeta_g^2), \quad (1.27)$$

$$\rho \simeq \frac{3}{4}(1 - 2\zeta_g^2), \quad (1.28)$$

where

$$t = \frac{g_R^2 m_1^2}{g_L^2 m_2^2}, \quad (1.29)$$

$$t_\theta = \frac{g_R^2 m_1^2 |V_{ud}^R|}{g_L^2 m_2^2 |V_{ud}^L|}, \quad (1.30)$$

$$\zeta_g = \frac{g_R}{g_L} \zeta, \quad (1.31)$$

$\alpha$  is a CP violating phase in the right-handed CKM matrix, and  $V_{ud}^{L,R}$  are elements of the left and right-handed CKM matrices. Therefore  $P_\mu\xi$  and  $\rho$  allow limits to be set on the mass ratio,  $t$ , and the mixing angle,  $\zeta_g$ . Note that if muons are produced by  $K^+$  decays, then the substitutions  $V_{ud}^R \rightarrow V_{us}^R$  and  $V_{ud}^L \rightarrow V_{us}^L$  must be made.

There are specific cases of LRS models that make further assumptions. In “manifest” LRS models the right- and left-handed CKM matrices are assumed to be the same,  $g_R = g_L$  and  $\omega = 0$  so that  $t_\theta = t$  and  $\alpha = 0$ . Equations (1.26) and (1.27) then reduce to

$$P_\mu\xi \approx 1 - 4t^2 - 4\zeta^2 - 4t\zeta, \quad (1.32)$$

so that

$$\zeta = \frac{1}{2} \left( -t \pm \sqrt{1 - P_\mu\xi - 3t^2} \right). \quad (1.33)$$

In pseudo-manifest LRS models,  $\omega \neq 0$  (CP violation is still present), and

$$P_\mu\xi \approx 1 - 4t^2 - 4\zeta^2 - 4t\zeta \cos(\alpha + \omega). \quad (1.34)$$

For a more detailed discussion of the LRS models, see Ref. [19].

Direct searches for an additional heavy gauge boson have been made at the Tevatron. The most stringent lower mass limit is 1.00 TeV at 95% C.L., by the D0 collaboration[20]. These experiments must assume a manifest LRS model, and they are insensitive to  $\zeta$ . The Particle Data Group regularly reviews these searches[3].

The TWIST experiment’s most precise lower mass limits are  $m_2 > 360 \text{ GeV}/c^2$  (90% C.L.,

manifest LRS) and  $(g_L/g_R)m_2 > 325 \text{ GeV}/c^2$  (90% C.L., general LRS)[21]. The TWIST best limit on the left-right mixing angle is currently  $|\zeta_g| < 0.022$ [10].

## 1.6 Muon depolarisation mechanisms

In order to measure the polarisation at the time of muon production, all sources of depolarisation must be accurately known. This section will describe changes to  $P_\mu$  during the muon's transport through a magnetic field, and after thermalisation in a metal foil.

### 1.6.1 Depolarisation in a magnetic field

Non-relativistically, the propagation of a spin vector is governed by the equation

$$\frac{d\vec{s}}{dt} = \frac{g}{2} \frac{e}{m} (\vec{s} \times \vec{B}), \quad (1.35)$$

where  $g$  is the Landé  $g$  factor, which is measured as  $g = 2.00234$  for the muon[3]. The motion of a particle in a magnetic field is given non-relativistically as

$$\frac{d\vec{v}}{dt} = \frac{e}{m} (\vec{v} \times \vec{B}). \quad (1.36)$$

Equations (1.35) and (1.36) have precession frequencies  $\omega_p = e/m$  and  $\omega_s = eg/2m$  that differ by

$$\frac{\omega_p - \omega_s}{\omega_p} = \frac{g - 2}{2} = 1.17 \times 10^{-3}, \quad (1.37)$$

which demonstrates that if the momentum and spin vectors start anti-parallel, they will remain anti-parallel to a high degree while passing through a magnetic field.

The relativistic treatment of spin in electromagnetic fields can be found in Jackson[22]. In summary, the propagation is governed by the BMT (Bargmann, Michel, Telegdi) equation[23],

$$\frac{dS^\alpha}{d\tau} = \frac{e}{mc} \left[ \frac{g}{2} F^{\alpha\beta} S_\beta + \frac{1}{c^2} \left( \frac{g}{2} - 1 \right) U^\alpha (S_\lambda F^{\lambda\mu} U_\mu) \right], \quad (1.38)$$

where  $S^\alpha$  is the particle's spin 4-vector,  $\tau$  is the proper time,  $F^{\alpha\beta}$  is the electromagnetic field tensor and  $U^\alpha$  is the 4-velocity. Jackson manipulates this expression into the Thomas equation,

$$\frac{d\vec{s}}{dt} = \frac{e}{mc} \vec{s} \times \left[ \left( \frac{g}{2} - 1 + \frac{1}{\gamma} \right) \vec{B} - \left( \frac{g}{2} - 1 \right) \frac{\gamma}{\gamma + 1} (\vec{\beta} \cdot \vec{B}) \vec{\beta} - \left( \frac{g}{2} - \frac{\gamma}{\gamma + 1} \right) \vec{\beta} \times \vec{E} \right], \quad (1.39)$$

which is the form used to simulate the spin (see Section 4.4). There are theoretical limitations to Eq. (1.38), since it is derived for spatially homogeneous electromagnetic fields, and can only be used in inhomogeneous situations when the field gradients are “sufficiently small and the relevant effects are of first order in the spin variable”[24]; such inhomogeneous effects are completely negligible for TWIST ( $\sim 10^{-12}$ )[25]. In addition, quantum mechanical contributions are not a concern since the magnetic field does not change on a distance scale comparable to the de Broglie and Compton wavelengths of the muon.

### 1.6.2 Depolarisation while decelerating

When a muon encounters material, there is an electric field between the nucleus and the atomic electrons, which is Lorentz transformed to a magnetic field in the muon’s rest frame. This magnetic field rotates the polarisation vector, and for muons with momentum 29.6 MeV/c that entirely slow down in aluminium, the resulting depolarisation is  $\approx 4 \times 10^{-5}$ [26].

Inside material the muon is multiple scattered, which changes the momentum vector but not the polarisation vector. This changes their relative orientation, but this is not a depolarisation for TWIST, since the polarisation is unchanged relative to a fixed axis.

As the muon velocity becomes comparable to the atomic electron velocity, the time between collisions is reduced, and electron capture and subsequent electron loss can repeatedly take place. The muon forms muonium ( $\mu^+e^-$ )<sup>8</sup>, which is a hydrogen-like state that depolarises due to the hyperfine interaction between the muon and electron spins (there is a transfer of the muon’s spin to the electron)[28]. This only becomes important at a few keV, and does not occur in metals since the conduction electron concentration effectively screens the muon from interactions with individual electrons[29]. For the current measurement, muons were selected that stopped inside a metal target, so that depolarisation from muonium formation is not a concern.

Finally, there is depolarisation due to muon-electron scattering. This has been calculated for 29.6 MeV/c muons, and is at the level of  $1 \times 10^{-5}$ [29, 30].

---

<sup>8</sup>The “onium” suffix is usually reserved for bound states of a particle and its antiparticle, such as positronium, pionium and quarkonium. Therefore the assignment of “muonium” to the state  $\mu^+e^-$  is not strictly correct, and means that the bound state  $\mu^+\mu^-$  is referred to as the “bound muon-antimuon state”. After more than two decades of widespread usage, the name “muonium” for  $\mu^+e^-$  was eventually recommended by the International Union of Pure and Applied Chemistry (IUPAC)[27] in 2001.

### 1.6.3 Depolarisation after thermalisation

In the present experiment, muons were stopped in aluminium and silver foils of purity greater than 99.999%, while immersed in an external 2.0 T longitudinal magnetic field. After motional thermalisation, the muons can be depolarised by nuclear dipole moments, conduction electrons, and paramagnetic impurities. The form of the resulting depolarisation has been studied by the condensed matter community using the  $\mu^+$ SR technique[31], but not to the precision required for this measurement of  $P_\mu^\pi \xi$ .

The behaviour of the muon after motional thermalisation and the possible depolarisation mechanisms will now be described.

#### Muon motion

The muon is positively charged, which limits its instantaneous position to interstitial sites (*i.e.* between nuclei), or substitutional sites, (*i.e.* “vacancies”, where a nucleus is absent from the lattice). When nearly thermalised, a muon lowers its energy by attracting a screening charge of conduction electrons[32]. After motional thermalisation, room temperature ensures that a muon is not stationary, but instead it diffuses (“hops”) between energetically allowed sites before decaying. The conduction electrons in aluminium and silver efficiently screen the ionic potentials, allowing for high mobility, even over macroscopic distances of  $\approx 1 \mu\text{m}$ [33, 34].

Muons can become trapped at defects, of which there are a wide variety. The most common originate from the manufacturing process, such as when an aluminium sheet is cold-rolled to produce a thin foil, and these defects can limit the muon mobility with a strong sample dependence[34]. The defects can be enhanced by quenching, where the sample is heated and then rapidly cooled. They can be removed by annealing, a process in which the metal is maintained close to melting point for several hours and then slowly cooled. The current silver target was annealed in an inert argon atmosphere, after machining. High purity aluminium has been studied under annealing and quenching, over a temperature range of 19 K to 900 K: most defects were found to be absent after allowing the quenched sample to reach room temperature[35].

Thermalisation of the muon itself can result in lattice defects. The muon imparts recoil energy to the lattice on a time scale  $10^{-17}$  s, and the lattice distributes this energy to neighbouring atoms in about  $\sim 10^{-12}$  s[36]. A nucleus can be knocked out of its lattice position and into an interstitial site, leaving a vacancy (a “Frenkel pair”). However, these vacancies are unlikely to affect the muon’s diffusion since they are eliminated in  $\sim 10^{-11}$  s[36], and the location of thermalisation is of order  $1 \mu\text{m}$  from the last defect introduced[37].

## Nuclear dipole moments

The magnetic field experienced by a muon due to nuclei and lattice impurities can be modelled as static, isotropic and Gaussian. At each hop, the muon sees a new, randomised field, and the depolarisation is then given by[38, 39],

$$P_\mu(t) = P_\mu(0) \exp \left\{ -\frac{2\Delta^2}{\nu^2} [\exp(-\nu t) - 1 + \nu t] \right\}, \quad (1.40)$$

where  $\gamma_\mu$  is the muon's gyromagnetic ratio,  $\Delta$  is a parameter describing the magnetic field distribution<sup>9</sup> and  $1/\nu$  is the mean time between hops. If an external field  $\vec{B}_{\text{ext}}$  is now applied in a direction *transverse* to the muon polarisation, the muon spins precess and are depolarised according to the Abragam formula<sup>10</sup>,

$$P_\mu(t) = P_\mu(0) \exp \left\{ -\frac{\Delta^2}{\nu^2} [\exp(-\nu t) - 1 + \nu t] \right\} \cos(\omega_\mu t), \quad (1.41)$$

where  $\omega_\mu = \gamma_\mu B_{\text{ext}}$ . In the “motional narrowing” limit, the muons move quickly so that  $\nu$  is large,  $\exp(-\nu t) \rightarrow 0$ , and the envelope of Eq. (1.41) limits to an exponential time dependence. In the static limit, the envelope limits to a Gaussian time dependence. If a *longitudinal* field  $B_0$  is applied instead, the static relaxation function becomes[41],

$$\begin{aligned} P_\mu(t) = & 1 - \frac{2\Delta^2}{\omega_0^2} [1 - \exp(-\frac{1}{2}\Delta^2 t^2) \cos \omega_0 t] \\ & + \frac{2\Delta^4}{\omega_0^3} \int_0^t \exp\left(-\frac{1}{2}\Delta^2 \tau^2\right) \sin \omega_0 \tau d\tau, \end{aligned} \quad (1.42)$$

where  $\omega_0 = \gamma_\mu B_0$ , and the longitudinal field is seen to suppresses the depolarisation due to nuclear dipole moments. The largest observed field on a muon in a crystal cell is  $\Delta/\gamma_\mu = 4.7 \text{ G}$ [39], and the field at the metal target in TWIST is longitudinal with  $B_0 = (20 \times 10^3) \text{ G}$ , so that  $(2\Delta^2/\omega_0^2) < 10^{-7}$ . Depolarisation by nuclear dipole moments is therefore negligible for TWIST in the static limit (no muon hopping)<sup>11</sup>.

Depolarisation in aluminium and silver from nuclear dipole moments has been measured in  $\mu^+$ SR experiments, using a transverse magnetic field arrangement[31]. There are more studies

---

<sup>9</sup>Each field component is modelled by  $\mathcal{D}(B_{\text{local}}) \sim \exp[-B_{\text{local}}^2/(2\Delta^2/\gamma_\mu^2)]$ , so that  $\Delta/\gamma_\mu$  is the standard deviation of a Gaussian distribution.

<sup>10</sup>See p.439 of Ref. [40]. Note that this is also called the Anderson form, or the Kubo-Tomita form.

<sup>11</sup>If the muon hops at exactly the Larmor frequency, it “sees” a magnetic field that fluctuates at the resonant frequency to drive transitions between Zeeman states. Since the muon moves stochastically, this mechanism is only relevant for a small fraction of hops. Usually the higher the field, the smaller the fraction, and the slower the relaxation[34].

on aluminium since its nuclear dipole moment is about 35 times larger than silver. Even with its large dipole moment, high purity aluminium leads to almost negligible depolarisation down to 1 K[42, 43, 44, 45, 46]. As a result, experimenters have to dope the sample with impurities to actually measure depolarisation[32, 47, 48].

There is a contradictory measurement in Ref. [49], which used aluminium and silver targets of 99.99% purity in a *transverse* field arrangement, at room temperature, and observed a Gaussian form for the depolarisation in aluminium. They explained this anomalous result as muons trapping in defects, which originated from the cold-rolling during manufacture of the foil[50]. Note that a later publication by the same group used a *longitudinal* field, and found no clear evidence of depolarisation, as expected from Eq. (1.42).

### Korringa relaxation

A hyperfine contact interaction between the muon spin and the conduction electron spins can lead to a depolarisation. The theory for such an interaction was originally treated in the context of NMR<sup>12</sup> by Korringa[51], and is therefore named “Korringa relaxation”. In the context of muons, the conduction electrons hop on and off the muon, making the net hyperfine coupling experienced an average of the electron spin orientations[52, 53]. A simultaneous flip of the electron and muon spins can take place, with the energy provided by a change in the electron’s kinetic energy[40]. The participating electrons are within  $kT$  of the Fermi surface, and the exponential relaxation rate ( $\lambda$ ) is proportional to  $K_\mu^2 T$ . The constant  $K_\mu$  is the “muon Knight shift”, which is a characteristic value associated with the host material; the signature of Korringa relaxation is an increase in rate with temperature, and insensitivity to applied magnetic field[52].

Korringa relaxation has been observed in several non-magnetic metals (lead, cadmium, zinc, copper), where the relaxation rates increased with temperature, and were robust to field changes in the range 0.010 T to 0.200 T[54].

---

<sup>12</sup>In NMR spectroscopy, a substance is immersed in a static magnetic field and then exposed to electromagnetic (EM) radiation. For the nuclei in the substance that have intrinsic magnetic moments (those with an odd number of protons or neutrons), the static magnetic field creates an energy difference between the spin states. The frequency of the EM radiation is swept, and peak absorption will occur (“resonance”) when the energy of the photons matches the energy difference between the spin states.

## Impurities

The aluminium stopping target was purchased from Goodfellow, who gave the typical impurities as Cu 0.3 ppm<sup>13</sup>, Fe 0.3 ppm, Mg 1.2 ppm, and Si 0.8 ppm. The silver stopping target was purchased from ESPI Metals, who gave the typical impurities as Fe 2 ppm, Bi < 2 ppm, Cu 0.6 ppm, and Pd 0.6 ppm. The impurities take the place of an aluminium or silver nucleus. In aluminium, the muons are not trapped by impurities above  $\approx 100$  K[46]. In silver, there is evidence that room temperature trapping at impurities can occur[55].

The non-paramagnetic ions can depolarise muons due to their nuclear dipole moments, but this is heavily suppressed by a longitudinal magnetic field (see Section 1.6.3). Paramagnetic ions (Fe in this case) are a concern since they can depolarise due to their electronic dipole moment, which is much larger than the nuclear dipole moment, producing fields up to 1 kG at a distance of one lattice spacing[56, 57]. The depolarisation form for a muon trapped at a paramagnetic ion is exponential[40, 55, 56].

## Summary

Muon spin relaxation due to nuclear dipole moments, whether the source is metal nuclei or non-paramagnetic impurities, is heavily suppressed by the presence of a longitudinal field. Even if there were contributions from nuclear dipole moments, the muons are expected to be in rapid motion, for which the appropriate form is exponential. If the muons become trapped at defects or vacancies, which is possible in our aluminium foil since it was not annealed, the longitudinal field holds the muon spin against depolarisation. Later it will be shown that the measured relaxation rates for silver and aluminium differ by a factor of two, yet the nuclear dipole moments differ by a factor of 35, providing further evidence that the depolarisation is not from nuclear dipole moments.

In the silver foil, trapping at paramagnetic impurities cannot be excluded. The appropriate form is then exponential, as long as the muons diffuse sufficiently fast to find the impurities promptly, which is a good assumption in an annealed sample such as the TWIST foil. For both foils, Korringa relaxation is expected to occur; this has been observed in other metals, and has an exponential form.

---

<sup>13</sup>ppm = parts per million. A concentration of 1 ppm corresponds to one impurity for every 100 crystal cells.

## 1.7 Previous $P_\mu^\pi \xi$ measurements

In 1956, Lee and Yang observed that parity is conserved in strong and electromagnetic interactions, but in weak interactions “is so far only an extrapolated hypothesis unsupported by experimental evidence”[58]. They suggested several experiments to investigate parity conservation in the weak interaction, including the asymmetry of muon decay.

The angular distribution of decay positrons will generally follow a distribution  $(1 + a \cos \theta)$ . For  $\eta = 0$ ,  $a = P_\mu^D \xi / 3$ , where  $\xi$  is the intrinsic asymmetry parameter, and  $P_\mu^D$  is the polarisation of the muon at the moment of decay. The polarisation at the time of muon production can only be inferred if all sources of depolarisation are evaluated.  $a = 0$  implies that parity is conserved, and  $P_\mu \xi = \pm 1$  implies maximal violation of parity.

Two classes of asymmetry measurements will now be described:  $P_\mu^\pi \xi$  and  $P_\mu^K \xi$ , where muons are produced from pion and kaon decay respectively. The results are interpreted differently in the context of LRS models (see Section 1.5.2). In addition,  $\tau$  decay experiments have confirmed  $P_\mu^\tau \xi$  is consistent with 1.0 using the modes  $\tau^\pm \rightarrow \mu^\pm \nu \bar{\nu}$  and  $\tau^\pm \rightarrow e^\pm \nu \bar{\nu}$ , but these measurements have statistical uncertainties greater than 10%[59, 60, 61].  $\tau$  decay experiments are more useful as a check on lepton universality, rather than as a precision asymmetry measurement.

### 1.7.1 Measurements of $P_\mu^\pi \xi$

A year after Lee and Yang’s publication, positive muons from pion decay were stopped in carbon, and the angular distribution of decay positrons was found to follow  $(1 + a \cos \theta)$ , and “ $a = -\frac{1}{3}$  with an estimated error of 10%”[62]. Assuming no depolarisation took place while slowing down, stopping, and during the  $1 \mu\text{s}$  the muon spent in the carbon target, this result suggested  $P_\mu \xi = 1.0 \pm 0.1$ , which was consistent with maximal parity violation.

Over the next three years (1957 to 1960) many similar experiments took place[63]. A popular technique was to stop a beam of pions in nuclear emulsion<sup>14</sup>; this had the advantage of delivering muons with full polarisation, but the disadvantages of low statistics and poorly determined depolarisation within the emulsion itself due to muonium formation. This depolarisation was found to depend on the applied magnetic field, yielding values of  $P_\mu \xi$  in the range  $0.33 \pm 0.03$  (zero field) to  $0.97 \pm 0.06$ [63].

Other techniques suffered from problems in producing a high polarisation muon beam. Before the surface muon beam was developed, a production target was simply placed inside

<sup>14</sup>A photographic plate is exposed to particles and later developed. The emulsion is predominantly silver bromide by weight, but by number of atoms, it’s 25% silver bromide, 75% gelatin[63].

a cyclotron, leading to a a muon beam with poorly determined polarisation.

The Bardon, Berley and Lederman experiment instead used a  $\pi^+$  beam that decayed in-flight, to produce a highly transverse polarised  $\mu^+$  beam at the Jacobian angle[64]. The  $\mu^+$  were stopped in a bromoform target, which had small but unknown depolarising effects; in consequence, the experiment's result was a lower limit. Depolarisation from magnetic fields was eliminated by using Helmholtz coils to cancel the cyclotron's field. Decay positrons were detected with opposing counters. A solenoid surrounding the target rotated the muon spin by  $\pm 90^\circ$ , allowing the  $e^+$  distribution to be turned around in one hour cycles. The experiment found  $|\xi| \geq 0.97 \pm 0.05$ .

Muons were also stopped in liquid hydrogen in bubble chamber experiments. The particles left ionisation tracks that were curved by a magnetic field to determine their momentum. The most accurate experiment was carried out by Plano, who measured  $P_\mu\xi$ ,  $\delta$  and  $\rho$ , and found  $|\xi| = 0.94 \pm 0.07$ [65].

There was apparently no improvement in direct measurements until 1967, when a nuclear emulsion experiment with a 14 T pulsed magnetic field determined that  $P_\mu\xi = 0.975 \pm 0.015$ , which is  $1.7\sigma$  from the (V-A) prediction[66].

Prior to the TWIST experiment, the most precise direct measurement of  $P_\mu^\pi\xi$  was reported in Ref. [67]. A  $\pi^+$  beam with a momentum of 150 MeV/c decayed in-flight, and a transversely polarised muon beam was extracted close to the Jacobian angle; this is the same approach taken by the Bardon experiment described above[64]. The muons were moderated by aluminium and stopped in a Beryllium (Be) target. The  $\mu^+$ SR technique was then used to measure the decay  $e^+$  asymmetry, with the muon spins precessed by a 3 mT field. A pure exponential depolarisation form for  $P_\mu(t)$  was assumed in the Be target. The experiment did not measure the decay  $e^+$  momentum, so there was no magnetic field requirement, and hence no associated systematic uncertainty. The contribution from muons stopping in a trigger scintillator immediately before the Be target was measured by removing the target, and found to be negligible ( $2 \times 10^{-3}$  per event). The final result was  $1.0027 \pm 0.0079$  (stat.)  $\pm 0.0030$  (syst.).

The most precise direct measurement is  $P_\mu^\pi\xi = 1.0003 \pm 0.0006$  (stat.)  $\pm 0.0038$  (syst.), published by the TWIST collaboration in 2006[21, 57]. The leading term in the systematic uncertainty was  $33 \times 10^{-4}$ , due to limitations in the reproducibility of the muon beam's initial position and angle; the current measurement aims to reduce this uncertainty by improving the knowledge of the muon beam and solenoidal magnetic field through which the beam passes.

In Fig. 1.5, the *direct* measurements that have been described so far are summarised. All are seen to be consistent with  $P_\mu\xi = 1$ . Additional *indirect* measurements are possible

using the result  $P_\mu \xi \delta / \rho > 0.99682$  (90% C.L.) [29, 30], where muons were stopped in several targets, including high purity silver and aluminium foils. The confidence interval can be combined with the latest  $\rho$  and  $\delta$  measurements to determine  $0.99524 < P_\mu^\pi \xi \leq \xi < 1.00091$  (90% C.L.) [10].

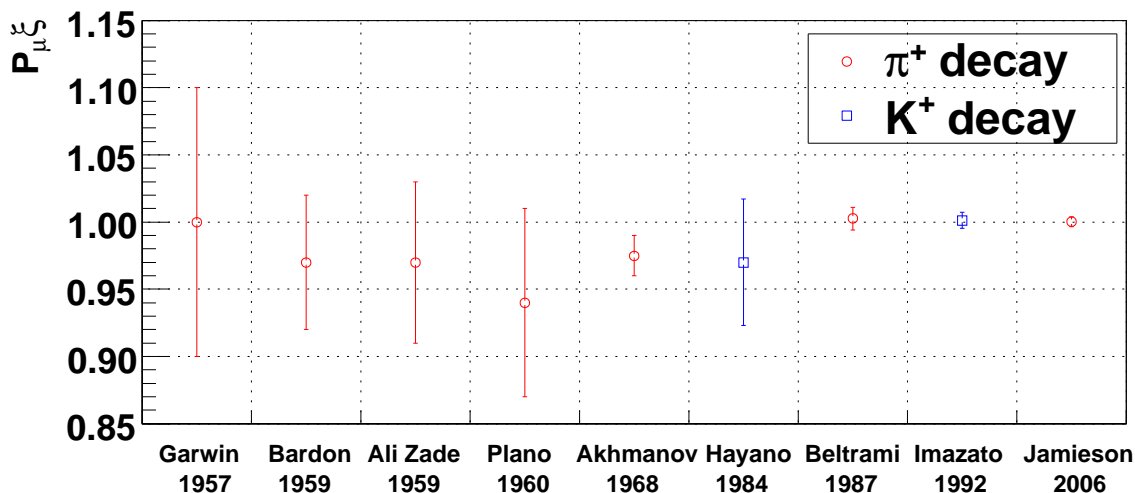


Figure 1.5: Previous direct measurements of  $P_\mu \xi$  with uncertainties less than 10%. The statistical and systematic uncertainties have been added in quadrature. Measurements are from Refs [21, 62, 64, 65, 66, 67, 68, 69, 70].

### 1.7.2 Measurements of $P_\mu^K \xi$

The first measurement of  $P_\mu^K \xi$  with an uncertainty below 10% is described in Refs. [69, 71]. (There were three prior experiments that were consistent with  $P_\mu^K \xi = 1$ , but with uncertainties  $> 10\%$  [72, 73, 74].) A 236 MeV/c muon beam was produced from stationary  $K^+$  decays via the mode  $K^+ \rightarrow \mu^+ \nu$ . The  $\mu^+$  were degraded by carbon, and stopped in an aluminium target of 99.99% purity. The muon trajectory immediately before the target was measured using a pair of orthogonal multiwire proportional chambers (MWPCs), which established the muon spin, and the decay positrons were measured with a different pair of MWPCs. A transverse magnetic field was applied to precess the muon spin, and the asymmetry's dependence on time was fit to determine  $P_\mu^K \xi = 0.970 \pm 0.047$  (stat.)  $\pm 0.005$  (syst.), under the assumption of no depolarisation while slowing down, and within the aluminium target; these are safe assumptions at the few percent level of precision. The measurement was limited by statistical uncertainty.

A more precise measurement using a similar technique is described in Ref. [70]. The muon source was the same, but with higher flux, and the muons were again degraded by carbon and stopped in high purity aluminium ( $> 99.999\%$  in this case). The incident muon beam was measured more carefully to determine its spin, using four  $x$  and  $y$  layers of drift chambers before the carbon degrader, and two MWPCs after the degrader and before the aluminium stopping target. The decay positrons were measured using two arms, each with four horizontal and four vertical drift chambers. A transverse magnetic field precessed the muon's spin. The polarisation was allowed to relax in the aluminium target, but the form for  $P_\mu(t)$  was not stated. The final result was  $P_\mu^K \xi = 1.0013 \pm 0.0030$  (stat.)  $\pm 0.0053$  (syst.), where the leading systematic uncertainty was from a correction due to knock-on electron production in the stopping target.

# Chapter 2

## Apparatus

### 2.1 Overview

This chapter will describe the production and delivery of muons, the time expansion chambers that measured the muon beam, and the detector used to track the muons and reconstruct the positron trajectories. The alignment of the apparatus will also be described. There are publications that provide more detail on the detector[75] and the time expansion chambers[76]. The beam line has been described in an earlier publication[77], but the tune used for the current experiment is only available as an internal report[78].

### 2.2 Muon production and delivery

#### 2.2.1 Location

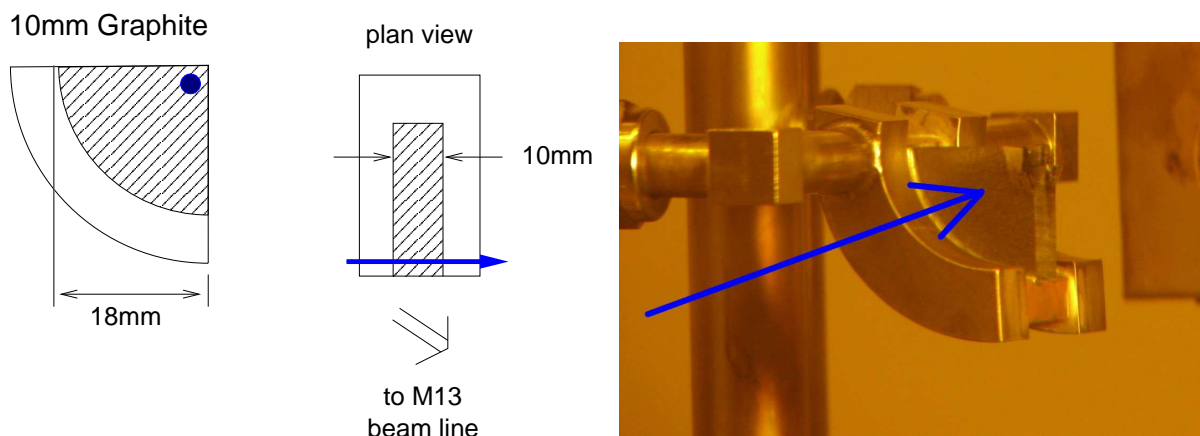
The experiment was performed at the TRIUMF laboratory, located on the University of British Columbia's campus in Vancouver. The TRIUMF cyclotron delivered a 500 MeV proton beam to the T1 production target in the TRIUMF meson hall. The protons were produced in bunches of  $\approx 4$  ns width, separated by 43 ns. A 10 mm thick graphite production target was used at the T1 position. The particles from the graphite target were selected by a secondary beam line named M13. The experiment occupied the M13 beam line area from November 2001 to September 2007.

#### 2.2.2 Muon production

The proton beam incident on the graphite target produced pions. The dominant pion decay mode is to a muon and a neutrino, a two body process that ensures the muon has momentum 29.79 MeV/c in the pion centre of mass frame. The experiment selected positive muons that decayed from stationary pions at the surface of the production target. These are called "surface muons", and are highly polarised as described in Section 1.3.

The graphite production target was housed in a water cooled steel holder; it is shown

schematically in Fig. 2.1(a). The targets typically lasted longer than a month, and were changed either due to destructive damage from the proton beam (see Fig. 2.1(b)) or after producing measurable levels of radioactive gas; this did not impair the data quality since the gas was mostly stopped by a  $3\ \mu\text{m}$  polyester (Polyethylene terephthalate) window valve in the beam line<sup>15</sup>.



(a) Schematic of the graphite production target. The blue arrow indicates the proton beam.

(b) Photograph of a damaged graphite production target. The blue arrow indicates the proton beam direction.

Figure 2.1: Schematic and photograph of a graphite production target.

### 2.2.3 M13 beam line

The M13 beam line[77] that selected and transported the muons is shown schematically in Fig. 2.2. The graphite production target is labelled as 1AT1, and this was seen by M13 at  $135^\circ$ . The channel had two dipole magnets (B1 and B2) that selected the particle momentum by bending the beam through  $60^\circ$ , three vertically focusing quadrupole magnets (Q1, Q4, Q7), and four horizontally focusing quadrupole magnets (Q2, Q3, Q5, Q6). The M13 beam line was upgraded for the current measurement by adding current sources to certain quadrupole magnets, allowing additional muon beam steering; this technique will be described in Section 2.4.

The S1 label in Fig. 2.2 indicates the position of a horizontal slit and vertical jaw, which

<sup>15</sup>During the 2006 data acquisition, a small amount of gas was able to enter the detector via a bypass line. The particles making it to the detector were successfully identified using the off-line data analysis. For the 2007 data acquisition, a pump was installed to remove any radioactive gas in the bypass line.

controlled both the rate and the emittance of the beam. A compromise was reached that minimised emittance while maintaining an acceptable rate; this measurement used between  $2000\text{ s}^{-1}$  and  $5000\text{ s}^{-1}$ . Even at the highest rate the muons were separated by nearly 100 lifetimes, ensuring that most events had just one muon in the detector at a time.

There are three possible focal points (F1, F2 and F3) indicated in Fig. 2.2. The tune for this measurement aimed for horizontal focii at F1, F2 and F3, and a vertical focus at F3. The beam's vertical divergence was limited at F2 by a slit. After B1 had dispersed the beam, the position of a horizontal slit at F1 selected the average momentum, and the width of this slit defined the momentum resolution of the channel.

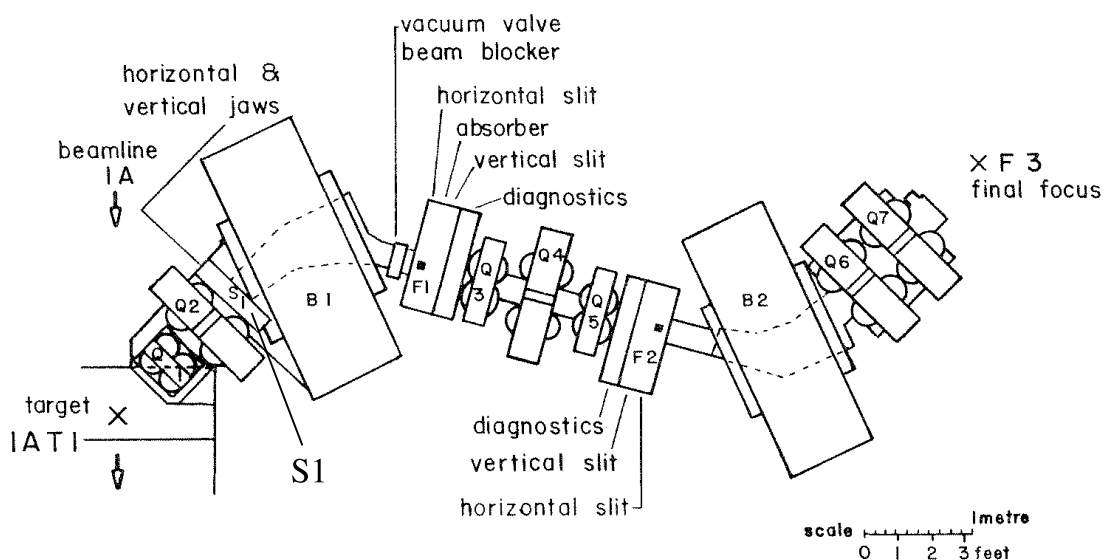


Figure 2.2: Schematic of the M13 beam line[77]. The distance from the production target to the centre of the detector (not shown) is approximately 10m.

### 2.2.4 Beam line momentum calibration

The initial muon momentum distribution was measured on a weekly basis using the dependence of the muon rate on channel scaling. An example is shown in Fig. 2.3, where the shape arises from a convolution of the initial muon momentum at the target and the approximately Gaussian acceptance of the channel. The “surface muon edge” is a calibration feature, corresponding to muons from the surface of the target that have a momentum of exactly  $29.79\text{ MeV}/c$  (kinetic energy  $4.12\text{ MeV}$ ). Note that for  $p > 30\text{ MeV}/c$  the rate is non-zero, since muons from pion decay-in-flight are accepted.

Operating at the surface muon momentum is undesirable since the rate is low. Instead the experiment used an average momentum of 29.6 MeV/c (kinetic energy 4.07 MeV) corresponding to a thin layer close to the production target’s surface. The selected muons underwent a small amount of multiple scattering inside the production target, which breaks the relationship between the momentum and spin.

The beam line was set to a momentum resolution<sup>16</sup> of FWHM 0.7%, which is a factor two smaller than the previous measurement. This increased the initial beam polarisation, but not by a significant amount.

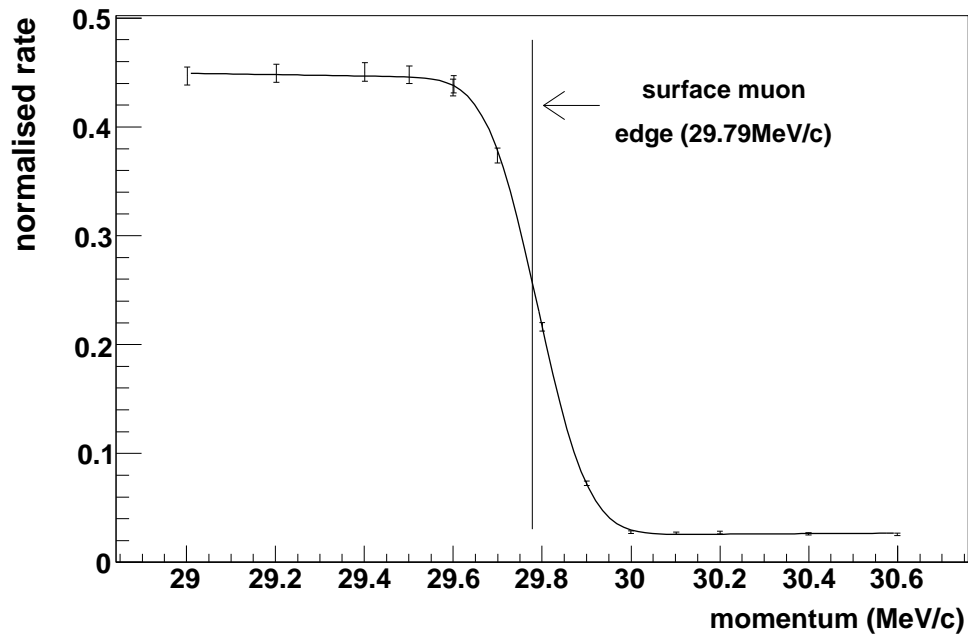


Figure 2.3: Rate dependence on channel momentum. The shape arises from a convolution of the initial muon momentum at the target and the beam line’s approximately Gaussian acceptance. The “normalised rate” on the ordinate is proportional to muon rate divided by the proton current.

<sup>16</sup>The momentum resolution,  $\Delta p/p$ , is sometimes referred to as the momentum “bite”. In either case the meaning of  $\Delta p$  must be qualified, since there can be confusion between a Gaussian RMS and FWHM.

### 2.2.5 Particles delivered

The muon beam had a contamination of “cloud muons”, “beam positrons”, pions and protons. The “cloud muons” originated from pions moving between the production target and B1 that decayed with a muon in the direction *opposite* to their motion. This decay must occur before the pion reaches the momentum selection at B1, and is therefore prompt. These muons had opposite polarisation to the surface muons, and were removed by a conservative time-of-flight cut.

The contamination of “beam positrons” mainly originated from muon decays within the production target and surrounding materials. There were also contributions from neutral pion decays ( $\pi^0 \rightarrow \gamma\gamma$ ) since the  $\gamma$ 's shower in the production target and beam pipe. The trigger scintillator was set to mostly ignore positrons, but they were high rate (1.9 to 3.6 times the muon rate, depending on beam tune) and therefore still produced a significant background in muon-triggered events. The off-line analysis easily identified the beam positron trajectories since they passed through the entire detector.

The proton contamination was removed by a beam line window, and the pion contamination could be separated by time-of-flight due to their heavier mass<sup>17</sup>. The time-of-flight selection is described later in Section 3.3.1.

### 2.2.6 M13 configurations

The alignment and calibration runs used different M13 settings. For example, the drift chamber alignment used higher momentum pions, and the calibration of the time expansion chambers used a spread muon beam. Three smaller data sets were taken at lower momentum as a consistency check. The special configurations and data sets are described in more detail in Section 5.3.

---

<sup>17</sup>The experiment has observed the decay  $\pi^+ \rightarrow e^+\nu_\mu$ , by selecting pions using their time-of-flight and pulse height in the trigger scintillator. However the statistics were too low to make a useful energy calibration feature.

## 2.3 Measuring the muon beam

The muon beam was measured at the end of the M13 channel, before the muons had encountered any significant material or magnetic field, so that the momentum and spin vectors were anti-parallel to an acceptable approximation. A simulation then propagated the muons to the stopping target to estimate the final polarisation of the beam. A pair of orthogonal time expansion chambers (TECs) measured  $x$  ( $y$ ) and  $\theta_x$  ( $\theta_y$ ). The mass of the system was kept as low as possible to minimise multiple scattering, which would otherwise degrade the resolution. Despite these efforts, the multiple scattering meant that the TECs could not remain in place during normal data acquisition. Instead the modules were inserted on a weekly basis for approximately one hour of beam measurements.

The positioning of the box containing the modules is shown in Fig. 2.4. The TEC modules were located close to the F3 focus, where the beam had a small extent. When the muon beam encountered the TECs, it had passed through no material except for a single thin ( $6\ \mu\text{m}$  Mylar) beam line window. The low magnetic field meant that trajectories were well approximated by straight lines, which simplified the analysis.

The TEC modules are labelled “X Module” and “Y Module” in Fig. 2.5. Each module was 8.0 cm long with an active area of  $6.0\ \text{cm} \times 6.0\ \text{cm}$ . They were inside a box that was filled with low pressure (8 kPa) dimethyl ether<sup>18</sup> gas that constantly flowed at a rate of  $100\ \text{cm}^3/\text{min}$ . An electric field was maintained over the drift volume by a graded voltage applied to the (drift) field wires, as shown in Fig. 2.6. Charged particles ionised the gas, and the ionisation electrons then drifted towards the sense plane. The electrons entered a high field region, separated by grid (“guard”) wires. In this “multiplication region” the electrons were accelerated towards small diameter ( $25\ \mu\text{m}$ ) sense wires where they avalanched and created a signal. During the analysis, the time of the signal relative to the muon trigger was converted into a distance using space-time relationships (STRs). Each TEC had 24 sense wires at 0.2 cm pitch. Thicker shield wires were placed between the sense wires to ensure that the avalanches remained localised.

The electric field in the drift volume was nominally uniform with a strength of 16 V/mm. However, there were non-uniformities of up to 10% due to the field at the sense planes leaking into the drift volume, and by  $\sim 1\%$  due to modular interference[76]. Ultimately the non-uniformity in the electric field is addressed by iterating the STRs using real tracks.

The analysis and calibration of the TECs is described in Appendix G.

---

<sup>18</sup>This gas was chosen since it was already in use in the drift chambers. See Section 2.8 for the advantages of dimethyl ether.

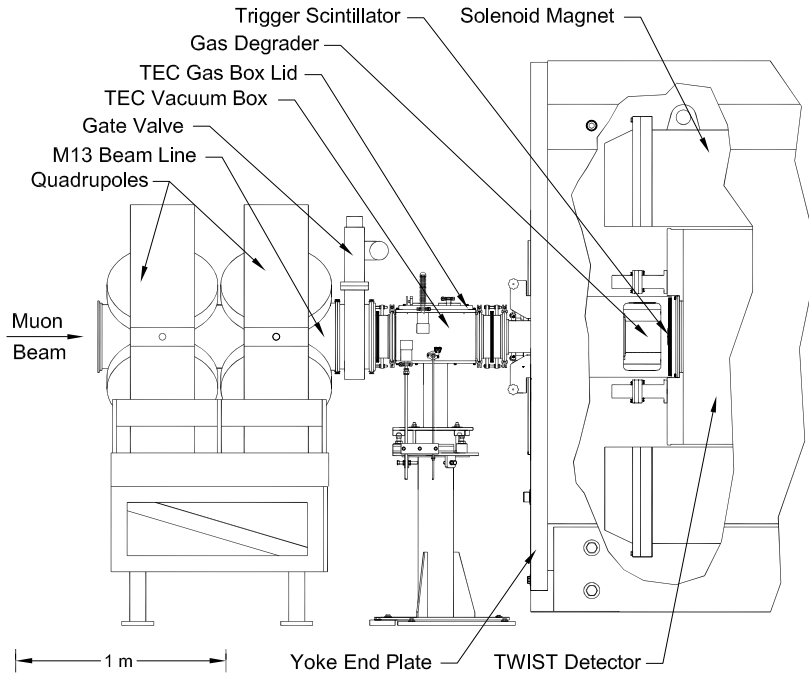


Figure 2.4: Positioning of the time expansion chambers relative to the M13 beam line and solenoid[76].

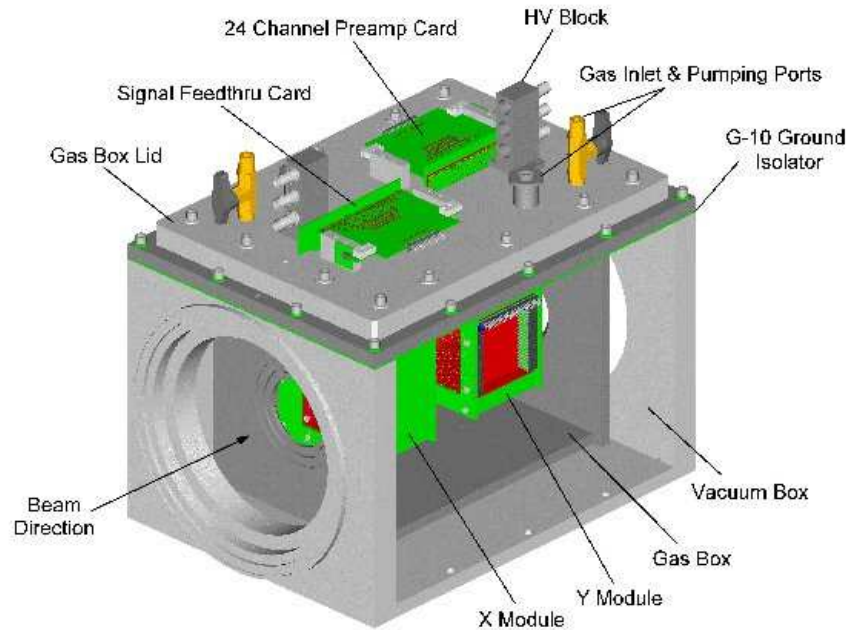
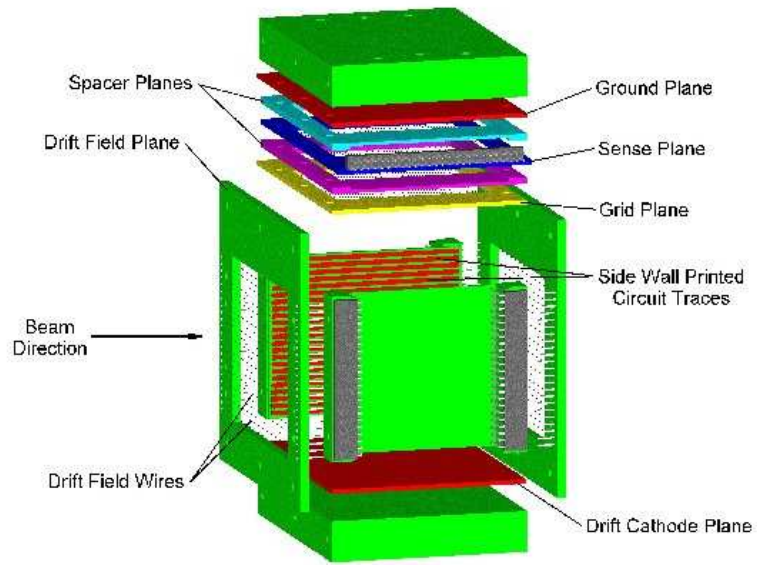
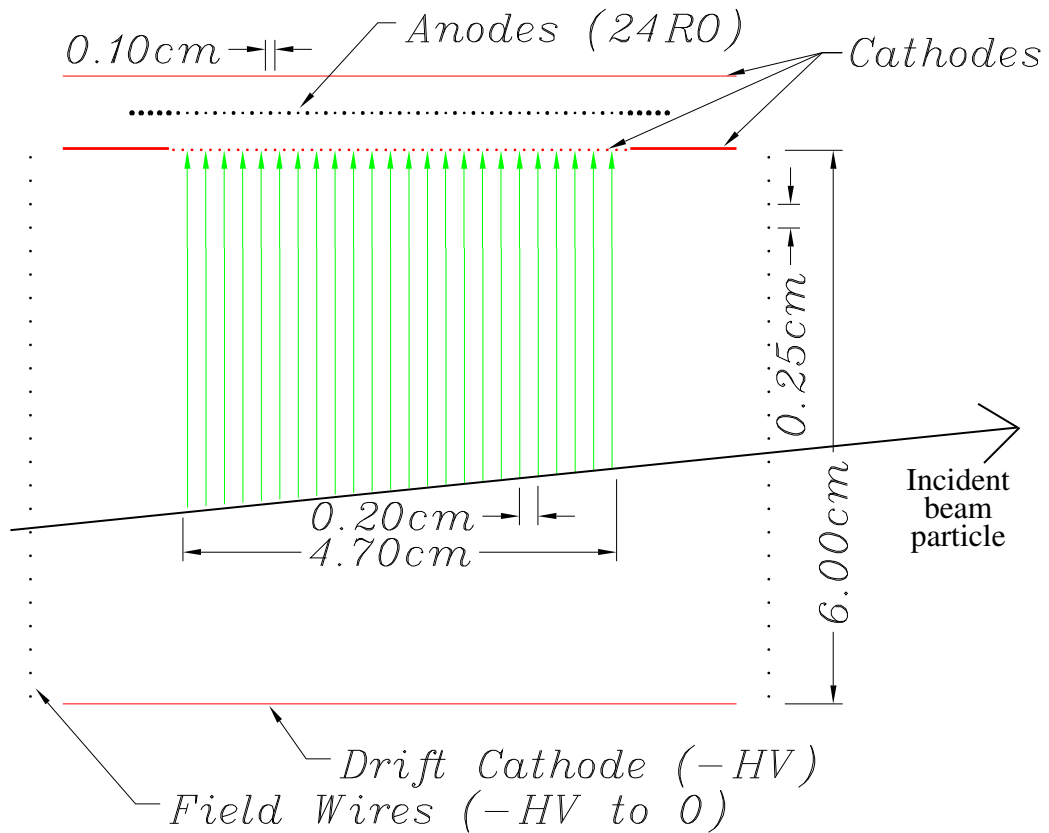


Figure 2.5: Location of the time expansion chamber modules and their electronics inside the gas box[76].



(a) Components of a single time expansion module[76].



(b) Cross section through a single time expansion module. The initial ionisation is indicated by the green line through the entire module. The green arrows show the direction of the drift electrons[57].

Figure 2.6: An individual time expansion chamber module.

## 2.4 Quadrupole steering

In the previous  $P_\mu^\pi \xi$  analysis the muon beam was found to be approximately 1 cm too high at the TECs, with an average  $y$ -angle of about 20 mrad; this resulted in a larger depolarisation than the design specification. The deflection was blamed on interference between the quadrupoles Q3, Q4, Q5, and the solenoid's fringe field[79]. The dipole magnets only steered horizontally, so they were not able to correct for this deflection. A major improvement for the current  $P_\mu^\pi \xi$  measurement was a correction of the deflected beam by applying additional currents to the poles of the M13 quadrupole magnets<sup>19</sup>.

The left hand side of Fig. 2.7 illustrates the behaviour of an unmodified vertically focusing quadrupole magnet. In the vertical direction the charged particles are focussed, and in the orthogonal horizontal direction the particles are defocussed. If the poles of the quadrupole are asymmetrically excited using additional current sources then the field zero is shifted to a new location, and a charged beam is both focussed and steered[81]. For example, the right hand side of Fig. 2.7 shows that current sources added to two of the poles results in a horizontal steering force.

There are theoretical calculations of the steering effect[81]. However, since the experiment is able to precisely measure the muon beam after the quadrupoles and before the detector's fringe field, no theoretical predictions were made. The beam was simply observed with the TECs while increasing currents were applied to the pole(s) of the accessible quadrupole magnets.

Five power supplies were available to be placed over the poles of Q4, Q6 and Q7. Horizontal steering used Q6 and the dipole magnet B2. Q4 and Q7 were used to steer vertically, with Q4 providing most of the steering. The response of the beam's average position ( $\langle x \rangle, \langle y \rangle$ ) and angle ( $\langle \theta_x \rangle, \langle \theta_y \rangle$ ) were determined by steering with each element separately. While attempting to steer primarily in the  $x$  or  $y$  direction, all four parameters of the beam were changed. For example, Fig. 2.8 shows that when primarily steering horizontally, there is a second order beam movement in the vertical direction.

Relationships such as the example in Fig. 2.8 were determined for each quadrupole. Fortunately the response was almost always linear, and assuming the beam's response didn't

---

<sup>19</sup>Using quadrupoles to deflect a charged particle beam is not a new technique. Prior to installation in M13, it was already in use in the TRIUMF proton beam line. Also new beam lines such as  $\mu E4$  at PSI are being constructed with quadrupole steering as part of the design[80].

change as the beam was steered, the results were combined according to

$$\begin{pmatrix} \langle x \rangle' \\ \langle y \rangle' \\ \langle \theta_x \rangle' \\ \langle \theta_y \rangle' \end{pmatrix} = \begin{pmatrix} \langle x \rangle \\ \langle y \rangle \\ \langle \theta_x \rangle \\ \langle \theta_y \rangle \end{pmatrix} + \begin{pmatrix} r_x^{B2} & r_x^{Q6} & r_x^{Q4} & r_x^{Q7} \\ r_y^{B2} & r_y^{Q6} & r_y^{Q4} & r_y^{Q7} \\ r_{\theta_x}^{B2} & r_{\theta_x}^{Q6} & r_{\theta_x}^{Q4} & r_{\theta_x}^{Q7} \\ r_{\theta_y}^{B2} & r_{\theta_y}^{Q6} & r_{\theta_y}^{Q4} & r_{\theta_y}^{Q7} \end{pmatrix} \begin{pmatrix} \Delta B2 \\ I_6 \\ I_4 \\ I_7 \end{pmatrix},$$

where the primed quantities are the final beam parameters,  $\Delta B2$  is the change in B2's magnetic field, and the  $I$  terms refer to the additional currents applied to the quadrupoles. The  $r$  quantities are the gradients of relationships such as Fig. 2.8, where the subscript refers to the beam parameter and the superscript refers to the steering element. For example,  $r_x^{Q6}$  and  $r_y^{Q6}$  are the gradients in Fig. 2.8. The beam tuning criteria will be described later.

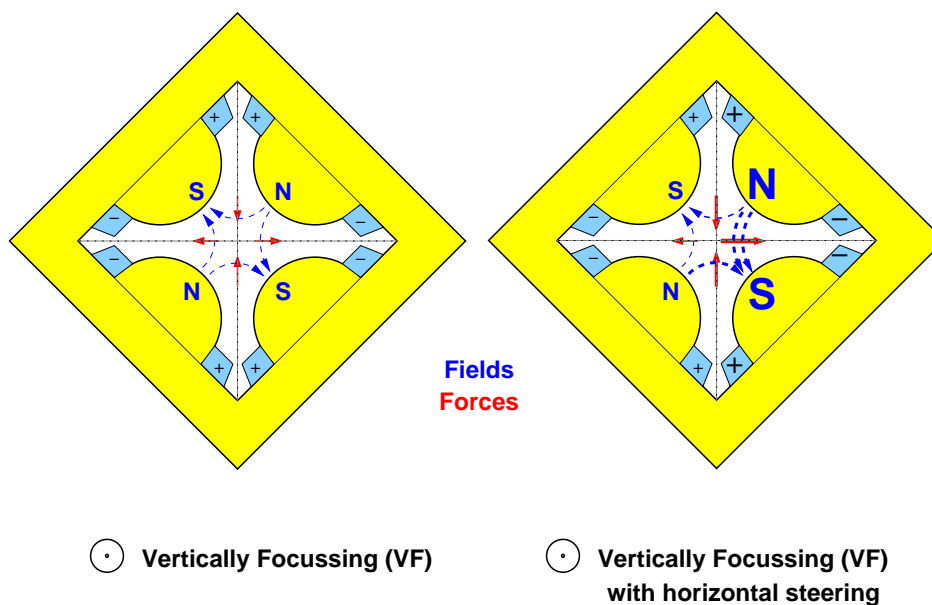


Figure 2.7: An unmodified vertically focusing quadrupole is shown on the left. The same quadrupole with asymmetrically excited poles is shown on the right. The modified quadrupole both focusses and deflects the beam.

## 2.5 The detector

Prior to this measurement, the TWIST detector had been in operation for four years, and has been described in detail elsewhere[18, 57, 75]. A schematic of the apparatus is shown in Fig. 2.9. The essential features are a superconducting magnet with an iron yoke, a stack

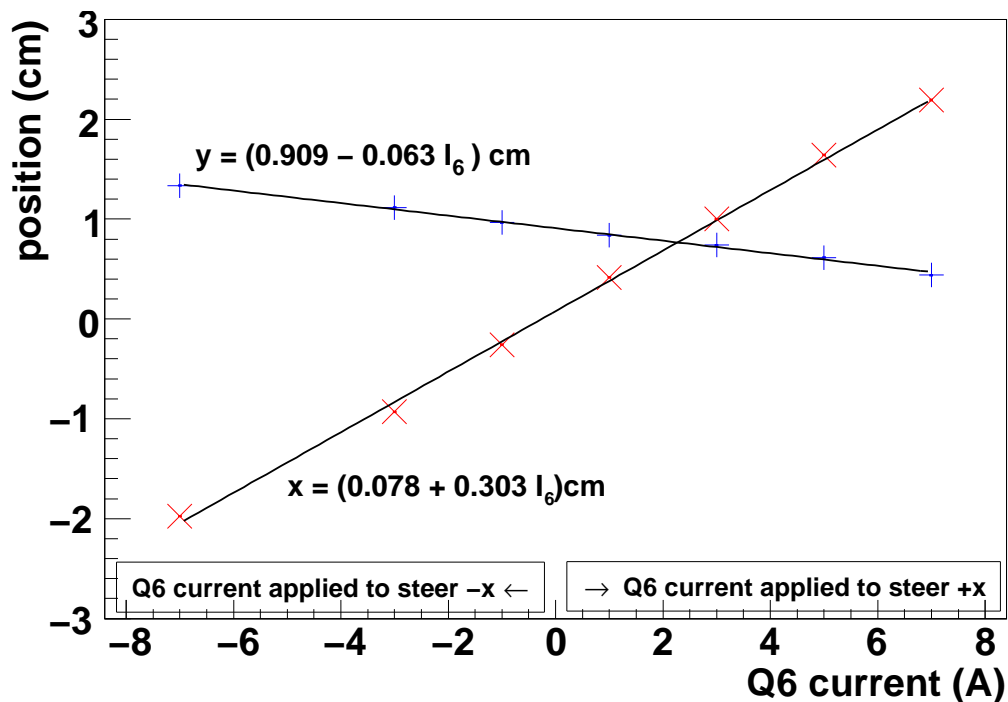


Figure 2.8: The response of the muon beam to changes in the horizontal steering of Q6.

of proportional and drift chambers, and a metal foil at the centre. For simplicity, the figure does not show the material immediately upstream and downstream of the chamber stack. Muons entered the detector and were stopped in a high purity metal target. The decay positrons spiralled in the magnetic field, leaving ionisation in the chambers. This allowed the positron’s position to be measured and its trajectory to be reconstructed, from which the initial energy and angle were inferred. The spacing of the chambers was changed since the previous analysis; this has helped to resolve wavelength degeneracies.

## 2.6 Coordinate system

The longitudinal direction,  $z$ , is along the beam line axis shown in Fig. 2.9 and the  $y$  direction is vertical.  $z$  is positive in the beam direction (“downstream”), and  $z = 0$  is defined to be half way between the wire planes of the central proportional chambers. As will be described in Section 2.8, the wire chambers are rotated by  $45^\circ$  with respect to the vertical, and this rotated system is described by  $u$  and  $v$  coordinates.

In terms of decay positrons,  $\theta$  is measured with respect to the  $z$ -axis, so that ( $0 < \cos \theta < 1$ ) corresponds to downstream decays, and ( $-1 < \cos \theta < 0$ ) to upstream decays.

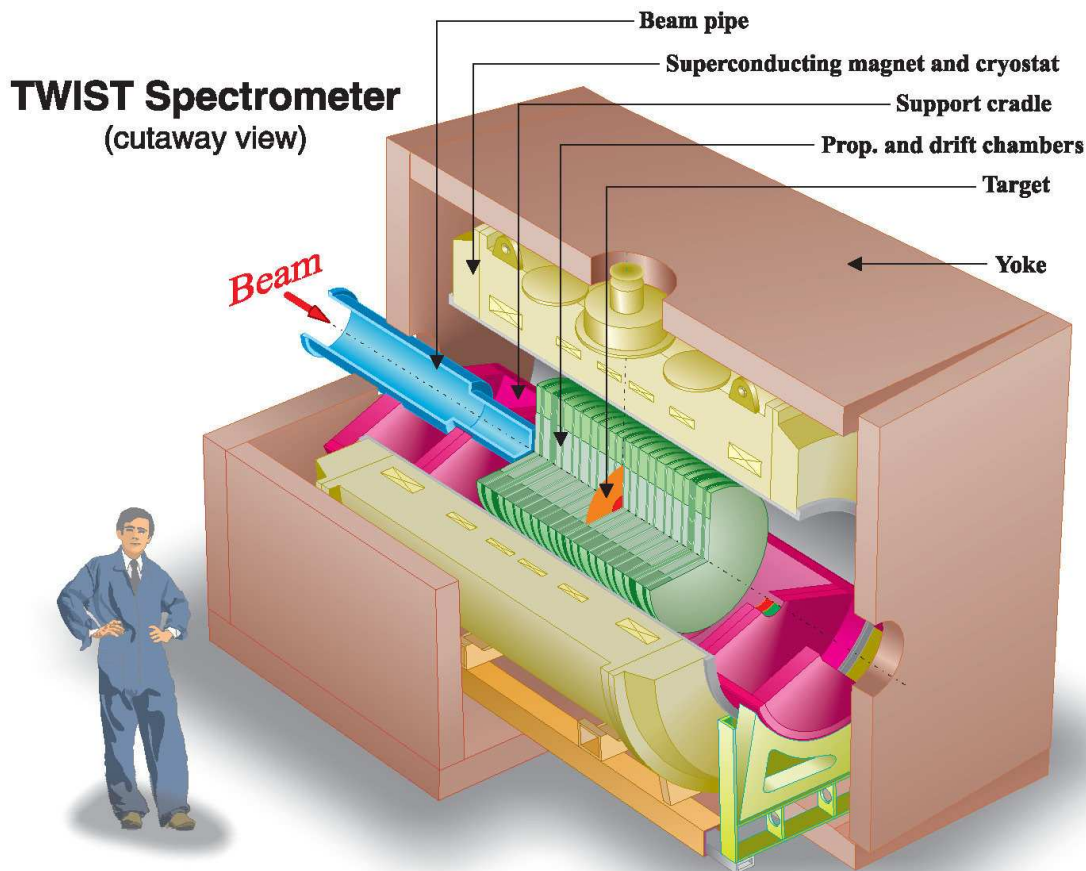


Figure 2.9: Schematic of the detector.

## 2.7 Solenoid magnet

The solenoid magnet and surrounding iron yoke are shown in Fig. 2.9. The magnet is a liquid helium cooled superconductor that is used in persistent mode; it was manufactured by Oxford Magnet Technologies Limited (UK), and was originally part of medical apparatus used for magnetic resonance imaging<sup>20</sup>. The resulting uniform magnetic field was needed for the following reasons:

1. Inside the solenoid, where the field was strong (nominally 2 T), uniform, and longitudinal ( $z$ ), the decay positrons spiralled, with the radius and pitch angle related to the positron momentum and decay angle.

<sup>20</sup>The magnet is no longer at TRIUMF. In September 2008 it was transported to Michigan State University, home of the National Superconducting Cyclotron Laboratory.

2. While muons were inside the target, the strong field held their spin against depolarisation due to nuclear dipole moments. The field also suppressed depolarisation due to muonium formation in the gas immediately before the target, although muons that stopped in the gas were removed in the analysis.
3. In the fringe field region upstream of the detector’s chambers, the field radially focussed the muon beam, which maintained a high polarisation with respect to the  $z$ -axis.

The solenoid had a bore of diameter 1.05 m, and a length of only 2.23 m, resulting in significant departures from uniformity. For this reason the magnet had doors of high permeability steel at both ends (visible in Fig. 2.9), at which the field lines must be close to perpendicular, resulting in increased uniformity through the central region. The thickness of the doors (8 cm) was carefully chosen to maximise uniformity. Each door had a 40 cm diameter circular hole that detracted from the field uniformity<sup>21</sup>. The doors were part of a custom built iron “yoke” with square cross-section of side 3 m and thickness 0.20 m, which provided an easy return path for the magnetic flux. The yoke limited the solenoid’s fringe field in the  $z$ -direction, which minimised interference with the beam line, and allowed the experiment to measure the muons after the beam line but before the magnetic field. This can all be seen in Fig. 2.10, where the direction of the magnetic field lines are shown in blue, and the red contours indicate the magnitude of the field.

The strength of the field dictated the radius and angle that could be reconstructed. The nominal field strength at the centre was  $|B| = 2$  T, but data were also taken at  $B = 1.96$  T and  $B = 2.04$  T as a consistency check. The field was continuously monitored using an NMR probe just outside the tracking region, and it was found to decrease by 0.02 mT over a period of approximately 3.5 months[82]. The analysis corrected for the field decrease by scaling the field map for each data set. Note that the solenoid required about 8 hours to ramp from 0 T to 2 T (and from 2 T back to 0 T).

The magnetic field was measured with a specially constructed Hall probe apparatus. A simulated field was produced using the OPERA software package[83], and this simulated field was used for the analysis. Further detail can be found in Appendix D. The agreement between the Hall probe measurements and the OPERA field will contribute to the largest systematic uncertainty for  $P_{\mu}^{\pi} \xi$ .

---

<sup>21</sup>The extent of the muon beam is  $\sim 5$  cm, yet the holes in the door are 40 cm. There are two reasons for this: the trigger and light guides required a significant amount of space, and the muon beam will be less sensitive to imperfections in the doors’ steel if it is further from the hole’s boundary.

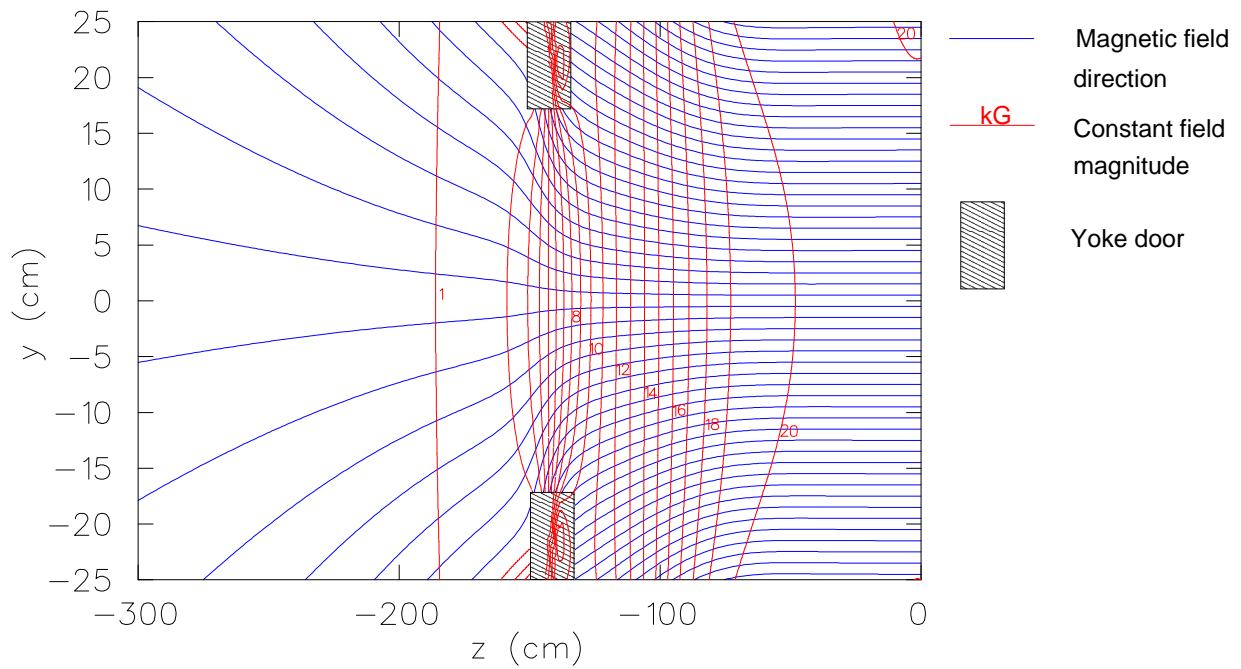


Figure 2.10: The magnetic field for  $x = 0$ . The blue lines indicate the direction of the magnetic field vector. The red contours indicate the field strength in kG. The line 20 kG corresponds to 2 T. The scales on the ordinate and abscissa differ significantly[84].

## 2.8 Wire chambers

The 120 cm detector stack included 44 multiwire drift chambers and 12 multiwire proportional chambers, which are shown in Fig. 2.11, and will now be referred to as DCs and PCs. The construction of the DCs and PCs was very similar, and a chamber is shown schematically in Fig. 2.12. Wires of diameter  $15\ \mu\text{m}$  were placed at pitches of 0.4 cm (DCs) and 0.2 cm (PCs), with a total of 80 wires per plane for the DCs, and 160 wires per plane for the PCs. All of the DC wires were individually instrumented, but the outer wires of the PCs were joined together in groups of four and then read out<sup>22</sup>. The cathodes (which served as gas windows) for each chamber were separated by 0.4 cm, and constructed from  $6.35\ \mu\text{m}$  thick Mylar foil that was aluminised on both sides to allow conduction<sup>23</sup>. A pair of proportional chambers was just  $1 \times 10^{-4}$  radiation lengths in thickness[85]; the low mass was important to minimise multiple scattering and energy loss, which ultimately improved the reconstruction of the positron trajectories.

The DCs used dimethyl ether (DME) gas, and the PCs used a mixture of  $\text{CF}_4$  and isobutane. The DME had the advantage of a high number of clusters per cm ( $30\ \text{cm}^{-1}$ ), small Lorentz angle between the electric field and electron drift velocity ( $5^\circ$ ), and a low drift velocity ( $2.5\ \text{cm}/\mu\text{s}$ ) that resulted in DC response times up to  $1\ \mu\text{s}$ [86]. These properties allowed a high precision position measurement. The PC gas was chosen to minimise response time ( $\lesssim 20\ \text{ns}$  was achieved), allowing separation of particles in time, and muon/positron identification based on pulse width. Proportional chambers were chosen over scintillators to minimise material, cover a large area, and operate efficiently in the experiment's strong magnetic field. Unfortunately a proportional chamber could not be used as the trigger since the time resolution was insufficient to separate cloud muons from surface muons; instead a dedicated trigger scintillator was used, which is described in Section 2.9. Note that the chamber efficiencies were  $> 99.95\%$ [75].

Between the chambers a mixture of helium and nitrogen in the ratio 97:3 was used. The helium minimised material, and the nitrogen prevented sparking<sup>24</sup>. The chamber gas was flowed due to a leakage of the He/N mixture through the cathode foils and outgassing of materials. As a consequence, the chamber gas pressure tracked atmospheric pressure, and

---

<sup>22</sup>The availability of TDCs (time-to-digital converters) limited the instrumentation of the PCs. The chosen instrumentation was adequate since the spatial distribution at the PCs was only used to select muons close to the target, and these target PC wires *were* individually instrumented.

<sup>23</sup>The Mylar foils were doubly aluminised regardless of whether they were exposed to chamber gas or the helium/nitrogen mixture. This reduced static charge build-up.

<sup>24</sup>The cross section for electrons in pure helium is very small, allowing a long mean free path. Hence the electron can accelerate and ionise, eventually causing a spark. The nitrogen significantly reduces the mean free path, and therefore minimises sparking.

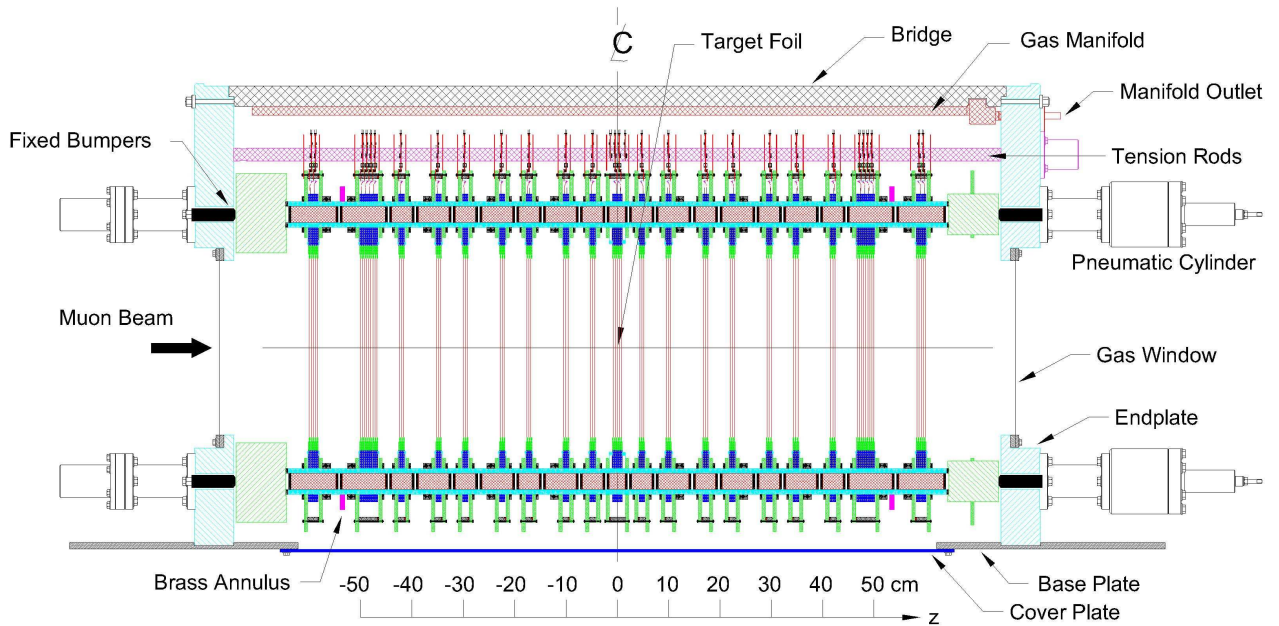


Figure 2.11: Side view of the detector.

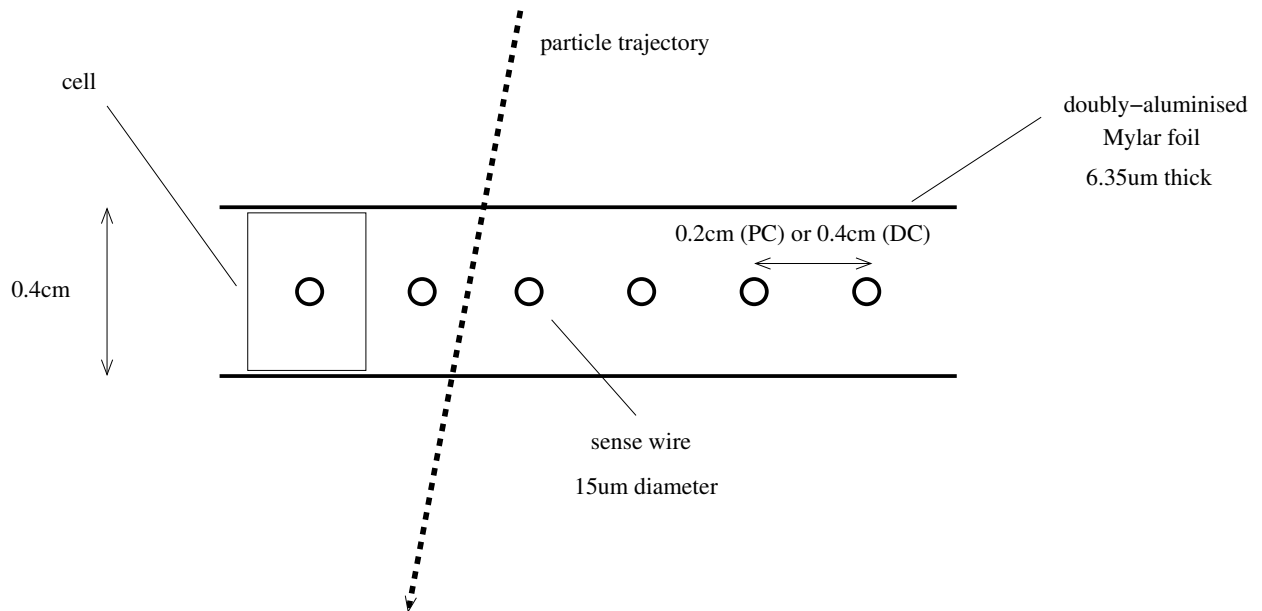


Figure 2.12: Schematic of a wire chamber. Both the DCs and PCs have cathodes of Mylar coated with aluminium; these also act as gas windows. The cathode-to-cathode distance was always 0.4 cm.

the He/N mixture was flowed to control the differential pressure and keep the cathode foils flat; this pressure difference was maintained to 4 mTorr[57].

The chambers were assembled into modules with shared cathodes. In the simplest case two planes were orthogonal with a single shared cathode. These two plane modules were used in the region  $-45.0 \text{ cm} < z < 45.0 \text{ cm}$  in Fig. 2.11, and made up the “sparse stack”. There were also two “dense stacks” of eight DCs, where the seven internal cathodes were shared. At the beginning and end of the detector there were four plane modules of proportional chambers. The module containing the stopping target used the target’s material as a shared cathode. For all modules the wire planes were inclined at  $45^\circ$  with respect to the vertical, and the rotated system was described by  $u$  and  $v$  coordinates, rather than  $x$  and  $y$ . The rotation allowed the electronics to be placed at the same position on each plane.

For this measurement the voltages on the two PCs immediately before the stopping target were reduced. The resulting pulse widths were sensitive to the muon’s energy loss, allowing muons that stopped before the metal target to be rejected; see Section 3.3.3.

The detector was symmetric in  $z$  about the central muon stopping target (see Fig. 2.11). The modules were positioned in  $z$  using ceramic spacers provided by the experiment’s Russian collaborators. The material was “Sitall CO-115M”, which had a coefficient of linear thermal expansion of just  $\sim 1 \times 10^{-7}(\text{dL/L})/^\circ\text{C}$ [75]. For comparison, the coefficients of diamond and carbon steel are  $1 \times 10^{-6}(\text{dL/L})/^\circ\text{C}$  and  $11 \times 10^{-6}(\text{dL/L})/^\circ\text{C}$  respectively. The Sitall material was strong and had surfaces that were flat and parallel to  $< 0.5 \mu\text{m}$ [75]. The spacers were 0.4 cm for the chambers, and 2.0 cm or 4.0 cm for spacing between the modules. The  $z$  position was maintained by four pneumatic cylinders, which are indicated in Fig. 2.11, and these exerted a force of 1470 N on the chamber stack. The length of the detector assembly was measured “with a precision considerably better than  $50 \mu\text{m}$ ” so that the “relative position of each 4 mm Sitall in the stack is known with a precision of a few microns”[75].

## 2.9 The upstream “beam package”

The beam line vacuum extended into the iron yoke (see Fig. 2.13), and the first material traversed by the muons was the upstream window of the gas degrader. The other components in Fig. 2.13 made up a removable upstream “beam package”. The 20.4 cm gas degrader was filled with a helium / carbon dioxide mixture; the gas ratio was automatically adjusted to stabilise the muon stopping distribution, in response to ambient pressure changes. In the previous  $P_\mu^\pi \xi$  analysis the feedback loop was only in operation towards the end of data acquisition. The original design specification estimated the helium and carbon dioxide should

have a 50:50 volume ratio. In the winter of 2006 the degrader typically contained  $\approx 35\%$   $\text{CO}_2$  by volume, and in the summer of 2007 the fraction was  $\approx 43\%$ . For the previous  $P_\mu^\pi \xi$  analysis the fraction was  $\approx 37\%$ .

Figure 2.13 shows a central muon scintillator, which provided the trigger for the experiment, and an annular positron scintillator, which was used as part of the wire time offset calibration. The muon scintillator was a circular plastic scintillator of radius 3 cm, thickness  $240 \mu\text{m}$ , wrapped in aluminised Mylar. The muon scintillator was read out with two light guides (M1 and M2), and the coincidence of M1, M2 and M1+M2 was used as the trigger<sup>25</sup>.

The annular scintillator was expected to establish the decay positron track time. However, the helix reconstruction software was able to establish this time itself. Therefore the only use of the annular scintillator was in the calibration of the wire time offsets. The scintillator also shielded the upstream half of the detector from backscatters.

Lastly, Fig. 2.13 shows a “filmstrip degrader”. This allowed up to 0.10 cm of Mylar to be put in the path of particles. For nominal data acquisition, this degrader was set to the hole (no material) position. Special data were taken with the muons stopped far upstream in the detector (see Section ??), and this required the use of the filmstrip degrader.

In nominal operation there is no corresponding downstream package, and this is expected to cause an asymmetry in backscatters<sup>26</sup>. In order to study this asymmetry, a copy of the beam package was specially constructed and placed downstream of the chamber stack for a single data set. This set will later be shown to produce a consistent  $P_\mu^\pi \xi$  result.

## 2.10 Muon stopping target

Muons were stopped in high purity foils of silver (2006) and aluminium (2007), which both had purity  $> 99.999\%$ . The aluminium target was the same foil used for the previous  $P_\mu^\pi \xi$  measurement. The nominal thicknesses were  $29.5 \mu\text{m}$  ( $31 \text{ mg}/\text{cm}^2$ ) for silver, and  $71.0 \mu\text{m}$  ( $19 \text{ mg}/\text{cm}^2$ ) for aluminium. Both targets were expected to depolarise the muons by a small amount, with a simple exponential form for  $P_\mu(t)$ , as described in Section 1.6.3

The target region is shown in Fig. 2.14, where the metal target is seen to be part of the cathode between PC6 and PC7. The figure shows Kapton masks that avoid problems with the high electric fields where the metal target is attached to the aluminised Mylar foil.

---

<sup>25</sup>The coincidence of M1 and M2 is used to suppress false triggers due to photomultiplier noise. The sum of M1 and M2 provides a larger pulse for improved time resolution.

<sup>26</sup>The primary backscatter process in the experiment is a positron rebounding, following a Coulomb interaction with a nucleus. Therefore the number of measured backscatters in the experiment depends on the thickness and positioning of materials outside of the tracking volume. Secondary processes such as showering are possible, but for low energy positrons this is less of a problem.

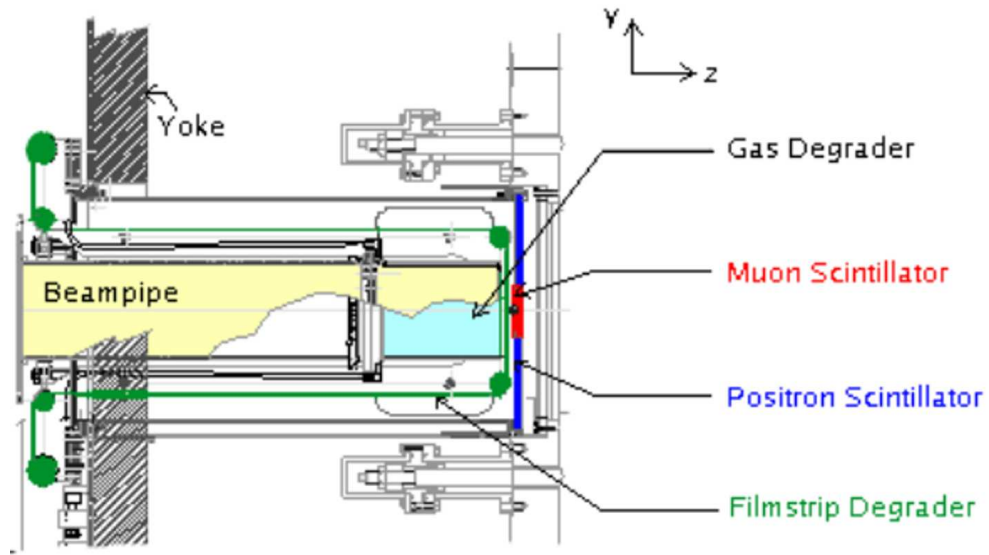


Figure 2.13: Beam package for the upstream end of the detector[57]. Note that the beam does not encounter material until the upstream window of the gas degrader.

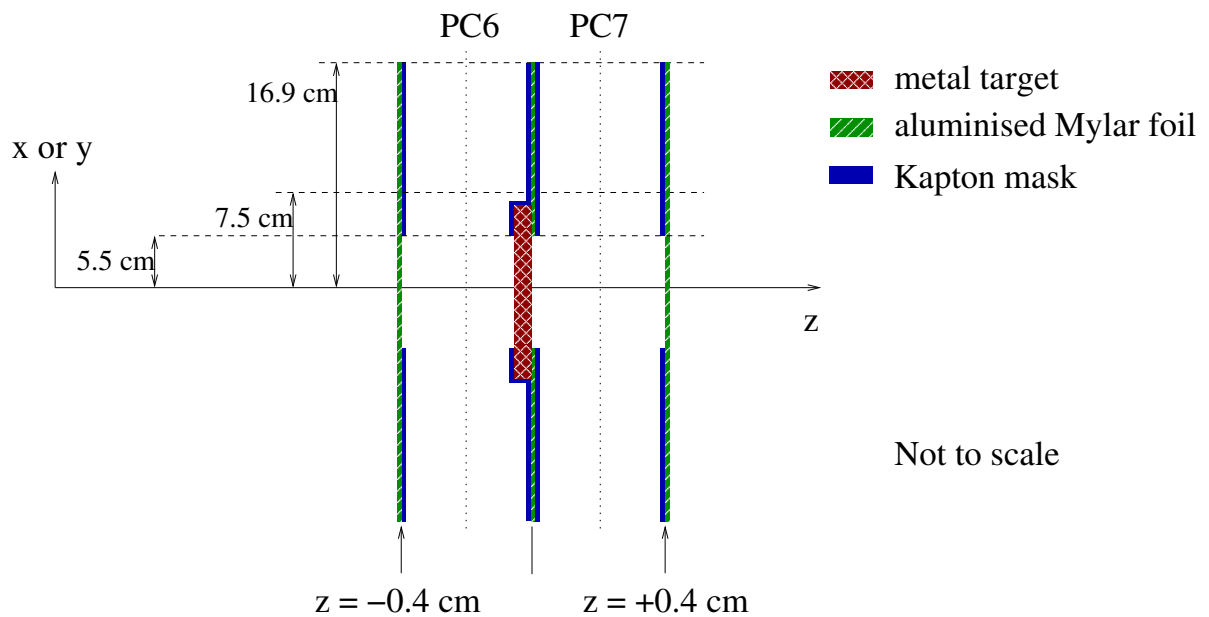


Figure 2.14: Schematic of the muon stopping target, which is part of the cathode foil for PC6 and PC7.

## 2.11 Muon ranging

The total range of the muons in this experiment was about 0.14 cm of water. The materials traversed by muons stopping in the target are summarised in Table 2.1. The previous  $P_{\mu}^{\pi} \xi$  measurement found that if the adjustable gas degrader in the simulation was set to the real value, then an extra 12.8 mg/cm<sup>2</sup> of material was needed to match the stopping distribution from data[57]. The apparatus has now been disassembled and the materials were reweighed; the upstream gas degrader window was found to have a thickness of 93.0  $\mu\text{m}$  instead of 79.3  $\mu\text{m}$ , and the muon scintillator had a thickness of 240  $\mu\text{m}$  instead of 195  $\mu\text{m}$ <sup>27</sup>. The simulation now only required an extra 1.9 mg/cm<sup>2</sup> of material, which is within the uncertainties from matching the stopping distribution (see Section 6.3.5), the unsimulated bulge in the vacuum window ( $\approx 1.0$  mg/cm<sup>2</sup> of extra gas), uncertainties in other material thicknesses (stopping target, cathode foil, cathode foil bulges), and uncertainties in modelling the energy loss for highly ionising particles in thin foils.

## 2.12 Electronics

The electronics and data acquisition system have been described elsewhere[57, 82, 85]. In summary, time-to-digital converters (TDCs) recorded the start- and stop-times for pulses on each wire. The TDCs recorded in the interval starting 6  $\mu\text{s}$  before, to 10  $\mu\text{s}$  after the trigger. If the TDCs were busy, or an additional trigger particle arrived, a new event was *not* started. Instead the hits were recorded and the events were later identified as having multiple trigger particles.

An individual TDC channel could suffer from non-linearities. The internal oscillator may not have been exactly at the manufacturer’s frequency, leading to a so-called “integral non-linearity”. The TDCs used by the experiment (LeCroy model number 1877) had an integral non-linearity of  $< 25$  ppm[87], which is beyond the required accuracy. The TDCs had a least significant bit of 20 ns, yet claimed a precision of 0.5 ns[88]. The interpolation used to reach the 0.5 ns precision introduced a differential non-linearity. Again, the LeCroy 1877 TDCs had a negligible differential non-linearity of  $\pm 0.1$  ns[87]. The experiment spread signals through multiple TDCs, further reducing the effects of non-linearities.

---

<sup>27</sup>The muon scintillator was not properly weighed before construction, and was assumed to be 8 thou instead of its correct thickness of 10 thou.

Table 2.1: Materials traversed by a muon reaching the centre of an aluminium target. The gas densities assume a pressure of 750 torr, temperature 31.0°C.

Description	Thickness (mg/cm <sup>2</sup> )
Graphite production target	3.8 <sup>a</sup>
Polyester window valve	0.4
Upstream gas degrader foil ("vacuum window")	12.9
Downstream gas degrader foil	0.9
Adjustable degrader gas (He/CO <sub>2</sub> )	3.6 (pure He) to 40.3 (pure CO <sub>2</sub> )
Air	5.2
Muon scintillator	24.8
Scintillator wrapping (Aluminised Mylar)	8.9
Cradle window	0.9
Detector gas (He/N mixture)	12.6
PC module (4 chambers)	9.2
Dense stack (8 chambers)	13.4
Sparse stack (7 chambers)	27.9
Target PCs	4.2
$\frac{1}{2}$ of Al target	9.6
	138.3 to 175.0

<sup>a</sup> This is the average amount of material seen. The momentum resolution of the channel allows muons with a range of production target depths to be accepted.

## 2.13 Alignments

All components were ultimately aligned to the steel yoke, using the techniques summarised in Fig. 2.15, which will now be briefly described. Further detail can be found elsewhere[89].

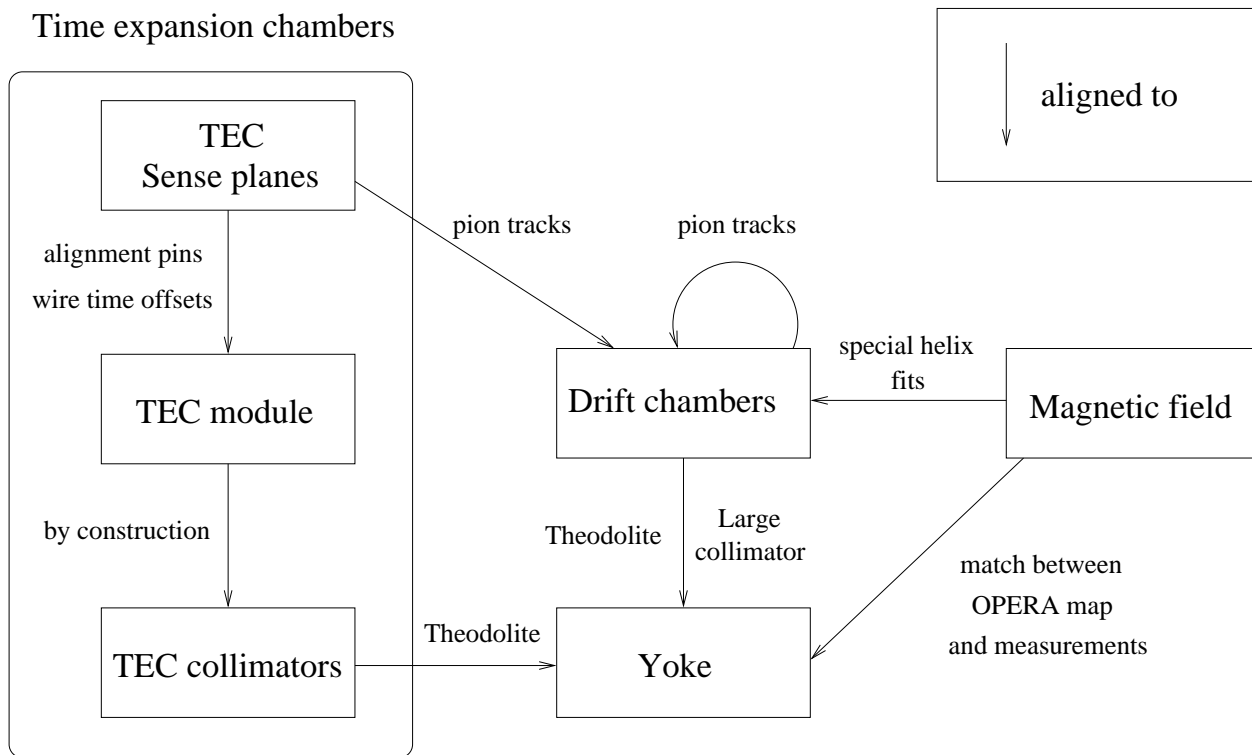


Figure 2.15: Summary of alignments relative to the steel yoke.

The sense planes were positioned in each TEC module using alignment pins, allowing a precision of  $< 200 \mu\text{m}$ . The angle of the sense planes relative to the TEC gas box was part of the wire time offset calibration, and was determined to better than 1 mrad (see Section G.4.1). To determine the positional alignment of the TEC gas box relative to the yoke, collimators were screwed onto each end of the box, and these were aligned to the yoke using a theodolite; the precision was limited by the positioning of the collimators, which was better than  $< 500 \mu\text{m}$ . The angle of the sense planes relative to the drift chambers was determined by turning off the magnetic field, tuning the M13 beam line to accept 120 MeV/c pions, and selecting trajectories that passed through both the TEC modules and the detector. These trajectories were well approximated by straight lines, which allowed the angle of the sense planes relative to the detector to be determined to better than about 2 mrad. Later it will be shown that these alignments were all smaller than the limitations of reproducibility when

the TECs were removed/inserted into the beam line.

A new technique aligned the drift chambers to the yoke. Identical collimators with 14 holes of 2 cm diameter were placed over the upstream and downstream yoke windows. Pions with momentum 120 MeV/c were put through the collimators while the magnetic field was off, and their straight line trajectories were reconstructed with the drift chambers. The drift chambers were consistent with being at  $(x, y) = (0, 0)$ , to a precision of 400  $\mu\text{m}$ . The angle of the stack relative to the yoke was found to be  $-1.4$  mrad in  $\theta_x$ , and  $-0.4$  mrad in  $\theta_y$ , with a precision of 0.1 mrad.

The drift chambers were aligned relative to each other using using 120 MeV/c straight line pion trajectories. The drift chamber residuals were minimised to determine the translational  $(u, v)$  and rotational alignment (about the  $z$ -axis) simultaneously. The precision was better than 10  $\mu\text{m}$  in translation, and 0.2 mrad in rotation. The  $z$  alignment of the chambers was known to a few  $\mu\text{m}$ , as discussed in Section 2.8.

The magnetic field was rotationally aligned with the drift chambers by applying a special analysis to the nominal muon decay data. Simple helices were fit to the decay positron, with no energy loss or scattering, but the helix axis was allowed to have a non-zero angle with respect to the  $z$ -axis. This technique found that the magnetic field was misaligned with the drift chambers by 1.15 mrad in  $\theta_x$ , and  $-0.33$  mrad in  $\theta_y$ , with precision  $< 0.03$  mrad. The translational alignment of the magnetic field is less certain; this was determined from matching the OPERA field to the Hall probe measurements, and had a precision of  $\lesssim 0.2$  cm.

Long term stability measurements were also taken. For example, there were concerns that the box containing the TEC modules moved by a small amount. This might happen when inserting the box and pumping down the beam line to vacuum, and while turning on the 2 T solenoid. There was also the question of reproducibility over a period of several weeks. The position was therefore monitored in three ways: total station<sup>28</sup> measurements at intervals of several months, a laser crosshair directed onto the box while changing the magnetic field, and the same theodolite used for alignment was placed on a catwalk overlooking the beam line. The only conclusive measurement came from the total station, which was accurate to  $\sim 0.1$  cm, and found movements of  $\lesssim 0.1$  cm in  $x$  and  $y$ , but up to 0.4 cm in  $z$ .

---

<sup>28</sup>A total station measures both position and angle of a target. For this experiment a laser based total station was used. The device could only be used every few months since it was required elsewhere on site, and needed an expert to setup.

# Chapter 3

## Analysis

### 3.1 Overview

The analysis procedure is summarised in Fig. 3.1. The time and position of signals from the detector’s wires (“hits”) were used to identify the different particles, and then to characterise the events. Wherever possible, the particle trajectories were reconstructed. Information for every event and track were written into a ROOT tree structure database[90]. Track selection and cuts were then applied to construct a clean and unbiased decay positron spectrum.

At this point the spectrum from data could have been fit with a function that allowed for non-standard model muon decay parameters. However, this would have required a careful correction for detector acceptance and inefficiency. Instead, the analysis used a `GEANT3` simulation[91] that included the full detector response (see Chapter 4). The simulation was analysed with the same software and cuts as the real data to produce a simulated spectrum, *except* it was generated with hidden values of the muon decay parameters. The difference between the data and simulation spectra was then fit to obtain the difference in  $P_\mu^\pi$ ,  $\xi$ ,  $\rho$  and  $\delta$ . All systematic uncertainties were determined on the difference in the decay parameters from their hidden values. The hidden simulation parameters were only revealed after all the systematic uncertainties had been evaluated. This “blind” analysis procedure was adopted to reduce the influence of human bias.

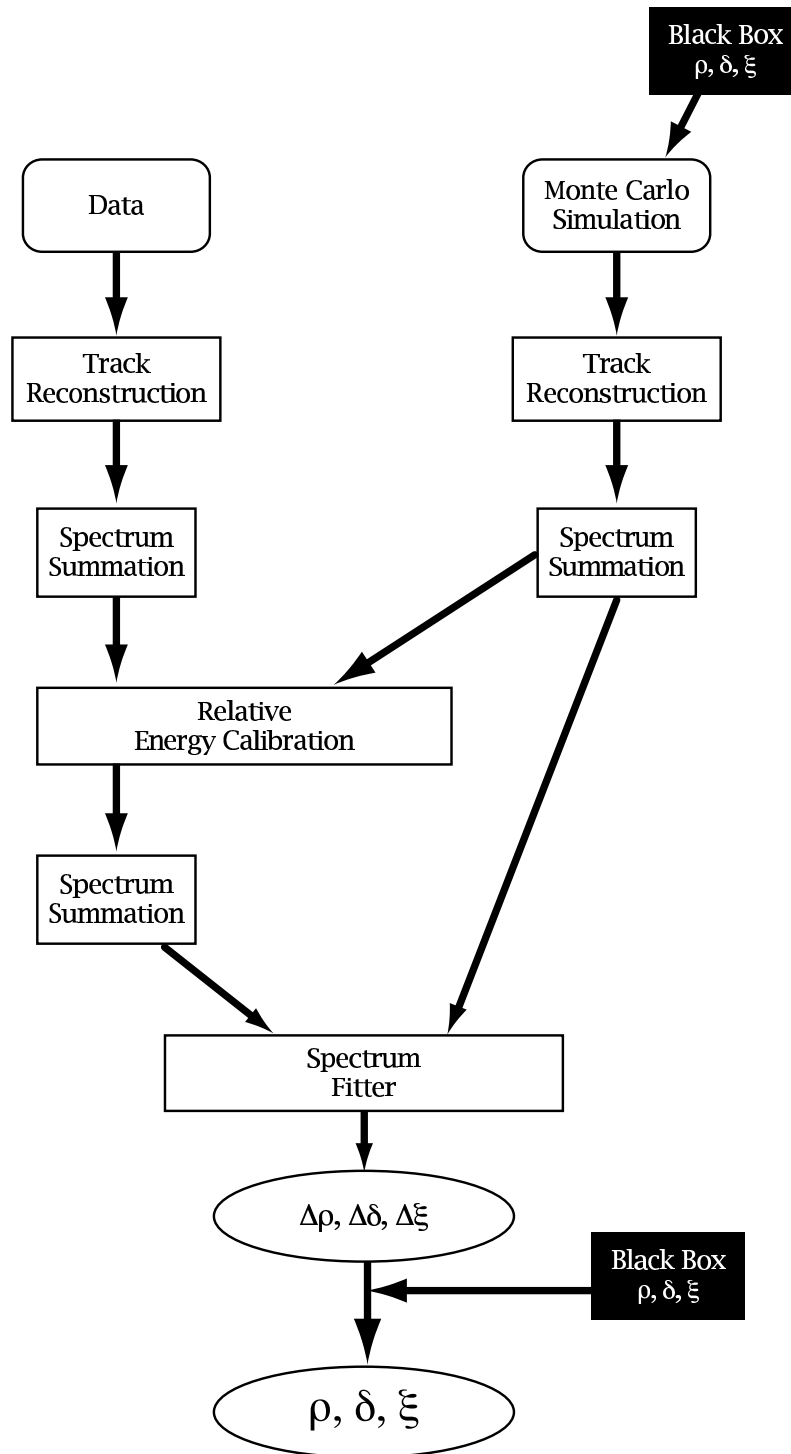


Figure 3.1: Flow diagram of the analysis procedure[18]. The “Black Box” corresponds to the hidden values of the muon decay parameters.

## 3.2 Track reconstruction

The collaboration used internally authored software to identify particles, classify events, and reconstruct trajectories. For this measurement almost every code module was reviewed and improved where necessary. The software will now be described, except for the time expansion chamber analysis, which appears separately as Appendix G.

### 3.2.1 “Unpacking”

The data acquisition system and the simulation created data files with the leading and trailing edge times of the signals from the scintillators and wires. These were first “unpacked” according to the following steps:

- Pulses where the time-to-digital converter reported an error were recovered or discarded as appropriate.
- Wire time offsets (see below) were applied, and the leading/trailing edge times were converted into a time and width.
- The trigger scintillator used a “pulse amplitude charge-to-time converter” (PACT), which converted the integrated charge to a leading/trailing edge time. This signal was converted back to an energy deposit during unpacking. This is the only place in the electronics where the pulse amplitude is used.

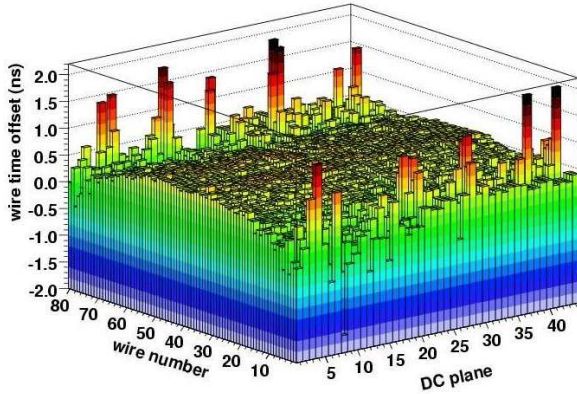
A new technique determined the wire time offsets, which varied from wire-to-wire due to variations in cable lengths (up to  $\sim$  cms), electronics (primarily the TDCs, up to 1 ns), and discriminator amplitude time walk. A selection was made on decay positrons that triggered the annular scintillator upstream (see Section 2.9), or a newly constructed downstream scintillator, which is described in Appendix E. The time of each wire’s hit relative to the trigger scintillator was histogrammed, after correcting for the time-of-flight using a simple helix fit; these histograms were then fit to determine the zero-time.

An additional analysis selected beam positrons that passed through the entire detector, including both the upstream annular scintillator and the downstream scintillator. These positrons illuminated the central wires and allowed the determination of a very precise relationship between the two detector halves.

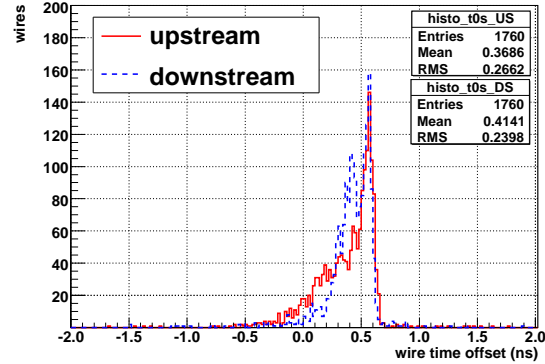
The technique was validated using the simulation, where the wire time offsets are known to be zero. The results are shown in Fig. 3.2(a), where a wire-dependent bias is evident. The wires at the edge of the planes had poor statistics, resulting in anomalous offsets. Figure

3.2(b) shows a histogram of the wire time offsets in each detector half; the bias changes both halves by about 0.4 ns on average.

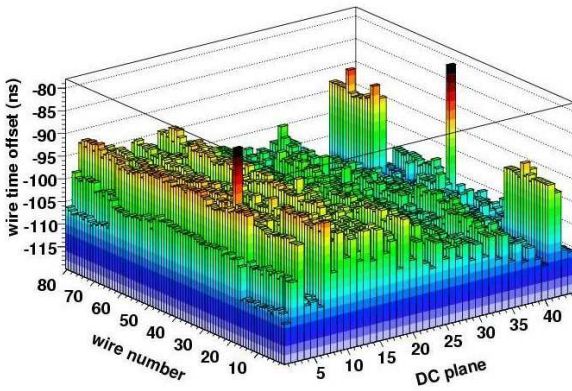
The wire time offsets for one set of the data are shown in Figs. 3.2(c) and 3.2(d). As expected, there is rich structure, and the scale of variations is much greater than the bias shown in Fig. 3.2(a).



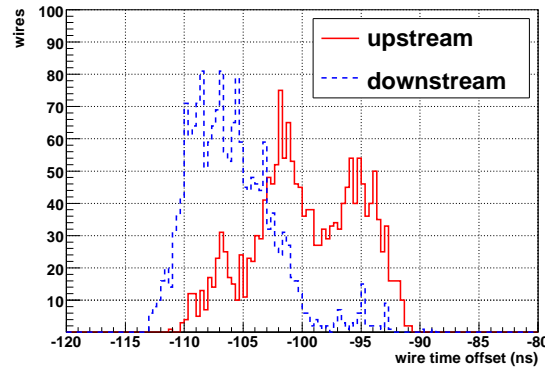
(a) Wire time offset technique applied to simulation. This shows the bias in the technique, since ideally all wires would be at zero.



(b) Simulation wire time offsets.



(c) Wire time offsets for the data, showing rich structure. The scale differs significantly from Fig 3.2(a).



(d) Wire time offsets for the data.

Figure 3.2: Results of the wire time offset analysis, applied to simulation and data.

### 3.2.2 Crosstalk removal

Electronic crosstalk occurred when a large pulse induced a false smaller pulse nearby. This could occur inside a drift chamber, where an avalanche at a wire created photons, and these underwent a secondary process resulting in ionisation at a nearby wire. Crosstalk could also occur within the pre-amplifier cards, where a large pulse (*e.g.* from a muon) could induce a signal in a nearby conductive path on the pre-amplifier board. (In the time expansion chambers, described in Section 2.3, the finer spacing of the sense wires required guard wires to be placed in between, to minimise the crosstalk.)

The crosstalk pulses were identified and removed by the analysis software: if a narrow pulse (less than 50 ns wide in a DC, and 60 ns in a PC) occurred within 50 ns of a good pulse, then it was removed. In previous analyses, only the 10 (32) wires closest to the good DC (PC) hit were checked for crosstalk. For this measurement, it was found safe to expand the check to all wires in the same plane.

Crosstalk removal was disabled when analysing the simulation. This was the only place in the track reconstruction code where the data and simulation were treated differently.

### 3.2.3 Windowing

A “time window” was started by a hit in a proportional chamber (PC). All subsequent hits within  $1.05\ \mu\text{s}$  were put into this time window. The  $1.05\ \mu\text{s}$  was necessary to allow the ionisation in the drift chamber’s slow gas to register at the wires. The time window was intended to contain all hits of a track. If additional PC hits occurred while filling the window, a new window was not started. The window code and its modern review are described in more detail elsewhere[57, 89].

### 3.2.4 Classification

The identification of the particle in a window used several pieces of information. The muons were identified from their pulse widths in the upstream PCs. Positrons from the beam line were distinguished from decay positrons since they passed through all the chambers, rather than just one half of the detector. Delta electrons were identified, as well as broken trajectories due to a large multiple scatter from the detector material, and backscatters from material outside the DC region. Events were then classified according to the particles observed and their time separation. The full list of events and their recent review can be found elsewhere[89].

### 3.2.5 Pattern recognition

A helix with centre  $(x, y) = (\Delta_x, \Delta_y)$  can be written in the notation

$$\begin{pmatrix} x \\ y \end{pmatrix} = r \begin{pmatrix} \cos(f(z)) \\ \sin(f(z)) \end{pmatrix} + \begin{pmatrix} \Delta_x \\ \Delta_y \end{pmatrix}, \quad (3.1)$$

where  $(x, y, z)$  is the position in space,  $r$  is the radius, and

$$f(z) = \frac{2\pi z}{\lambda} + \phi, \quad (3.2)$$

where  $\lambda$  is the wavelength and  $\phi$  is the phase. The pattern recognition algorithm made a first estimate of the parameters in Eqs. (3.1) and (3.2).

A helix with  $\lambda = 1$  and  $\phi = \pi/4$  is shown in Fig. 3.3(a). Projecting this helix onto the  $x - y$  plane allows both the radius,  $r$ , and the centre,  $(\Delta_x, \Delta_y)$ , to be determined. If the angle between each point and the line  $x = 0$  is then plotted against  $z$ , the wavelength ( $\lambda$ ) and phase ( $\phi$ ) can be determined, as shown in Fig. 3.3(b).

A real measurement samples the helix at discrete  $z$  locations, which allows the centre and radius to be readily estimated, but results in a wavelength ambiguity. This is illustrated in Fig. 3.4(a), where the circles show the helix phase if it's assumed to be in the range  $0 < f(z) < 2\pi$ . The other markers are mathematically allowed solutions, of which there are an infinite number.

The projection of coordinates from the drift chambers were used in combinations of three to estimate the radius. The combination with the smallest  $\chi^2$  was kept, and the phase for each combination was determined by the procedure already described. The wavelength degeneracy was resolved using two additional pieces of information: higher angle tracks registered in more than one drift cell<sup>29</sup>, and tracks could not be reconstructed if they changed by more than  $2\pi$  between pairs of drift chambers[57]. At this stage there was no estimate made of the positron energy loss, or changes in angle due to multiple scattering.

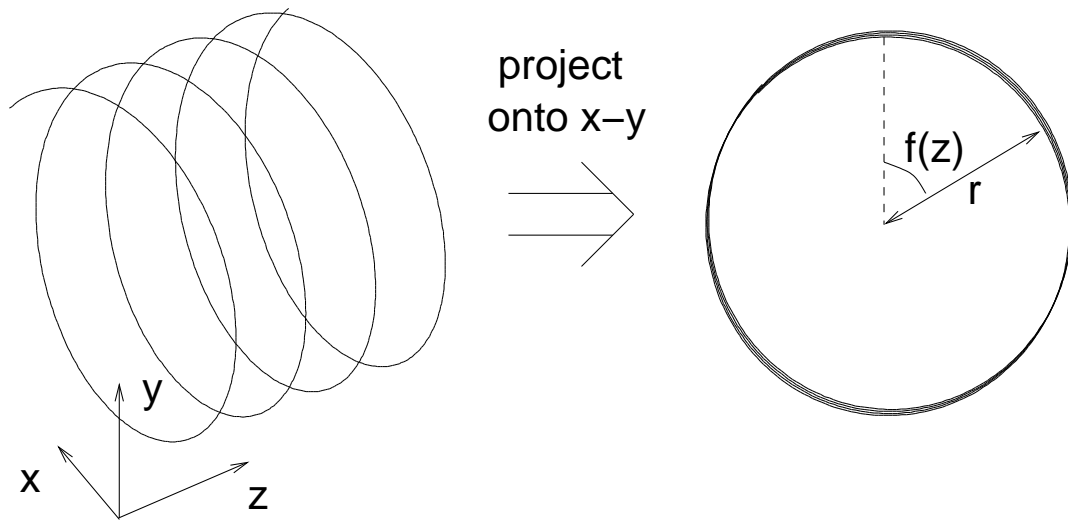
The modules in the sparse stacks (see Section 2.8) were re-arranged prior to this measurement in order to minimise “magic wavelengths”. This concept is illustrated in Fig. 3.4(b), which shows the worst case scenario where the wavelength is ambiguous. Wavelengths close to this situation were poorly reconstructed.

For this measurement, the existing quality cuts were upgraded to depend on track angle and radius, and the range of potential helix parameters was reduced. The changes were tuned

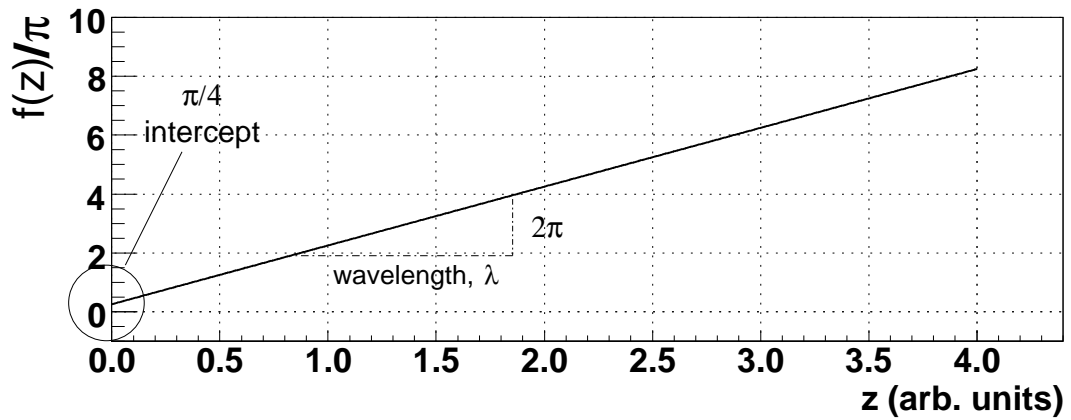
---

<sup>29</sup>Further detail can be found in Section 4.2.1 of Ref. [92].

to help situations where multiple tracks overlapped, and tracks that had smaller angles.

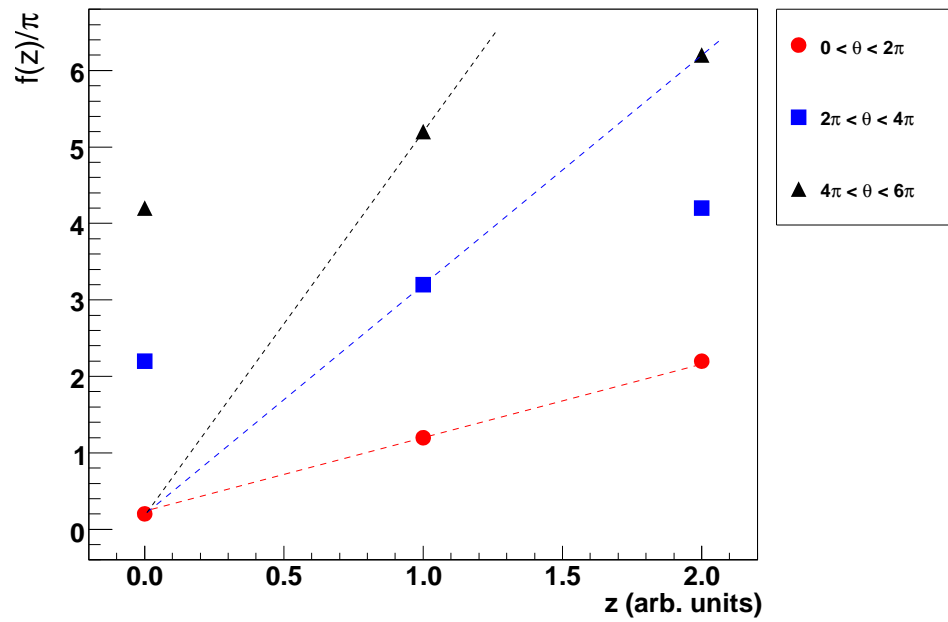


(a) Projecting onto the transverse plane to determine  $r$  and  $(\Delta_x, \Delta_y)$ .

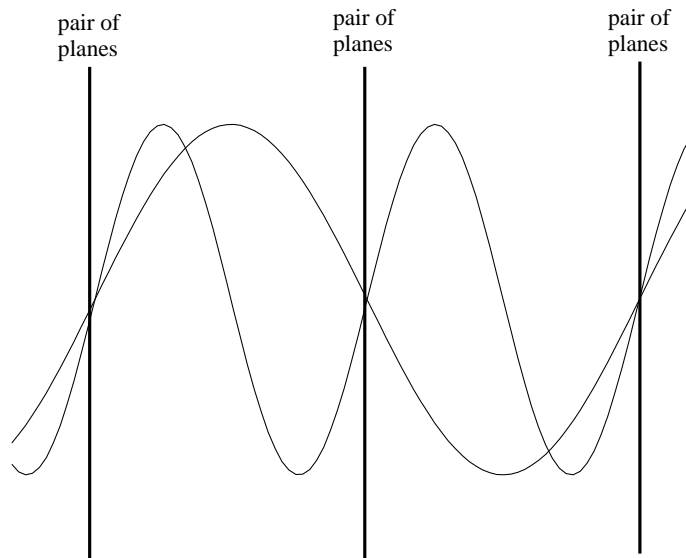


(b) Angle with respect to  $x = 0$  can determine  $\lambda$  and  $\phi$ .

Figure 3.3: Determining helix fit parameters.



(a) There is a  $2\pi$  ambiguity in determining the angle, which leads to an infinite number of possible wavelengths.



(b) The concept of a “magic wavelength” is illustrated. Wavelengths close to the spacing of the chambers in the sparse stack will have poor longitudinal momentum reconstruction.

Figure 3.4: Demonstration of the difficulties in estimating the wavelength of helical trajectories.

### 3.2.6 Fitting the helical trajectory

The pattern recognition described in the previous section gave initial estimates to the helix fitting algorithm. The fitter then “swam” helices with parameters close to those determined by the pattern recognition, and iterated using a least squares approach. For the swimming, the trajectory was divided up into segments where the magnetic field changed by less than 0.75 G. The field was assumed to be uniform over these segments, so that the trajectory was a perfect helix arc. This approach was validated using the simulation, by comparing the true and reconstructed trajectories.

Initially a fit was made to the positions of the wires, ignoring any drift time information from the chambers. The final iterations then used the drift times<sup>30</sup>. There was a left-right ambiguity that was resolved iteratively, by choosing the side of the wire that best fit the rest of the trajectory at each iteration. The final fit to drift times includes energy loss and allowed for a scatter in the trajectory at pairs of planes.

The helix fitter minimised

$$\chi^2 = \sum_{\text{hits}} \frac{(d_f - d_m)^2}{\sigma_d^2} + \sum_{\text{scatters}} \frac{\theta_s^2}{\sigma_\theta^2}, \quad (3.3)$$

where  $d_f$  is the fitted position,  $d_m$  is the position from the space-time relationship,  $\sigma_d$  is the resolution,  $\theta_s$  is the scatter angle and  $\sigma_\theta$  is the theoretical scattering distribution width, which is set to the approximate expression for multiple scattering from the Particle Data Group[3]. The fitting algorithm established its own track time, and reported the position and momentum at the first plane that sees the positron, along with a code that described the algorithm’s success. This success code is later used to select good tracks. The helix fitting algorithm is described in more detail elsewhere[18]. An example of an event with a successful fit is shown in Fig. 3.5.

Sections of the fitting code were reviewed for the current analysis. A small improvement was made to the algorithm that calculated the scatter angle. The energy loss model used by the fitter was reviewed with the conclusion that bremsstrahlung can be safely neglected, instead assuming that all the energy loss is from ionisation. There were significant improvements made to the space-time relationship and drift cell resolution, and these will be described later (Sections 3.2.7 and 3.2.8).

Note that muons and beam positrons were not reconstructed since their transverse momenta (and hence their radii) were too small.

---

<sup>30</sup>The PCs were not used in the final helix fit since their resolution was limited to the wire spacing.

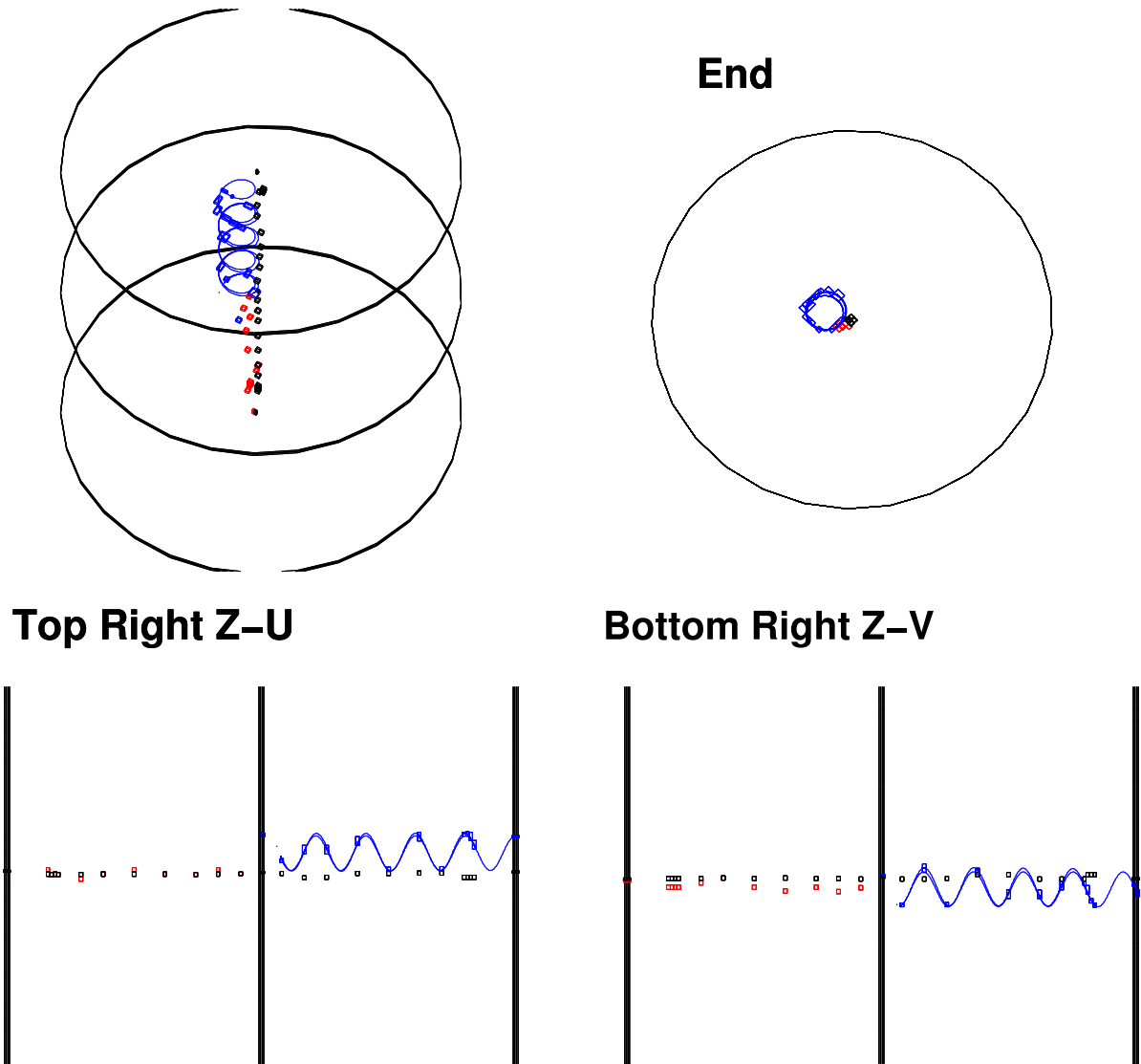


Figure 3.5: A muon (red) stops in the metal foil (centre of the Z-U and Z-V displays) and decays to a positron (blue). The black hits that span the length of the detector are a beam positron.

### 3.2.7 Improved drift chamber space-time-relationship

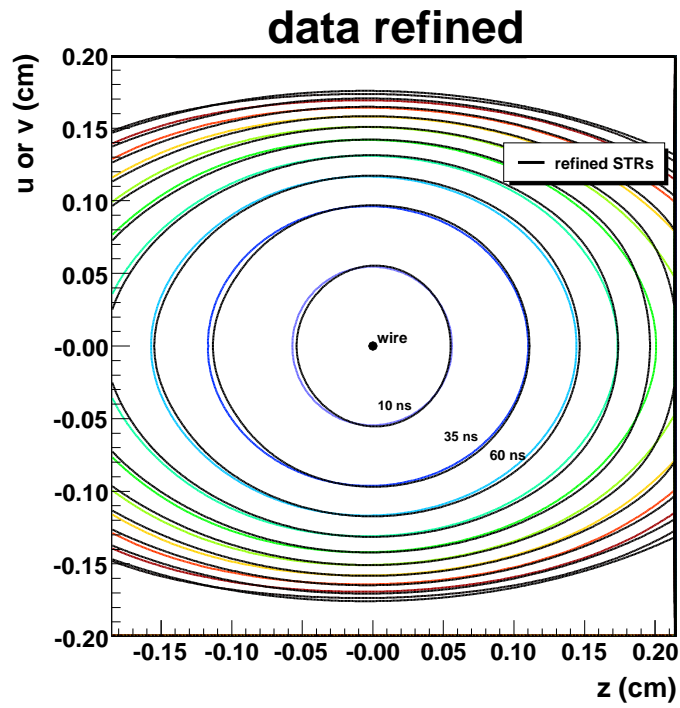
The drift chambers measured the arrival time of the ionisation at a wire, and this was converted into a distance using a drift time map, also known as a space-time-relationship (STR). The STR map for a single drift cell was generated using GARFIELD[93] at intervals of  $20\ \mu\text{m}$ . For the current analysis the STRs were refined by analysing events using the experiment's helix fitting code, and adjusting the STR at each space point to minimise the average drift time residual. This was performed iteratively, and allowed the STRs to correct for biases in the helix fitting software, and for uncertainties in the GARFIELD inputs such as voltage, gas densities and geometry<sup>31</sup>.

The refined drift cell isochrones are shown in Fig. 3.6(a), along with the GARFIELD STRs. The significant differences are close to the wire, and in the corners of the cells. The refined STRs reduced the average  $\chi^2$  of the positron helices, and improved the momentum bias and resolution. The method was extended to make refined STRs that were dependent on drift plane, thereby correcting for small variations in plane assembly such as wire placement and cathode-to-cathode differences. Although temperature gradients exist in the detector, the STRs for each plane were dominated by mechanical variations, not by temperature. For each drift plane there was just one cell specified; STRs depending on the region of the plane were investigated and found to be unwarranted.

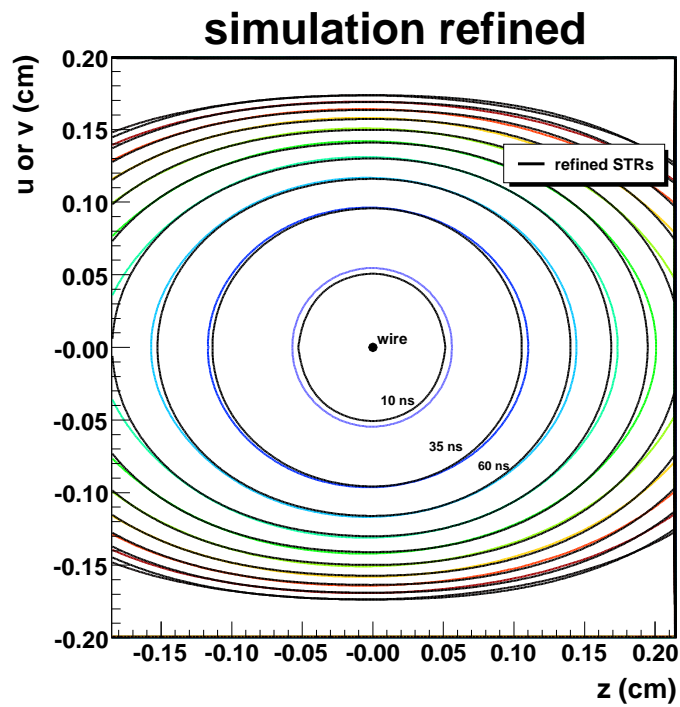
Refined STRs were also produced from the simulation, and these are shown in Fig. 3.6(b). This was done independently from the data, and in this case any differences from GARFIELD must be due to biases in the helix reconstruction software. The simulation was then analysed using these refined STRs, allowing the data and simulation to be treated in the same way; in other words, for both cases the reconstruction biases were absorbed into the STRs. For convenience, the analysis chain is described schematically in Fig. 3.7.

---

<sup>31</sup>The previous  $P_\mu^\pi \xi$  analysis used GARFIELD STRs. The most recent  $\rho$  and  $\delta$  measurements did not use refined STRs for the analysis since they were not initially available, but *did* make a correction for them at the end of the analysis.



(a) STRs refined from helix fits to data.



(b) STRs refined from helix fits to simulation.

Figure 3.6: Comparison of drift cell space-time-relationships from the GARFIELD, and after refinement.

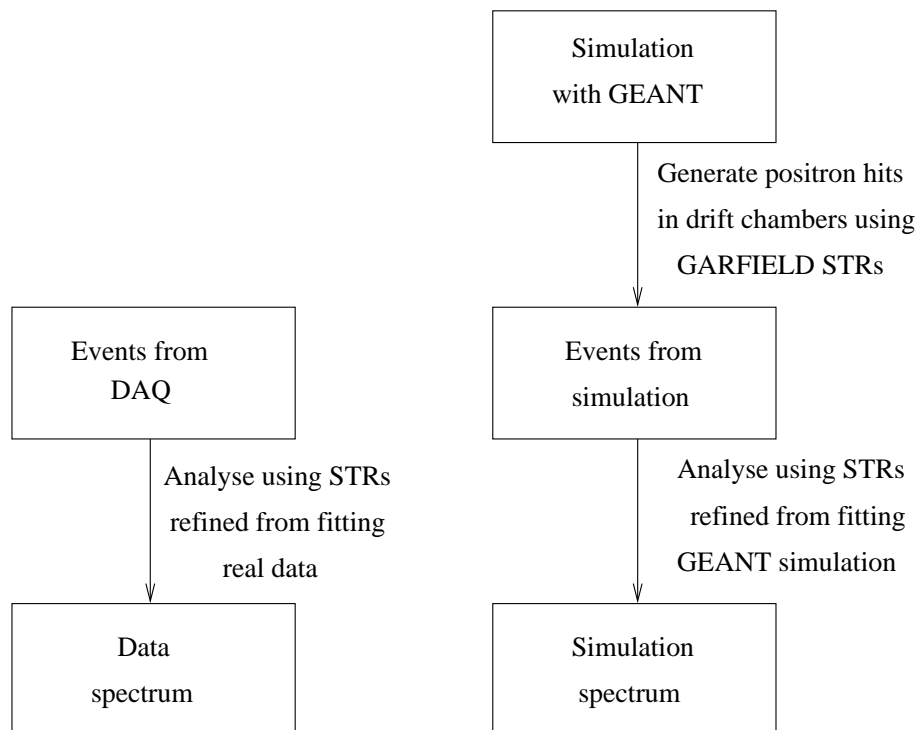


Figure 3.7: Analysis chain for using refined STRs.

### 3.2.8 Improved resolution function

The helix fitting routine must assign a weight to each point ( $\sigma_d$  in Eq. (3.3)). In the past a constant has been used,  $\sigma_d = 100 \mu\text{m}$ . A study using the simulation tested many reasonable functions, and concluded that the best choice was the one shown in Fig. 3.8. This was an “effective resolution”, which incorporated the effects of bias in the fitting procedure.

Figure 3.8 shows a degradation of resolution at longer times; this was due to diffusion spreading out the ionisation clusters, resulting in several smaller pulses. The baseline in the figure was expected from the timing resolution. The resolution from ionisation statistics degraded closer to the wire, but Fig. 3.8 shows that the *effective* resolution was nearly constant. This was because the “left-right ambiguity” dominated the resolution from ionisation statistics; specifically, the wires only recorded time, and this alone could not determine which side of the wire the particle went past. The left-right ambiguity was resolved by iterating the fit, keeping the side that was compatible with the rest of the trajectory. In the first iteration, ionisation with distance ( $x$ ) closer to the wire than 0.1 cm was assigned  $\sigma_d = 2x + \sigma(x)$ , where  $\sigma$  is taken from Fig. 3.8. In subsequent iterations, as the ambiguity was resolved, this

weighting only occurred for hits closer than 0.05 cm, 0.025 cm *etc.* The dominance of the left-right ambiguity therefore resulted in almost no sensitivity to the choice of  $\sigma(x)$  below 0.1 cm.

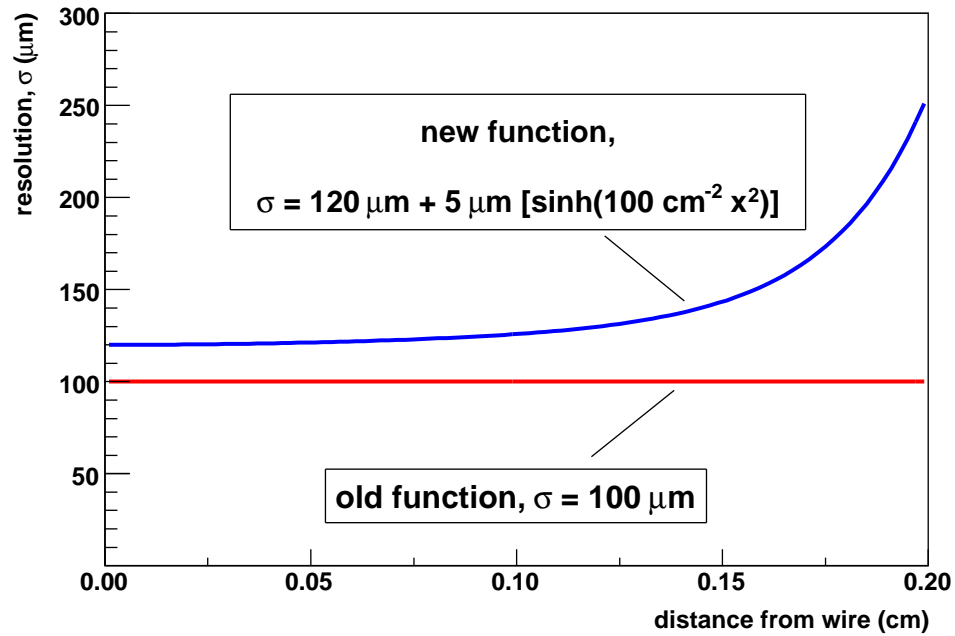


Figure 3.8: Resolution function used during the helix fitting.

### 3.3 Track selection and cuts

Cuts and selections were applied to produce a clean, unbiased decay positron spectrum. The analysis was the same for the data and simulation, with the exception of a time-of-flight cut that was applied in data to remove cloud muons and pions, which are not simulated. The order of these selections and their effect on statistics is shown in Fig. 3.9. The fraction of events removed at each stage was well matched in data and simulation, with about 13% of surface muon events entering the region used to extract muon decay parameters (the “kinematic fiducial”). Each of these selections and cuts will now be briefly described.

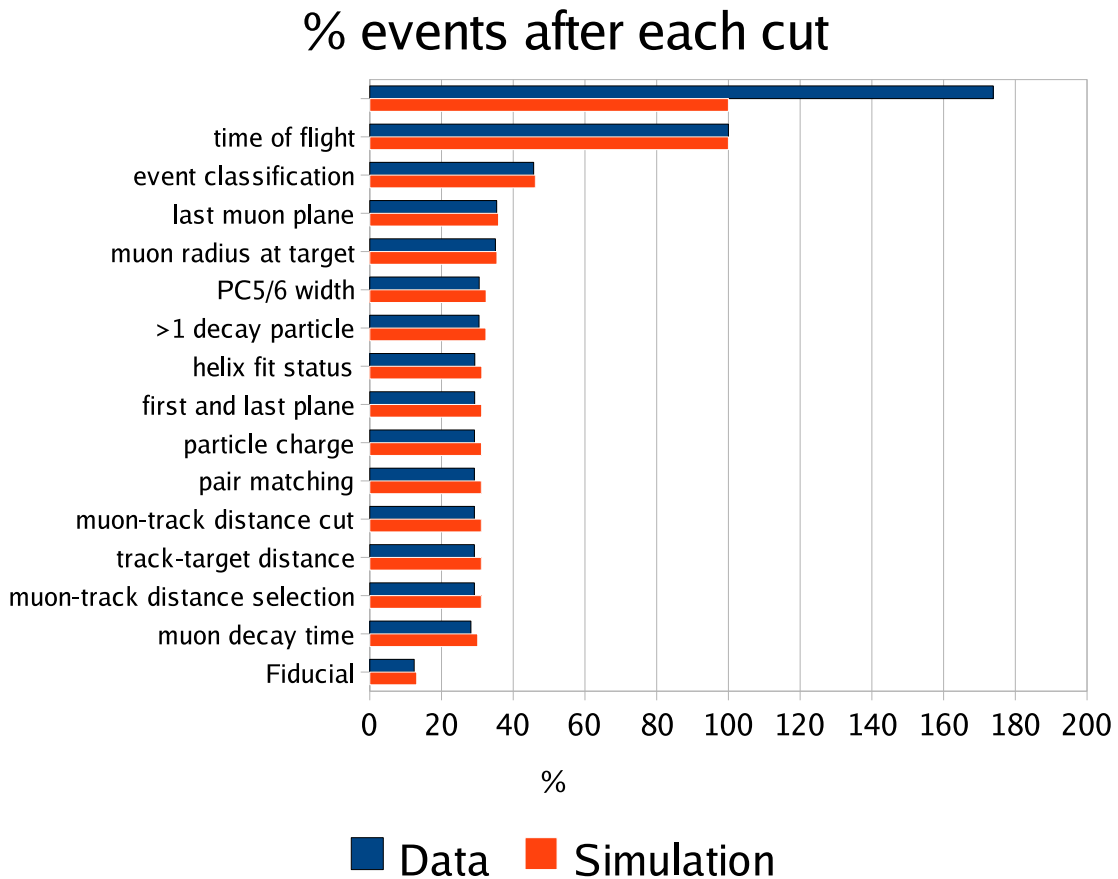
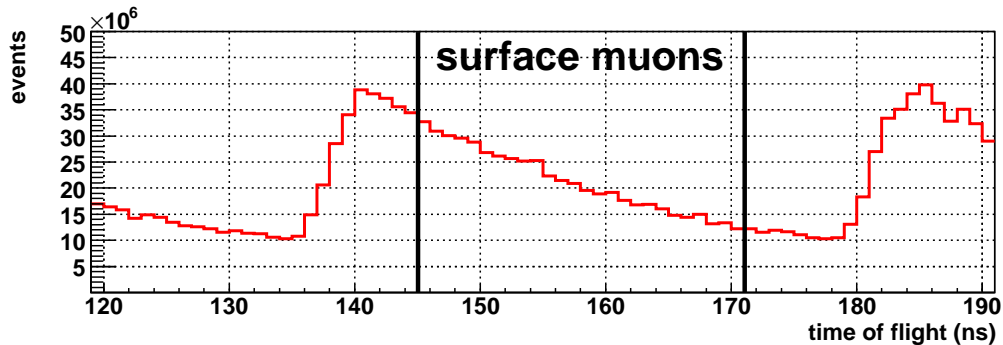


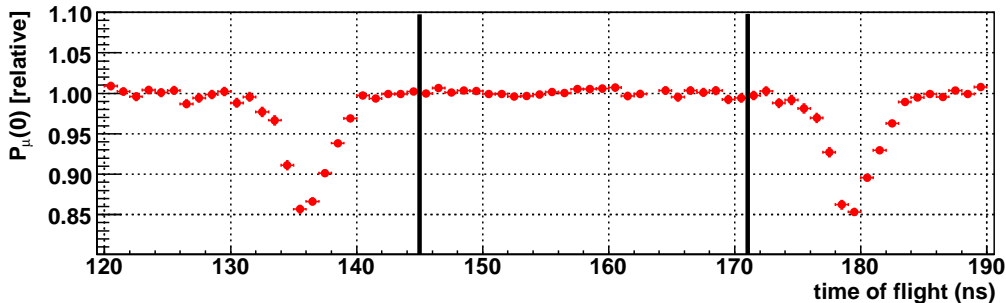
Figure 3.9: Fraction of events after each selection or cut is applied. The data has an additional time-of-flight cut to remove cloud muons and pions; for this reason, 100% in the figure corresponds to surface muons.

### 3.3.1 Trigger particle time-of-flight

A cut on the time-of-flight through the M13 beam line allowed heavier pions and prompt cloud muons to be eliminated (see Section 2.2.5). The cut was tuned by observing the asymmetry in the data, as shown in Fig. 3.10, which includes the conservative setting that was adopted. This cut was not applied to the simulation since only surface muons and positrons were generated<sup>32</sup>.



(a) Number of events for each time-of-flight.



(b) Relative asymmetry for each time-of-flight.

Figure 3.10: Tuning the time-of-flight cut to select surface muons. The vertical lines indicate the setting adopted for this analysis.

### 3.3.2 Event classification cut

The classes of events selected at this stage are shown in Table 3.1. Nearly 90% of events that subsequently pass the remaining cuts are of the simplest type. The remaining  $\approx 10\%$  have a beam positron that doesn't interfere with the decay positron's reconstruction. Events

<sup>32</sup>The capability to simulate proton bunches on the target and the M13 beam line existed, but there was little motivation since the experiment had a high precision muon beam measurement at the end of the channel.

with multiple muons have been removed. Note that the event classification cut includes an implicit time cut at  $1.05 \mu\text{s}$ , which removes 38% of events due to the muon’s lifetime.

Table 3.1: Fraction of event types in the fiducial.

Event type <sup>a</sup>	Description	% of fiducial events	
		data	simulation
1	$\mu^+$ and decay- $e^+$ , separated by $> 1.05 \mu\text{s}$	88	87
2	$\mu^+$ , decay- $e^+$ , beam- $e^+$ (s), all separated by $1.05 \mu\text{s}$	11	12
6	As (1), with delta- $e^-$ removed	0.6	0.5
7	As (2), with delta- $e^-$ removed	$< 0.1$	$< 0.1$
10	As (1), decay- $e^+$ scattered	$< 0.1$	$< 0.1$
11	As (2), decay- $e^+$ scattered	$< 0.1$	$< 0.1$
21	As (1), but beam- $e^+$ overlapping $\mu^+$ or decay- $e^+$ in PCs <sup>b</sup>	$< 0.1$	0.2
22	As (2), but beam- $e^+$ overlapping any particle in PCs	$< 0.1$	$< 0.1$

<sup>a</sup> This is an identifier used internally by the collaboration. See the appendix of Ref. [18] for more detail.

<sup>b</sup> Events where the beam- $e^+$  overlap in the DCs are removed, since DC hits are used to reconstruct the decay- $e^+$ .

### 3.3.3 Muon cuts

#### Last muon plane

The muon must have a hit in the PC immediately before the stopping target, but not in the PC following the target.

#### Muon radius at target

A radial cut was needed on the muon’s final position to ensure that the decay occurred in the metal target rather than the surrounding foils (see Fig. 2.14). A cut was also needed to keep decay positrons with high transverse momentum inside the tracking region; otherwise they could strike external material (*e.g.* glass frames) and scatter. This cut demanded

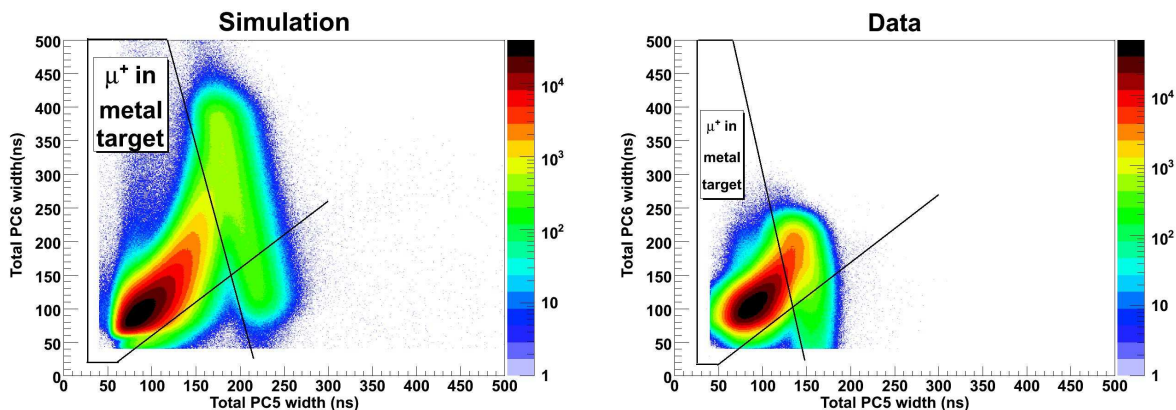
$$r = \sqrt{u_{\text{PC5}}^2 + v_{\text{PC6}}^2} < 2.5 \text{ cm}, \quad (3.4)$$

where  $(u_{\text{PC5}}, v_{\text{PC6}})$  were the positions of the wire centres in the PCs immediately before the target.

### Pulse width at target

This analysis used a new cut on the pulse widths in the PCs immediately before the target (PC5 and PC6). The voltages on these PCs were deliberately lowered while acquiring data, which increased the sensitivity to the muon energy deposited, but lowered the positron efficiency. The pulse widths were used to reject muons stopping in the PC gas rather than in the metal target.

The cut positions for data and simulation are shown in Fig. 3.11. Note that no effort was made to tune the simulation's response. The cut was applied to both since it affected the average positron energy loss within the target. Separate cuts were made for multiple hit combinations in each PC. The data setting is very conservative to ensure gas stops are completely eliminated. The simulation setting matched the fraction of muons removed from the data.



(a) PC5 and PC6 widths in simulation.

(b) PC5 and PC6 widths in data.

Figure 3.11: Pulse widths in the PCs immediately before the target. Muons that stop in the target can be separated from those stopping in the gas of the final PC. The cut positions differ in data and simulation since the simulation's PC response has not been tuned.

### 3.3.4 Decay particle trajectories

The event classification cut from Section 3.3.2 permitted events with more than one candidate decay trajectory. These multiple tracks could originate from a hard scatter (*i.e.* a large angle multiple scatter which breaks the trajectory to the point where it is reconstructed as two tracks), delta-electrons, decay positrons that scatter off material and cause a second track, or a real beam positron that has survived the earlier selections. This section describes the selections and cuts that result in a single decay trajectory.

#### Number of tracks

There had to be at least one decay trajectory in the event.

#### Helix fit status

The helix fitting algorithm reported a code to describe how successful it was in fitting a track. Only completely successful fits were used.

#### First and last plane

A track had to be fully contained in either the upstream or downstream half of the detector. Tracks could not cross the target module. There was no cut on the number of planes crossed, or the first plane crossed.

#### Particle charge

Only particles that were reconstructed with positive charge were accepted (this was determined by their direction of winding). There were genuinely negative particles in the detector; principally these were delta-electrons, but there were also small contributions from bremsstrahlung (the  $\gamma$  could undergo pair production), and the decay process  $\mu^+ \rightarrow e^- \bar{\nu}_e \nu_\mu e^+ e^-$ . The analysis could incorrectly identify particles as negative; for example, a beam positron that only appears in the upstream detector half due to a scatter in the stopping target could look like an upstream-going decay particle with negative charge.

#### Pair matching

Pairs of track candidates were extrapolated to find their closest distance-of-approach. If both tracks were on the same side of the target, and they appeared to overlap (came within 2 cm), the track furthest from the target was removed since it probably corresponded to a large

angle scatter. If there was a track in each detector half, and they appeared to overlap at the target (came within 0.5 cm), then both tracks were removed since they were probably one beam positron traversing the entire detector.

### **Muon-track distance cut**

Tracks were extrapolated to the  $z$ -position of the stopping target. If the distance between the extrapolated position and the muon's last position exceeded  $(1 + 1/|\cos\theta|)$  cm, then the track was removed. The  $\cos\theta$  dependence of this cut was a result of the reconstruction quality depending on angle.

### **Track-target distance**

The track with a starting plane closest in  $z$  to the target was selected.

### **Muon-track distance selection**

If there was still more than one decay positron candidate, the extrapolation of the track to the  $z$ -position of the target was used to select the track closest to the muon's last position.

### **Muon decay time**

If a muon decayed in less than  $1.05\ \mu\text{s}$ , and the decay positron was upstream, then the drift chambers could still receive late ionisation from the muon, reducing the efficiency of upstream positron reconstruction. The event classification selection has already made an implicit time cut on the decay positron at  $1.05\ \mu\text{s}$ . However, this was determined from the PC times, which had a resolution of  $\approx 20\ \text{ns}$ . An additional cut was now made at  $1.05\ \mu\text{s}$ , using the time determined while fitting the helix, which has better resolution. There was also a cut made at  $9.0\ \mu\text{s}$ , since this allowed  $1\ \mu\text{s}$  of decay positron information to be analysed up to the data acquisition limit of  $10\ \mu\text{s}$ .

## **3.3.5 Kinematic fiducial region**

The helix fitting routine determined the radius and wavelength of each track, from which the transverse momentum was approximately given by

$$p_t [\text{MeV}/c] = 300 \times B [\text{T}] \times r [\text{m}], \quad (3.5)$$

and the longitudinal momentum was approximately given by

$$p_z [\text{MeV}/c] = \frac{300}{2\pi} \times B [\text{T}] \times \lambda [\text{m}]. \quad (3.6)$$

After all the selections and cuts from the previous section, the decay spectrum was reconstructed; this is shown alongside the theoretical spectrum in Fig. 3.12.

The region of  $(p, \cos \theta)$  for spectrum fitting (the “fiducial”) was then chosen to minimise bias and inefficiency, maximise resolution and sensitivity, and ensure that any deficiencies were well matched between data and simulation; this selection is shown in Fig. 3.12(c). These fiducial boundaries will now be described.

### **Total momentum, $p < 52.0 \text{ MeV}/c$**

An upper momentum cut was placed at  $p = 52.0 \text{ MeV}/c$  for several reasons. First, the spectrum was most affected by radiative corrections at higher momenta; the cut therefore reduced the systematic uncertainty due to radiative corrections. Second, the momentum calibration of the spectrum used the higher momentum region; as a result, the region was excluded from the decay parameter extraction to be conservative. Third, the momentum resolution was degraded at higher momenta.

### **Longitudinal momentum, $|p_z| > 14.0 \text{ MeV}/c$**

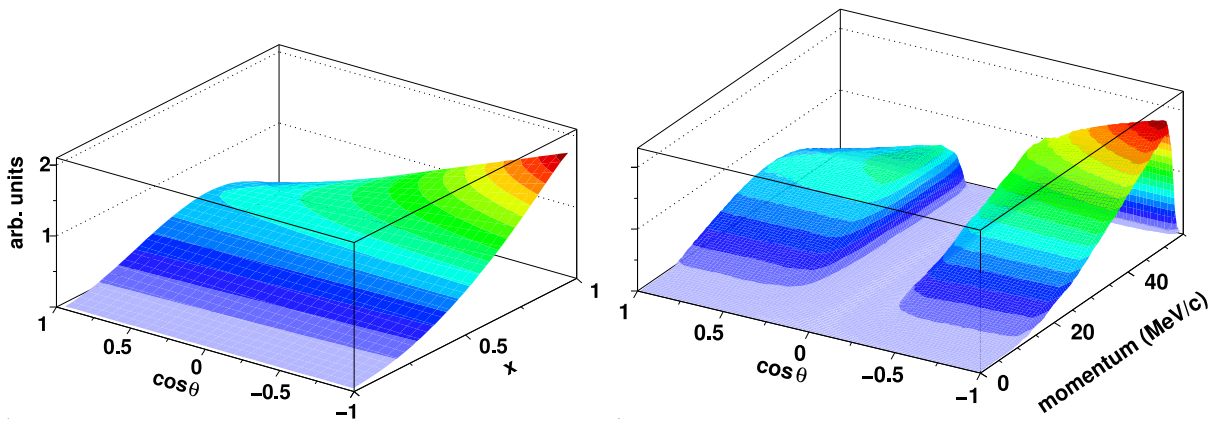
The cut was necessary to avoid a wavelength ambiguity (see Section 3.2.5). Although the chambers were specifically repositioned to reduce this ambiguity, it was still present and had to be avoided. The statistical gain from adjusting this cut was insignificant for  $P_\mu^\pi \xi$ .

### **Angle, $0.54 < |\cos \theta| < 0.96$**

At small angles (large  $|\cos \theta|$ ) the wavelength was poorly resolved, and the helix fitting algorithm began to fail. At large angles (small  $|\cos \theta|$ ) the reconstruction became unreliable due to increased multiple scattering.  $P_\mu^\pi \xi$  benefits the most by including larger angles, but the improvement is still only marginal.

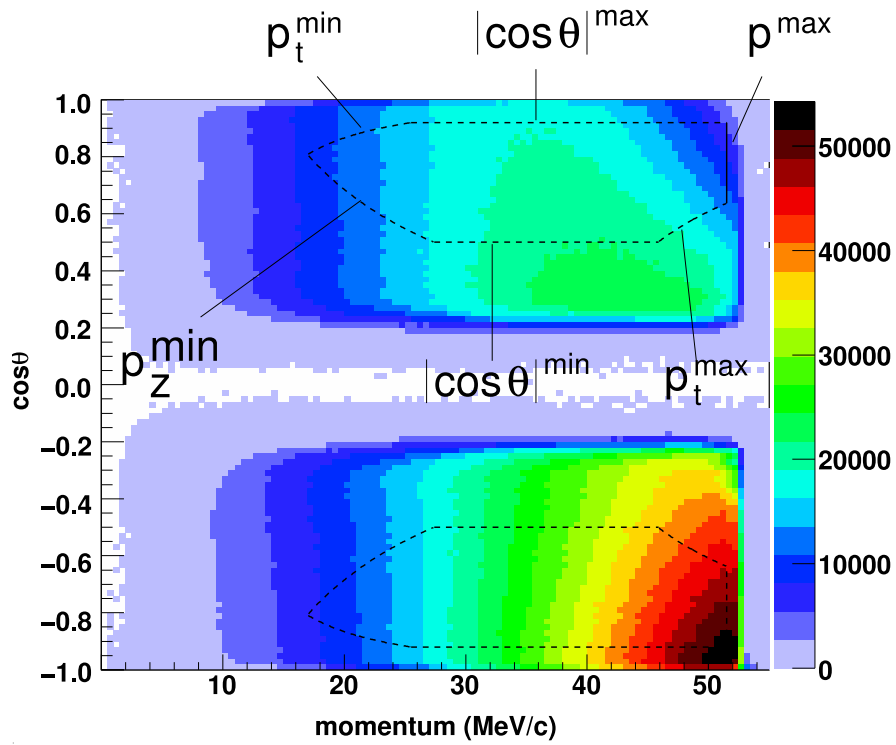
### **Transverse momentum, $(10.0 < p_t < 38.0) \text{ MeV}/c$**

The maximum transverse momentum cut was coupled to the target radius cut of 2.5 cm; together these cuts kept the positron trajectory within the instrumented region of the chambers.



(a) Theoretical spectrum.

(b) Reconstructed spectrum.



(c) Reconstructed spectrum with fiducial boundaries.

Figure 3.12: Comparison of theoretical and reconstructed muon decay spectra. The lower plot shows the fiducial region.

There was a minimum transverse momentum cut to avoid small angle difficulties where the track radius became comparable to the wire spacing.

### 3.4 Extraction of muon decay parameters

The spectrum from data was compared to a simulation that was generated with hidden values of  $\rho$ ,  $\delta$  and  $P_\mu^\pi \xi$ ; the hidden range was limited to  $\pm 1\%$  of the standard model values.  $\eta$  was fixed to the world average, for the reasons already described in Section 1.4.5. The same analysis was applied to both data and simulation, so that biases and inefficiencies cancelled to first order.

The hidden values were only revealed after all the systematic uncertainties were evaluated on the *difference* between the data and simulation spectra. Since the result from the data was unknown until the end, this removed potential biases from tuning cuts, rejecting anomalous data, and evaluation of systematic uncertainties.

The method of comparing the data and simulation spectra will now be described. Recall the expression for the differential decay rate,

$$\frac{d^2\Gamma}{dx d\cos\theta} = k(x) \{F_{IS}(x) + P_\mu \cos\theta F_{AS}(x)\}, \quad (3.7)$$

where,

$$k(x) = \frac{m_\mu}{4\pi^3} W_{e\mu}^4 G_F^2 \sqrt{x^2 - x_0^2} \quad (3.8)$$

$$F_{IS}(x) = x(1-x) + \frac{2}{9}\rho(4x^2 - 3x - x_0^2) + \eta x_0(1-x) + F_{IS}^{RC}(x), \quad (3.9)$$

$$F_{AS}(x) = \frac{1}{3}\xi\sqrt{x^2 - x_0^2} \left[ 1 - x + \frac{2}{3}\delta \left( 4x - 3 + \left( \sqrt{1 - x_0^2} - 1 \right) \right) \right] + F_{AS}^{RC}(x), \quad (3.10)$$

and the terms were defined in Section 1.4. The expression is linear in  $P_\mu^\pi \xi$ ,  $P_\mu^\pi \xi \delta$ ,  $\rho$  and  $\eta$ . Assuming standard model radiative corrections, this allows exact derivatives of the spectrum

to be constructed,

$$S = \frac{d^2\Gamma}{dx d \cos \theta}, \quad (3.11)$$

$$\left. \frac{\partial S}{\partial P_\mu^\pi \xi} \right|_{P_\mu^\pi \xi, \delta, \rho, \eta} = k(x) \cdot \frac{2}{9}(4x^2 - 3x - x_0^2), \quad (3.12)$$

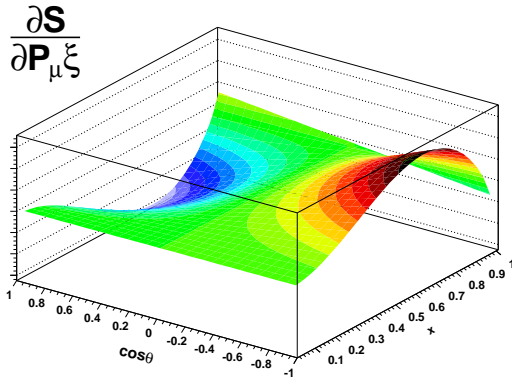
$$\left. \frac{\partial S}{\partial P_\mu^\pi \xi \delta} \right|_{P_\mu^\pi \xi, \delta, \rho, \eta} = k(x) \cdot x_0(1 - x), \quad (3.13)$$

$$\left. \frac{\partial S}{\partial \rho} \right|_{P_\mu^\pi \xi, P_\mu^\pi \xi \delta, \eta} = k(x) \cdot \frac{1}{3} \cos \theta \sqrt{x^2 - x_0^2}(1 - x), \quad (3.14)$$

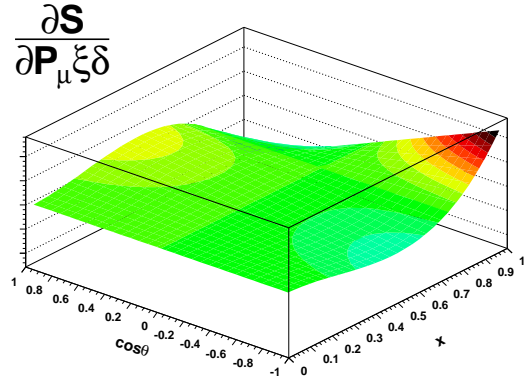
$$\left. \frac{\partial S}{\partial \eta} \right|_{P_\mu^\pi \xi, P_\mu^\pi \xi \delta, \rho} = k(x) \cdot \frac{2}{9} \sqrt{x^2 - x_0^2}(4x - 3 + \sqrt{1 - x_0}). \quad (3.15)$$

Each derivative is independent of the muon decay parameters. The shape of each derivative is shown in Fig. 3.13. The *difference* between the data and simulation spectrum can be used with the derivatives to determine how much of each muon decay parameter is needed to make the spectra agree. The validation of this method is described elsewhere[85]. For  $P_\mu^\pi \xi$ , the method can introduce a bias at a level that is negligible for this measurement, but may be of interest to future experimenters; this is described in Appendix F.

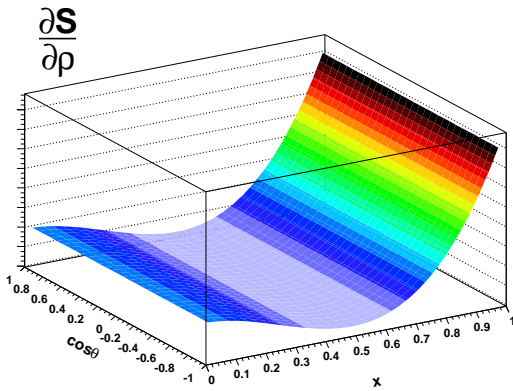
The technique required five spectra to be reconstructed with the same analysis software and cuts: data, simulation and one spectrum for three of the four derivatives (Eqs. (3.12) to (3.14)). Since the derivative spectra had negative regions (they were, after all, just a spectrum shape), a positive value was used to generate the  $(p, \cos \theta)$  for a decay positron, but the sign of the spectrum was passed to the analysis software, which applied it when reconstructing the derivative spectra.



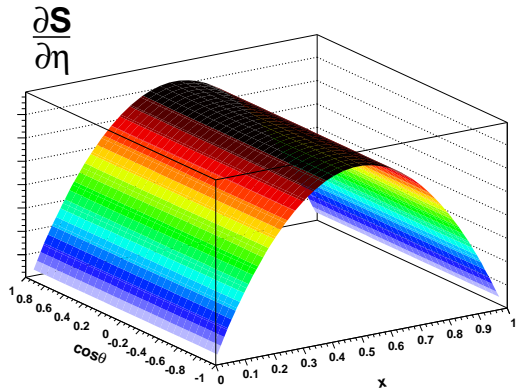
(a) Derivative with respect to  $P_\mu^\pi \xi$ .



(b) Derivative with respect to  $P_\mu^\pi \xi \delta$ .



(c) Derivative with respect to  $\rho$ .



(d) Derivative with respect to  $\eta$ .

Figure 3.13: The shape of each muon decay parameter's contribution to the total spectrum. The vertical scales are inconsistent between the figures since only the *shape* is important here.

### 3.5 Energy calibration

The maximum positron energy from kinematics is  $\approx 52.83$  MeV; this feature was used to calibrate the energy scale of the reconstruction. The region close to the kinematic endpoint is shown for a limited angular range in Fig. 3.14, where the sharp edge is smeared by the reconstruction resolution and radiative corrections. The figure includes a fit, where a step function has been convoluted with a Gaussian to model the resolution. The position of the step function had a linear dependence on  $1/|\cos\theta|$  due to the planar construction of the detector, and this is shown for data and simulation in Fig. 3.15. They are both displaced from the kinematic endpoint due to positron energy loss in the metal target and reconstruction bias. The previous  $P_\mu^\pi \xi$  analysis had endpoints that were further away from the kinematic prediction since energy loss was not taken into account when fitting the positron helices.

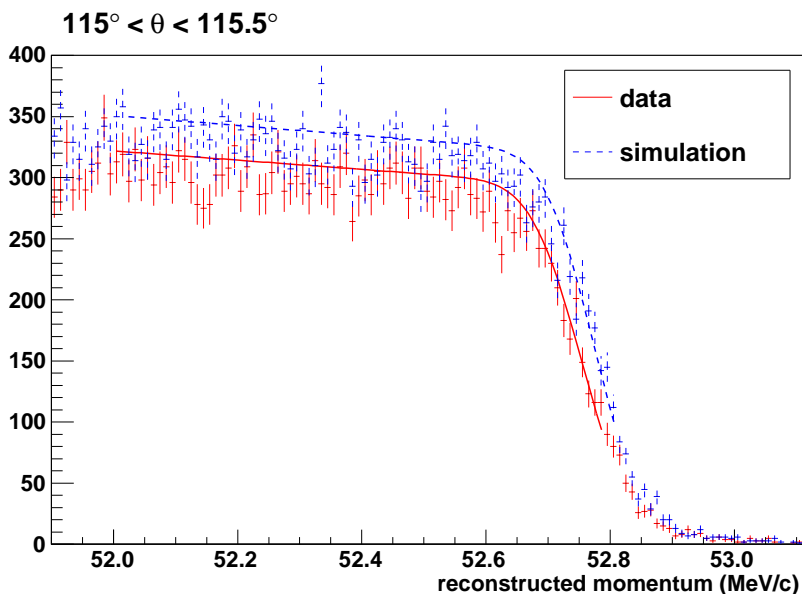


Figure 3.14: Example of fitting the kinematic endpoint in data and simulation.

The discrepancy between data and simulation has at least three causes: the mismatch in stopping distribution between data and simulation, the thickness of the stopping target used in the simulation, and the scale of the magnetic field map in the data. These will be briefly explained.

The muon stopping distribution in the simulation could be tuned with arbitrary precision, since the exact muon stopping location is known. However, in the data, the only available measurement was the location where the muon was last seen. This was an imperfect measure

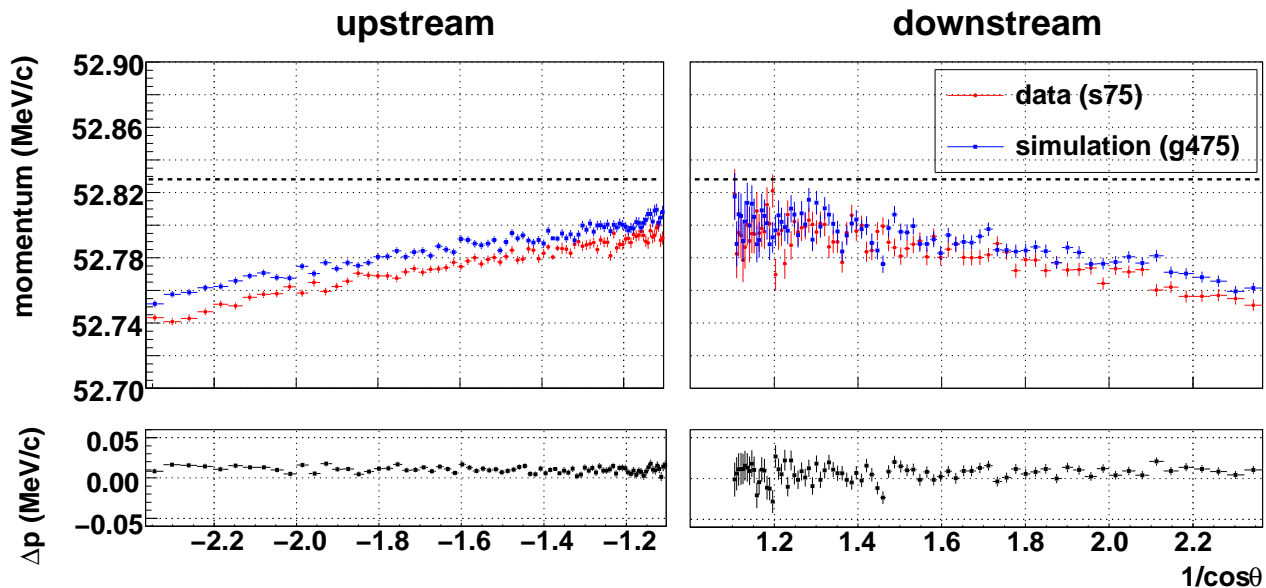


Figure 3.15: Dependence of endpoint position on  $|1/\cos\theta|$ . The black dashed line is the expected endpoint from kinematics.

due to an extra muon source in the data from pions that decayed at the end of the M13 beam line, which were not included in the simulation (see Section 6.3.5). Since the stopping distributions were not matched, the decay positrons in data and simulation traversed a different amount of target material.

The target foil thickness was not measured directly, since such a measurement would have been destructive. Instead the thickness for the simulation was an average derived from the mass and density of the foil. The thickness of the 5 cm diameter region where the muons stopped may not be equal to this average value due to foil non-uniformity.

The stopping distribution and target thickness were expected to affect the angular dependence of Fig. 3.15. The final discrepancy, the magnetic field scale, was expected to affect the vertical offset. In the simulation the same field is used to generate and subsequently analyse. However, in the data, the field map is scaled according to an NMR probe measurement taken at a single location. This probe is positioned at a region where the field is less well known, allowing a possible error in the overall field scale used to analyse the data.

The analysis procedure corrected the data so that the endpoint overlapped the simulation, which from Fig. 3.15 is a change of about 10 keV, with a weak dependence on  $1/\cos\theta$ . This change can be propagated to the rest of the spectrum assuming a constant shift, a constant scale, or a combination of shift and scale. The choice of propagation model will be later treated as a systematic uncertainty.

### 3.6 Time dependence of depolarisation

The previous  $P_\mu^\pi \xi$  analysis determined the time dependent relaxation of the polarisation by fitting

$$G = \frac{N_U - N_D}{N_U + N_D} = KP_\mu(t), \quad (3.16)$$

where U and D are the number of the upstream and downstream counts within the standard fiducial region, and  $K$  is a constant that depends on this region. Equation (3.16) can be explicitly written

$$G = \frac{\int_p^q \int_a^b n(x, \cos \theta) dx d \cos \theta - \int_p^q \int_{-b}^{-a} n(x, \cos \theta) dx d \cos \theta}{\int_p^q \int_a^b n(x, \cos \theta) dx d \cos \theta + \int_p^q \int_{-b}^{-a} n(x, \cos \theta) dx d \cos \theta}. \quad (3.17)$$

If only the time dependence of  $G$  is sought, then a new quantity with the same time dependence can be defined as

$$G' = \frac{\int_p^q \int_a^b w_1 n dx d \cos \theta - \int_p^q \int_{-b}^{-a} w_1 n dx d \cos \theta}{\int_p^q \int_a^b w_2 n dx d \cos \theta + \int_p^q \int_{-b}^{-a} w_2 n dx d \cos \theta}, \quad (3.18)$$

where  $w_1(x, \cos \theta)$  and  $w_2(x, \cos \theta)$  are weighting terms that can be freely chosen. Since  $\cos \theta > 0$  corresponds to downstream decays, and  $\cos \theta < 0$  to upstream decays, Eq. (3.18) can be simplified by making  $w_1 \propto \cos \theta$  and  $w_2 \propto |\cos \theta|$ ; the sum over the bins, both upstream and downstream, is then

$$G' = \frac{\sum_{\text{US,DS}} w_1 N}{\sum_{\text{US,DS}} w_2 N}, \quad (3.19)$$

where  $N$  is the number of integrated counts in the bin.

For this measurement  $w_1$  and  $w_2$  were related to the theoretical asymmetry itself[94]. The full expression for the differential decay rate was given in Eq. (3.7). Neglecting radiative corrections and the positron mass, and assuming standard model values for  $\rho$  and  $\delta$ , the differential decay rate is

$$\frac{d^2 \Gamma}{dx d \cos \theta} = x^2 [(3 - 2x) + P_\mu^\pi \xi \cos \theta (2x - 1)], \quad (3.20)$$

which produces a theoretical asymmetry of

$$A(x, \cos \theta) = P_\mu^\pi \xi \cos \theta \left( \frac{x - \frac{1}{2}}{\frac{3}{2} - x} \right). \quad (3.21)$$

After integration over  $\cos \theta$ , Eq. (3.21) is shown in Fig. 3.16. The greatest contribution to the integral asymmetry comes from the highest energy positrons; the positrons with  $x \approx 0.5$  contribute little to the total asymmetry yet add statistical noise. Positrons with  $x < 0.5$  actually detract from the total asymmetry, and add more statistical noise. The optimum sensitivity is achieved by weighting each positron according to how much it contributes to the asymmetry, by relating  $w_1$  and  $w_2$  to Eq. (3.21).

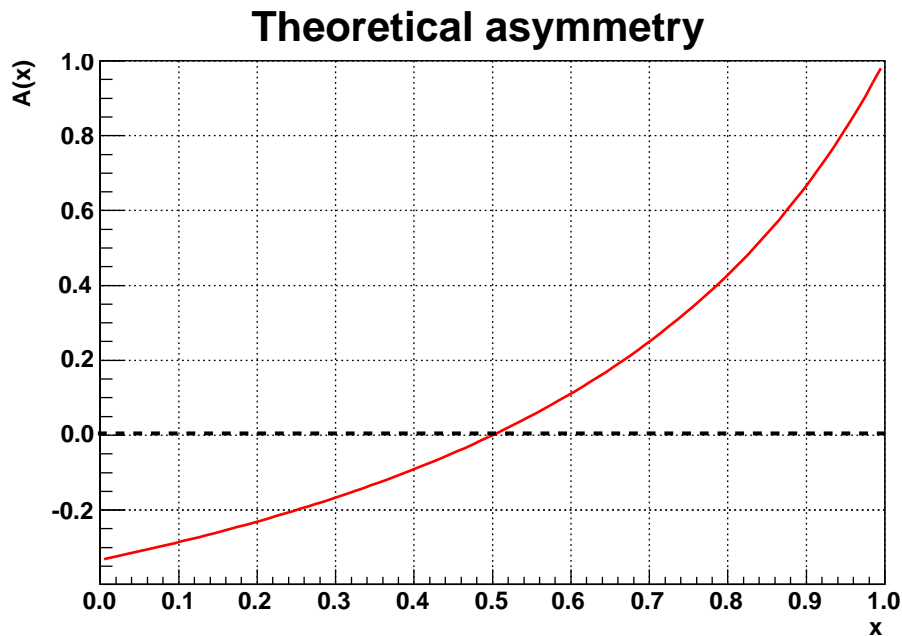


Figure 3.16: Theoretical prediction for the asymmetry, assuming standard model values for the muon decay parameters (Eq. (3.21)). Positrons with  $x < 0.59$  are excluded from the analysis.

The weighting factors used in the current analysis were

$$w_1 = A(x, \cos \theta) |A(x, \cos \theta)|^n, \quad (3.22)$$

$$w_2 = |A(x, \cos \theta)| |A(x, \cos \theta)|^n, \quad (3.23)$$

$$n = 1. \quad (3.24)$$

Different powers of  $n$  were examined, but  $n = 1$  combined with rejection of positrons with  $x < 0.59$  was found to be close to optimum<sup>33</sup>. The combination of weighting the counts, and removing low energy positrons significantly reduced the uncertainty on the depolarisation

<sup>33</sup>The lower momentum positrons could be included, and their sign could be reversed for  $x < 0.5$ , but this doesn't improve the statistical precision by a significant amount.

rate. An example of a fit to a single set is shown in Fig. 3.17, where  $P_\mu(t) = P_\mu(0) \exp(-\lambda t)$  has been used.

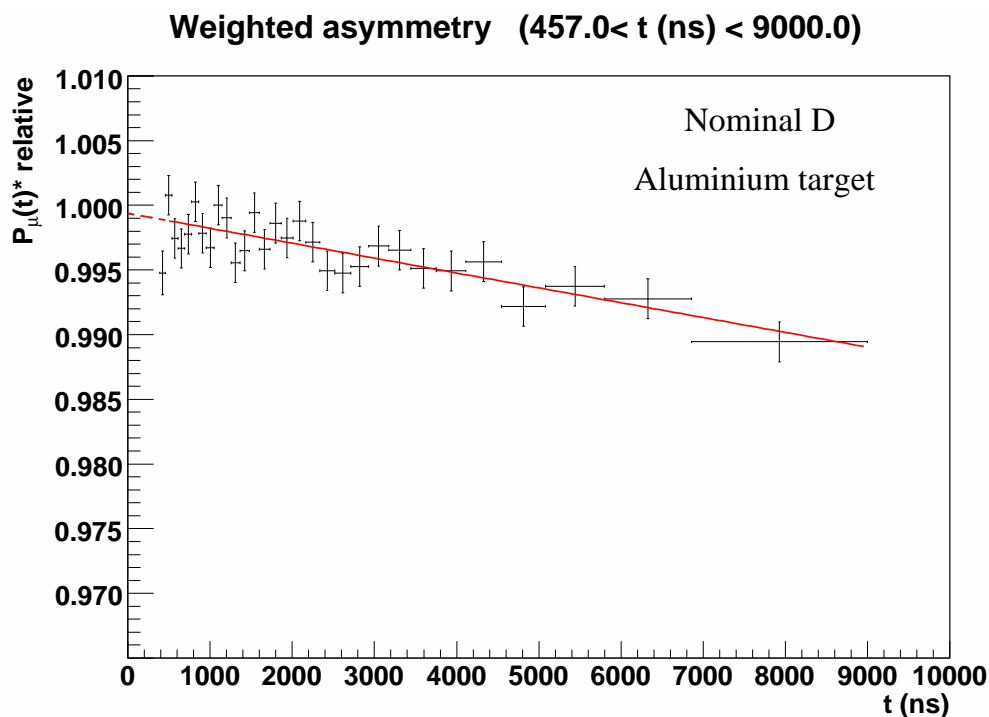


Figure 3.17: Example of an exponential fit to the asymmetry. The vertical scaling is arbitrary.

### 3.7 Muon beam average

Individual muon trajectories could not be reconstructed due to their low transverse momentum, significant energy loss, and the muons suffering from more electronic crosstalk than the positrons. However, the average position of the muon beam within the chamber region was found to be well described by a helix with decaying amplitude and wavelength; this is demonstrated in Fig. 3.18, which shows the trajectory of a simulated beam with large average transverse momentum. The solid markers indicate a pair of orthogonal detector planes, and the positions of these were fit with

$$\begin{pmatrix} \langle x \rangle \\ \langle y \rangle \end{pmatrix} = (A - A_d \cdot z') \begin{pmatrix} \cos(f(z')) \\ \sin(f(z')) \end{pmatrix} + \begin{pmatrix} \Delta_x \\ \Delta_y \end{pmatrix}, \quad (3.25)$$

where  $z' = z + 59.59$  cm,  $\langle x \rangle$  and  $\langle y \rangle$  are the mean muon positions,  $\Delta_x$  and  $\Delta_y$  are the positions of the helix centre,  $A$  is the amplitude of the helix at  $z' = 0$ ,  $A_d$  is a linear decay parameter, and

$$f(z') = 2\pi \frac{z'}{\lambda - \lambda_d z'} + \phi, \quad (3.26)$$

where  $\lambda$  is the helix wavelength at  $z' = 0$ ,  $\phi$  is the phase at  $z' = 0$  and  $\lambda_d$  is a linear decay parameter. The parameters  $A$  and  $\lambda$  approximately corresponded to average transverse and longitudinal momentum.

The fit used the mean positions at all chambers except the final proportional chambers and the last two pairs of drift chambers. This gave a total of 11 points, from which 7 fit parameters were determined. The parameters of the average muon beam were used to tune the M13 beam line, and monitor the muon beam's stability (see Sections 5.2 and 5.4.7 respectively).

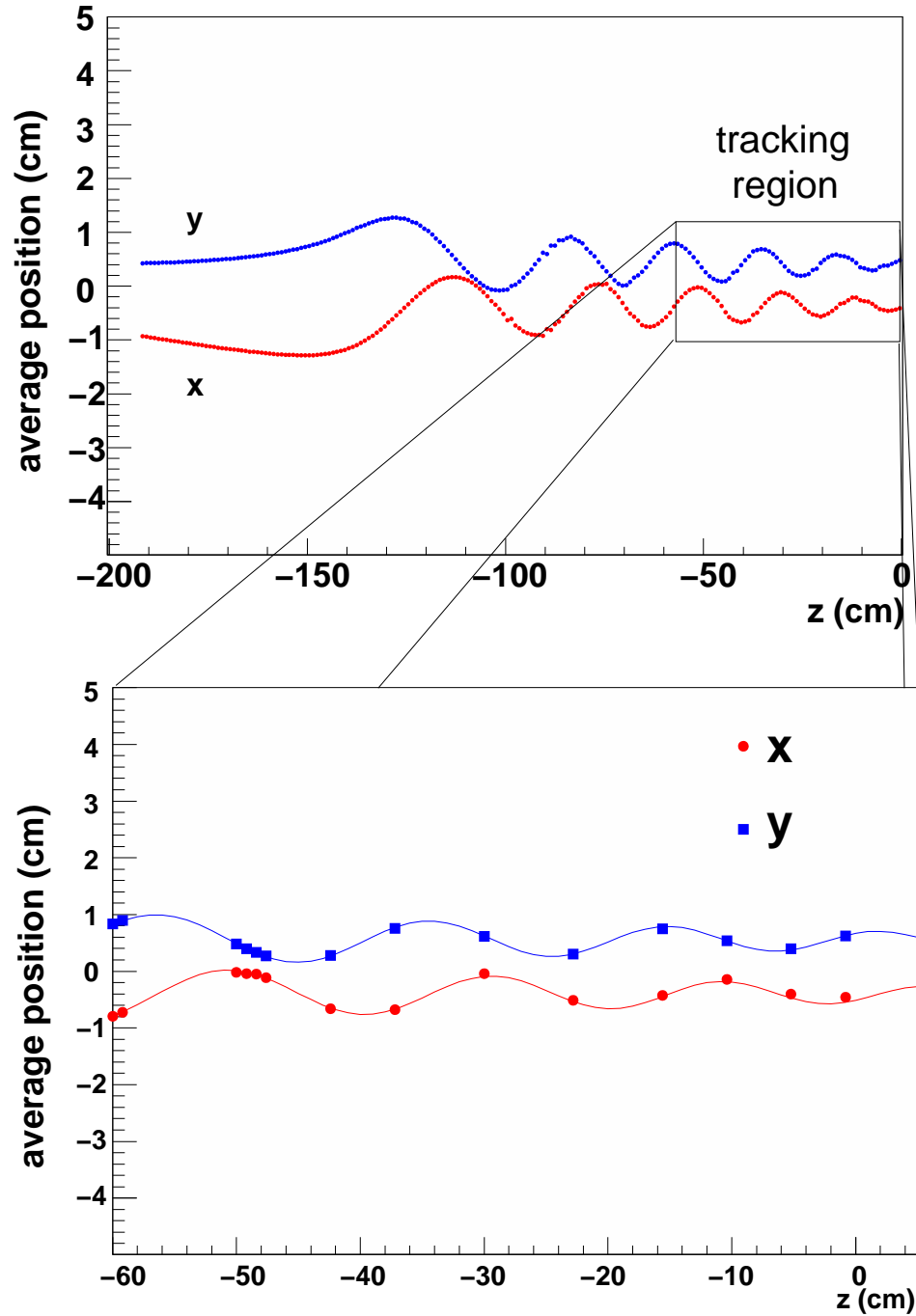


Figure 3.18: A simulated beam with large average transverse momentum. The upper figure shows the mean trajectory from the end of the M13 beam line up to the stopping target. The lower figure shows the beam inside the chambers, where the solid markers indicate a pair of planes.

# Chapter 4

## Simulation

### 4.1 Introduction

A detailed simulation of the detector was implemented in `GEANT3.2.1`[91] for several purposes. First, the performance of the reconstruction was studied and optimised. Second, the muon decay parameters could be measured while remaining blind to their data values (see Section 3.4). Third, the final polarisation of the muons was determined by using the simulation to transport their momentum and spin to the stopping location. An outline will be given of the `GEANT3` features that were important to the TWIST experiment, and the custom code modules most relevant to  $P_\mu^\pi \xi$  will be described in more detail.

### 4.2 Overview of the simulation

Simulation events started with the generation of muons and beam line positrons at the end of the M13 channel, with rates that matched the data<sup>34</sup>. Pions, protons, cloud muons and radioactive beam line particles were not simulated, since they were removed from the real data by physical windows and a time-of-flight cut on the trigger particle (see Section 3.3.1). The simulated particles and their secondaries, including  $\gamma$ 's,  $e^+$  and  $e^-$ , were transported through the detector materials. The response of the chambers to the subsequent ionisation was tuned to match the data.

When a muon decayed, the simulation produced a positron with energy and angle following a pre-defined spectrum that used a hidden value of  $P_\mu^\pi \xi$ . Transportation of the particles through the magnetic field used a fourth order Runge-Kutta numerical method to propagate the momentum. The muon's spin was transported with equivalent precision. The simulation demanded that at least one transportation step was taken in every material; this was important for the energy loss in thin materials such as the cathode foils, which each had a thickness of just  $0.9 \text{ mg/cm}^2$ .

---

<sup>34</sup>The muon rate matched the average trigger rate from the DAQ. The beam positron rate was tuned so that the probability of observing a positron within an event was matched in data and simulation.

The physics processes in the simulation included ionisation energy loss,  $\delta$ -electron production, Bremsstrahlung, multiple Coulomb scattering, position annihilation, Compton scattering, pair production, the photo-electric effect and Bhabha scattering; these processes were *not* tuned from their GEANT defaults. Materials external to the tracking volume were included, such as the beam pipe and the upstream “beam package” (see Section 2.9); the positrons could backscatter from these materials and re-enter the tracking volume, introducing extra hits and a resulting inefficiency that the simulation had to reproduce.

The output of the simulated wire chambers and scintillators were written to disk through a digitisation routine that mimicked the real DAQ. This allowed the data and simulation to undergo an almost identical analysis, with the exception of the crosstalk removal routine, since the simulation did not contain this level of electronics detail.

For each data set accumulated, a simulation with double the statistics was generated; this was adequate since the  $P_\mu^\pi \xi$  precision is limited by systematic uncertainties, not statistical uncertainties.

The customised code modules that are important for  $P_\mu^\pi \xi$  will now be described. Specifically these are the routine that generated the initial position/angle/momentum of the beam line particles, the muon depolarisation mechanisms, the generator of decay positrons, and the simulation of the wire chamber response. The simulation’s performance is later compared to the data when evaluating the systematic uncertainties.

### 4.3 Primary particle generation

The simulated beam (muons and positrons) is generated based on measurements of the real beam. For the muons this was achieved with a pair of time expansion chambers (TECs) that were inserted at the beginning and end of each data set, at a  $z$  location upstream of the solenoidal fringe field. The TECs had low positron efficiency, so that the beam line positrons were instead measured using the upstream drift chambers, while the magnetic field was off. The precision was inferior to the muon beam measurement, but it was adequate since  $P_\mu^\pi \xi$  was relatively insensitive to the quality of the simulated positron beam.

The initial position and angle of the muons and beam line positrons were generated with the same algorithm. The position was selected by dividing up the  $x - y$  distribution of the number of muons into  $0.1 \text{ cm} \times 0.1 \text{ cm}$  bins, and using this as a probability distribution. The  $\theta_x$  and  $\theta_y$  angles were drawn from independent Gaussian distributions with means and widths that matched the data measurement for the particular  $(x, y)$  bin; the widths of the Gaussian angle distributions were multiplied by  $c_x = 63.9\%$  in the  $x$ -module and  $c_y = 48.0\%$  in the

$y$ -module in order to correct for multiple scattering (the muons were multiple scattered by the gas within the TECs while they were being measured, which increased the apparent emittance of the beam).

The initial  $z$ -position of the muons was always at the centre of the TEC modules. The initial momentum ( $p$ ) depended linearly on the  $x$ -position at the TECs according to

$$p(x) = p_0 - p_1 x. \quad (4.1)$$

The  $p_1$  parameter was tuned using comparisons such as Fig. 4.1, and  $p_1 = 0.17 \text{ MeV/c}$  per cm was found to be optimal. The  $p_0$  parameter was then determined by setting the average momentum to  $29.6 \text{ MeV/c}$  so that

$$\begin{aligned} p_0 &= \langle p(x) \rangle + p_1 \cdot \langle x \rangle \\ &= 29.6 \text{ MeV/c} + (0.17 \text{ MeV/c}) \cdot \langle x \rangle, \end{aligned} \quad (4.2)$$

and  $\langle x \rangle$  was different for each data set. Muons were not generated above the kinematic maximum momentum of  $29.79 \text{ MeV/c}$ .

The materials traversed by the muons were described earlier (Section 2.11), where it was noted that the simulation required an extra  $1.9 \text{ mg/cm}^2$  of material to match the data distribution of where the muon was last seen. However, this was within the uncertainties of the thickness measurements and the vacuum window bulge, meaning we could not be sure that the small amount of extra material was justified. For half the simulations the  $1.9 \text{ mg/cm}^2$  of material was added at a  $z$  location within the strong magnetic field region, so that it did not change the muons' polarisation. The energy calibration procedure then indicated the material was unnecessary, and for the remaining simulations this additional material was removed.

## 4.4 Depolarisation

The simulation must transport the muon's spin through the solenoidal magnetic field, and reproduce the time dependence of the spin once inside the stopping material. These routines did not exist in `GEANT3`, and were specially written for the TWIST experiment.

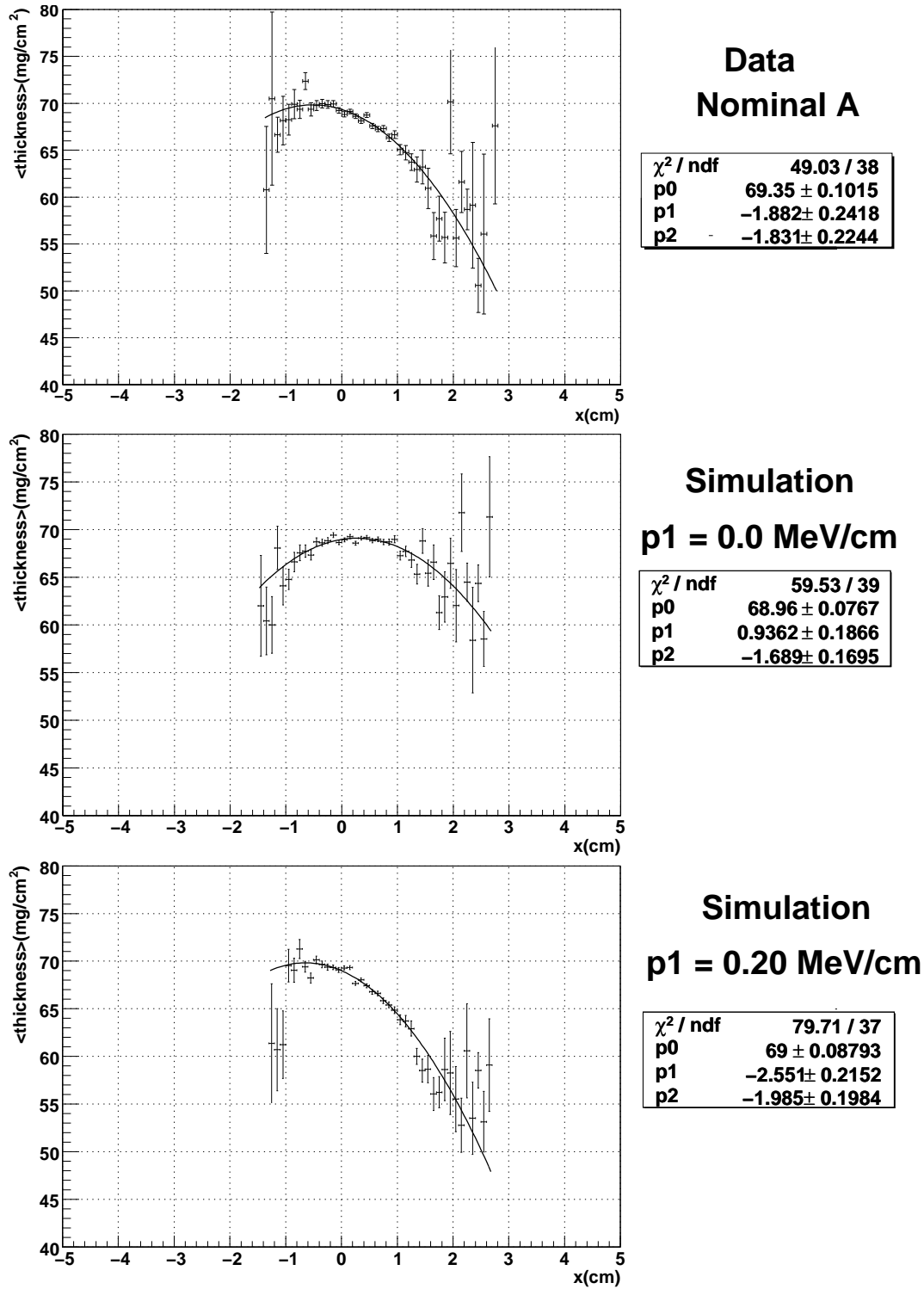


Figure 4.1: Average muon range ( $\text{mg}/\text{cm}^2$ ) depends on the  $x$ -position of the muon at the TECs. The relationship is well approximated by a quadratic function. The simulation required  $p_1 = \frac{dp}{dx} = 0.17 \text{ MeV}/\text{cm}$  in order to match the data.

### 4.4.1 Initial polarisation

The simulation started the muons with anti-parallel spin and momentum vectors. This is an approximation with two limitations; first the muons were selected from the graphite production target at an average depth of  $16 \mu\text{m}$ . While exiting the target, multiple scattering changed the momentum vector but not the spin vector, causing them to no longer be exactly anti-parallel. This effect is later treated as a correction. Second, the muons have already passed through the magnetic fields in the M13 beam line, and the difference in precession frequencies between the momentum and spin vectors (Eq. (1.37)) can change the angle between them. This second effect is negligible, changing  $P_\mu$  at the level  $\sim 10^{-8}$ ; see Appendix I.

### 4.4.2 Electromagnetic field

Recall the Thomas equation from Section 1.6.1, which described the propagation of the spin vector in an electromagnetic field,

$$\frac{d\vec{s}}{dt} = \frac{e}{mc} \vec{s} \times \left[ \left( \frac{g}{2} - 1 + \frac{1}{\gamma} \right) \vec{B} - \left( \frac{g}{2} - 1 \right) \frac{\gamma}{\gamma + 1} (\vec{\beta} \cdot \vec{B}) \vec{\beta} - \left( \frac{g}{2} - \frac{\gamma}{\gamma + 1} \right) \vec{\beta} \times \vec{E} \right]. \quad (1.39)'$$

The  $E$  field term was not included in the simulation. The drift and proportional chambers have significant electric fields, but a field of  $(+E)$  between the entrance cathode foil and wire was followed by a symmetric  $(-E)$  field between the wire and exit cathode foil, effectively cancelling the change in spin from this term. For programming convenience, the Thomas equation was manipulated into this form:

$$\frac{d\vec{s}}{dx} = \frac{d\vec{s}}{dt} \frac{1}{|\beta|} = \frac{e}{mc} \left[ U_1(\vec{s} \times \vec{B}) - U_2(\vec{s} \times \vec{v}) \right], \quad (4.3)$$

where

$$U_1 = \left[ \frac{1}{|\beta|} \left( a + \frac{1}{\gamma} \right) \right], U_2 = \left[ a \frac{\gamma}{\gamma + 1} |\beta| (\vec{v} \cdot \vec{B}) \right],$$

and  $a = (g - 2)/2$ . The spin was then propagated using a Taylor expansion,

$$\vec{s} = \vec{s}' + \frac{d\vec{s}}{dx} \Delta x, \quad (4.4)$$

where  $\vec{s}$  is the new spin vector and  $\vec{s}'$  is the spin at the previous step. In order to correct for numerical precision errors, the components of the spin vector were renormalised at each

step. For example,

$$s_z = \frac{s_z}{\sqrt{s_x^2 + s_y^2 + s_z^2}}, \quad (4.5)$$

and similarly for  $s_x$  and  $s_y$ . For each **GEANT** particle transportation step, smaller sub-steps were taken that depended on the magnitude of the magnetic field and muon velocity.

The Thomas equation can be solved exactly in a uniform and stationary magnetic field[95], and this solution was used to validate the numerical method[57]. A more recent test found that  $P_\mu$  (the polarisation  $z$ -component) decreased by  $4 \times 10^{-4}$  within the tracking volume of the detector, where the field is  $\approx 2.0$  T and uniform so that  $P_\mu$  should be unchanged. This was due to not enough sub-steps being taken at low velocities to propagate  $s_x$  and  $s_y$ , which caused a  $s_z$  error due to the renormalisation in Eq. (4.5). This was fixed by increasing the number of sub-steps by a factor of ten. A new validation used the simulation with energy loss and multiple scattering disabled, to show that momentum and spin remained anti-parallel to  $< 2 \times 10^{-5}$ .

### 4.4.3 Time-dependent depolarisation

In the time interval between thermalisation and decay, the muon's spin is precessed, and can be flipped ( $\vec{s} \rightarrow -\vec{s}$ ) so that  $P_\mu(t)$  matches the data. The simulation does not implement the random walk of the muon in the metal stopping target.

### 4.4.4 Other depolarisation

The simulation did not include depolarisation due to the field between the nucleus and atomic electrons, muonium formation at low velocities, and muon-electron scattering, since they were all negligible (see Section 1.6.2). Also the spin of the positron was not transported since the experiment could not detect this quantity.

## 4.5 Muon decay

The default **GEANT3** program could simulate muon decays assuming the standard model ( $V - A$ ) interaction ( $P_\mu^\pi \xi = 1$ ). For non-standard model values of the decay parameters and radiative corrections with the required accuracy, a special program was used[85]. The software ran on a dedicated server at TRIUMF, and each time a simulation began, the list of decay positron ( $p, \cos \theta$ ) pairs was retrieved from the server. The custom program also produced the derivative spectra that were described in Section 3.4. In this mode of operation, a ( $p, \cos \theta$ )

pair *and* the relevant sign ( $\pm$ ) were supplied to the simulation. The simulation passed the sign to the analysis, allowing a derivative spectrum with positive and negative regions to be produced.

## 4.6 Wire chamber response

The response of the drift and proportional chambers were simulated in detail, with the aim of accurately reproducing inefficiencies, bias and resolution. As a particle passed through the chamber gas, ion clusters were randomly produced along the trajectory, with a mean cluster spacing that was tuned to match the data. The drift distance to the wire was converted into a time using space-time-relationships from the `GARFIELD` software[93] (see Section 3.2.7). The time was then smeared to include electronics effects and diffusion. Signals from wires that were dead in the data (typically one or two out of more than 3500) were deactivated in the simulation.

The muons produced more ionisation than the positrons, which deadened the wire within 0.06 cm, with a mean recovery time of  $3.0 \mu\text{s}$  (both of these parameters were measured using data). This effect is included in the simulation since it caused a small upstream inefficiency.

‘

# Chapter 5

## Data

### 5.1 Overview

The commissioning run of the TWIST experiment was in 2001. The first sets for muon decay parameter extraction were acquired in 2002, and results for  $\rho$  and  $\delta$  were published in 2005[82, 85]. An engineering run took place in 2003, followed by the second set of physics data in 2004, which have been analysed twice: the first publication in 2006 was for  $P_\mu^\pi \xi$ [57], and the second publication in 2008 was for  $\rho$  and  $\delta$ [18].

The author commenced his studies in September 2005, and the experiment soon undertook an engineering run from October 2005 to December 2005. The data analysed for this measurement were acquired in two periods: muons were stopped in a silver target from October 2006 to December 2006, and in an aluminium target from May 2007 to August 2007. From June 2006 to September 2006 data were accumulated on the same aluminium target, but this was not analysed<sup>35</sup>.

### 5.2 Muon beam tuning

The muon beam was tuned using both the TECs, which measured individual muon trajectories before the solenoidal field, and the internal beam that was described in Section 3.7.

A muon beam directed along the magnetic field axis with minimised transverse momentum will have the highest polarisation. This beam is claimed to have the smallest polarisation uncertainty since it experiences minimal transverse magnetic field components, and is more robust to angle and position misalignments of the original beam. At the time of tuning the TECs were not calibrated or aligned, allowing only an approximate measure of the beam's position and angle. The muon beam was steered to be roughly on-axis ( $x \approx y \approx 0$ ), with small average angle, using the quadrupole steering that was described in Section 2.4. The same quadrupole steering was then used to minimise the transverse momentum of the beam, as measured by the chambers. (Even though the drift and proportional chambers were not

---

<sup>35</sup>Two metal spanners were accidentally left inside the detector over this period, affecting the tracking field in a way that could not be easily corrected. In other words, it was less effort to re-take the data in 2007.

aligned at this stage, their relative placement was known with higher precision than the removable TECs.) An example of the beam spots inside the detector after tuning is shown in Fig. 5.1.

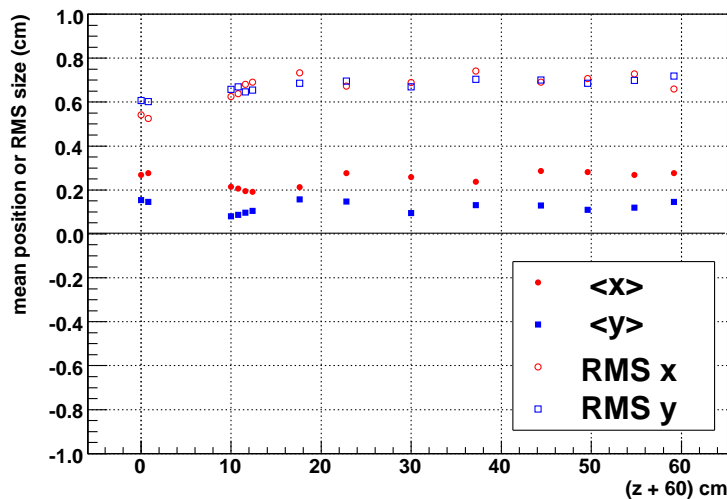


Figure 5.1: Muon beam inside the detector, after tuning.

### 5.3 Data sets

Data were accumulated in “runs” with a nominal file size of 2 GB, which typically took 10 minutes. These were grouped into “sets”, which are listed in chronological order in Table 5.1. A set contained about 900 runs, which required nearly six days of continuous acquisition; this amounted to about  $0.9 \times 10^9$  triggers, which is a factor of three larger than the sets used for the previous  $P_\mu^\pi \xi$  measurement. In total, there were  $\approx 8 \times 10^9$  events before cuts, compared to  $1.5 \times 10^9$  in the previous measurement.

Table 5.1 shows there were four nominal sets (74, 75, 84, 87), two for each stopping target. Nominal was defined as an initial muon momentum of 29.6 MeV/c, a stopping distribution peaked at the centre of the target, a uniform magnetic field with a central value of 2.0 T, and no downstream beam package in place (see Section 2.9). The nominal muon beam at the TECs is shown in Fig. ??, where the average position is approximately (0, 0) cm, and the beam has an average angle of  $\approx 0$  mrad with respect to  $x$  and  $y$ . In the  $x$ -plane the beam is slightly divergent, and in the  $y$ -plane the beam is convergent.

Set 68 had an incorrect stopping distribution, and was therefore used as a consistency

check of the energy scale. The B= 1.96 T and B=2.04 T sets were tests of the magnetic field's effect on reconstruction. The set with the downstream beam package was used to validate the simulation of back-scattered positrons.

The sets with the steered beam (76 and 86) will be used later to evaluate the largest  $P_\mu^\pi \xi$  systematic uncertainty. In these sets, the transverse momentum of the beam was maximised to deliberately lower the final polarisation of the muons. For the silver target (set 76), an average angle of  $\theta_y \approx 30$  mrad was introduced, and for the aluminium target (set 86), the beam was steered so that  $\langle x \rangle \approx -1$  cm, and  $\langle \theta_x \rangle \approx -10$  mrad.

In normal operation, the TECs were inserted at the start and end of each data set, but they were removed during the data set since they introduced additional depolarisation. Two special sets (72 and 82) were acquired with the TECs in place, to measure the long term stability of the muon beam, and the aging of the TEC sense planes.

Three smaller sets were taken at lower momenta: one at 28.75 MeV/c, and two at 28.85 MeV/c. These will later be used to validate the correction due to multiple scattering within the graphite production target.

Sets 73, 80 and 89 had the muons stopped immediately after the trigger scintillator, so that the decay positron was reconstructed independently in each half of the detector. These data were taken using the standard silver and aluminium targets, and a special large radius aluminium target that allowed the relaxation of certain analysis cuts. These sets will be used to measure the systematic uncertainties due to upstream-downstream inefficiencies, and from a resolution difference between data and simulation.

Table 5.1: Data sets accumulated in 2006/2007, in chronological order. For the sets used to extract  $\Delta P_\mu^\pi \xi$ , the number of events within the final spectrum is shown. The sets numbered 68-76 (80-93) used a silver (aluminium) stopping target. Set 89 used a special larger radius aluminium target that had lower purity.

Set num.	Description	Number of events ( $\times 10^6$ )		
		Before quality checks	Before cuts/ selections	Final spectrum
68	Stopping distrib. peaked $\frac{1}{3}$ into target	741	560	40
70	B = 1.96 T	952	780	60
71	B = 2.04 T	879	708	54
72	TECs-in, nominal beam	926	771	59
73	Muons stopped far upstream	1113	1036	-
74	Nominal A	580	497	38
75	Nominal B	834	759	59
76	Steered beam A	685	610	46
80	Muons stopped far upstream	363	274	-
82	TECs-in, spread beam	861	612	-
83	Downstream beam package in place	943	830	59
84	Nominal C	1029	727	52
86	Steered beam B	1099	1015	71
87	Nominal D	854	782	54
91	Lower momentum I ( $p = 28.75 \text{ MeV}/c$ )	225	206	17
92	Lower momentum II ( $p = 28.85 \text{ MeV}/c$ )	322	272	22
93	Lower momentum III ( $p = 28.85 \text{ MeV}/c$ )	503	463	38
89	Muons stopped far upstream	708	495	-

## 5.4 Data quality checks

The previous  $P_{\mu}^{\pi} \xi$  measurement could not rule out muon beam instabilities as the cause of the dominant systematic uncertainty. The abundant statistics for the current round of measurements allowed extremely conservative rejection of suspicious data, which will now be described.

### 5.4.1 Data acquisition system

The DAQ (data acquisition system) included the TDCs described in Section 2.12, and the computer to which they were interfaced. This computer used the software MIDAS. Runs were excluded due to the following DAQ problems:

- A TDC would sometimes receive too much information due to an electronics problem, and become out-of-synchronisation with the others. This was more common while the TECs were in place.
- A TDC would sometimes stop responding.
- A TDC channel could temporarily become corrupted.
- The computer’s event accumulating software would sometimes crash.
- The computer could fail to make a database entry for a run, or write a run with zero events.
- While data were accumulating, a periodic pulser signal was added that could be subsequently analysed to make sure all the TDCs were operating correctly. If a run contained more than three pulser problems it was eliminated.

Any run that completed with too few events was conservatively eliminated, since it was indicative of a DAQ problem.

### 5.4.2 Chamber signals

During maintenance periods when the proton beam was off for several weeks, the detector was “opened up” to carry out maintenance work such as broken wire repairs, or changing the target foil. This took place in a special clean room, but some contamination due to dust was inevitable. In the days following such a maintenance period the current or voltage in a chamber occasionally exceeded a threshold and the run was stopped; the cause was believed to

be residual dust, and these runs were eliminated. More seriously, after maintenance the pre-amplifiers sometimes suffered “electrical oscillations”, and produced signals that overloaded the DAQ. This could make the detector unusable for hours while post amplifier thresholds were adjusted. The periods of time where this occurred were eliminated.

### 5.4.3 Rates

The DAQ computer recorded several accumulated counts:

- The number of upstream counts from the muon-counter.
- The number of upstream counts in the annular counter that surrounded the muon-counter (see Section 2.9).
- The number of downstream counts from the new downstream scintillator, which included muons, beam positrons and decay positrons.
- The current from an ion chamber close to the production target, which was proportional to the proton current.

The counts were converted into normalised rates using the ion chamber current, and then used to eliminate periods of beam instability.

### 5.4.4 Beam line stability

The DAQ recorded the currents and voltages across the M13 elements (dipoles, quadrupoles), and the positions of the slits and jaws. NMRs on the dipoles allowed the field to be automatically regulated to  $< 0.01$  mT. Occasionally a regulator was not set properly by the operator, or the beam line settings were accidentally changed during a set, or the NMR signal became weak. Such occurrences were easily detected, and the runs eliminated.

There were periods where the operator observed instabilities in several of the beam line quadrupoles (Q4, Q6, Q7). Some of these instabilities were read-back errors, and therefore had no effect on the muon beam. The known genuine instabilities were eliminated, but the questionable runs were kept at this stage, and investigated more carefully using the muon beam itself.

### 5.4.5 Chamber foil bulging

Recall from Section 2.8 that the chamber gases were vented to the atmosphere. A difference between the temperature in the experimental hall and the slowly changing internal temperature led to a change in the STR due to the chamber foils bulging. For an acceptable systematic uncertainty the bulge had to be  $< \pm 50 \mu\text{m}$ . A temperature difference of  $\pm 3^\circ\text{C}$  was tolerated, which corresponded to a bulge of  $\pm 35 \mu\text{m}$ [96]. The operators maintained this difference by adjusting the air flow to the experimental hall, and were successful since only 10% of a single set had to be excluded.

### 5.4.6 Muon stopping distribution

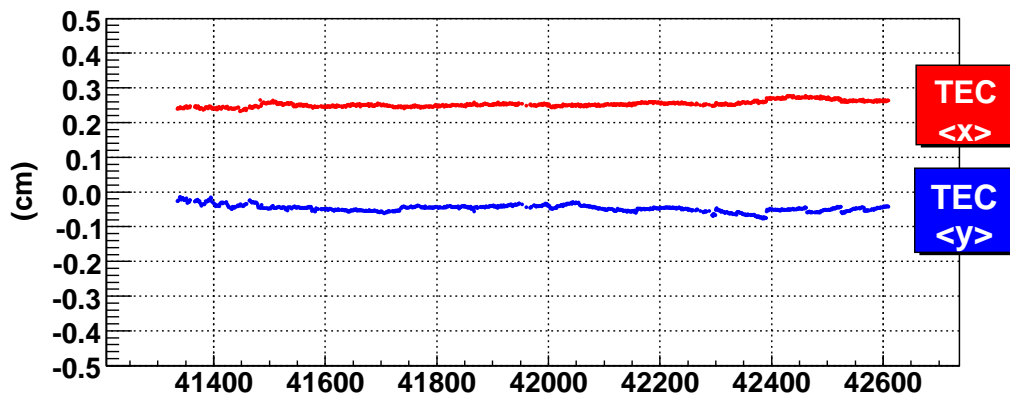
Section 2.9 described a chamber in which the  $\text{CO}_2$  and He concentration could be adjusted to control the muon range. This adjustment was automated by analysing a sample of the muons while accumulating data, and maintaining the average last- $z$  position at which the muon registered. Runs were rejected if this average was outside of statistical fluctuations.

### 5.4.7 Muon beam stability

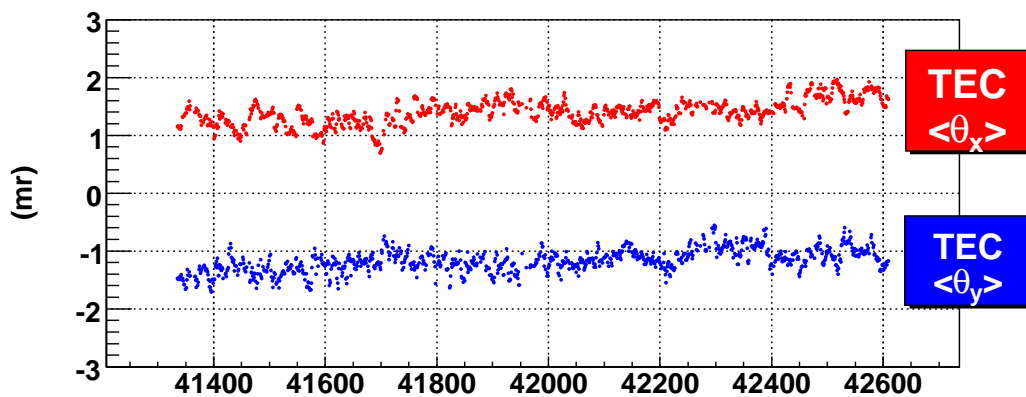
The set with the nominal beam tune and the TECs in place allowed a high precision measurement of the muon beam stability. The average positions and angles from the TECs and the internal beam ( $\Delta_x, \Delta_y$ ) are shown in Fig. 5.2. The beam position was stable to  $< 0.1 \text{ cm}$ , and the angles to  $< 1 \text{ mrad}$ , which are negligible variations. The internal beam parameters had no sensitivity to these small changes in the TEC parameters.

The internal beam measurement was carefully examined for each data set. For five sets the beam had very low transverse momentum, and only the position of the internal beam was meaningful. Figure 5.3 is an example where all the internal beam parameters are available, and it demonstrates the stability of the internal muon beam; the position is notably stable to  $< 0.02 \text{ cm}$ , but subject to small systematic steps. The TEC characterisations from the start and end of each set allowed an upper limit on the change in polarisation due to these steps.

The examination of the internal beam led to several important conclusions. Firstly, the set with the most stable internal beam had the largest change in start/end-of-set TEC characterisations. This strongly suggested that TEC non-reproducibility dominates any systematic uncertainty from muon beam instability. Secondly, the low polarisation sets were found to be stable, which will be important when the fringe field systematic uncertainty is determined in Chapter 6. Lastly, a handful of runs were excluded due to clear changes in the internal beam.

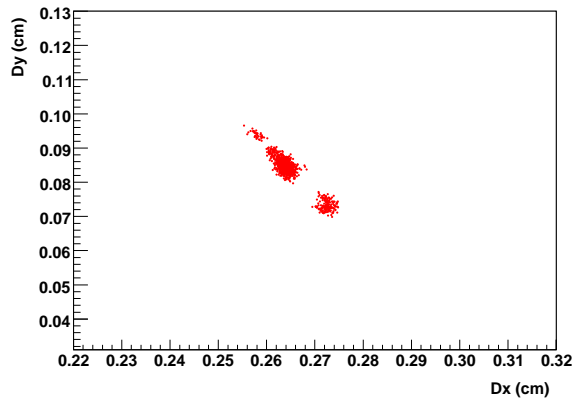


(a) TEC average position.

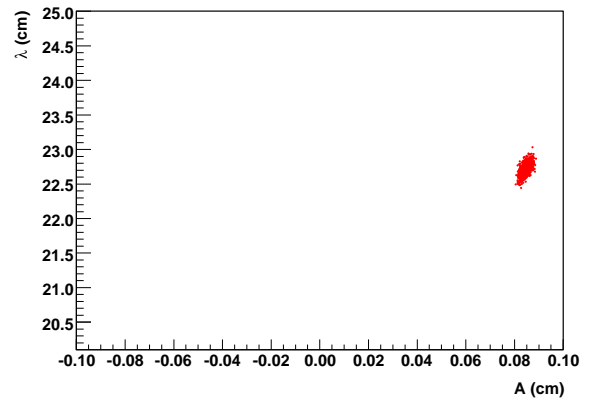


(b) TEC average angle.

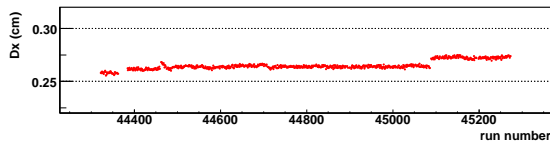
Figure 5.2: The mean position and angle of the beam at the TECs were stable over the course of a set ( $\approx 1$  week). The internal beam had no sensitivity to fluctuations within the set that is shown. The abscissa is labelled with a run number.



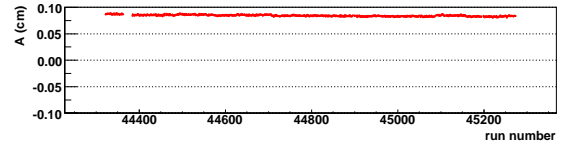
(a)  $(\Delta_x, \Delta_y)$ .



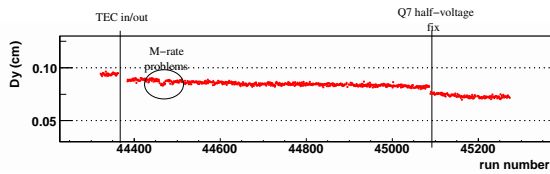
(b) Amplitude,  $A$  and wavelength  $\lambda$ .



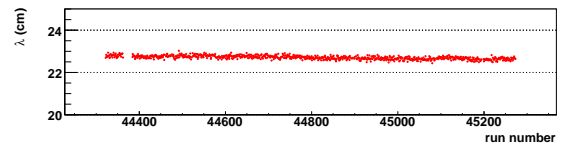
(c) Stability of  $\Delta_x$ .



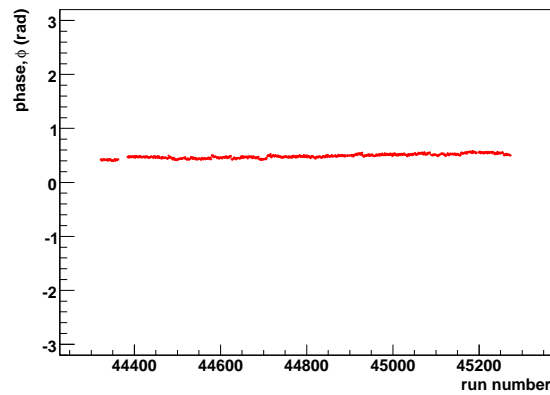
(d) Stability of  $A$ .



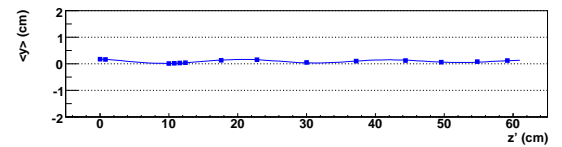
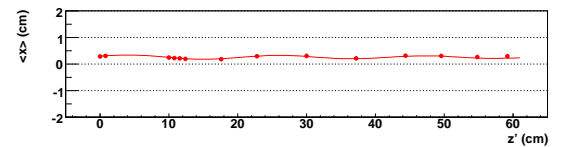
(e) Stability of  $\Delta_y$ .



(f) Stability of  $\lambda$ .



(g) Stability of  $\phi$ .



(h) Example decaying helix fit.

Figure 5.3: Stability of the internal beam measurement for a single nominal data set. The average position,  $(\Delta_x, \Delta_y)$ , and the amplitude of oscillations,  $A$ , are stable at the level of  $< 0.02$  cm. This set is chosen since there are systematic steps observed in the average position. The abscissa is labelled with run number.

# Chapter 6

## Systematic Uncertainties

### 6.1 Introduction

There are two classes of  $P_\mu^\pi \xi$  systematic uncertainties: those related to the accuracy of the  $P_\mu$  simulation, and a separate group from the decay positron and its reconstruction. The latter are evaluated simultaneously for  $\rho$ ,  $\delta$  and  $P_\mu^\pi \xi$ , by exaggerating an effect in the simulation or the analysis software; the exaggerated spectrum is then fit to the original spectrum in order to determine the change in the muon decay parameters (MPs). The exaggeration factors are made as large as possible to obtain a statistically meaningful MP change, while maintaining a linear relationship with the MPs. The changes in MPs are then scaled down according to how large the effect could actually be, resulting in the systematic uncertainty. When the original and exaggerated spectra are highly correlated (*i.e.* they contain a large number of events with identical energy and angle), the uncertainties in the MP differences are scaled down until the reduced  $\chi^2$  from the fitting procedure is equal to one.

### 6.2 Overview

The  $P_\mu^\pi \xi$  uncertainties for the nominal sets are summarised in Table 6.1, which shows that the measurement is limited by the accuracy of the muon beam and the magnetic field map. The entries in this table will be described fully in the current chapter. The table indicates three statistical uncertainties; these could be reduced by accumulating more data and/or simulation under the same running conditions. The most recent TWIST analysis (MacDonald '08 in the table) did not re-evaluate the polarisation uncertainties, since it was a measurement of  $\rho$  and  $\delta$ . A selection of the systematic uncertainties are set-dependent, and in these cases Table 6.1 contains the uncertainty for the nominal sets only.

Two corrections to  $\Delta P_\mu^\pi \xi$  (the difference in  $P_\mu^\pi \xi$  between the data and a hidden simulation value) will be described. First, the simulation does not include depolarisation of the muons while leaving the production target, resulting in a correction of  $+0.9 \times 10^{-4}$  to the nominal sets, and  $+5.9(5.2) \times 10^{-4}$  for the sets at  $\langle p \rangle = 28.75 \text{ MeV}/c$  ( $28.85 \text{ MeV}/c$ ). Second, the

time dependent depolarisation in the simulation used a preliminary relaxation rate, resulting in a correction of  $+3.3 \times 10^{-4}$  for silver (2006) and  $+4.5 \times 10^{-4}$  for aluminium (2007).

Table 6.1: Uncertainties for  $P_\mu^\pi \xi$ : these are systematic unless marked (stat.). For this analysis, (0) indicates the uncertainty is no longer evaluated.

Category	Thesis section	$\Delta P_\mu^\pi \xi$ uncertainty ( $\times 10^{-4}$ )		
		This analysis	MacDonald '08 [10, 18]	Jamieson '06 [21, 57]
<b>Polarisation</b>				
$\mu^+$ beam/ fringe field	6.3.2	<b>-4.8,+14.9</b>	34.0	34.0
Stopping material				
Systematic effects	6.3.3	<b>6.0</b>	12.0	12.0
$\lambda$ (stat.)	6.3.3	2.3	Not eval.	Not eval.
Production target	6.3.4	0.3	2.1	2.1
Background muons	6.3.5	0.7	2	1.8
Beam intensity	6.3.6	0.8	0.2	1.8
<b>Chamber response</b>				
DC STR	6.4.1	0.0	6.0	Not eval.
Wire time offsets	6.4.2	0.5	0.4	8.9
US-DS efficiency	6.4.3	1.3	1.1	1.9
Dead zone	6.4.4	0.2	0	0.1
Foil bulge	6.4.5	0.5	0.7	2.2
Cell asymmetry	6.4.6	(0)	0	2.2
Density variations	6.4.7	(0)	0.2	0.2
<b>Detector alignment</b>				
DC alignment	6.5	0.02	0.02	2.2
$z$ length scale	6.5	0.1	0.7	2.2
$u/v$ width scale	6.5	0.05	0.2	Not eval.
B-field to axis	6.5.1	0.3	Not eval.	0.3
<b>Positron interactions</b>				
$\delta$ -electron rate	6.6.1	0.1	1.4	2.9
Bremsstrahlung rate	6.6.1	0.7	0.03	
Outside material	6.6.2	0.5	0.6	0.2
Multiple scattering	6.6.3	(0)	0	0.8
<b>Resolution</b>	6.7	1.3	0.7	Not eval.
<b>Momentum calibration</b>				
Tracking B-field	6.8.1	0.3	1.1	0.9
Kinematic endpoint				
Propagation	6.8.2	0.7	0.01	1.6
Parameters (stat.)	6.8.2	1.4	0.5	
<b>External</b>				
Radiative corrections	6.9.1	0.5	0.5	1.0
$\eta$ correlation	6.9.2	1.1	1.1	Not eval.
Extraction of $\Delta P_\mu^\pi \xi$ (stat.)	7.1	2.0	3.7	6
<b>Total systematic</b>		<b>-8.2,+16.3</b>	-	38
<b>Total statistical</b>		<b>3.3</b>	-	6

## 6.3 Polarisation

### 6.3.1 Measures of polarisation

Throughout this chapter the muon beam's polarisation is always the average of the  $z$ -components of the muons' spins, *not* the average of the spin projected onto the momentum vector. The three available measurements of polarisation will now be described.

In the simulation the absolute polarisation is available *before* any time dependent target depolarisation has taken place. This is the polarisation after passing through the solenoidal magnetic field, and is calculated by simply averaging the  $z$ -components of the muons' spins. From here on the simulation's absolute polarisation is written as  $P_\mu(0)$ , where the (0) is a reminder that it is determined at effectively  $t = 0$ . Since the simulation knows the spin of each muon exactly,  $P_\mu(0)$  can be determined with high precision using a relatively small number of muons. The  $P_\mu(0)$  values in this chapter use simulations with  $1 \times 10^5$  muons, which results in a statistical uncertainty of  $0.1 \times 10^{-4}$  for nominal sets, and  $0.2 \times 10^{-4}$  for sets with a steered beam profile. This high precision allows the simulation's systematic uncertainties to be determined without producing a full generation ( $\sim 4 \times 10^8$  muons). This chapter will make wide use of  $P_\mu(0)$ .

A muon decay parameter fit between two decay positron spectra (data or simulation) measures  $\Delta P_\mu^D \xi$ , where  $P_\mu^D$  is the decay polarisation of the muon, after time dependent depolarisation has taken place. If the spectra have the same  $\xi$  and time dependence, then this quantity is directly comparable to changes in  $P_\mu(0)$ . Spectrum fits between the data with a nominal and steered beam will later be used to estimate the leading systematic uncertainty for this measurement.

The analysis of the asymmetry's time dependence was described in Section 3.6: the form  $P_\mu(t) = P_\mu^*(0) \exp(-\lambda t)$  is fit to the asymmetry, and  $P_\mu^*(0)$  is a *relative* (*i.e* not absolute) measure of the polarisation. It can be used to compare two data sets that only differ in their depolarisation due to the solenoidal fringe field. Since this comparison effectively forces the  $\rho$  and  $\delta$  decay parameters (and the relaxation rate,  $\lambda$ ) to be the same, the difference in  $P_\mu^*(0)$  is determined with higher precision than a decay spectrum fit. However, such a comparison requires a model to be assumed for  $P_\mu(t)$  (a single exponential in this case), and for that reason the asymmetry fit  $P_\mu^*(0)$  will *not* be used to establish any systematic uncertainties from the fringe field.

### 6.3.2 Muon beam and fringe field

#### Overview

The simulation transports the muon spin from the end of the M13 beam line to the metal stopping target. This relies on the accuracies of the muon beam measurement and the magnetic field map, both of which will contribute to the assessment of the  $P_\mu^\pi \xi$  uncertainty.

The systematic uncertainties from the muon beam and fringe field are summarised in Table 6.2, in the order they appear in this chapter. Note that the muon beam uncertainties are separated into two approximately orthogonal parts: contributions from the average position/angle of the beam, and those from the width of the beam’s angular distributions. Before describing the uncertainties, a description of the fringe field map and beam tunes will be given.

Table 6.2: Summary of muon beam and fringe field uncertainties, for sets with a nominal beam tune.

Description	$\Delta P_\mu^\pi \xi$ uncertainty ( $\times 10^{-4}$ )
$\mu^+$ beam average position/angle	
Initial position/angle	2.5
Magnetic field map	
Translational alignment	1.3
Rotational alignment	0.9
Transverse field components	<b>-0.0,+14.1</b>
$\mu^+$ beam angular distributions	
Simulation of multiple scattering	3.1
Noise from TEC electronics	1.7
Aging of TEC sense planes	1.5
<b>Quadratic sum</b>	<b>-4.8,+14.9</b>

#### Magnetic field map

The term “fringe field” will refer to the magnetic field from the end of the M13 beam line up to the first drift chamber ( $-200 \text{ cm} < z < -50 \text{ cm}$ ). The three components of the field map used for the analysis are shown in Fig. 6.1. These were generated using the OPERA software package[83], which will be described in more detail later. The longitudinal components ( $B_z$ ) increase steadily until the drift chamber (DC) tracking region. The on-axis transverse components ( $B_x, B_y$ ) are less than 1.5 mT, but become more significant away from the axis.

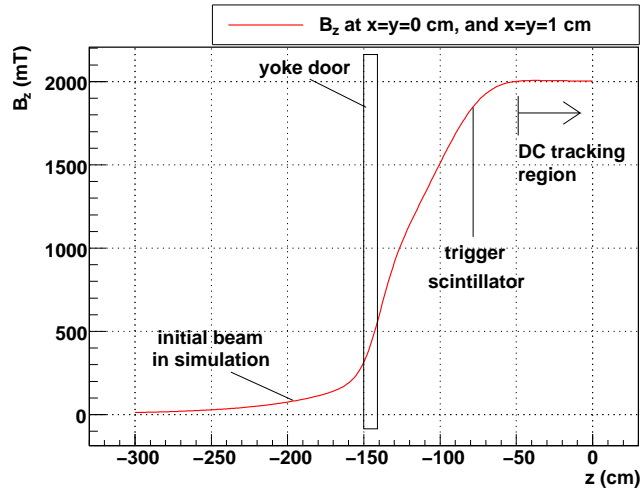
These components have approximate radial symmetry and are maximised just inside the door of the yoke. The transverse components are closely related to the depolarisation, which is shown for the simulation of a nominal profile in Fig. 6.1(c). For example, the onset of rapid depolarisation coincides with the maximisation of the transverse components, and the field’s inflection at  $z = -100$  cm is accompanied by an inflection in the depolarisation.

Clearly the quality of the fringe field downstream of the door is important since it controls the rate of depolarisation. In addition, the field upstream of the door must be known since it affects which part of the fringe field the beam is transported through.

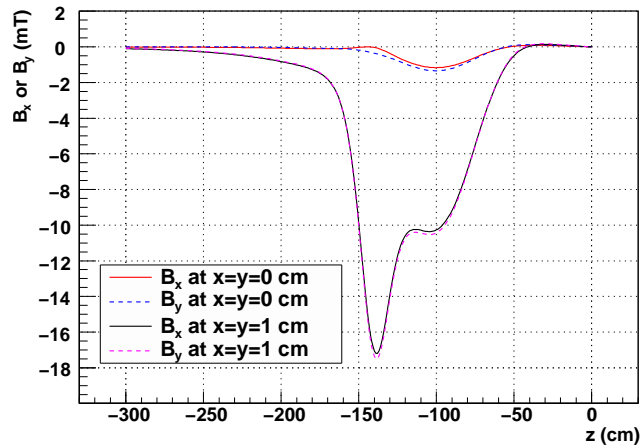
### Muon beam tunes

The nominal beam tune was described in Section 5.2; initially the position of the beam at the time expansion chambers (TECs) was steered to be close to  $x = y = 0$ , with the angles  $\theta_x$  and  $\theta_y$  minimised, but ultimately the tune was chosen to place the muon beam spots within the detector along a straight line, corresponding to minimised transverse momentum. The “envelope” of a simulated nominal muon beam, defined as the mean plus or minus one root-mean-square, is shown in Figs. 6.2(a) and 6.2(b). The bulk of the beam remains within 1.0 cm of the solenoid’s axis, and is focussed by the field to a few millimetres in extent at  $z = -100$  cm. After this focus the envelope develops oscillations in its mean position and size.

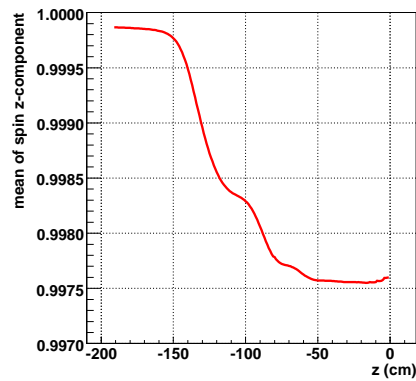
Three additional beam tunes are shown in Fig. 6.2. These will be used to assess the systematic uncertainties for the fringe field. They are set 76, where the muon beam was steered to have  $\langle\theta_y\rangle \approx 28$  mrad at the TECs, set 86, where the beam was placed off-axis and pointed away from the axis ( $\langle x \rangle \approx -1.0$  cm,  $\langle\theta_x\rangle \approx -10$  mrad), and set 72 where the TECs were in place throughout, which increased the muon beam’s emittance due to the additional multiple scattering. In the range where rapid depolarisation takes place, ( $-150 < z < -100$ ) cm, the beams for sets 76 and 86 sample the fringe field at a different location to the nominal beam, with a non-zero average angle. They undergo a dramatic focus, corresponding to an intersection of the field lines at a steep angle. As a result, these beams will be seen to undergo significantly more depolarisation, and the ability of the simulation to reproduce the data’s depolarisation will provide a stringent test of the fringe field model; such a validation was not available for the previous  $P_\mu^\pi \xi$  analysis.



(a)  $B_z$  component.

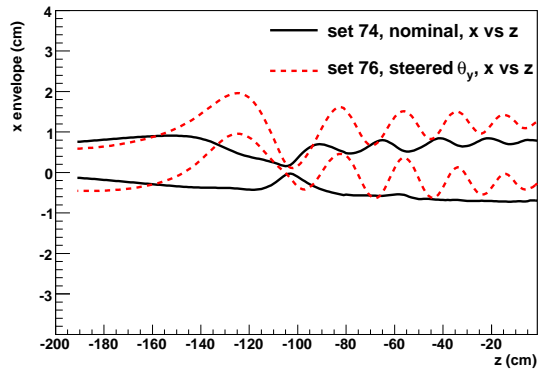


(b)  $B_x$  and  $B_y$  components.

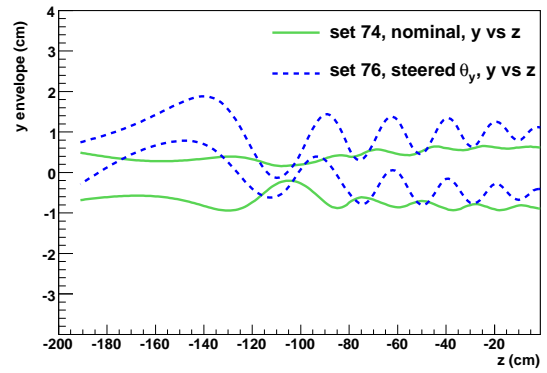


(c) Average of spin  $z$ -component, for a nominal beam profile.

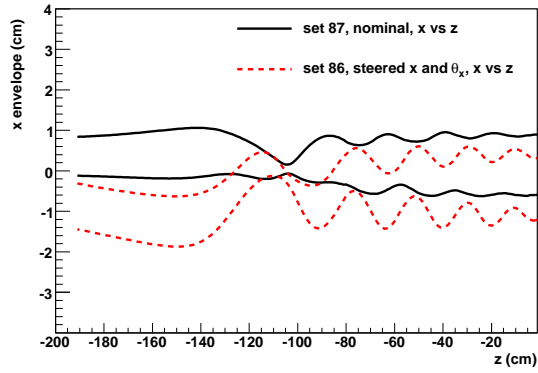
Figure 6.1: Fringe field components from the OPERA finite element analysis. The  $B_x$  and  $B_y$  components indicate radial symmetry. The average spin is also shown since its behaviour is closely related to the  $B_x$  and  $B_y$  components.



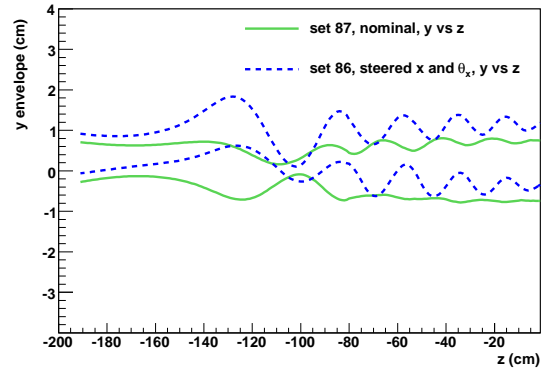
(a)



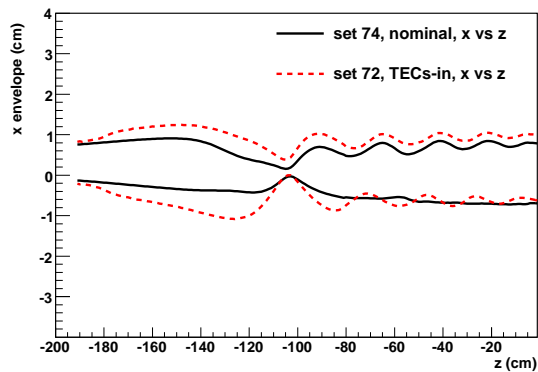
(b)



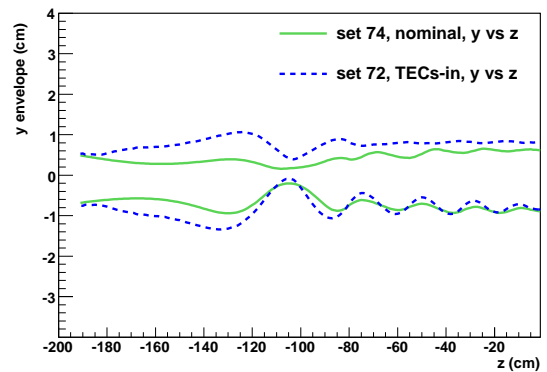
(c)



(d)



(e)



(f)

Figure 6.2: Simulation of muon beam *envelopes*, defined as the mean position plus or minus one root-mean-square.

**Muon beam: uncertainty in initial position and angle**

A muon beam measurement was made with the TECs at the beginning and end of most data sets. The two measurements have small differences in position and angle, resulting in different values of  $P_\mu(0)$ . Since the **GEANT** simulation can only use one of the beam measurements, these differences must be assessed as a systematic uncertainty.

The changes in average position and angle between the two muon beam measurements are listed in Table 6.3, where differences of up to 0.18 cm in position and 3 mrad in angle are observed. The origin of the changes could be muon beam instability, a limitation in the reproducibility of the TECs, or an instability in the TEC drift cell response. Each of these will now be discussed.

Table 6.3: Muon beam differences for the beginning and end of set TEC measurements. The temperature difference between the measurements is denoted by  $\Delta T$ .

Set	Target	Description	$\Delta \langle x \rangle$ (cm)	$\Delta \langle y \rangle$ (cm)	$\Delta \langle \theta_x \rangle$ (mrad)	$\Delta \langle \theta_y \rangle$ (mrad)	$\Delta T^a$ (°C)
68	Ag	Stopping distrib. peaked $\frac{1}{3}$ into target	0.11	-0.05	0.2	-3.2	-0.3
70	Ag	B = 1.96 T	0.03	0.00	1.0	-0.4	-1.2
71	Ag	B = 2.04 T	0.09	-0.05	0.0	0.1	2.4
74	Ag	Nominal A <sup>b</sup>	-				
75	Ag	Nominal B	0.04	-0.10	-0.5	1.5	3.2
76	Ag	Steered beam	-0.04	-0.06	-0.6	1.9	1.3
83	Al	Downstream beam package in place	0.12	-0.09	0.6	0.7	-0.3
84	Al	Nominal C	0.18	-0.15	0.2	1.4	-0.4
86	Al	Steered beam B	0.04	-0.01	1.0	-0.01	-0.4
87	Al	Nominal D	0.13	-0.11	-0.1	0.7	-1.3
91/92/93	Al	Lower momentum <sup>b</sup>	-				

<sup>a</sup>  $\Delta T = T_{\text{end}} - T_{\text{start}}$ .  $\Delta T > 0$  indicates a temperature rise between measurements.

<sup>b</sup> These sets only had one TEC measurement.

Muon beam instabilities were caused by a change in the proton beam upstream of the production target or an instability in the M13 beam line elements. A special test displaced the proton beam at the production target by  $\pm 0.1$  cm vertically, which is about five times larger than the beam could have moved during normal operation<sup>36</sup>. The largest observed

<sup>36</sup>The proton beam was surrounded by four counters (top, bottom, left, right). In order to steer the beam vertically by 0.1 cm and avoid destroying the top or bottom counter, the proton beam current was reduced from the nominal setting of  $\approx 100 \mu\text{A}$  to  $\approx 20 \mu\text{A}$ . This suggests that during normal operation, the proton beam could not have moved by more than  $\approx 20/100 \times 0.1 \text{ cm} = 0.02 \text{ cm}$ .

TEC changes in the muon beam were  $\Delta \langle y \rangle = \pm 0.07$  cm in position and  $\Delta \langle \theta_y \rangle = \pm 1.0$  mrad in angle, which are negligible after scaling down by a factor of five.

The settings of the M13 beam line elements (*e.g.* quadrupoles, dipoles, slits, jaws, asymmetric currents for quadrupole steering) were all monitored with a slow control system, and runs with any instability were eliminated (see Section 5.4). Set 72 had the TECs in place throughout, and indicated that the average muon beam position and angle were stable to  $< 0.02$  cm and  $< 1$  mrad, respectively, over the period of a week (see Fig. 5.2). The muon beam measurement from the wire chambers was used to monitor the stability for the nominal sets, which did not have the TECs in place. The sensitivity of the internal beam to M13 instabilities was determined by adjusting the currents in each quadrupole and dipole by  $\pm 5\%$ . An examination of the internal beam found that the observed variations corresponded to negligible changes at the TECs, and did not correlate with the differences in Table 6.3.

The space-time-relationship in the TEC drift cells depended on temperature. A variation of  $\pm 3^\circ\text{C}$  was predicted to change the average reconstructed positions<sup>37</sup> by between 0.028 cm and 0.050 cm, depending on the proximity of the beam to the sense plane of the TEC; the predicted changes in angle were all  $< 0.05$  mrad, except for set 76, which was still predicted to only change by 0.4 mrad. The observed temperature differences between the two TEC measurements in Table 6.3 are therefore not large enough to fully explain the changes in beam parameters, ruling out temperature as the dominant cause of beginning/end of set differences.

The insertion/removal of the TECs required the beam line elements to be switched off, and a breaking of the vacuum in the beam line, which then had to be pumped down again before the TECs could be used. This process exerted significant forces on the beam line components and the box containing the TECs, and these forces are the prime candidate for the measured variation in average initial position and angle.

Using the OPERA field map, the simulation determined the  $P_\mu(0)$  sensitivity to position and angle changes of  $\pm 0.2$  cm and  $\pm 3$  mrad, respectively. These are the limits of the observed changes in Table 6.3, but they are not overly conservative for a number of reasons: first there are not enough entries in Table 6.3 to establish whether the changes in position and angle follow a predictable distribution; second, the TECs were aligned to the drift chambers with a systematic uncertainty of about 2 mrad; and third, the long term stability measurements of the TECs found movements of 0.1 cm, but only had an accuracy of about 0.1 cm (see Section 2.13 for more information on the alignments and stability measurements).

The dependence of  $P_\mu(0)$  on changes in initial position and angle is well approximated

---

<sup>37</sup>The  $x$ -positions increased with temperature and the  $y$ -positions decreased; see Ref. [76] for further detail.

by a quadratic form. This is demonstrated in Fig. 6.3 for a nominal beam profile. The systematic uncertainty is assessed by first finding the largest increase/decrease in  $P_\mu(0)$  for each profile; these results are listed in Table 6.4. Note that the uncertainties for set 68, 70, 71 and 72 use a larger angle range of  $\pm 6$  mrad since the sense planes were not calibrated<sup>38</sup>. The simulation predicts the  $P_\mu(0)$  changes are asymmetric, but later it will be shown that the simulation does not have the required accuracy to make this asymmetry credible. Each set's uncertainty is instead taken as half of the difference between the largest increase/decrease in  $P_\mu(0)$ , and the ultimate systematic uncertainty is the average over the nominal sets, which is  $2.5 \times 10^{-4}$ .

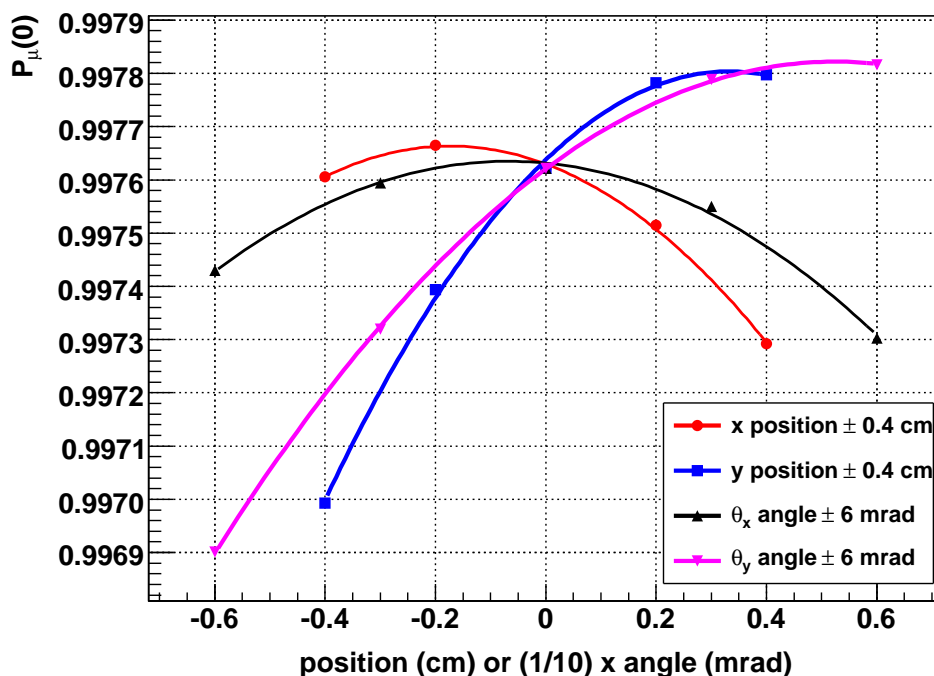


Figure 6.3: The polarisation of the muons after the fringe field depends quadratically on changes in the initial position and angle of the beam. The results of simulating a nominal beam profile are shown. The initial beam position has been displaced by  $\pm 0.2$  cm,  $\pm 0.4$  cm, and the initial beam angle by  $\pm 3$  mrad,  $\pm 6$  mrad.

<sup>38</sup>The TEC sense planes that were used to measure the muon beam for sets 68, 70, 71 and 72 were not calibrated, and instead the calibrations from another set of planes were used for the analysis. Appendix G.4 shows that the calibration removes a rotation of the TEC sense planes within of TEC box of between 7 and 12 mrad. Since this angle was not determined for sets 68  $\rightarrow$  72, they suffer from an additional TEC angle uncertainty of  $\sim 2.5$  mrad. Therefore the simulation used a range of  $\pm 6$  mrad to find the sensitivity of  $P_\mu(0)$  to initial beam/angle uncertainties.

Table 6.4: The simulation’s muon beam was scanned in position and angle. The largest increase and decrease in  $P_\mu(0)$  are averaged to obtain a systematic uncertainty from the initial position/angle of the muon beam.

Set num.	Target	Description	$P_\mu(0)$ from OPERA	Largest $P_\mu(0)$ change ( $\times 10^{-4}$ ) $\pm 0.2$ cm in $\langle x \rangle, \langle y \rangle$ , $\pm 6$ mrad in $\langle \theta_x \rangle, \langle \theta_y \rangle$	Uncertainty (average of $\pm$ ) ( $\times 10^{-4}$ )
68	Ag	Stopping distrib. peaked $\frac{1}{3}$ into target	0.99778	-2.9, +0.1	1.5
70	Ag	B = 1.96 T	0.99745	-7.0, +2.1	4.6
71	Ag	B = 2.04 T	0.99694	-9.6, +3.8	6.7
72	Ag	TECs-in, nominal beam	0.99461	-8.6, +2.8	5.7
				$\pm 0.2$ cm in $\langle x \rangle, \langle y \rangle$ $\pm 3$ mrad in $\langle \theta_x \rangle, \langle \theta_y \rangle$	
74	Ag	Nominal A	0.99749	-3.5, +2.3	2.9
75	Ag	Nominal B	0.99767	-1.5, +0.3	0.9
76	Ag	Steered beam A	0.99221	-13.2, +11.5	12.4
83	Al	Downstream beam package in place	0.99780	-2.7, +1.7	2.2
84	Al	Nominal C	0.99763	-2.8, +1.8	2.3
86	Al	Steered beam B	0.99311	-12.3, +10.9	11.6
87	Al	Nominal D	0.99782	-2.4, +1.0	1.7
91	Al	Lower momentum I	0.99686	-1.9, +0.7	1.3
92	Al	Lower momentum II	0.99660	-3.0, +1.4	2.2
93	Al	Lower momentum III	0.99673	-1.1, +0.1	0.6

### Magnetic field map uncertainties

The analysis used a fringe field map that was generated with the OPERA software package[83], which had accuracy limitations. Most importantly, the software used a finite element method to solve Maxwell’s equations, and the 40 cm diameter circular hole in the yoke door was expected to introduce difficulties in this modelling<sup>39</sup>. (The hole was in a critical region for the transverse field components, and hence the depolarisation.) Also, the field map used for the analysis did not include the steel in the floor of the M13 area and the final M13 quadrupoles.

The  $B_z$  components from OPERA are compared to measurements using Hall probes in Fig.

<sup>39</sup>Specifically, finite element analyses are expected to encounter difficulties when there are scales involved that are several orders of magnitude apart. In this case, the important region for the depolarisation of the muons is within  $\lesssim 4$  cm of the axis (see Fig. 6.2), there is a circular hole in the yoke of diameter 40 cm, and the whole map must be determined over a  $z$ -length of about 5 m.

6.4(a). Only the  $z$  components are shown since the Hall probes were single axis, and did not measure  $B_x$  and  $B_y$ . Extensive efforts were made to resolve the observed disagreement by adjusting the OPERA inputs, such as the solenoid's coil positions in  $x/y/z$ , the radii of these coils and their current densities, the  $B - H$  curve for the iron yoke, and the position of the door in  $z$ . The previous  $P_\mu^\pi \xi$  measurement found that variations in these inputs affected  $P_\mu(0)$  by  $3 \times 10^{-4}$  at most[57]; as a result of this low sensitivity, and the limitations of the finite element analysis, the tuning of OPERA was not pursued further.

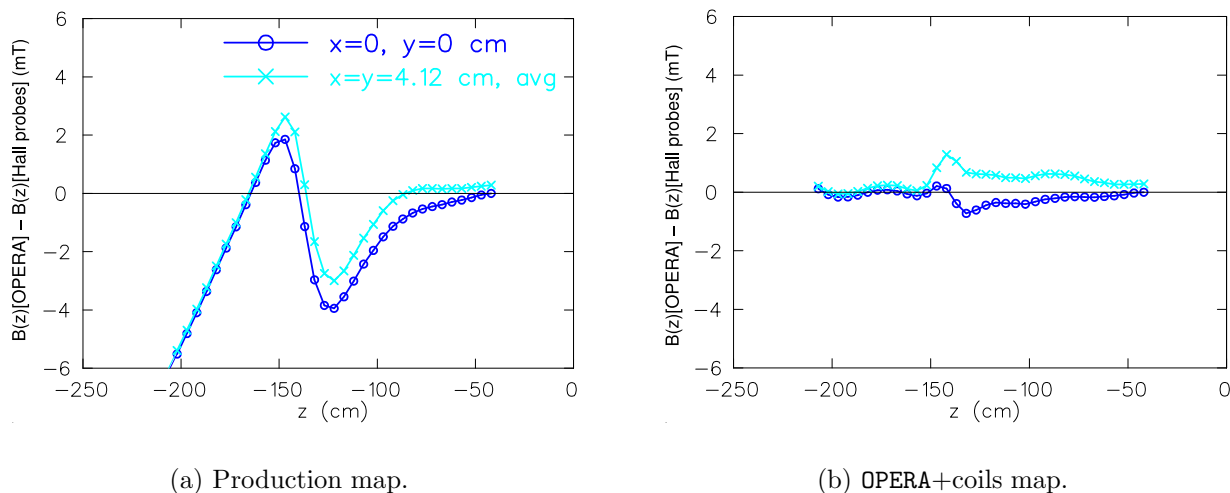


Figure 6.4: Difference in  $B_z$  between the magnetic field maps from OPERA and the Hall probes. Two comparisons are shown: the on-axis ( $x = y = 0$ ) and an off-axis average of  $x = \pm 4.12$  cm,  $y = \pm 4.12$  cm. The OPERA+coils map has the field from three current loops added; these loops are at  $z = -265.1$  cm,  $-147.1$  cm,  $-127.1$  cm, with radii 55.1 cm, 25.1 cm, 25.1 cm and central field strengths of +20 mT, -5.5 mT and +5.5 mT. Note that muons start in the simulation at  $z = -191.944$  cm.

The apparatus that supported the Hall probes had alignment limitations: the Hall probes were attached to an arm that was deflected by gravity, introducing a vertical misalignment of up to 0.1 cm, and the whole mapping device was aligned in the yoke's coordinate system to  $< 0.1$  cm in  $x$  and  $y$ [84]. A comparison of the Hall probes and OPERA could not produce a precise translational alignment in  $x$  and  $y$ , but the position of the muon beam inside the detector did have sensitivity. On a set-by-set basis, a field translation was determined such that the data and simulation positions matched. On average, this required a translation of the entire map by  $(\Delta x, \Delta y) = (0.18, 0.19)$  cm. Although this translation was determined precisely, we cannot be sure that it was accurate for a number of reasons. First, the position of the

internal muon beam was also sensitive to the solenoid's coil positions<sup>40</sup>; their positions were not measured, and were instead initially placed according to a sketch from the manufacturer (Oxford Magnet Technologies Limited UK), and then tuned to match the  $B_z$  components in the tracking region, but not in the fringe field. Second, the field through the hole in the yoke should be constrained to have its symmetry axis pass through the centre of the hole. Third, the translation was determined from beam profiles that have already been shown to suffer from their own alignment uncertainties. Fourth, the translation may be compensating for the problems in the  $B_x$  and  $B_y$  components of the field map. For these reasons, the magnetic field translation is treated as an additional uncertainty.

The central value for  $P_\mu^\pi \xi$  uses the translated map, but an uncertainty is assigned as the difference in  $P_\mu(0)$  between translation and no-translation. The values for these uncertainties appear in Table 6.5; the average  $P_\mu(0)$  change for the nominal sets ( $1.3 \times 10^{-4}$ ) will be assigned as the systematic uncertainty. The increased sensitivity for the aluminium target sets is due to the lower quality of the muon beam<sup>41</sup>.

There is also an uncertainty from the rotation of the magnetic field map. Specifically, this is the angle between the detector's  $z$ -axis and the symmetry axis of the magnetic field. The observed decay positron helix axis requires a well determined rotation of  $(\theta_x, \theta_y) = (0.3, 1.2)$  mrad, which is applied by rotating the entire field map. However, there is no guarantee that the fringe field should also be rotated by this amount. The change in  $P_\mu(0)$  from making this rotation is shown in Table 6.6. Again, the average  $P_\mu(0)$  change for the nominal sets ( $0.9 \times 10^{-4}$ ) is used as the systematic uncertainty.

---

<sup>40</sup>A change in the solenoid coil positions by  $\approx 1$  cm caused the internal muon beam to move by about  $\approx 0.3$  cm. The coil positions were only known to about  $\approx 0.2$  cm[97].

<sup>41</sup>For the data accumulated with the aluminium target, a vertical aperture was in place within the M13 beam line. As a result the slits and jaws at the front end of M13 were opened wider, and the beam was not as well focussed at F3. In addition, muons with  $y > 1.0$  cm at the TECs did not converge towards the solenoid's axis.

Table 6.5: Uncertainty from the translational alignment of the magnetic field map. Both maps are unrotated.

Set num.	Target	Description	$P_\mu(0)$ from OPERA simulation ( $x, y$ ) translation of (0.18, 0.19) cm	No translation	Difference ( $\times 10^{-4}$ )
68	Ag	Stopping distrib. peaked $\frac{1}{3}$ into target	0.99777	0.99770	-0.7
70	Ag	B = 1.96 T	0.99762	0.99755	-0.7
71	Ag	B = 2.04 T	0.99714	0.99710	-0.4
72	Ag	TECs-in, nominal beam	0.99492	0.99492	0.0
74	Ag	Nominal A	0.99762	0.99766	-0.4
75	Ag	Nominal B	0.99767	0.99755	-1.2
76	Ag	Steered beam A	0.99174	0.99068	-10.6
83	Al	Downstream beam package in place	0.99788	0.99773	-1.5
84	Al	Nominal C	0.99776	0.99755	-2.1
86	Al	Steered beam B	0.99244	0.99334	+9.0
87	Al	Nominal D	0.99787	0.99760	-2.7
91	Al	Lower momentum I	0.99691	0.99672	-1.9
92	Al	Lower momentum II	0.99669	0.99648	-2.1
93	Al	Lower momentum III	0.99675	0.99665	-1.0

Table 6.6: Uncertainty from the rotational alignment of the magnetic field map. Both maps are translated in  $(x, y)$  by  $(0.18, 0.19)$  cm.

Set num.	Target	Description	$P_\mu(0)$ from OPERA simulation		Difference ( $\times 10^{-4}$ )
			No rotation	With rotation	
68	Ag	Stopping distrib. peaked $\frac{1}{3}$ into target	0.99777	0.99778	+0.1
70	Ag	B = 1.96 T	0.99762	0.99745	-1.7
71	Ag	B = 2.04 T	0.99714	0.99694	-2.0
72	Ag	TECs-in, nominal beam	0.99492	0.99480	-1.2
74	Ag	Nominal A	0.99762	0.99749	-1.3
75	Ag	Nominal B	0.99767	0.99767	0.0
76	Ag	Steered beam A	0.99174	0.99221	+4.7
83	Al	Downstream beam package in place	0.99788	0.99780	-0.8
84	Al	Nominal C	0.99776	0.99763	-1.3
86	Al	Steered beam B	0.99244	0.99311	+6.7
87	Al	Nominal D	0.99787	0.99782	-0.5
91	Al	Lower momentum I	0.99691	0.99686	-0.5
92	Al	Lower momentum II	0.99669	0.99660	-0.9
93	Al	Lower momentum III	0.99675	0.99673	-0.2

Now that the uncertainties from the initial beam and magnetic field alignments are evaluated, the fringe field validation can be revisited. The difference in polarisation between the nominal and steered beams from a decay parameter fit are shown in the first row of Table 6.7, where the uncertainties are statistical. The next row shows the OPERA predictions for these polarisation differences, where the uncertainties are the quadratic sum of the initial beam position/angle and field translation/angle uncertainties<sup>42</sup>. The OPERA predictions are consistent for sets 87/86, and sets 74/72, but underestimate the polarisation difference for sets 74/76 by  $43 \times 10^{-4}$ , which is well outside of the systematic uncertainties already established. There are no additional uncertainties from the TECs that can explain this discrepancy, so we are left with a problem in the components of the OPERA field map.

Table 6.7: Validation of the fringe field map by establishing how well the simulation reproduces large polarisation differences in the data.

	Difference in polarisation ( $\times 10^{-4}$ )		
	Sets 74,76	Sets 87,86	Sets 74,72
Data	$102 \pm 8$	$57 \pm 7$	$16 \pm 8$
Simulation with OPERA field	$59 \pm 17$	$54 \pm 16$	$28 \pm 7$
OPERA+coils map, with translation	78	133	61
OPERA+coils map, no translation	117	112	63
OPERA field, match $A^a$	104	75	27
OPERA+coils map, match $A$	108	73	62

<sup>a</sup>  $A$  is the amplitude of muon beam oscillations measured by the wire chambers. The technique that matches  $A$  in data and simulation will be described later in the text.

An attempt has been made to overcome the limitations of the OPERA finite element method, and resolve the discrepancy in Fig. 6.4(a). An additional field from three on-axis coils has been added to the OPERA map; the coils are located at  $z = -265.1$  cm,  $-147.1$  cm,  $-127.1$  cm, with radii 55.1 cm, 25.1 cm, 25.1 cm and their central field strengths are +20 mT, -5.5 mT and +5.5 mT. This approach is motivated by observing that Fig. 6.4(a) resembles the field from a pair of gradient coils, and the final result is shown in Fig. 6.4(b). This approach obeys Maxwell's equations over the region that the muons passed through, but is unlikely to satisfy boundary conditions at the yoke. We feel it is not a coincidence that the coils'  $z$ -locations correspond to the outer and inner sides of the yoke door where the circular hole was located, and the last M13 quadrupole, which is not included in OPERA.

If only the  $B_z$  components from the OPERA map are replaced with those from the OPERA+coils

<sup>42</sup>For the nominal sets 74 and 87 the uncertainties from Table 6.2 were used. For the other sets the uncertainties were taken from Tables 6.4, 6.5 and 6.6.

map, then the  $P_\mu(0)$  estimates are changed by  $< 1 \times 10^{-4}$  for all profiles (this approach does not obey Maxwell's equation). More significant changes occur when the transverse ( $B_x$  and  $B_y$ ) components from the OPERA+coils map are used; these are identical for the two maps along the symmetry axis ( $x = y = 0$ ) but off-axis they differ significantly, as demonstrated for  $x = y = 1$  cm in Fig. 6.5. (The distance  $x = y = 1$  cm is chosen since the beam envelopes in Fig. 6.2 already demonstrates that a large fraction of muons are within this region.) Using the OPERA+coils map has a dramatic effect on  $P_\mu(0)$ , with decreases of 10 to  $20 \times 10^{-4}$  for the nominal beam profiles, and up to  $93 \times 10^{-4}$  for the steered beam profiles; the  $P_\mu(0)$  changes are listed for each set in Table 6.8.

Unfortunately a direct validation of the transverse components is not possible since they were not measured for the real field. Instead we rely on guidance from the simulation's ability to match the large differences in  $P_\mu(0)$  from the data. The results from the OPERA+coils field appear in Table 6.7; the increase in the transverse components using this map allows the simulation to match the difference in  $P_\mu^\pi \xi$  between sets 74 and 76, but the agreement is then worse for the other two entries in the table. These results alone do not allow a strict limit on the  $B_x$  and  $B_y$  components.

Table 6.8: Relative polarisation for the simulation, using the OPERA and the OPERA+coils fringe field maps.

Set num.	Target	Description	$P_\mu(0)$ from simulation		Difference ( $\times 10^{-4}$ )
			OPERA map With translation	OPERA+coils map With translation	
68	Ag	Stopping distrib. peaked $\frac{1}{3}$ into target	0.99777	0.99681	-9.6
70	Ag	B = 1.96 T	0.99762	0.99628	-13.4
71	Ag	B = 2.04 T	0.99714	0.99596	-11.8
72	Ag	TECs-in, nominal beam	0.99492	0.99021	-47.1
74	Ag	Nominal A	0.99762	0.99633	-12.9
75	Ag	Nominal B	0.99767	0.99659	-10.8
76	Ag	Steered beam A	0.99174	0.98857	-31.7
83	Al	Downstream beam package in place	0.99788	0.99586	-20.2
84	Al	Nominal C	0.99776	0.99595	-18.1
86	Al	Steered beam B	0.99244	0.98317	-92.7
87	Al	Nominal D	0.99787	0.99646	-14.1
91	Al	Lower momentum I	0.99691	0.99548	-14.3
92	Al	Lower momentum II	0.99669	0.99533	-13.6
93	Al	Lower momentum III	0.99675	0.99515	-16.0

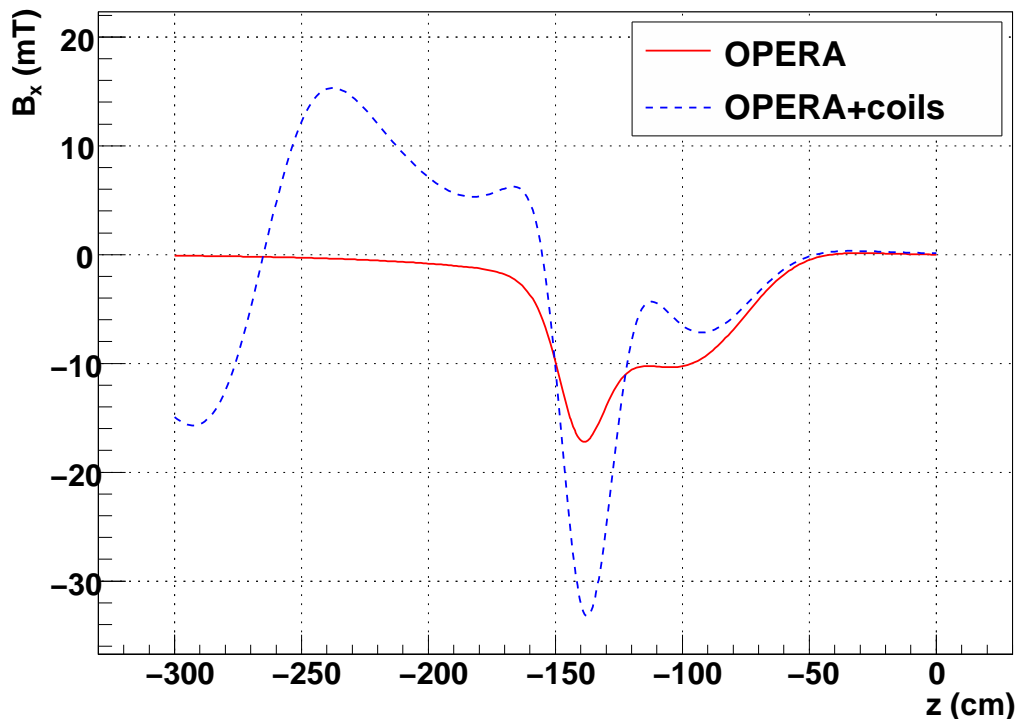


Figure 6.5: A comparison of the  $B_x$  components from OPERA and the OPERA+coils map, for  $x = y = 1$  cm. The maps are identical for  $x = y = 0$  cm since the coils have  $B_x = B_y = 0$  on-axis.

For further guidance on the field components we use the internal muon beam amplitude,  $A$  (see Section 3.7); this describes how much the mean position of the muon beam moves around. There is a strong link between  $A$  and  $P_\mu(0)$ , which is shown for the nominal and steered beams in Fig. 6.6. For all combinations of magnetic field translation and initial beam position/angle, the points in Fig. 6.6 are well approximated by a quadratic function.

The panels on the left-hand side of Fig. 6.6 show the results from the OPERA map. For set 76 and 86 there is disagreement in  $A$  between data and simulation, and a “stretch” of the quadratic curve is needed. The panels on the right-hand side of Fig. 6.6 show the same results for the OPERA+coils map, where the larger transverse components are seen to provide the necessary “stretch”. The OPERA+coils map allows  $A$  to match for set 76, but causes set 86 to overshoot. This suggests the true transverse field components are somewhere between the OPERA and OPERA+coils field maps, which is consistent with the earlier observations from Table 6.7.

At the same time as providing a stretch, the larger transverse field components lower the polarisation for all profiles (the quadratic curve is displaced vertically). For the nominal profiles the vertical displacement is more significant than the “stretch”, and the magnitude

of the  $P_\mu(0)$  change will be used to estimate the nominal uncertainty.

If the quadratic relationship between  $A$  and  $P_\mu(0)$  is used to extrapolate the simulation's  $A$  values to match the data, then the difference in  $P_\mu(0)$  between sets 76 and 74 is exactly matched in data and simulation, and the differences between sets 86 and 87 are in reasonable agreement; these results have been added to Table 6.7. However, we note from Table 6.7 that the polarisation difference between sets 72 and 74 is in bad disagreement when matching  $A$  using the OPERA+coils map, which prevents us from simply making  $A$  in data and simulation agree and then correcting  $P_\mu(0)$  accordingly. The result for sets 72 and 74 strongly suggests that the true transverse field components are closer to the original OPERA map.

A systematic uncertainty from the fringe field must be assigned to the nominal sets, for which the beam was carefully steered onto our beam axis to avoid the larger uncertainties associated with sets 76 and 86, and the TECs were removed in order to minimise the beam size through the field. Therefore simply taking discrepancies from Table 6.7 as an uncertainty would be a gross overestimate. Instead we note from Table 6.7 and the above discussion that the true field is probably closer to OPERA (supported by the results from sets 87/86 and 74/72), but we have to admit the possibility that the  $B_x$  and  $B_y$  components could be as large as those from the OPERA+coils field map, since these are needed to accommodate the result for sets 76/74. The strong evidence that OPERA is closer to reality makes it wrong to place the  $P_\mu^\pi \xi$  central value half way between the two field maps, so we instead use the OPERA map for the central value, and the differences between OPERA and the OPERA+coils map as an asymmetric systematic uncertainty. After averaging over the nominal sets, Table 6.8 gives the uncertainty on the simulation's absolute polarisation as  ${}_{-14.1}^{+0.0} \times 10^{-4}$ ; we believe that the polarisation cannot be higher than the OPERA field map value, since this map *underestimates* the polarisation difference between sets 74 and 76. The uncertainty on the quantity  $\Delta P_\mu^\pi \xi$  (the difference between the data and a hidden simulation value) is then  ${}_{-0.0}^{+14.1} \times 10^{-4}$ . The OPERA magnetic field map is used to evaluate the remaining polarisation systematic uncertainties in the next section.

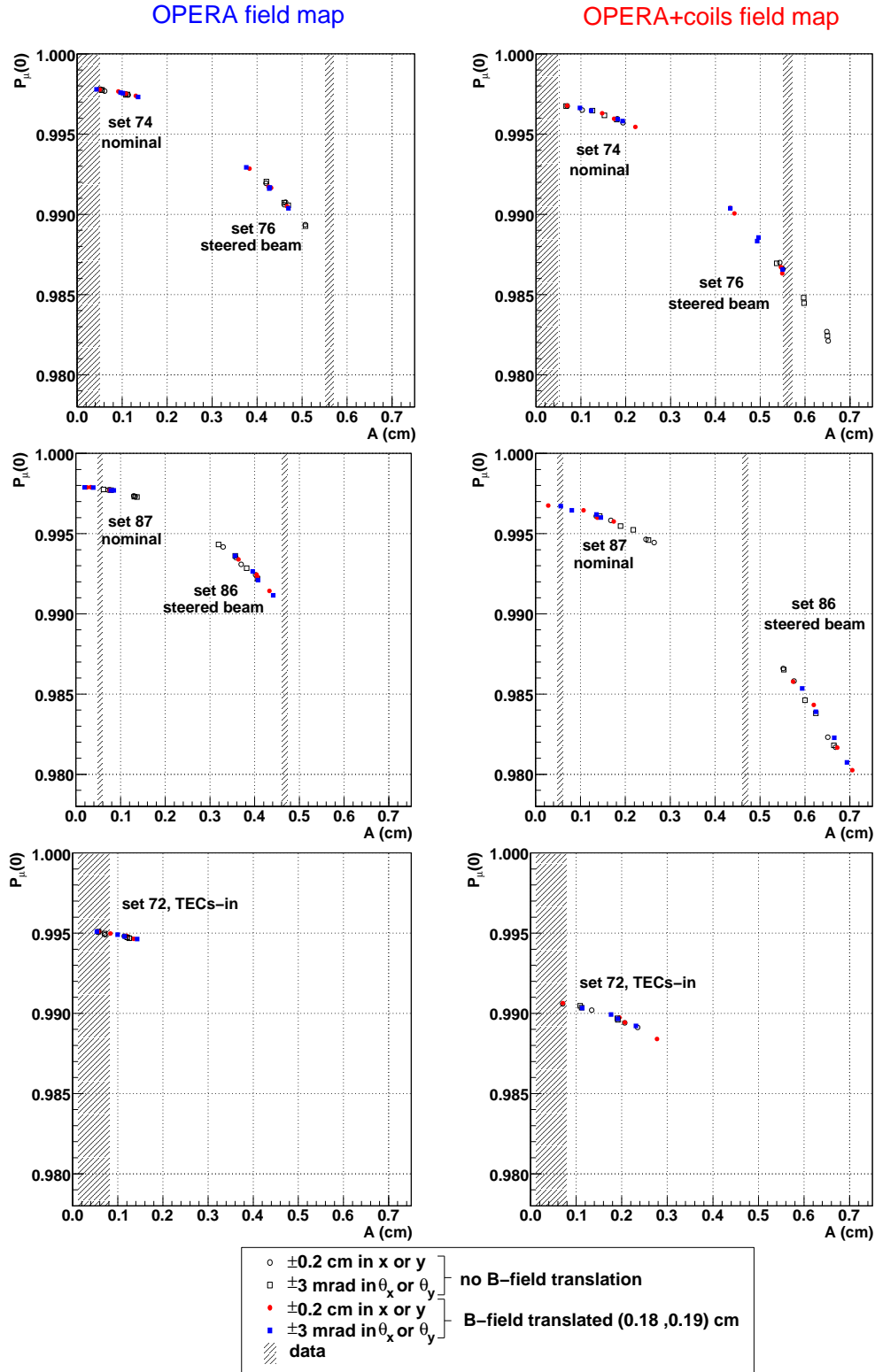


Figure 6.6: The simulation’s absolute polarisation,  $P_\mu(0)$  depends quadratically on the amplitude ( $A$ ) of the internal muon beam oscillations. Each point in the figure corresponds to an alignment uncertainty. The top row shows the OPERA magnetic field map that was used for the production simulations. The bottom row shows the results from a special field map with larger  $B_x$  and  $B_y$  field components; see the text for more details.

### Muon beam angular distribution width

The muons were multiple scattered as they passed through the TECs, resulting in a measured angle distribution that was larger than the distribution in the absence of the TECs. A GEANT3 simulation of the TECs finds that the root mean square of the angles should be reduced by a factor of  $c_x = 0.6391$  in the  $x$ -module, and  $c_y = 0.4795$  in the  $y$ -module to account for this multiple scattering. The dependence of  $P_\mu(0)$  on the choice of  $c_x$  is shown in Fig. 6.7 for a nominal and a steered beam. To an acceptable approximation,  $dP_\mu(0)/dc_x$  and  $d^2P_\mu(0)/dc_x^2$  are independent of the beam steering. For example, if  $c_x = 0.6391$  then a variation of  $\pm 10\%$  in  $c_x$  changes  $P_\mu(0)$  by  ${}_{+2.1}^{-1.8} \times 10^{-4}$  for the nominal case, and  ${}_{+2.0}^{-1.9} \times 10^{-4}$  for the steered beam. As a result, the choice of  $c_x$  and  $c_y$  has no bearing on the comparison of polarisation differences between data and simulation, and the systematic uncertainties from these factors can be treated as orthogonal to those already evaluated.

Note that although the simulation predicts the systematic uncertainties in this section are asymmetric, this asymmetry is at the  $10^{-5}$  level, which is an unjustified level of accuracy; the systematic uncertainties are therefore quoted as symmetric, with the magnitude set to the average of the upper and lower bounds.

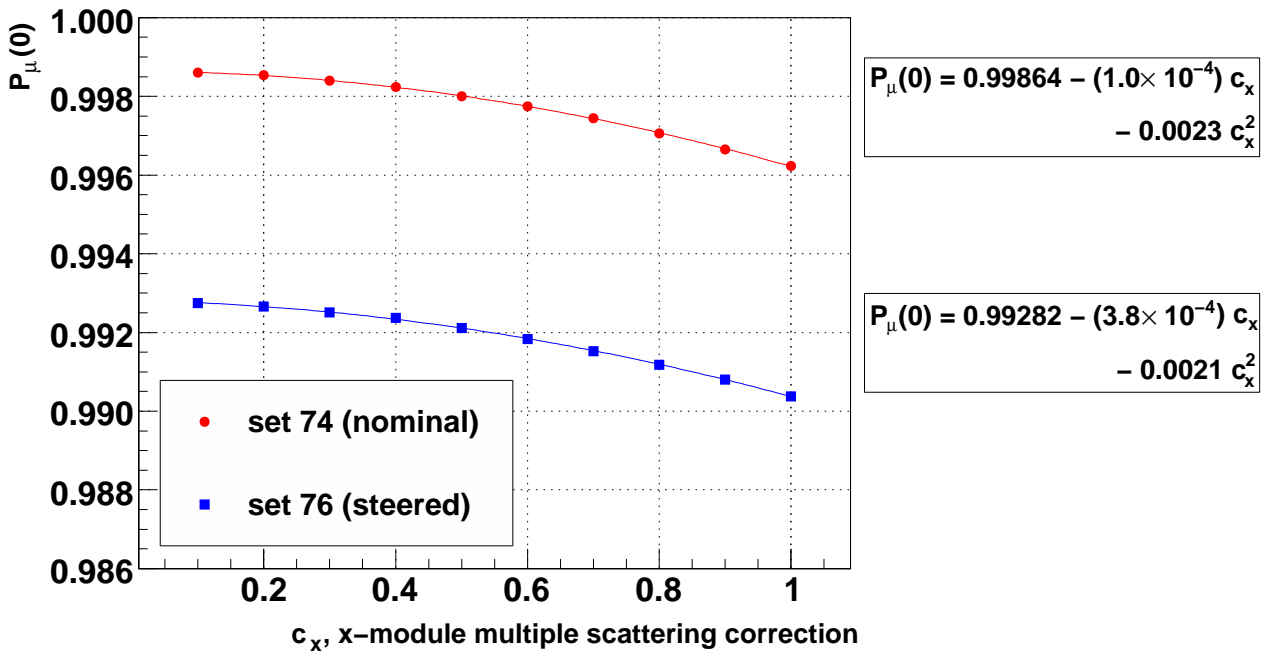


Figure 6.7: Sensitivity of the simulation's  $P_\mu(0)$  to  $c_x$ , the multiple scattering correction factor in the  $x$ -module. The ratio  $c_x/c_y = 63.91/47.95$  was maintained.

The parameters  $c_x$  and  $c_y$  relied on the accuracy of multiple scattering in GEANT3. The author is unaware of any validation studies for the multiple scattering of muons with  $p \approx 30$  MeV/c in thin materials (the entire TEC apparatus was equivalent to just  $\approx 7$  mg/cm<sup>2</sup> of material). Our most direct test of the GEANT3 accuracy used five runs with the upstream window on the TECs changed from the nominal  $6 \mu\text{m}$  of Mylar to a thicker  $25 \mu\text{m}$  ( $3.2$  mg/cm<sup>2</sup>) window. The additional  $19 \mu\text{m}$  of material increased the scattering distribution so that<sup>43</sup>

$$\theta_{\text{TECs}+25 \mu\text{m}} \approx \sqrt{\theta_{\text{TECs}+6 \mu\text{m}}^2 + \theta_{19 \mu\text{m}}^2}. \quad (6.1)$$

The results for  $\theta_{19 \mu\text{m}}$  from data and simulation are shown in Table 6.9, where the simulation overestimates the root mean square width of the scattering distributions by 18.3% in the  $x$ -module and 15.6% in the  $y$ -module. This implies that the  $c_x$  and  $c_y$  factors were reliable to 17.0% (the average of the overestimate in each module), which results in a systematic uncertainty of  $3.1 \times 10^{-4}$ . The observed discrepancy of 17.0% must not be taken as a formal validation of multiple scattering in GEANT3, since there are systematic uncertainties associated with the values in Table 6.9 that have not been evaluated.

Table 6.9: Width of reconstructed angle distributions for TEC Mylar windows of thickness  $6 \mu\text{m}$  and  $25 \mu\text{m}$ . The bracketed number indicates the statistical uncertainty in the final digits.

Mylar window thickness ( $\mu\text{m}$ )	RMS of $\theta_x$ (mrad)		RMS of $\theta_y$ (mrad)	
	data	simulation	data	simulation
6	14.50 (5)	14.10 (7)	19.79 (7)	19.89 (6)
25	17.25 (8)	17.90 (9)	22.01 (6)	22.8 (1)
$\Rightarrow 19$	<b>9.3 (2)</b>	<b>11.0 (2)</b>	<b>9.6 (2)</b>	<b>11.1 (2)</b>

The TEC analysis code was reviewed for this measurement, and the accuracy of the reconstruction algorithm was found to be limited by noise from the electronics. This did not affect the mean position/angle, only the width of the angular distributions. An attempt to overcome this limitation resulted in two variants of the algorithm (see Appendix G.3.4). Since an event-by-event investigation could not distinguish which variant was the most accurate, the difference between the two is taken as a systematic uncertainty. For all sets this difference in  $P_\mu(0)$  was less than  $1.7 \times 10^{-4}$ , except for set 76 (steered) where  $P_\mu(0)$  changed by  $6.3 \times 10^{-4}$  between the two variants of the algorithm. A conservative systematic uncertainty of  $1.7 \times 10^{-4}$

<sup>43</sup>The multiple scattering distribution is non-Gaussian, and adding the widths of layers in quadrature will systematically underestimate the total width[3]. However, in this case we are comparing data and simulation where the same error is made in both.

is assigned for the nominal sets.

The width of the angular distributions depended on the mean number of hits in the final track ( $\langle n_x \rangle$  in the  $x$ -module,  $\langle n_y \rangle$  in the  $y$ -module), which decreased depending on the length of time that the sense planes were exposed to the beam. The same  $c_x$  and  $c_y$  correction factors were used for all muon beam measurements, despite differences in the age of the planes, and this resulted in a systematic uncertainty. For each set,  $\langle n_x \rangle$  and  $\langle n_y \rangle$  are shown in Fig. 6.8. The  $c_x$  and  $c_y$  factors were tuned using set 75, which had  $\langle n_x \rangle = 15.0$  and  $\langle n_y \rangle = 15.9$ . For all the sets, the ranges of  $\langle n_x \rangle$  and  $\langle n_y \rangle$  were 13.0 to 16.7, and 14.4 to 18.5 respectively, which is almost symmetric about the values used for tuning. The set 75 data were reanalysed, with hits removed at random to reduce  $\langle n_x \rangle$  to 13.0 and  $\langle n_y \rangle$  to 16.7. The root-mean-square decreased by 7.9% in the  $x$ -module, and 3.7% in the  $y$ -module. If the larger of these is used, then a conservative systematic uncertainty for the nominal sets due to sense plane aging is  $1.5 \times 10^{-4}$ .

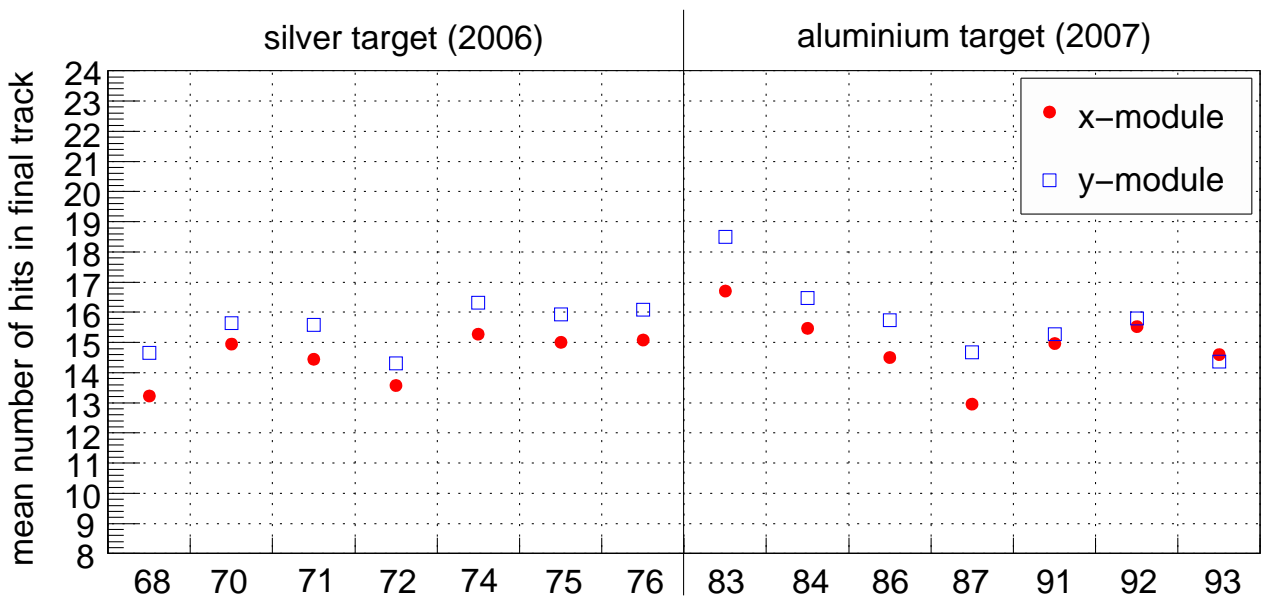


Figure 6.8: Number of hits in final TEC track, for each module. The  $c_x$  and  $c_y$  correction factors were tuned using set 75, which had  $\langle n_x \rangle = 15.0$  and  $\langle n_y \rangle = 15.9$ .

### 6.3.3 Stopping material

#### Overview

About 80% of the muons stopped in a metal target, which also served as the shared cathode foil for the proportional chambers PC6 and PC7 (see Fig. 2.14). Events were accepted only if the muon produced a signal in PC6, but not in PC7. Muons that stopped in the PC6 gas (a mixture of  $\text{CF}_4$  and isobutane) or wires were then removed by cutting on the muon pulse width in the chamber (see Section 3.3.3). This selected a clean sample of muons that stopped in the metal foil. The relaxation was determined using a weighted asymmetry measurement (see Section 3.6). Each data set was fit with

$$P_\mu(t) = P_\mu^*(0) \exp(-\lambda t). \quad (6.2)$$

The simulation used the relaxation rate ( $\lambda$ ) from a preliminary analysis of the silver and aluminium data.

There is one correction, one statistical uncertainty and three systematic uncertainties related to the stopping material. A correction to  $\Delta P_\mu^\pi \xi$  is necessary since the simulation used preliminary values of  $\lambda$ . A statistical uncertainty results from the precision that  $\lambda$  can be determined from the data ( $2.3 \times 10^{-4}$ ). There is a systematic uncertainty from the degree to which stops in the PC6 chamber gas are eliminated ( $0.3 \times 10^{-4}$ ), and another uncertainty from muons that pass through the target and stop in PC7, but do not have enough energy to produce a signal ( $1.6 \times 10^{-4}$ ). However, these are dominated by a systematic uncertainty from a bias in the analysis ( $5.8 \times 10^{-4}$ ). After adding in quadrature, there is a total systematic uncertainty of  $6.0 \times 10^{-4}$ . Note that for this analysis there is no uncertainty due to choice of model for  $P_\mu(t)$  in the metals; see Section 1.6.3 for the theoretical arguments that demonstrate a strong preference for a single exponential form.

#### Correction and statistical uncertainty

The results of the asymmetry analysis applied to the data are shown in Table 6.10, where the fit is made over the nominal time range of  $(1.05 < t < 9.00) \mu\text{s}$ . A weighted average of these relaxation rates finds

$$\lambda_{\text{Ag}}^{\text{data}} = (0.840 \pm 0.072) \text{ ms}^{-1}, \quad (6.3)$$

$$\lambda_{\text{Al}}^{\text{data}} = (1.320 \pm 0.077) \text{ ms}^{-1}. \quad (6.4)$$

Note that these are consistent with the  $\mu^+$ SR results from Appendix H.8:

$$\lambda_{\text{Ag}}^{\mu\text{SR}} = (0.9 \pm 0.2 \text{ (stat.)} \pm 0.2 \text{ (syst.)}) \text{ ms}^{-1}, \quad (6.5)$$

$$\lambda_{\text{Al}}^{\mu\text{SR}} = (1.3 \pm 0.2 \text{ (stat.)} \pm 0.3 \text{ (syst.)}) \text{ ms}^{-1}. \quad (6.6)$$

The simulation used preliminary values of  $\lambda_{\text{Ag}} = 0.732 \text{ ms}^{-1}$  and  $\lambda_{\text{Al}} = 1.169 \text{ ms}^{-1}$ , and as a result the quantity  $\Delta P_{\mu}^{\pi} \xi$  must be corrected. The effect on the spectrum of a change in  $\lambda$  is calculated using

$$\frac{\int_{t_1}^{t_2} N(t) \cdot P_{\mu}^*(0) \exp(-\lambda_2 t) dt}{\int_{t_1}^{t_2} N(t) dt} - \frac{\int_{t_1}^{t_2} N(t) \cdot P_{\mu}^*(0) \exp(-\lambda_1 t) dt}{\int_{t_1}^{t_2} N(t) dt}, \quad (6.7)$$

where  $N(t) = N(0) \exp(-t/\tau_{\mu})$  and  $\tau_{\mu}$  is the muon lifetime, and  $\lambda_1$  and  $\lambda_2$  are the relaxation rates between which the correction is being made. The common  $P_{\mu}^*(0)$  factor is close to 1.0, and its choice has a negligible impact on the correction. The quantity  $\Delta P_{\mu}^{\pi} \xi$  (the difference between the data and a hidden simulation value) is then corrected by  $+3.3 \times 10^{-4}$  for Ag ( $\lambda_1 = 0.732 \text{ ms}^{-1}$ ,  $\lambda_2 = 0.840 \text{ ms}^{-1}$ ) and  $+4.5 \times 10^{-4}$  for Al ( $\lambda_1 = 1.169 \text{ ms}^{-1}$ ,  $\lambda_2 = 1.320 \text{ ms}^{-1}$ ). The statistical uncertainty in determining  $\lambda$  from the data causes a  $P_{\mu}$  uncertainty of  $2.3 \times 10^{-4}$  for both targets, again using Eq. (6.7).

Table 6.10: Relaxation rate  $\lambda$  for each data set.  $P_\mu(t) = P_\mu^*(0) \exp(-\lambda t)$  has been fit over the nominal time range of  $(1.05 < t < 9.00) \mu\text{s}$ .

Set num.	Target	Description	$\lambda$ ( $\text{ms}^{-1}$ )	Fit quality $\chi^2/\text{ndof}$	confidence
68	Ag	Stopping distrib. peaked $\frac{1}{3}$ into target	$0.88 \pm 0.21$	$16.0/20 = 0.80$	0.720
70	Ag	B = 1.96 T	$0.86 \pm 0.17$	$15.6/20 = 0.78$	0.742
71	Ag	B = 2.04 T	$0.98 \pm 0.18$	$26.4/20 = 1.32$	0.153
72	Ag	TECs-in, nominal beam	$0.93 \pm 0.18$	$25.9/20 = 1.29$	0.170
74	Ag	Nominal A	$1.02 \pm 0.22$	$19.4/20 = 0.97$	0.497
75	Ag	Nominal B	$0.86 \pm 0.18$	$12.9/20 = 0.65$	0.880
76	Ag	Steered beam A	$0.32 \pm 0.20$	$12.5/20 = 0.63$	0.897
83	Al	Downstream beam package in place	$1.41 \pm 0.18$	$32.7/20 = 1.63$	0.037
84	Al	Nominal C	$1.26 \pm 0.19$	$24.4/20 = 1.22$	0.225
86	Al	Steered beam B	$1.29 \pm 0.16$	$26.5/20 = 1.33$	0.149
87	Al	Nominal D	$1.28 \pm 0.18$	$13.9/20 = 0.70$	0.833
91	Al	Lower momentum I	$1.65 \pm 0.33$	$20.1/20 = 1.01$	0.449
92	Al	Lower momentum II	$1.30 \pm 0.29$	$16.1/20 = 0.81$	0.708
93	Al	Lower momentum III	$1.25 \pm 0.22$	$15.1/20 = 0.76$	0.770

### Muon stops in gas

The distribution of the pulse widths in the PCs immediately before the target is shown in Fig. 6.9. The majority of the distribution is made up of stops in the metal target, which primarily contribute to zones 1 and 2, and there is a “gas band” that runs approximately parallel to the cut-B line and contributes mostly to zones 2 and 3. The analysis only selects zone 1; the cut-B line removes almost all of the gas contamination, but a small fraction still make it to zone 1.

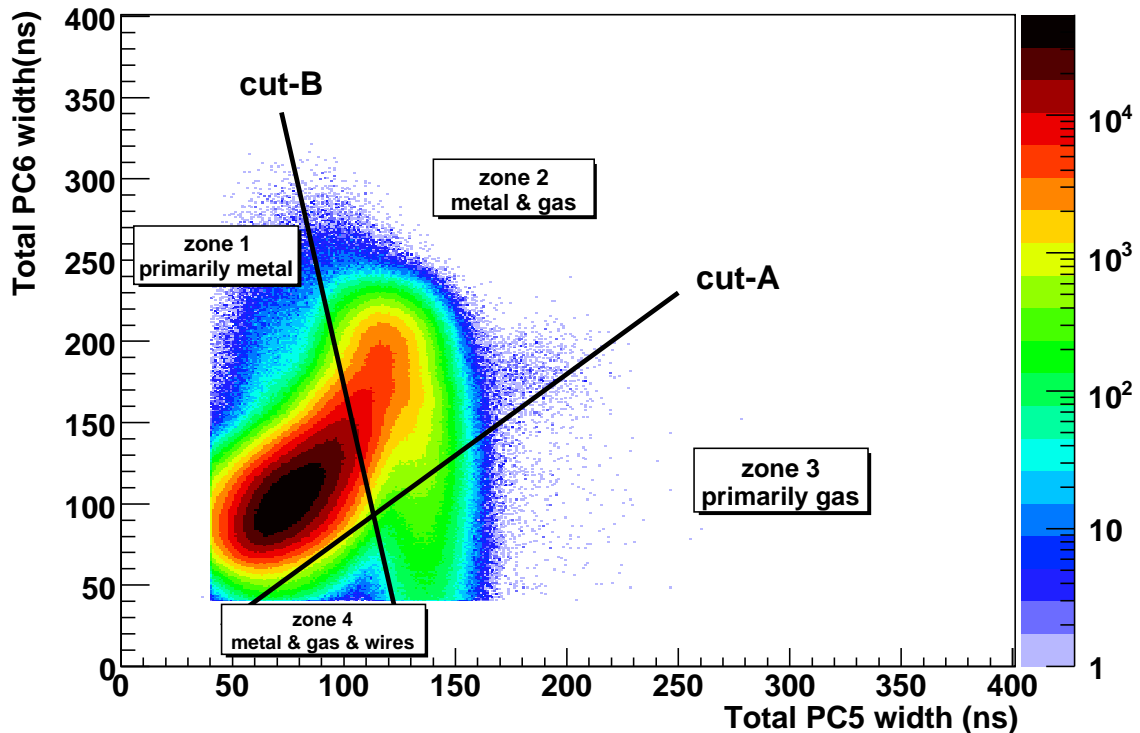


Figure 6.9: Muon pulse widths in PC5 and PC6 (the proportional chambers immediately before the metal stopping target). The stops in gas appear as a band that is approximately parallel to cut-B, primarily contributing to zones 2 and 3.

A systematic uncertainty was estimated using only the data. This required three numbers, which are described in Appendix J: the depolarisation in gas (8.0%), the fraction of the total PC6 stops in gas ( $f_g$ ), which is between 4% and 7% depending on the set, and the fraction of the gas distribution in zone 2 that leaks into zone 1 (tuned to be  $< 0.5\%$  by adjusting

cut-B). If the number of muons stopping in the gas in zone  $i$  is denoted  $N_i^g$ , then

$$f_g N_{\text{total}} = N_1^g + N_2^g + N_3^g + N_4^g, \quad (6.8)$$

$$N_1^g < 0.5\% \times (N_1^g + N_2^g), \quad (6.9)$$

which gives

$$\frac{N_1^g}{N_{\text{total}}} < 0.5\% \times \left[ f_g - \frac{N_3^g + N_4^g}{N_{\text{total}}} \right]. \quad (6.10)$$

If all the gas stops are conservatively assumed to be in zones 1 and 2 so that  $N_3^g = N_4^g = 0$ , and  $f_g$  is set to its maximum value of 7%, then an upper limit on the systematic uncertainty from muons stopping in PC6 gas is  $8.0\% \times 0.5\% \times 7\% = 0.3 \times 10^{-4}$ .

A special simulation found that 0.2% of muons entered PC7 (the wire chamber *after* the metal stopping target), but did not have enough energy to produce a signal. These stop in the PC gas, and experience a depolarisation of 8.0% (see above). The systematic uncertainty due to these stops is therefore  $\approx 0.2\% \times 8\% = 1.6 \times 10^{-4}$ .

### Analysis bias

The asymmetry analysis is applied to the simulation to confirm that the input value of  $\lambda$  can be recovered. The results of this study are shown in Fig. 6.10, where the simulation that accompanies set 74 (nominal) is seen to have a  $\lambda$  that is 3.5 standard deviations from the input value. As a result, the *weighted average* of  $\lambda$  for the silver simulations is 2.6 standard deviations from the input; the result for the aluminium simulations is consistent with the input  $\lambda$  ( $0.3\sigma$  below input value).

An exhaustive investigation attempted to find the cause of the discrepancies for the silver simulations. The results were found to be robust to the binning, weighting strategy and time range used in the asymmetry analysis. The confidence levels from the asymmetry analysis were spread evenly between 0 and 1, indicating the  $\lambda$  uncertainties are properly determined. A separate analysis that made fits to the upstream and downstream time distributions (*i.e.* an asymmetry was not constructed) confirmed the  $\lambda$  results, but with inferior statistical precision. The simulation for set 74 only differed from the others in its input beam profile and muon/positron rates; the beam profile produced a reasonable value for  $P_\mu(0)$ , and the rate differences from the other sets were insignificant. Therefore the investigation could not find a reason to reject the anomalous  $\lambda$  result. We are forced to admit the possibility that a systematic  $\lambda$  uncertainty exists due to an analysis bias, and this could be as large as 2.6 statistical standard deviations. Using Eq. (6.7), this results in a large systematic uncertainty

of  $5.6 \times 10^{-4}$  for silver and  $6.0 \times 10^{-4}$  for aluminium. The average of these,  $5.8 \times 10^{-4}$ , is taken as the systematic uncertainty due to an analysis bias.

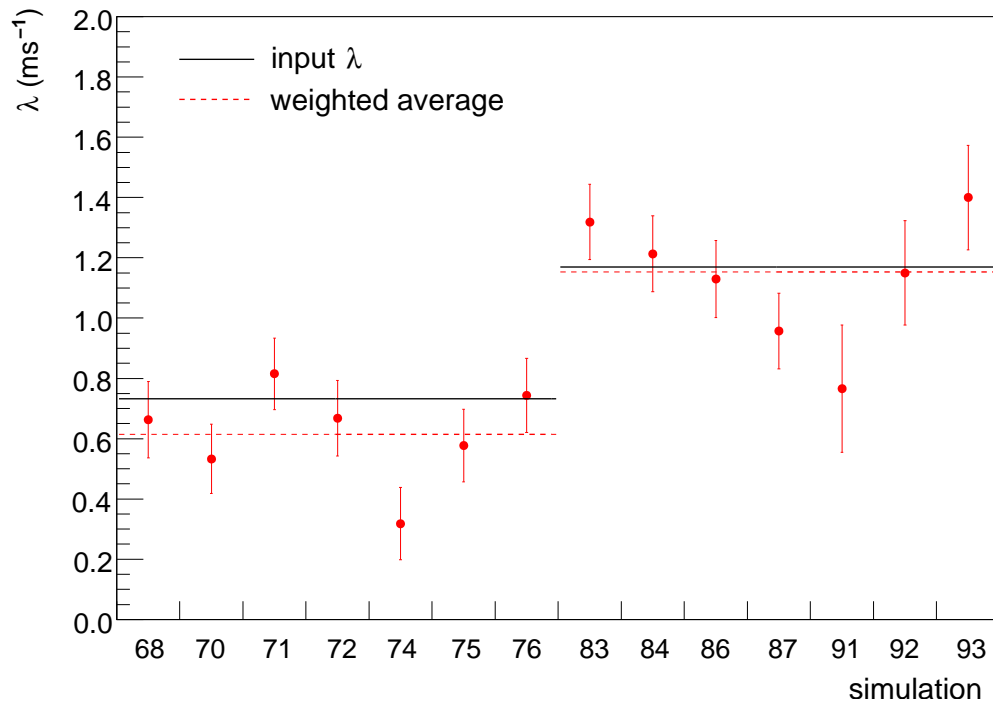


Figure 6.10: The result of the asymmetry analysis applied to the simulations. The relaxation rate ( $\lambda$ ) for the set 74 simulation is  $3.5\sigma$  away from the input value.

### 6.3.4 Production target

The simulation generated muons with anti-parallel spin and momentum vectors, starting from the end of the M13 beam line. This neglected multiple scattering in the graphite production target and the beam line vacuum window, which changed the momentum vector but not the spin. This is treated here as a systematic correction with an associated uncertainty. (The difference in precession frequencies of the momentum and spin through the M13 beam line is neglected since it introduced an error of  $< 10^{-8}$ ; see Appendix I).

Surface muons are produced with  $p \approx 29.79 \text{ MeV}/c$ , but the beam line was nominally tuned to accept muons with an average momentum of  $\langle p \rangle = 29.6 \text{ MeV}/c$ . Therefore the muons lost  $0.19 \text{ MeV}/c$  of momentum on average, which is equivalent to  $\approx 3.8 \text{ mg}/\text{cm}^2$  in graphite. (The  $3 \mu\text{m}$  beam line vacuum window is safely neglected since it corresponds to just  $0.3 \text{ mg}/\text{cm}^2$  of material.) The width of the resulting multiple scattering distribution<sup>44</sup>,  $\theta_0$ , was found to be  $9.3 \text{ mrad}$  using a **GEANT4** simulation. The uncertainty is conservatively estimated as  $\pm 17\%$  based on the observed discrepancy for **GEANT3** from Section 6.3.2. The degree to which the spin is depolarised with respect to the momentum is then estimated by  $\cos(\theta_{\text{space}}^{\text{rms}})$ , where  $\theta_{\text{space}}^{\text{rms}} = \sqrt{2}\theta_0$ . This results in a correction to the simulation's  $P_\mu$  of  $(-0.9 \pm 0.3) \times 10^{-4}$ , which is a correction to  $\Delta P_\mu^\pi \xi$  of  $(+0.9 \pm 0.3) \times 10^{-4}$ .

The previous  $P_\mu^\pi \xi$  analysis found a systematic uncertainty of  $2 \times 10^{-4}$  due to depolarisation in the production target; this was evaluated as a conservative upper limit, rather than making a correction[57].

The **GEANT4** simulations were repeated for the lower momentum sets. The widths were  $\theta_0 = 24.2 \text{ mrad}$  for  $\langle p \rangle = 28.75 \text{ MeV}/c$ , and  $\theta_0 = 22.9 \text{ mrad}$  for  $\langle p \rangle = 28.85 \text{ MeV}/c$ . These corresponded to  $\Delta P_\mu^\pi \xi$  corrections of  $(5.9 \pm 1.9) \times 10^{-4}$  and  $(5.2 \pm 1.6) \times 10^{-4}$  respectively.

---

<sup>44</sup> $\theta_0$  is the standard deviation of a Gaussian fit to the central 98% of the the plane-projected multiple scattering distribution.

### 6.3.5 Background muon contamination

The simulation's muon stopping distribution must match the data, since high angle muons that undergo more depolarisation are preferentially stopped further upstream. The true muon stopping distribution is not available for the data, so the simulation is instead tuned to match the distribution of the last wire plane that measures the muon. A source of uncertainty in this distribution and its consequence for  $P_\mu^\pi \xi$  will now be described.

In the previous  $P_\mu^\pi \xi$  analysis the distribution of the muon's last hit plane did not agree in data and simulation unless an additional source of pion decays was included in the "upstream beam package" area (see Fig. 6.11(a)). For the current analysis the agreement is better *without* the additional pion source; this is demonstrated in Fig. 6.11(b), where improvements in the classification have increased the number of downstream events in the simulation relative to the data. The residual discrepancy in Fig. 6.11(b) still introduces a small uncertainty in the muon stopping distribution.

The most accurate measurement of the muon stopping distribution comes from the energy calibration procedure (see Section 3.5). The reconstructed spectrum endpoint depends on the thickness of target (and detector) material traversed, which results in a dependence on  $1/\cos\theta$ . The gradient of this relationship,  $\alpha_{\text{up}}$  or  $\alpha_{\text{down}}$  for upstream and downstream respectively, is therefore a measure of the material traversed by the upstream and downstream decay positrons. The stopping distribution can then be measured using

$$\alpha_{\text{diff.}} = \alpha_{\text{up}} - \alpha_{\text{down}}. \quad (6.11)$$

Now the energy calibration procedure finds the difference in reconstructed spectrum endpoint between data and simulation, which has a gradient equal to

$$\alpha_{\text{up}}^{\text{data}} - \alpha_{\text{up}}^{\text{sim.}}, \quad (6.12)$$

in the upstream half of the detector, and

$$\alpha_{\text{down}}^{\text{data}} - \alpha_{\text{down}}^{\text{sim.}} \quad (6.13)$$

in the downstream half. The difference between the gradients in the upstream and downstream half (*i.e.* Eq. (6.12) minus Eq. (6.13)) is then

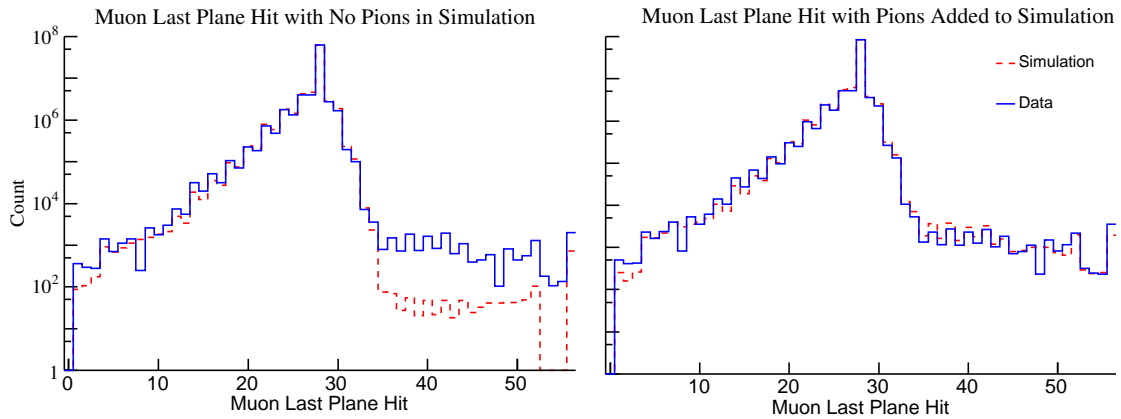
$$\left(\alpha_{\text{up}}^{\text{data}} - \alpha_{\text{down}}^{\text{data}}\right) - \left(\alpha_{\text{up}}^{\text{sim.}} - \alpha_{\text{down}}^{\text{sim.}}\right) = \alpha_{\text{diff.}}^{\text{data}} - \alpha_{\text{diff.}}^{\text{sim.}}, \quad (6.14)$$

which measures how well the muon stopping distributions agree in data and simulation.

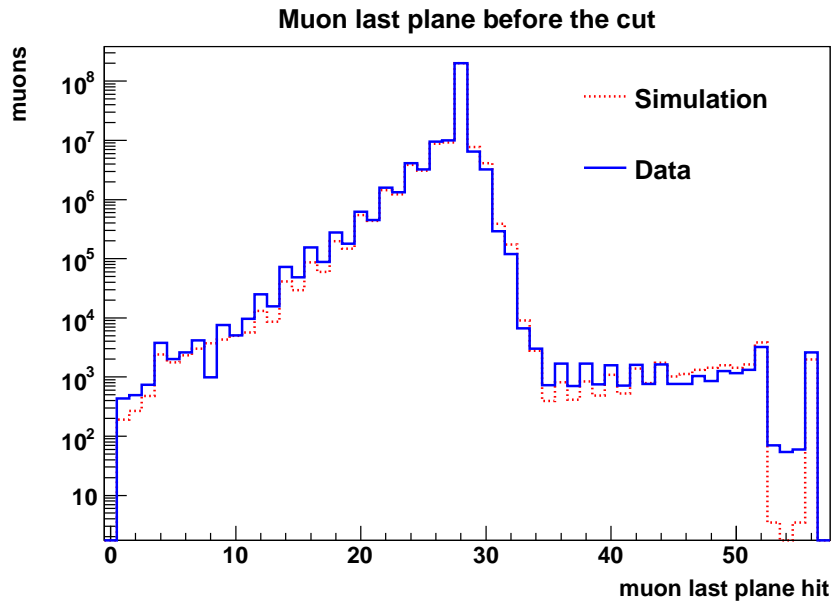
The stopping distribution measure from Eq. (6.14) is shown in Fig. 6.12. For five of the simulations, the mean of the muon last plane distribution was matched by adding an extra 1.9 mg/cm<sup>2</sup> of material to the simulation (see Section 2.11), and the resulting disagreement is  $(5.5 \pm 1.4)$  keV/c on average. For the other simulations no additional material was added, and this improved the data-simulation disagreement to  $(0.2 \pm 1.1)$  keV/c

The simulation can determine the relationship between  $P_\mu(0)$  and  $(\alpha_{\text{diff}}^{\text{data}} - \alpha_{\text{diff}}^{\text{sim}})$ . This depends on the beam profile, and is within the range  $0.04 \times 10^{-4}/(\text{keV}/c)$  to  $0.25 \times 10^{-4}/(\text{keV}/c)$ , with an average of  $0.13 \times 10^{-4}/(\text{keV}/c)$ . The systematic uncertainty from matching the stopping distribution is therefore  $5.5 \times 0.13 \times 10^{-4} = 0.7 \times 10^{-4}$  for the sets with the extra 1.9 mg/cm<sup>2</sup> of material. Since this is a small number and only applies to 5 of the 14 simulation, it is treated as a conservative systematic uncertainty rather than a correction.

*From here on the systematic uncertainties are evaluated by exaggerating a setting in the simulation or analysis, as described in the earlier overview (Section 6.2). The exaggeration is necessary to achieve a statistically meaningful change in  $P_\mu^\pi \xi$ . For each systematic it is validated that  $P_\mu^\pi \xi$  depends linearly on the exaggeration.*



(a) Distribution of last plane that measures the muon, for data and simulation, from the previous analysis (originally Fig. 6.9 from Ref. [57]). The mismatch is resolved by including an additional source of pion decays at the location of the “upstream beam package”.



(b) The same figure re-made for the current analysis, where *no* additional pion decays are added.

Figure 6.11: Background muon contamination in the two  $P_{\mu}^{\pi} \xi$  analyses.

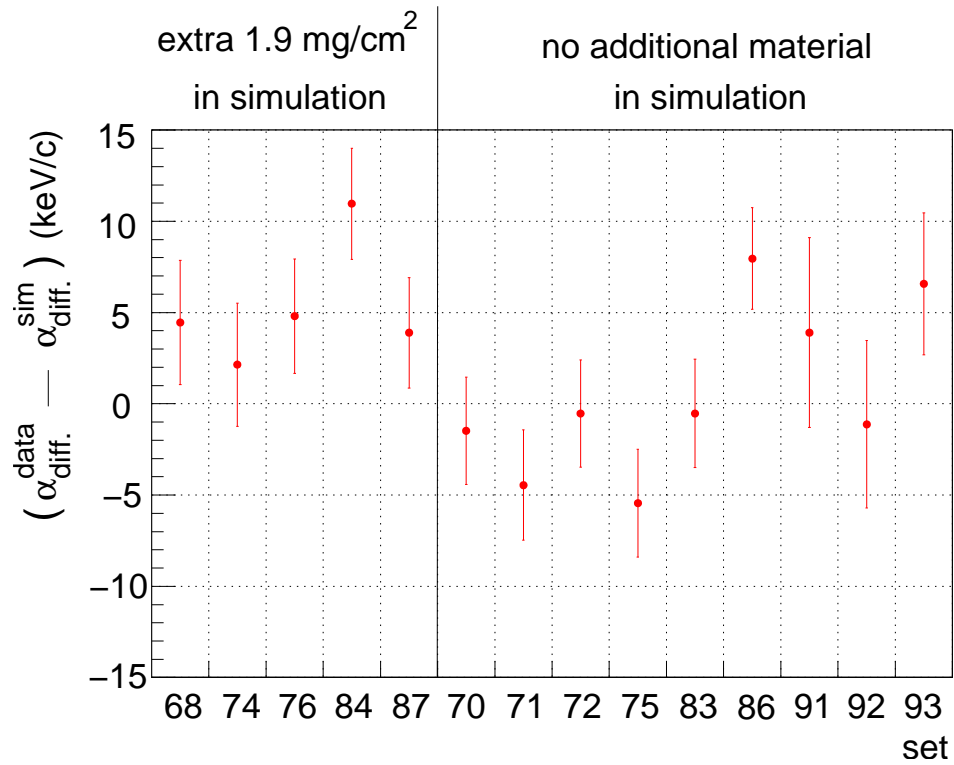


Figure 6.12: The muon stopping distribution is most accurately measured in data and simulation using the endpoint calibration; see the main text for a description of the ordinate. The data and simulation distributions are in agreement when  $\alpha_{\text{diff.}}^{\text{data}} - \alpha_{\text{diff.}}^{\text{sim.}} = 0$ .

### 6.3.6 Beam intensity

The simulation's muon and beam positron rates were tuned to match the data; a disagreement can change the number of hits in the wire chambers, which affects the performance of the classification. The simulation's muon rate was tuned to only approximately match the trigger rate in data. The simulation's beam positron rate was tuned to match the probability of a beam positron entering an event.

The most recent decay parameter analysis found that increasing the beam positron rate in the simulation by a factor of 10 only changed  $\Delta P_\mu^\pi \xi$  by  $(-5 \pm 7) \times 10^{-4}$  [18] (this was scaled down to obtain a systematic uncertainty; the point is that a very large exaggeration resulted in a sensitivity that was consistent with zero). This confirmed that beam positrons are efficiently removed by the analysis software, and therefore no systematic uncertainty due to the beam positron rate is assigned for the current measurement.

Increasing the muon rate in the simulation from  $2731 \text{ s}^{-1}$  to  $27310 \text{ s}^{-1}$  changes  $\Delta P_\mu^\pi \xi$  by  $(23 \pm 8) \times 10^{-4}$  [18]. This must be scaled down by repeating the procedure from Ref. [18] for the modern data and simulation. Specifically, the following steps are taken,

1. For each data set and accompanying simulation, calculate the following ratio of event types:

$$R_\mu = \frac{(\text{more than one } \mu^+)}{(\text{more than one } \mu^+) + (\text{one } \mu^+, \text{ one decay } e^+)}. \quad (6.15)$$

This is a measure of the probability of an event having more than one muon.

2. Calculate the relative ratio of  $R_\mu$  for data and simulation,

$$\frac{R_\mu(\text{sim.}) - R_\mu(\text{data})}{R_\mu(\text{data})}. \quad (6.16)$$

3. Multiply the relative ratio by the average trigger rate from the data, to estimate the error (in  $\text{s}^{-1}$ ) made in the simulation.
4. Divide the simulation's error by the exaggeration ( $27310 \text{ s}^{-1} - 2731 \text{ s}^{-1} = 24579 \text{ s}^{-1}$ ).

The calculations from each of these steps appear in Table 6.11. An upper limit on the effect of data-simulation rate discrepancies uses the smallest scale factor (28.7, from set 92), resulting in a systematic uncertainty of  $(1/28.7) \times (23 \pm 8) \times 10^{-4} = (0.8 \pm 0.3) \times 10^{-4}$ .

Table 6.11: Scale factors for the systematic uncertainty due to beam intensity.  $R_\mu$  is a measure of the probability of an event with more than one muon. Sets 68-76 were accumulated in 2006 using a silver target. Sets 83-93 were accumulated in 2007 using an aluminium target, with a muon rate that was intentionally higher. Simulation is abbreviated as Sim.

Set	$R_\mu$ Data	$R_\mu$ Sim.	$\frac{R_\mu(\text{sim.}) - R_\mu(\text{data})}{R_\mu(\text{data})}$	Avg. data trigger ( $\text{s}^{-1}$ )	Sim. error ( $\text{s}^{-1}$ )	Scale factor
68	0.00553	0.00495	-0.10615	2066.0	-219.3	112.1
70	0.00630	0.00541	-0.14129	2324.8	-328.5	74.8
71	0.00660	0.00619	-0.06305	2582.9	-162.8	150.9
72	0.00718	0.00552	-0.23151	2674.2	-619.1	39.7
74	0.00672	0.00617	-0.08089	2592.9	-209.7	117.2
75	0.00739	0.00641	-0.13216	2686.6	-355.1	69.2
76	0.00903	0.00640	-0.29114	2740.9	-798.0	30.8
83	0.01220	0.01029	-0.15728	4221.8	-664.0	37.0
84	0.01291	0.01103	-0.14616	4452.3	-650.7	37.8
86	0.01353	0.01205	-0.10914	4972.3	-542.7	45.3
87	0.01188	0.00977	-0.17768	4024.0	-715.0	34.4
91	0.01218	0.01004	-0.17531	4202.5	-736.7	33.4
92	0.01251	0.01002	-0.19897	4305.3	-856.6	28.7
93	0.01077	0.01003	-0.06851	3809.5	-261.0	94.2

## 6.4 Chamber response

### 6.4.1 Drift chamber space-time relationship

The space-time-relationships (STRs) in the drift cells were optimised by minimising the residual between the hit times from the drift cell, and the times that best fit the helix trajectories (see Section 3.2.7). In the simulation, where it was sufficient to use a single STR cell for all wires and planes, this procedure effectively absorbs the helix fitting bias into the STRs. In data, where a separate STR cell was obtained for each plane, the procedure corrects for plane-to-plane construction and response differences, in addition to subtle bias from the helix fitting algorithm.

The refinement procedure was carried out iteratively, with the STR forced to remain smooth at each step. After convergence, there were residuals in the drift cell corresponding to regions where manipulating the STRs could not bring the drift time closer to the fitted trajectory. The amount by which these residuals differ in data and simulation is the basis of the chamber response systematic uncertainty.

The difference between the data and simulation residuals at the final iteration is shown in Fig. 6.13. The data results are averaged over all planes. Only half a cell is shown, and in practice this is reflected about the line  $uv = 0$ . The largest discrepancies between data and simulation are at the edge of the cell ( $u$  or  $v = 1.8$  cm), where there were low statistics and the single hit resolution was degraded. In the rest of the cell the variations are at the impressive level of  $< 4$  ns.

The following approach exaggerated the differences between data and simulation without breaking the smoothness of the STRs:

1. Generate a separate refined STR cell for each plane in the simulation.
2. For each plane, find the difference in residuals at the final iteration, just like Fig. 6.13. Fit this distribution with a fifth order polynomial function.
3. Exaggerate the polynomial function until the  $\chi^2/\text{ndof}$  of positron helix fits becomes a factor of two worse. This corresponded to the single hit resolution being degraded by  $\approx (1 - \sqrt{2}) \approx 40\%$ , and required an exaggeration factor of ten in the polynomial function.
4. Re-analyse the simulation with the scaled STRs, and compare to the nominal simulation.
5. Reduce the  $P_\mu^\pi \xi$  change by a scale factor of ten.

This determined the uncertainty as  $(0.0 \pm 0.4) \times 10^{-4}$ .

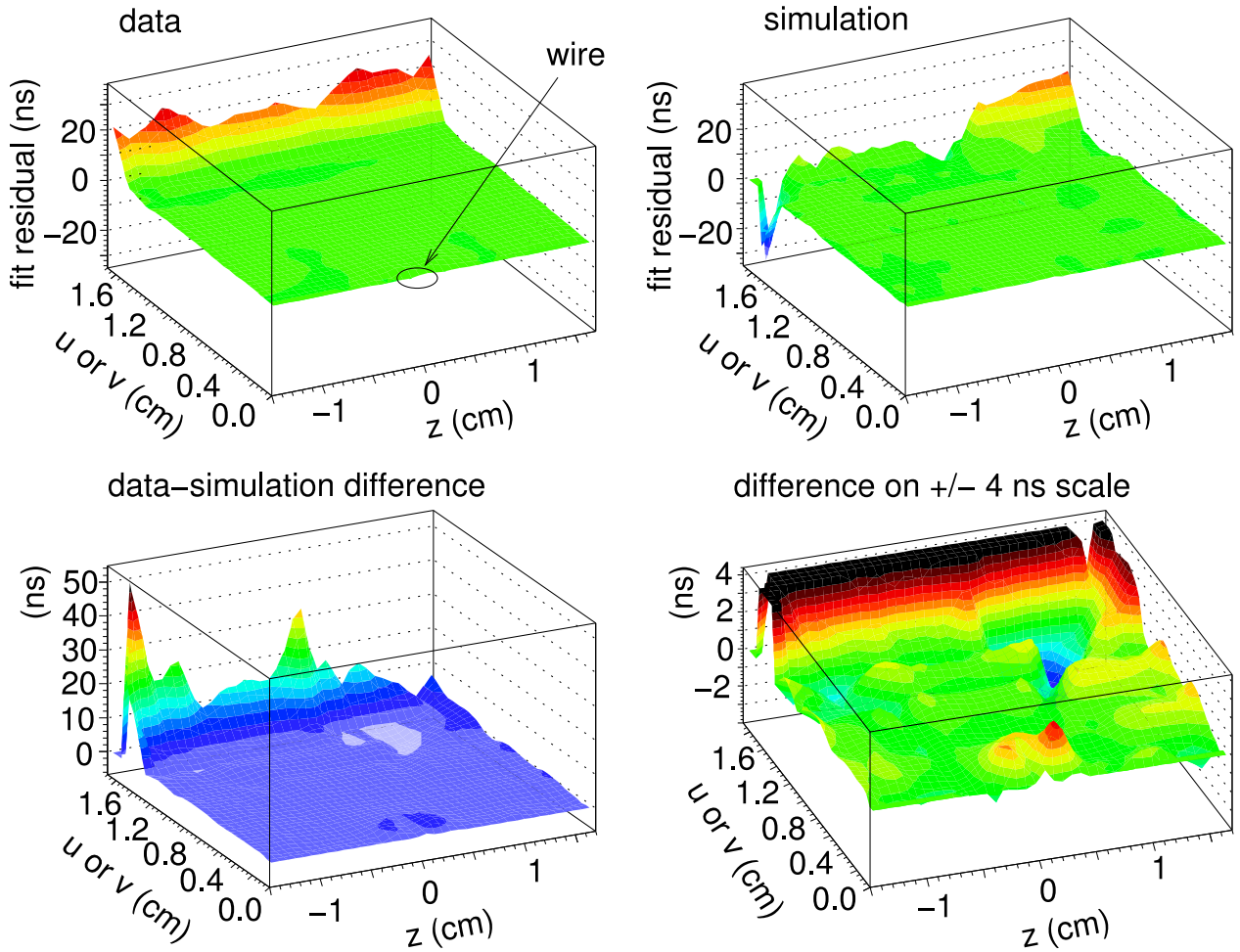


Figure 6.13: Time residuals of the helix fits, after refining the space-time-relationships. Only half a cell is shown, which in practice is reflected about  $uv = 0$ .

### 6.4.2 Wire time offsets

In the previous  $P_\mu^\pi \xi$  analysis the wire time offsets were only calibrated at the beginning and end of the run period. The calibration data were acquired with the magnetic field off, using 120 MeV/c pions and a special downstream trigger. There were significant differences between the two calibrations, and the  $P_\mu^\pi \xi$  result changed by  $9 \times 10^{-4}$  depending on which calibration was used[57].

For this measurement a reliable downstream trigger was in place throughout data acquisition. The wire time offsets in each half of the detector were calibrated on a set-by-set basis using the decay positrons (see Section 3.2.1). Beam positrons that passed through the entire detector were then used to determine the relative timing of the upstream and downstream halves of the detector.

The relative timing of the upstream and downstream halves was determined to 0.10 ns. An exaggerated upstream-downstream shift of 10 ns changes  $\Delta P_\mu^\pi \xi$  by  $(13 \pm 31) \times 10^{-4}$ . After scaling down by  $10 \text{ ns}/0.10 \text{ ns} = 100$ , this results in a systematic uncertainty of  $(0.1 \pm 0.3) \times 10^{-4}$ .

When fitting the time distribution in the data, there were background counts that distorted the fit. These introduced a negligible systematic uncertainty of  $0.4 \times 10^{-4}$ [98]. For this analysis the wire time offset calibration was also applied to the simulation. This included calibration bias to first order and degraded the resolution of the simulation, but not by a measurable amount. The width of the simulation's time distributions differ from the data, and this has been estimated to introduce a negligible systematic uncertainty of  $0.3 \times 10^{-4}$ [98].

The wire time offset uncertainty is the quadratic sum of the three pieces described above, which totals  $0.5 \times 10^{-4}$ .

### 6.4.3 Upstream-downstream efficiency

The simulation must reproduce the difference in track reconstruction efficiency (TRE) between the upstream and downstream halves of the detector. This is measured in data and simulation using a special ‘‘upstream stops’’ analysis, where muons were stopped close to the trigger scintillator, and the decay positrons were reconstructed independently in each half of the detector. The TRE is then calculated based on how often a positron is reconstructed in one half of the detector, but not the other.

The difference in TRE between data and simulation is shown in Fig. 6.14, where a cut has been placed at  $(23 < p < 29) \text{ MeV}/c$  to remove beam positrons. There is no evidence of a dependence on  $p$ , but there *is* statistical evidence of a linear dependence on  $|\cos \theta|$ . If this

is expressed as  $p_0 - p_1|\cos\theta|$ , then the upstream half has parameters

$$p_0^{US} = (5.1 \pm 1.7) \times 10^{-4}, p_1^{US} = (6.4 \pm 2.3) \times 10^{-4}, \quad (6.17)$$

and the downstream half has

$$p_0^{DS} = (3.5 \pm 2.1), p_1^{DS} = (5.3 \pm 2.8) \times 10^{-4}. \quad (6.18)$$

The systematic uncertainty was measured by taking a nominal spectrum and multiplying the number of upstream counts by

$$1 - 10 \times (5.1 - 6.4|\cos\theta|) \times 10^{-4}, \quad (6.19)$$

and the number of downstream counts by

$$1 - 10 \times (3.5 - 5.3|\cos\theta|) \times 10^{-4}, \quad (6.20)$$

where the factor of ten is an exaggeration. This changed  $P_\mu^\pi \xi$  by  $(12.7 \pm 0.5) \times 10^{-4}$ , which is a systematic uncertainty of  $1.3 \times 10^{-4}$  after scaling down by ten.

#### 6.4.4 Dead zone

When a decay positron hit the same wire as the muon, close to where the muon left ionisation, there was reduced gain for the positron due to lingering muon ionisation (the wire had a “dead zone”).

The simulation included the dead zone by removing hits within 0.06 cm of the muon hit, during a recovery time of  $3.0 \mu\text{s}$ . These parameters were tuned according to the fraction of hits removed by the dead zone in data. In the simulation this corresponded to 0.03% of hits, tuned to an accuracy of about 20% (*i.e.*  $\pm 0.006\%$  of the total number of hits)

A special simulation used an enhanced dead zone: instead of only deadening the wire within 0.06 cm of the muon hit, the entire wire was made insensitive to decay positrons for the  $3.0 \mu\text{s}$  recovery time. The enhanced simulation changes  $\Delta P_\mu^\pi \xi$  by  $(25 \pm 2) \times 10^{-4}$ , and removes 0.99% of hits. Compared to the nominal case, this special simulation exaggerates the removed hits by  $0.99\% - 0.03\% = 0.96\%$ , resulting in a scale factor of  $0.96\%/0.006\% = 160$ . The change in  $\Delta P_\mu^\pi \xi$  is then  $(1/160) \times 25 \times 10^{-4} = 0.2 \times 10^{-4}$ .

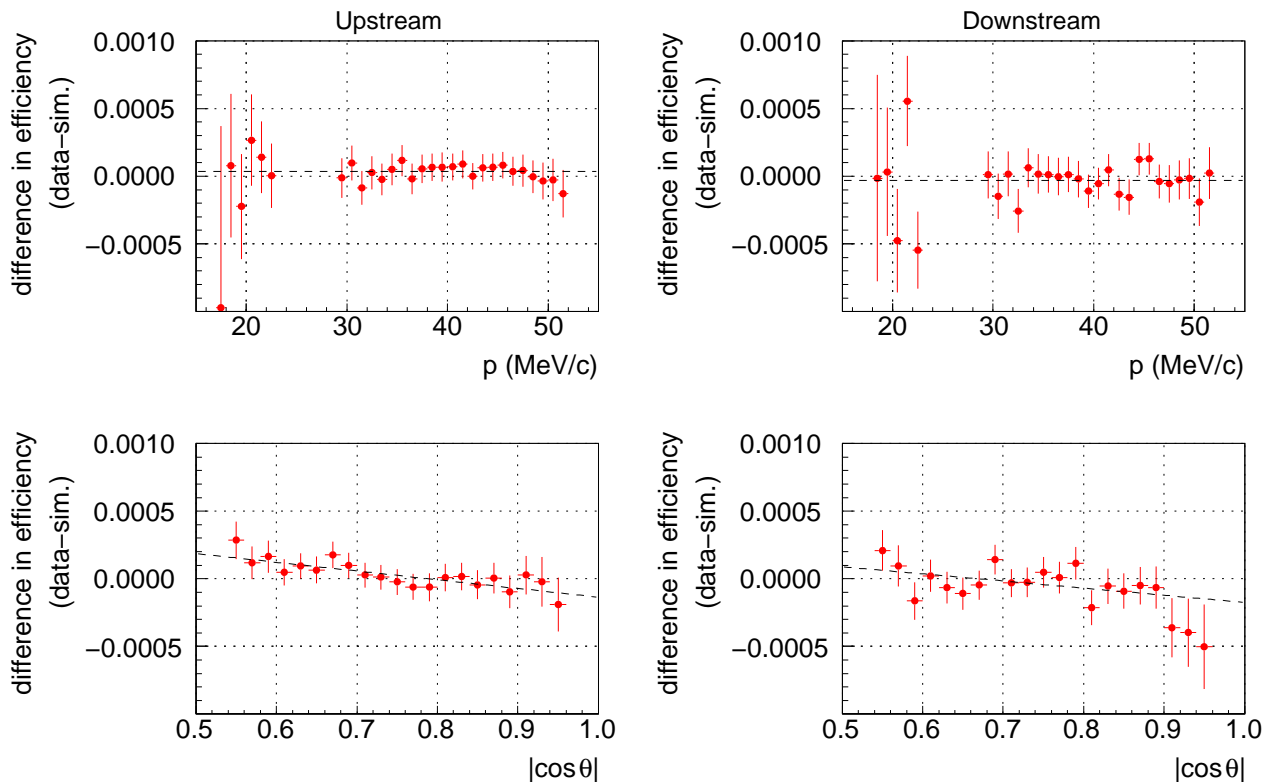


Figure 6.14: Track reconstruction inefficiency for the kinematic fiducial. The upstream inefficiency is determined by how often a positron is reconstructed in the downstream half of the detector, but not the upstream half. The definition is reversed for the downstream half. A cut has been placed at  $(23 < p < 29)$  MeV/c in order to remove beam positrons.

### 6.4.5 Chamber foil bulge

The chamber foils were always flat in the simulation, but in the real detector they could bulge when the gas system did not respond sufficiently quickly to ambient pressure changes (see Section 5.4.5). An inward bulge made the chambers thinner, reducing the number of hits that were available for the helix fitting algorithm, introducing a systematic uncertainty.

A previous analysis found that a bulge of  $50 \mu\text{m}$  changed  $\Delta P_\mu^\pi \xi$  by  $(0.7 \pm 0.7) \times 10^{-4}$ [18]. Since the current analysis rejected runs if they corresponded to a bulge of more than  $35 \mu\text{m}$ , the total systematic uncertainty cannot be larger than

$$\frac{35}{50} \times 0.7 \times 10^{-4} = 0.5 \times 10^{-4}. \quad (6.21)$$

### 6.4.6 Cell asymmetry

The previous  $P_\mu^\pi \xi$  analysis used a simulation that centred the wires in  $z$  between the cathode foils. In reality, they were determined to be offset from the centre by  $150 \mu\text{m}$ , and this introduced a systematic uncertainty of  $2.2 \times 10^{-4}$ . The modern simulation includes the offset, eliminating this uncertainty.

### 6.4.7 Density variations

In the simulation the gas density inside the drift chambers is constant, but for the data it tracks the atmospheric pressure and exterior temperature, which results in drift cell space-time-relationships (STRs) that vary over the set. The previous analysis used the same STRs for all the data, and a systematic uncertainty of  $(0.2 \pm 0.2) \times 10^{-4}$  was established based on the RMS variation in density[18], and  $(1.7 \pm 1.0) \times 10^{-4}$  based on the largest variation in density[57]. For the current analysis, each run was analysed with STRs that were corrected for the atmospheric pressure and temperature, meaning the systematic uncertainty is much smaller than  $0.2 \times 10^{-4}$ . Therefore the change in STRs due to gas density is a negligible effect, and is not evaluated here.

## 6.5 Detector alignment

An analysis in 2008 determined the  $P_\mu^\pi \xi$  uncertainty from translational and rotational drift chamber alignment as  $0.7 \times 10^{-4}$ [18]. This is adopted here as the  $P_\mu^\pi \xi$  uncertainty since the alignment procedures are just as accurate for the current analysis. A summary of this uncertainty will now be given.

Two systematic misalignments of the drift chambers were considered: a “shear”, where each detector plane is offset in  $u$  or  $v$  from the previous one by a constant amount, and a “corkscrew”, where each detector plane is rotated about the  $z$ -axis from the previous one by a constant angle. Stringent limitations from the detector design meant these systematic uncertainties had negligible values of  $0.009 \times 10^{-4}$  and  $0.020 \times 10^{-4}$  for the shear and corkscrew, respectively. Random misalignments were not considered, since these smear the tracking residuals and degrade the resolution, which is handled as an orthogonal systematic uncertainty in Section 6.7.

The length ( $z$ ) and width ( $u, v$ ) scales are used to determine the momentum components of the reconstructed helices. The systematic uncertainties from these scales are re-evaluated for the current measurement. The  $z$  length scale is known to  $50 \mu\text{m}$  out of  $100 \text{cm}$ , which

is a fractional uncertainty of  $5.0 \times 10^{-5}$ . A special analysis made a fractional change of  $1 \times 10^{-3}$  to the  $z$ -component of the momentum, which is a factor of 20 larger than the true uncertainty. The change in  $P_\mu^\pi \xi$  is  $(2.5 \pm 7.2) \times 10^{-4}$ , which leads to a systematic uncertainty of  $(1/20) \times 2.5 \times 10^{-4} = 0.1 \times 10^{-4}$ .

For the width scale, the wires were positioned in a plane to better than  $5 \mu\text{m}$ ; a wire plane is 32 cm in width, corresponding to a fractional uncertainty of  $2 \times 10^{-5}$ . The sensitivity of  $P_\mu^\pi \xi$  was determined in a similar way to the length scale: a special analysis made a fractional change of  $1 \times 10^{-3}$  in both the  $u$ - and  $v$ -components of the momentum, finding that  $P_\mu^\pi \xi$  changes by  $(2.5 \pm 7.2) \times 10^{-4}$ . This time the systematic uncertainty is scaled down to  $(2 \times 10^{-5}) / (1 \times 10^{-3}) \times 2.5 \times 10^{-4} = 0.05 \times 10^{-4}$ .

### 6.5.1 Magnetic field to axis

This section addresses systematic uncertainties from the alignment of the magnetic field for the decay positron reconstruction, which are distinct from the uncertainties associated with determining the decay polarisation of the muons.

The magnetic field is rotationally aligned to the drift chambers to better than 0.03 mrad within the drift chamber tracking region; specifically, this is the angle between the symmetry axis of the magnetic field and the detector's  $z$ -axis, not the azimuth (see Section 2.13). This level of uncertainty was previously found to change  $P_\mu^\pi \xi$  by just  $0.3 \times 10^{-4}$ [57]; this negligible value is adopted for the current analysis.

A translation uncertainty in the magnetic field of 0.2 cm in  $x$  and  $y$  was described earlier. A special analysis used a field displaced by 2 cm in both  $x$  and  $y$ , and the change in  $P_\mu^\pi \xi$  was  $(1.1 \pm 7.4) \times 10^{-4}$ . After scaling down by a factor of ten, this contributes a systematic uncertainty of just  $0.1 \times 10^{-4}$ .

## 6.6 Positron interactions

### 6.6.1 $\delta$ -electron and Bremsstrahlung rates

Uncertainties from the simulation's continuous energy loss model are part of the energy calibration uncertainties in Section 6.8.2. The current section describes uncertainties from discrete processes; the most important of these are  $\delta$ -electron production (where an electron is knocked out of an atomic orbital) and Bremsstrahlung ("braking radiation", where one or more photons, radiated using deceleration, can subsequently undergo pair production). The simulation must accurately reproduce these processes since the extra tracks interfere

with the reconstruction. Approximations in the **GEANT3** physics and uncertainties in material thicknesses will cause the simulation's rates to differ from data.

The  $\delta$ -electron rate is compared in data and simulation by selecting events where the decay positron trajectory is broken in two, with an additional electron track originating from the point where the track is broken. The momentum of the electron track is well correlated with the momentum difference between the two broken track halves, indicating that genuine  $\delta$ -electrons are being measured (see Fig. 6.15). A special simulation with the  $\delta$ -electrons disabled confirmed that the background of the measurement is small.

The momentum distributions of the reconstructed electrons are compared for nominal data and simulation on the left of Fig. 6.16, where the reconstruction inefficiency is seen to decrease below 6 MeV/c. Using the range ( $6 < p_\delta < 16$ ) MeV/c and all the available data sets, the ratio of  $\delta$ -electrons in data and simulation is  $1.007 \pm 0.009$  (*i.e.* the data has more  $\delta$ -electrons than the simulation).

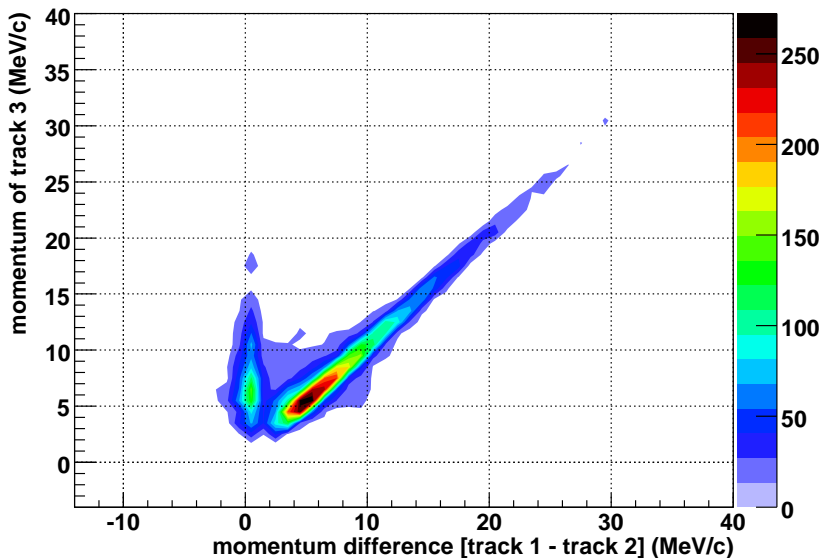


Figure 6.15: Validation of the  $\delta$ -electron measurement method. Events are selected with a decay positron track that is broken in half, becoming tracks 1 and 2, with an additional negative particle originating from the break point (track 3). The observed correlation indicates that  $\delta$ -electrons are being measured.

A special simulation increased the  $\delta$ -electron probability by a factor of three, changing  $P_\mu^\pi \xi$  by  $(25 \pm 7) \times 10^{-4}$ . For this simulation, the reconstructed  $\delta$ -electrons are compared for the nominal and special simulation on the right of Fig. 6.16, where the ratio of counts is

$2.80 \pm 0.04$ . The systematic uncertainty is then

$$\frac{1.007 - 1.0}{2.80 - 1.0} \times 25 \times 10^{-4} = 0.1 \times 10^{-4}. \quad (6.22)$$

The Bremsstrahlung rate is compared in data and simulation using a similar approach to the  $\delta$ -electrons: events are selected with a “broken” decay positron trajectory, and the momentum difference between the two halves of the track is shown on the left side of Fig. 6.17. A special simulation increased the Bremsstrahlung probability by a factor of three, and changed  $P_{\mu}^{\pi} \xi$  by  $(55 \pm 7) \times 10^{-4}$ ; the effect on the broken track momentum difference is shown on the right side of Fig. 6.17. Using the momentum range of  $(15 < p < 35)$  MeV/c, the ratio of Bremsstrahlung events in data and simulation averaged over all sets is  $1.024 \pm 0.004$ . The ratio between the nominal and increased Brem rate simulations is  $2.82 \pm 0.02$ . The systematic uncertainty is therefore

$$\frac{1.024 - 1.0}{2.82 - 1.0} \times 55 \times 10^{-4} = 0.7 \times 10^{-4}. \quad (6.23)$$

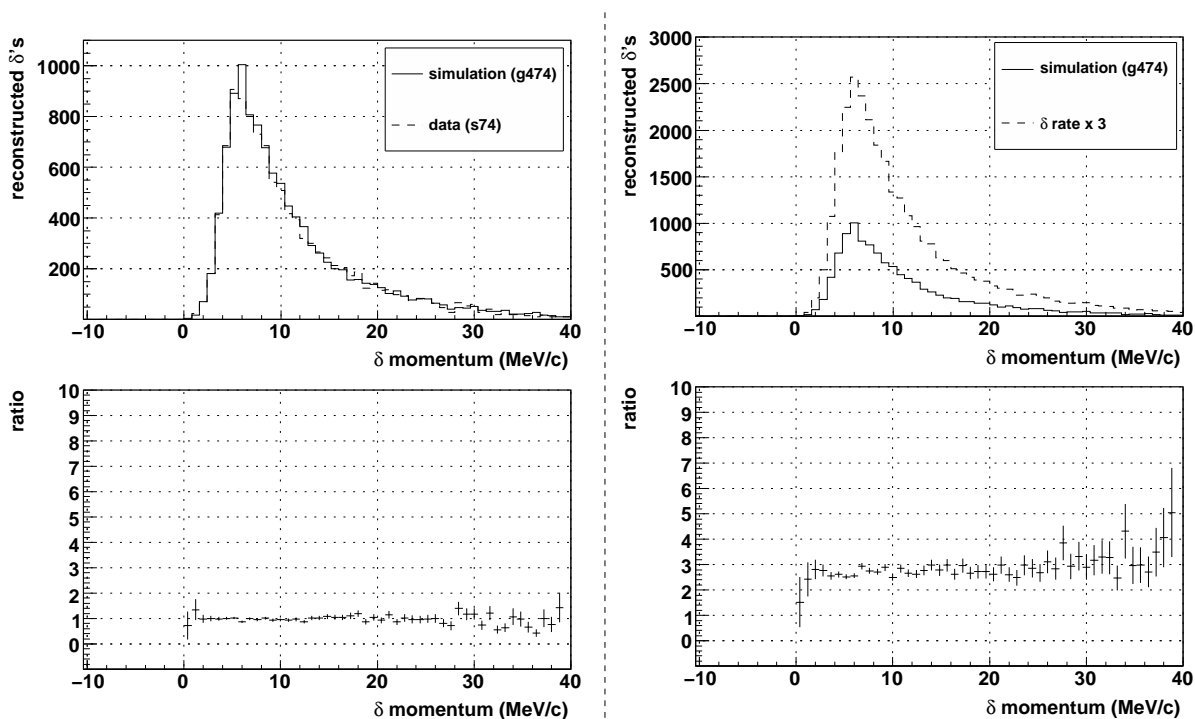


Figure 6.16: The left hand side compares the distribution of reconstructed  $\delta$ -electrons in data and simulation. The right hand side shows the simulation where the  $\delta$  production rate was increased by a factor of three.

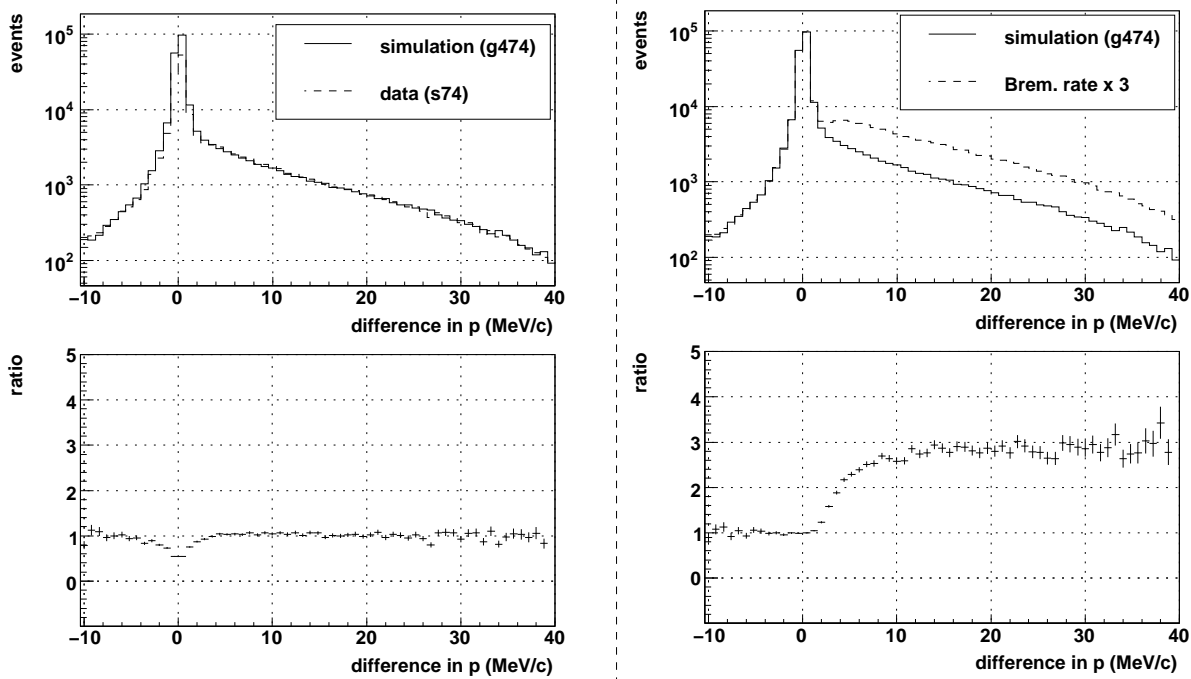


Figure 6.17: The left hand side compares the energy difference for the two halves of a broken track, for data and simulation. The right hand side shows the same distribution for a simulation where the Bremsstrahlung rate was increased by a factor of three.

### 6.6.2 Outside material

In the upstream half of the detector the positrons could be backscattered from the beam pipe and the upstream beam package (see Section 2.9 for a description). The door of the steel yoke was also a source of backscatters, but most of the yoke was shielded by the upstream beam package. In the downstream half of the detector, during nominal operation there was no corresponding downstream beam package, so positrons could only be backscattered from the steel yoke. The backscatters cause extra hits that interfere with the reconstruction of decay positrons. The simulation includes the beam pipe and most of the upstream beam package (excluding, for example, the light guides) but does not include the steel of the yoke since the additional showering significantly increases the computation time. The simulation's lack of the yoke, and imperfections in placement and/or thickness of materials is expected to introduce a systematic uncertainty.

The degree to which backscatters match in data and simulation can be compared by selecting the time window containing the decay positron, and then finding the difference in average times between the PCs at the far upstream and downstream ends of the detector.

A backscatter will cause extra hits in either the upstream or downstream PCs, resulting in an additional peak in the time distribution. The upper and middle plots in Fig. 6.18 show this time distribution for the windows where the decay positron is upstream and downstream respectively. The simulation shows evidence of a surplus in backscattered upstream decay positrons, and a deficit in backscattered downstream decay positrons that is consistent with the steel yoke being disabled.

The effect on  $P_\mu^\pi \xi$  can be estimated using two simulations, with and without the *downstream* beam package in place. This exaggerates the number of downstream decay positrons that are backscattered. The difference in  $P_\mu^\pi \xi$  between these simulations is  $(3.2 \pm 4.0) \times 10^{-4}$ , and the two time distributions are shown in the bottom of Fig. 6.18. The change in  $P_\mu^\pi \xi$  is then scaled down according to the ratio of differences in counts; specifically, the difference between data and simulation is divided by the difference between the simulations with and without the downstream beam package. After averaging over all sets, this results in scale factors of 7 and 14 for the upstream and downstream backscatters respectively. When added together quadratically, the systematic uncertainty is then  $0.5 \times 10^{-4}$ .

### 6.6.3 Multiple scattering

The helix reconstruction software in the previous  $P_\mu^\pi \xi$  analysis did not permit multiple scattering through the positron trajectory. As a consequence, a systematic uncertainty was assigned. The modern analysis allows for a change in track angle at each pair of planes in the “sparse stack”, and for one change of angle in the “dense stack” (see Section 2.8 for definitions of these terms and an explanation of the fit penalty). As a result of this improvement, there is no longer a systematic uncertainty due to multiple scattering of positrons.

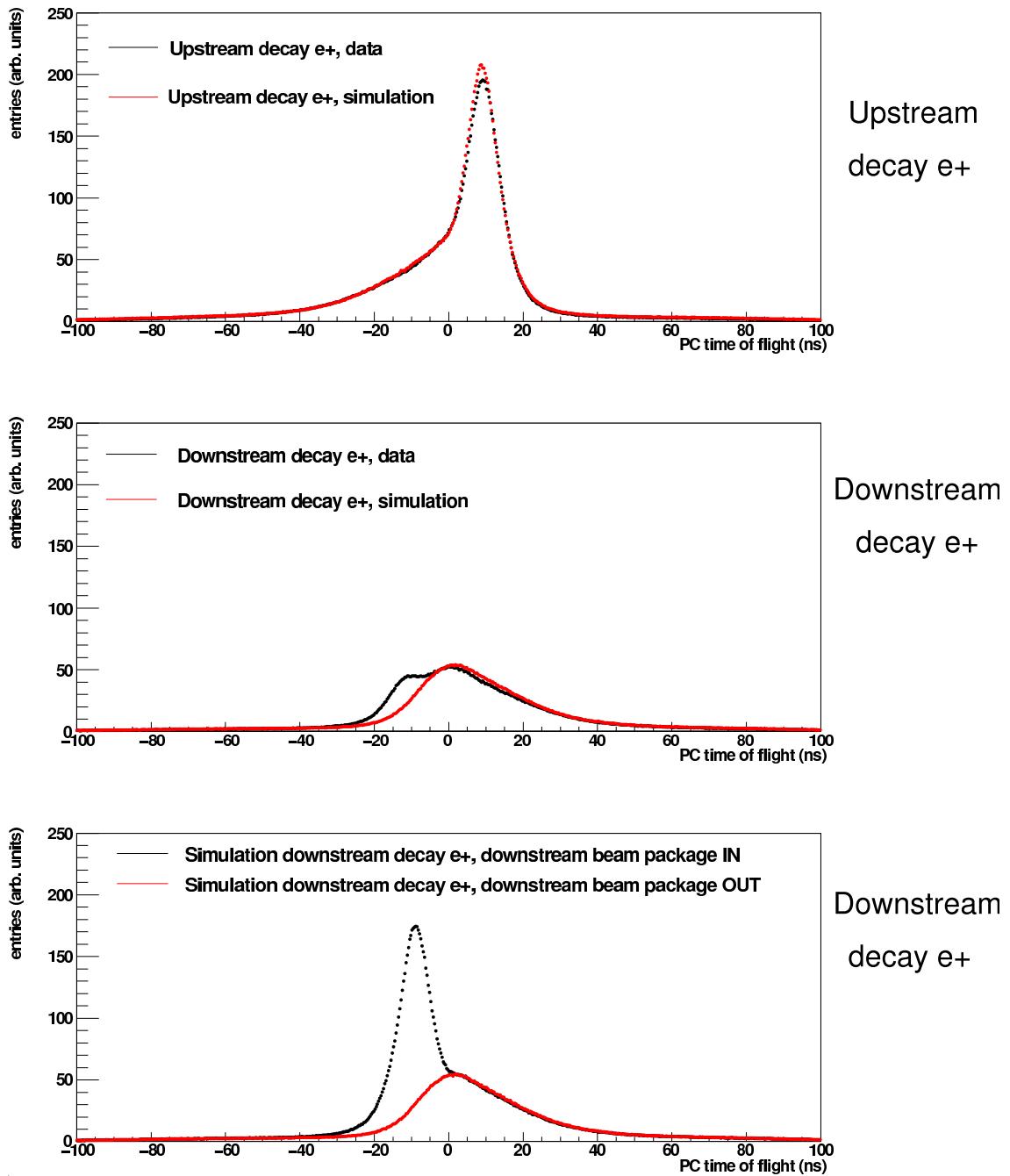


Figure 6.18: The distributions are the difference between the average upstream and downstream PC times. The backscatters from upstream and downstream decay positrons are compared for data and simulation in the upper and middle distributions. The effect of including a downstream beam package in the simulation is shown at the bottom.

## 6.7 Resolution

The momentum ( $p$ ) and angle ( $\cos\theta$ ) reconstruction resolutions differ in data and simulation. This discrepancy is relatively unimportant over the kinematic fiducial since the decay spectrum is smooth. However, the analysis uses the sharp kinematic endpoint to energy calibrate the spectrum, and a difference in resolution at this endpoint will introduce a systematic uncertainty.

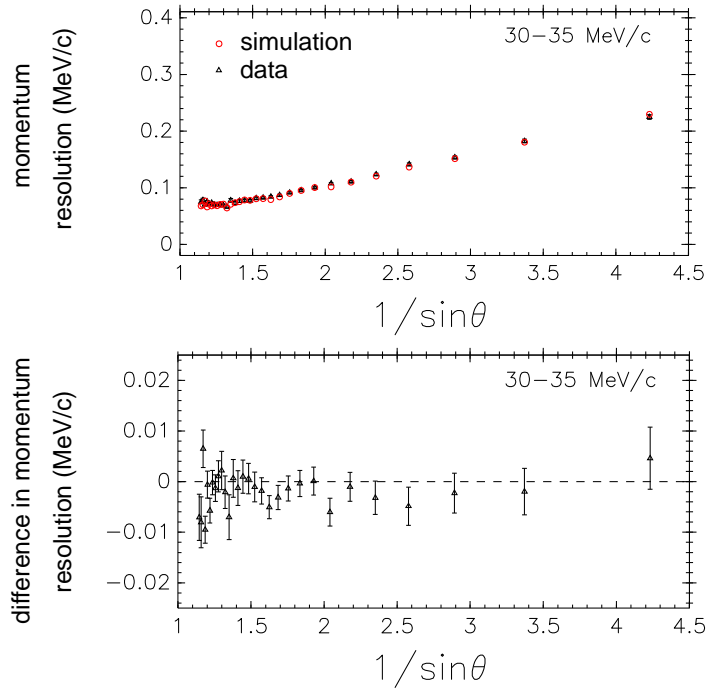
The resolution is measured using the special “upstream stops” data, where muons are stopped at the entrance of the detector, and the decay positron is reconstructed independently in each half of the spectrometer. The reconstructed  $p$  and  $\theta$  will differ in each half due to energy loss and multiple scattering through the target module. The distribution of the momentum/angle differences is dominated by a Gaussian resolution function, so that the difference in  $\sigma$  widths between data and simulation is a measure of how well the simulation reproduces the detector’s resolution. (This difference is also sensitive to discrepancies in target thickness and the simulation’s positron interactions physics, but here we conservatively blame the full difference on resolution).

The Gaussian widths are shown for a limited  $p$  range in Fig. 6.19. The absolute resolution is seen to depend on  $1/\sin\theta$ , but the *difference* between data and simulation is well approximated by a constant for both the momentum and angle resolution. A previous analysis found this difference in resolution had a non-trivial dependence on  $p$  and  $\cos\theta$ ; the current analysis is improved due to the use of better drift cell space-time-relationships, as described in Section 3.2.7.

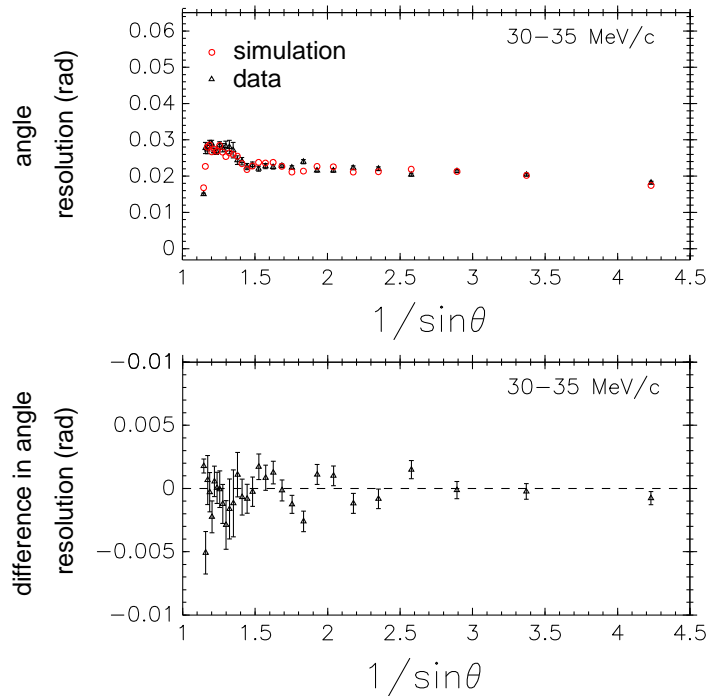
For each point in  $(p, \cos\theta)$ , the difference in  $p$  and  $\theta$  resolution between data and simulation is constructed according to

$$\Delta\sigma = \begin{cases} \sqrt{\sigma_{\text{data}}^2 - \sigma_{\text{sim}}^2} & \sigma_{\text{data}} > \sigma_{\text{sim}} \\ -\sqrt{\sigma_{\text{sim}}^2 - \sigma_{\text{data}}^2} & \sigma_{\text{sim}} > \sigma_{\text{data}} \end{cases} \quad (6.24)$$

The weighted average of this quantity over all  $(p, \cos\theta)$  is shown in Table 6.12. The systematic uncertainty is measured by exaggerating the largest differences from the table by a factor of five; specifically an additional smearing of 58 keV/c in momentum and 6 mrad in angle was added to the data. The momentum and angle resolutions were exaggerated simultaneously. This changed  $P_{\mu}^{\pi} \xi$  by  $(6.5 \pm 3.4) \times 10^{-4}$ , resulting in a systematic uncertainty of  $(6.5/5) \times 10^{-4} = 1.3 \times 10^{-4}$ .



(a) Momentum resolution.



(b) Angle resolution.

Figure 6.19: Resolution in data and simulation, derived from a special “upstream stops” analysis: muons stop at the entrance of the detector, and are reconstructed independently in each half of the spectrometer; the resolution is the width of the energy loss and angle change distributions.

Table 6.12: Difference in resolution between data and simulation, as defined in the text.

Target	Difference in $\sigma$ , defined by Eq. (6.24)	
	Momentum (keV/c)	Angle (mrad)
Aluminium	-6.3	-0.07
Silver	-11.5	1.1

## 6.8 Momentum calibration

### 6.8.1 Magnetic field shape

The simulation was self-consistent since it used the same OPERA field map for generating and reconstructing the positrons. The data reconstructed the positrons with the OPERA field map, but this had known discrepancies with the mapper measurements within the tracking region, which introduced a systematic uncertainty.

The difference in field shape between OPERA and the mapper measurements is well approximated by

$$\delta B_z = C_2 z^2 + C_3 z^3 + C_r r, \quad (6.25)$$

where the optimum  $C_2$ ,  $C_3$  and  $C_r$  values are recorded in Table 6.13. The three previous TWIST analyses have used the same coefficients for the nominal 2.0 T field. The coefficients were re-evaluated for the current measurement by weighting the mapper measurements more carefully[99].

Table 6.13: Coefficients of Eq. (6.25). These relate the OPERA magnetic field to the results from the mapper measurements.

Parameter	Nominal 2.0 T field		1.96 T	2.04 T
	Previously <sup>a</sup>	<b>This analysis</b>		
$C_2$ ( $\times 10^{-8}$ T/cm <sup>2</sup> )	-6	$-1.7 \pm 0.4$	$+11.4 \pm 0.3$	$-19.7 \pm 0.5$
$C_3$ ( $\times 10^{-10}$ T/cm <sup>3</sup> )	-4	$-7.8 \pm 0.9$	$+2.0 \pm 0.5$	$-2.2 \pm 0.7$
$C_r$ ( $\times 10^{-6}$ T/cm)	-12.5	$-8.3 \pm 0.3$	$-1.1 \pm 0.6$	$-2.8 \pm 0.9$

<sup>a</sup> The same parameters were used in Refs. [18, 57, 82, 85].

A new 2.0 T field was produced with the coefficients in Eq. (6.25) exaggerated by a factor

of 20. Maxwell's  $\nabla \cdot \delta \vec{B} = 0$  equation was satisfied by modifying the radial field components according to

$$\delta B_r = - \left( C_2 r z + \frac{3}{2} C_3 z^2 r \right). \quad (6.26)$$

A data set was then re-analysed with the exaggerated field and the change in  $P_\mu^\pi \xi$  is  $(5.1 \pm 7.8) \times 10^{-4}$ . After scaling down by a factor of 20, the systematic uncertainty for the nominal sets is  $0.3 \times 10^{-4}$ . Previous evaluations of this uncertainty used a smaller scale factor of ten, and did not apply Eq. (6.26), but still found an effect below  $1 \times 10^{-4}$  [18, 57].

The 1.96 T and 2.04 T data sets were analysed with a magnetic field map that was already corrected using Eq. (6.25). The difference between the measured maps and the ones used for the 1.96 T and 2.04 T analysis is much smaller than the difference between the OPERA and corrected 2.0 T maps. Therefore the systematic uncertainty is less than  $0.3 \times 10^{-4}$  for the 1.96 T and 2.04 T sets.

## 6.8.2 Use of kinematic endpoint

*The energy calibration of the spectrum is one of the largest systematic uncertainties for the  $\rho$  and  $\delta$  measurements, and is described in more detail in Refs. [89, 100]. Only a brief description is given here since for  $P_\mu^\pi \xi$  the uncertainties from the procedure are much smaller than the polarisation uncertainties.*

The motivation for an energy calibration and its implementation were described in Section 3.5. In summary, the reconstructed momenta of the data and simulation disagree at the kinematic endpoints by about 10 keV/c, and this must be corrected by shifting or scaling the entire data spectrum. (The same central value of  $P_\mu^\pi \xi$  is obtained if both spectra are corrected to the true kinematic endpoint of  $W_{e\mu} = 52.83$  MeV, instead of correcting the data relative to the simulation.) Note that the energy calibration procedure is applied to every systematic uncertainty test, which improves the robustness of the  $P_\mu^\pi \xi$  measurement. There are two uncertainties from the energy calibration: a statistical part since only a limited region of the spectrum is used to establish the required correction, and a systematic part since either a shift or scale (or combination) must be used to propagate the correction to the rest of the spectrum.

The difference in kinematic endpoints between data and simulation is shown for a nominal set (fiducial only) in Fig. 6.20. In previous analyses the upstream ( $1/\cos\theta < 1$ ) and downstream ( $1/\cos\theta > 1$ ) points have been fit separately with a straight line, yielding two slopes ( $a_{\text{up}}, a_{\text{down}}$ ) and two intercepts ( $b_{\text{up}}, b_{\text{down}}$ ), for a total of four parameters. In the current analysis the stopping distribution in data and simulation is better matched, introducing

the possibility of a fit with a single intercept and slope (two parameters). Using all available data/simulation spectra there is no preference from the reduced- $\chi^2$  for a two or four parameter fit, and the discussion of which model to use is ongoing since this choice is significant for the  $\rho$  and  $\delta$  parameters.

There are two extreme choices for how to propagate the difference in endpoint to the rest of the spectrum. In the first case the entire spectrum is *shifted* in momentum according to

$$p_{\text{corrected}} = p_{\text{reconstructed}} - \left( b - \frac{a}{|\cos \theta|} \right). \quad (6.27)$$

In the second case the spectrum is *scaled* depending on momentum so that

$$p_{\text{corrected}} = \frac{p_{\text{reconstructed}}}{1 + b/W_{e\mu}} + \frac{a}{|\cos \theta|}, \quad (6.28)$$

where  $W_{e\mu}$  is the maximum kinematic positron momentum (52.83 MeV/c). The statistical uncertainties for combinations of shift/scale and two/four parameter fits are explored in Table 6.14. Since there is no firm decision on the number of parameters, or a preference for shift over scale, the statistical uncertainty is conservatively taken as  $1.4 \times 10^{-4}$ , which is the largest entry from Table 6.14. For the systematic part, the central value of  $P_{\mu}^{\pi} \xi$  is placed half way between the shift and scale extremes, and a systematic uncertainty of  $0.5 \times 1.4 \times 10^{-4} = 0.7 \times 10^{-4}$  is assigned to cover both possibilities.

Table 6.14: Statistical and systematic uncertainties for the energy calibration, under the possible fitting scenarios that are described in the text.

Number of fit params.	$P_{\mu}^{\pi} \xi$ uncertainty ( $\times 10^{-4}$ )		
	Statistical		Systematic
	Shift model, Eq. (6.27)	Scale model, Eq. (6.28)	( $\frac{1}{2}$ difference between shift and scale)
4	0.6	1.4	0.2
2	0.5	0.3	1.4

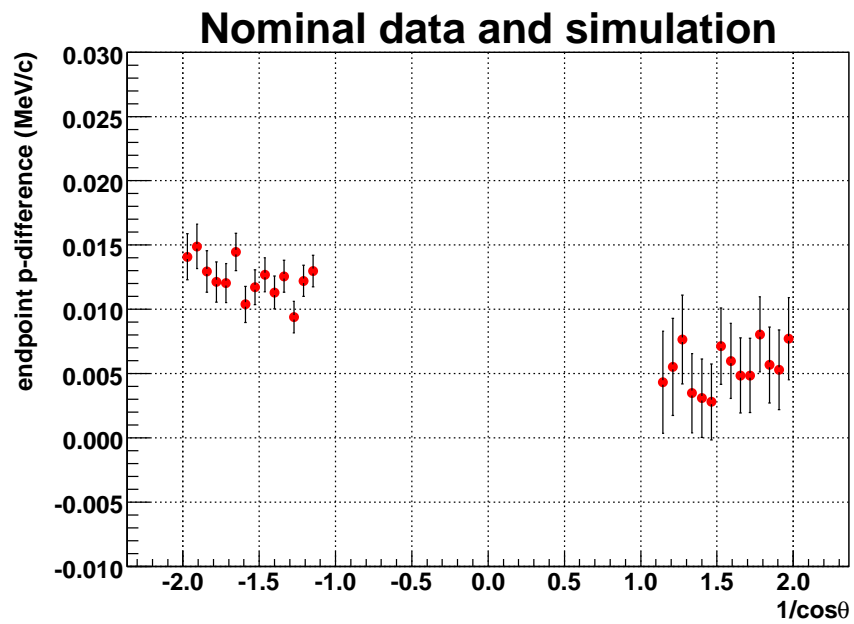


Figure 6.20: Difference between reconstructed momentum in data and simulation at the endpoint of the muon decay spectrum.

## 6.9 External

### 6.9.1 Radiative corrections

The simulation uses the following radiative corrections: full first order,  $O(\alpha^2 L^2)$  and  $O(\alpha^2 L^1)$  from the second order, and  $O(\alpha^3 L^3)$  from the third order. The term  $O(\alpha^2 L^0)$  was not used, despite becoming available in 2007 [16]; its effect on the decay parameters will now be shown as negligible.

Over the TWIST kinematic fiducial, the  $O(\alpha^2 L^0)$  term has a similar shape to the  $O(\alpha^2 L^1)$  term, and the ratio between the terms never exceeds 0.2; this is demonstrated in the paper where the  $O(\alpha^2 L^0)$  term is calculated [16]. The  $P_\mu^\pi \xi$  sensitivity to excluding the  $O(\alpha^2 L^0)$  term was estimated by adding a pure  $O(\alpha^2 L^1)$  spectrum to the nominal spectrum. This changes  $P_\mu^\pi \xi$  by  $(2.9 \pm 0.1) \times 10^{-4}$ . The ratio of counts in the nominal and combined spectrum is 1.11. Therefore the effect on  $P_\mu^\pi \xi$  of only adding 0.2 of the pure  $O(\alpha^2 L^1)$  spectrum is

$$(0.2/1.11) \times 2.9 \times 10^{-4} = 0.5 \times 10^{-4}, \quad (6.29)$$

which is used as the systematic uncertainty.

### 6.9.2 $\eta$ correlation

The muon decay spectrum does not allow a precise measurement of the parameter  $\eta$ . Therefore  $\eta$  was fixed to its world average value<sup>45</sup> of  $(-36 \pm 69) \times 10^{-4}$  [7], and the correlation between  $\eta$  and  $P_\mu^\pi \xi$  is assessed here as a systematic uncertainty. The correlation was found to be  $d\xi/d\eta = 0.01528$ , so that  $\Delta\eta = \pm 69 \times 10^{-4}$  corresponds to a  $P_\mu^\pi \xi$  systematic uncertainty of  $1.1 \times 10^{-4}$ .

---

<sup>45</sup>The evaluation of  $\eta$  in Ref. [7] uses a global analysis that includes the TWIST experiment's result for  $\rho$  and  $\delta$  from the 2002 datasets. The evaluation does *not* use the TWIST experiment's more recent  $\rho$ ,  $\delta$  and  $P_\mu^\pi \xi$  measurements from the 2004 datasets.

# Chapter 7

## Results

### 7.1 Blinded results

The results for  $\Delta P_\mu^\pi \xi$ , the difference between  $P_\mu^\pi \xi$  in data and a hidden simulation value, are shown in Table 7.1 and Fig. 7.1. The weighted average for all sets is  $+(77.4 \pm 2.0) \times 10^{-4}$  with a confidence level of 46%. Sets 72, 76 and 86 are excluded since they have significantly larger polarisation systematic uncertainties.

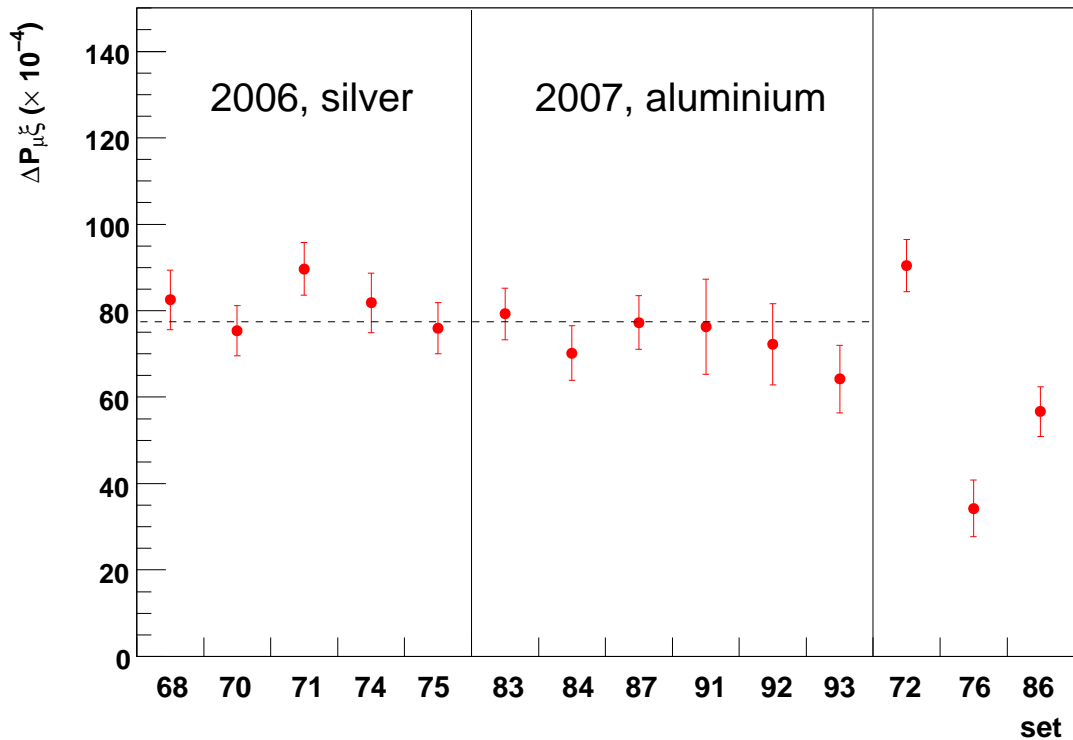


Figure 7.1: Consistency of  $\Delta P_\mu^\pi \xi$ , the difference in  $P_\mu^\pi \xi$  between the data and a hidden value in the simulation. The uncertainties are statistical. The weighted average is  $(77.4 \pm 2.0) \times 10^{-4}$ . Sets 72, 76 and 86 are not included in the  $\Delta P_\mu^\pi \xi$  result due to their significantly larger  $P_\mu$  systematic uncertainty.

Table 7.1: Difference between the data and a hidden simulation value of  $P_\mu^\pi \xi$ . The results have been averaged over the two energy calibration strategies in Section 6.8.2. The statistical spectrum fit uncertainties are shown. There are 2439 degrees of freedom. Sets 72, 76 and 86 are *not* used in the  $P_\mu^\pi \xi$  result. The corrections are from production target scattering and the time dependent relaxation rate, as described in Section 6.2.

Set	Target	Description	$\Delta P_\mu^\pi \xi (\times 10^{-4})$		$\chi^2$	Confidence
			Uncorrected	Corrected		
68	Ag	Stopping distrib. peaked $\frac{1}{3}$ into target	78.3	$82.5 \pm 6.9$	2376	81.5
70	Ag	B = 1.96 T	71.2	$75.4 \pm 5.8$	2426	57.2
71	Ag	B = 2.04 T	85.5	$89.7 \pm 6.1$	2389	76.0
74	Ag	Nominal A	77.6	$81.8 \pm 6.9$	2424	58.6
75	Ag	Nominal B	71.7	$75.9 \pm 5.9$	2494	21.6
83	Al	Downstream beam package in place	73.9	$79.3 \pm 6.0$	2376	81.5
84	Al	Nominal C	64.8	$70.2 \pm 6.3$	2537	8.2
87	Al	Nominal D	71.9	$77.3 \pm 6.2$	2442	48.1
91	Al	Lower momentum I	65.9	$76.3 \pm 11.0$	2549	6.0
92	Al	Lower momentum II	62.5	$72.2 \pm 9.4$	2475	29.9
93	Al	Lower momentum III	54.5	$64.2 \pm 7.8$	2439	49.6
72	Ag	TECs-in, nominal beam	86.3	$90.5 \pm 6.0$	2517	13.2
76	Ag	Steered beam A	30.1	$34.3 \pm 6.5$	2415	63.4
86	Al	Steered beam B	51.3	$56.7 \pm 5.7$	2419	60.9

# Bibliography

- [1] S. Weinberg. A Model of Leptons. *Phys. Rev. Lett.*, 19(21):1264–1266, Nov 1967.
- [2] Donald Hill Perkins. *Introduction to High-Energy Physics; 4th ed.* Cambridge Univ. Press, Cambridge, 2000.
- [3] C. Amsler *et al.* Review of Particle Physics. *Phys. Lett. B*, 667(1-5):1–6, 2008. Review of Particle Physics.
- [4] D. Griffiths. *Introduction to Elementary Particles.* Wiley, 1987.
- [5] M. Goldhaber, L. Grodzins, and A. W. Sunyar. Helicity of Neutrinos. *Phys. Rev.*, 109:1015 – 1017, 1958.
- [6] D. Binosi and L. Theu $\beta$ l. JaxoDraw: A graphical user interface for drawing Feynman diagrams. *Comput. Phys. Commun.*, 161:76–86, August 2004.
- [7] C.A. Gagliardi, R.E. Tribble and N.J. Williams. Global analysis of muon decay measurements. *Phys. Rev. D*, 72(7):073002, Oct 2005.
- [8] W. Fetscher, H.-J. Gerber and K.F. Johnson. Muon decay: complete determination of the interaction and comparison with the standard model. *Phys. Lett. B*, 173(1):102–106, 1986.
- [9] S. Eidelman *et al.* Review of Particle Physics. *Phys. Lett. B*, 592(1-4):1–5, 2004. Review of Particle Physics.
- [10] R.P. MacDonald *et al.* Precision measurement of the muon decay parameters  $\rho$  and  $\delta$ . *Phys. Rev. D*, 78(3):032010, 2008.
- [11] A. Sirlin, New York University, USA. Private communication.
- [12] A. B. Arbuzov. First-order radiative corrections to polarized muon decay spectrum. *Phys. Lett. B*, 524(1-2):99 – 106, 2002.

- [13] A. Arbuzov, A. Czarnecki and A. Gaponenko. Muon decay spectrum: Leading logarithmic approximation. *Phys. Rev. D*, 65:113006, 2002.
- [14] A. Arbuzov and K. Melnikov.  $\mathcal{O}(\alpha^2 \ln(m_\mu/m_e))$  corrections to electron energy spectrum in muon decay. *Phys. Rev. D*, 66:093003, 2002.
- [15] A. Arbuzov. Higher order QED corrections to muon decay spectrum. *J. High Energy Phys.*, 2003(03):063–063, 2003.
- [16] K. Melnikov C. Anastasiou and F. Petriello. The electron energy spectrum in muon decay through  $\mathcal{O}(\alpha^2)$ . *J. High Energy Phys.*, (09):014, 2007.
- [17] N. Danneberg *et al.* Muon Decay: Measurement of the Transverse Polarization of the Decay Positrons and its Implications for the Fermi Coupling Constant and Time Reversal Invariance. *Phys. Rev. Lett.*, 94:021802, 2005.
- [18] R.P. MacDonald. *A Precision Measurement of the Muon Decay Parameters  $\rho$  and  $\delta$* . PhD thesis, University of Alberta, 2008.
- [19] P. Herczeg. On muon decay in left-right-symmetric electroweak models. *Phys. Rev. D*, 34(11):3449–3456, Dec 1986.
- [20] V.M. Abazon *et al.* Search for  $W'$  Bosons Decaying to an Electron and a Neutrino with the D0 Detector. *Phys. Rev. Lett.*, 100:031804, 2008.
- [21] B. Jamieson *et al.* Measurement of  $P_\mu \xi$  in polarized muon decay. *Phys. Rev. D*, 74(7):072007, 2006.
- [22] J.D. Jackson. *Classical Electrodynamics*. John Wiley & Sons, 1999.
- [23] V. Bargmann, L. Michel and V.L. Telegdi. Precession of the Polarization of Particles Moving in a Homogeneous Electromagnetic Field. *Phys. Rev. Lett.*, 2:435–436, 1959.
- [24] A. Balakin, V. Kurbanova and W. Zimdahl. Precession of a particle with anomalous magnetic moment in electromagnetic and gravitational pp-wave fields. *Gravity Cosmology Supplement*, 82:6–9, 2002.
- [25] P. Depommier. The BMT equation. Presentation to TWIST collaboration, May 2006.
- [26] P. Depommier. Muon depolarization in multiple scattering (TN100). Technical report, TWIST collaboration, TRIUMF, 2005.

- [27] W.H. Koppenol. Names for muonium and hydrogen atoms and their ions(IUPAC Recommendations 2001). *Pure Appl. Chem.*, 73:377–379, 2001.
- [28] M. Senba. Muon spin depolarization in noble gases during slowing down in a longitudinal magnetic field. *J. Phys. B: At. Mol. Opt. Phys.*, 31:5233–5260, 1998.
- [29] A. Jodidio *et al.* Search for right-handed currents in muon decay. *Phys. Rev. D*, 34(7), 1986.
- [30] A. Jodidio *et al.* Erratum: Search for right-handed currents in muon decay. *Phys. Rev. D*, 37(1), 1988.
- [31] J. H. Brewer. Muon spin rotation/relaxation/resonance. In *Encyclopedia of Applied Physics 11*, pages 23–53. 1994.
- [32] S.F.J. Cox. Implanted muon studies in condensed matter science. *J. Phys. C: Solid State Phys*, 20:3187–3319, 1987.
- [33] O. Hartmann *et al.* Diffusion of positive muons in some cubic metals. *Phys. Lett. A*, 61(2):141 – 142, 1977.
- [34] J. Brewer, University of British Columbia, Canada. Private communication.
- [35] W.B. Gauster *et al.* Measurement of the depolarization rate of positive muons in copper and aluminum. *Solid State Commun.*, 24(9):619–622, 1977.
- [36] W. Schilling. The physics of radiation damage in metals. *Hyperfine Interact.*, 4:636–644, 1978.
- [37] D.K. Brice. Lattice atom displacements produced near the end of implanted  $\mu^+$  tracks. *Phys. Lett. A*, 66:53–56, 1978.
- [38] P. Dalmas de Réotier and A. Yaouanc. Muon spin rotation and relaxation in magnetic materials. *J.Phys: Condens. Matter*, 9:9113–9166, 1997.
- [39] P. Dalmas de Réotier and A. Yaouanc. Quantum calculation of the muon depolarization function: effect of spin dynamics in nuclear dipole systems. *J.Phys: Condens. Matter*, 4:4533–4556, 1992.
- [40] A. Abragam. *Principles of Nuclear Magnetism*. International series of monographs on physics. Oxford University Press, 1986.

- [41] R.S. Hayano *et al.* Zero- and low-field spin relaxation studied by positive muons. *Phys. Rev. B*, 20:850, 1979.
- [42] W.J. Kossler *et al.* Diffusion and Trapping of Positive Muons in Al:Cu Alloys and in Deformed Al. *Phys. Rev. Lett.*, 41:1558–1561, 1978.
- [43] O. Hartmann *et al.* Coherent Propagation and Strain-Induced Localization of Muons in Al. *Phys. Rev. Lett.*, 41:1055–1058, 1978.
- [44] K.W. Kehr *et al.* Muon diffusion and trapping in aluminum and dilute aluminum alloys: Experiments and comparison with small-polaron theory. *Phys. Rev. B*, 26:567–589, 1982.
- [45] K.W. Kehr. Empirical information on quantum diffusion. *Hyperfine Interact.*, 17-19:63–74, 1984.
- [46] O. Hartmann. Diffusion and trapping of muons in aluminum: New experiments and comparison with Kondo theory. *Phys. Rev. B*, 37:4425–4440, 1988.
- [47] O. Hartmann. New results on diffusion in fcc metals. *Hyperfine Interact.*, 64:641–648, 1990.
- [48] O. Hartmann *et al.* Studies of  $\mu^+$  Localization in Cu, Al, and Al alloys in the Temperature Interval 0.03 – 100 K. *Phys. Rev. Lett.*, 44:337–340, 1980.
- [49] D.P. Stoker *et al.* Search for Right-Handed Currents by Means of Muon Spin Rotation. *Phys. Rev. Lett.*, 54:1887–1890, 1985.
- [50] D.P. Stoker, University of California, Irvine, USA. Private communication.
- [51] J. Korrynga. Nuclear magnetic relaxation and resonance (sic.) line shift in metals. *Physica*, 7-8:601–610, 1950.
- [52] S.J. Blundell and S.F.J. Cox. Longitudinal muon spin relaxation in metals and semimetals and the Korringa law. *J. Phys.: Condens. Matter*, 13:2163–2168, 2001.
- [53] J.H. Brewer *et al.* *Positive muons and muonium in matter*. Muon Physics. Academic Press Inc (London) Limited, 1975.
- [54] S.F.J. Cox *et al.* Muon Korringa relaxation. *Physica B*, 289-290:594–597, 2000.

- [55] R.H. Heffner. Muon spin depolarization in nonmagnetic metals doped with paramagnetic impurities. *Hyperfine Interact.*, 8:655–662, 1981.
- [56] J.A. Brown *et al.* Muon Depolarization by Paramagnetic Impurities in Nonmagnetic Metals. *Phys. Rev. Lett.*, 47:261–264, 1981.
- [57] B. Jamieson. *Measurement of the muon decay asymmetry parameter with the TWIST spectrometer.* PhD thesis, University of British Columbia, 2006.
- [58] T.D. Lee and C.N. Yang. Question of Parity Conservation in Weak Interactions. *Phys. Rev.*, 104(1):254–258, Oct 1956.
- [59] ARGUS collaboration. Determination of the Michel Parameters  $\rho$ ,  $\xi$ , and  $\delta$  in  $\tau$ -Lepton Decays with  $\tau \rightarrow \rho\nu$  Tags. *Phys. Lett. B*, 431:179–187, 1998.
- [60] L3 Collaboration. Measurement of the Michel parameters and the average tau-neutrino helicity from tau decays at LEP. *Phys. Lett. B*, 438:405–416, 1998.
- [61] R. Bartoldus. Measurements of the Michel Parameters in Leptonic Tau Decays using the OPAL Detector at LEP. *Nucl. Phys. B (Proc. Suppl.)*, 76:147–157, 1999.
- [62] R.L. Garwin, L.M. Lederman and M. Weinrich. Observations of the Failure of Conservation of Parity and Charge Conjugation in Meson Decays: the Magnetic Moment of the Free Muon. *Phys. Rev.*, 105:1415, January 1957.
- [63] G. R. Lynch, J. Orear, and S. Rosendorff. Muon decay in nuclear emulsion at 25 000 gauss. *Phys. Rev.*, 120(6):2277, Dec 1960.
- [64] M. Bardon, D. Berley, and L. M. Lederman. Asymmetry parameter in muon decay. *Phys. Rev. Lett.*, 2(2):56–57, Jan 1959.
- [65] Richard J. Plano. Momentum and asymmetry spectrum of  $\mu$ -meson decay. *Phys. Rev.*, 119(4):1400–1408, Aug 1960.
- [66] Akhmanov *et al.* *Sov. J. Nucl. Phys.*, 6:230, 1968.
- [67] I. Beltrami *et al.* Muon decay: Measurement of the integral asymmetry parameter. *Phys. Lett. B*, 194(2):326–330, 1987.
- [68] Ali-Zade *et al.* *Soviet Phys.-JETP*, 36 (9):940, 1959.

- 
- [69] R.S. Hayano *et al.* Search for Right-Handed Currents in the Decay  $K^+ \rightarrow \mu^+ \nu$ . *Phys. Rev. Lett.*, 52(5):329–332, Jan 1984.
- [70] J. Imazato *et al.* Search for right-handed currents in the decay chain  $K^+ \rightarrow \mu^+ \nu$ ,  $\mu^+ \rightarrow e + \nu \bar{\nu}$ . *Phys. Rev. Lett.*, 69(6):877–880, Aug 1992.
- [71] T. Yamanaka *et al.* Search for right-handed currents in the decay  $K^+ \rightarrow \mu^+ \nu$ . *Phys. Rev. D*, 34(1):85–96, Jul 1986.
- [72] C.A. Coombes *et al.* Polarization of  $\mu^+$  Mesons from the Decay of  $K^+$  Mesons. *Phys. Rev.*, 108(5):1348–1351, Dec 1957.
- [73] D. Cutts, T. Elioff, and R. Stiening. Muon Polarization and Energy Spectrum in  $K^+ \rightarrow \pi^0 + \mu^+ + \nu$ . *Phys. Rev.*, 138(4B):B969–B979, May 1965.
- [74] D. Cutts, R. Stiening, C. Wiegand, and M. Deutsch. Measurement of the Muon Polarization Vector in  $K^+ \rightarrow \pi^0 + \mu^+ + \nu$ . *Phys. Rev.*, 184(5):1380–1392, Aug 1969.
- [75] R.S. Henderson *et al.* Precision planar drift chambers and cradle for the TWIST muon decay spectrometer. *Nucl. Instrum. Methods Phys. Res., Sect. A*, 548:306–335, August 2005.
- [76] J. Hu *et al.* Time expansion chamber system for characterization of TWIST low-energy muon beams. *Nucl. Instrum. Methods Phys. Res., Sect. A*, 566:563–574, October 2006.
- [77] C.J. Oram, J.B. Warren and G.M. Marshall. Commissioning of a new low energy  $\pi - \mu$  channel at TRIUMF. *Nucl. Instrum. Methods*, 179:95–103, January 1981.
- [78] J. Doornbos. The tuning of M13 for TWIST, theory and some results. Internal TWIST bulletin boards, December 2000.
- [79] R.E. Mischke, TRIUMF, Vancouver, Canada. Private communication.
- [80] T. Prokscha *et al.* The new  $\mu$ E4 beam at PSI: A hybrid-type large acceptance channel for the generation of a high intensity surface-muon beam. *Nucl. Instrum. Methods Phys. Res., Sect. A*, 595.
- [81] J.E. Draper. Beam Steering with Quadrupole and with Rectangular Box Magnets. *Rev. Sci. Instrum.*, 37:1390, October 1966.
- [82] J. Musser. *Measurement of the Michel parameter  $\rho$  in muon decay*. PhD thesis, Texas A&M University, 2005.

- [83] Vector Fields. OPERA 3D simulation software. <http://vectorfields.com>.
- [84] G.M. Marshall, TRIUMF, Vancouver, Canada. Private communication.
- [85] A. Gaponenko. *A Precision Measurement of the Muon Decay Parameter  $\delta$* . PhD thesis, University of Alberta, 2005.
- [86] D. Wright. TN1: DME / He WC Gas Comparison. Technical report, TWIST collaboration, TRIUMF, October 1996.
- [87] LeCroy Corporation. 1877 Multihit Time-to-Digital Converter: Specification. <http://www.lecroy.com/lrs/dsheets/1877.htm>.
- [88] LeCroy Corporation. LeCroy 1877 Fastbus TDC Manual.
- [89] A. Hillairet. *Measurement of  $\delta$  (in preparation)*. PhD thesis, University of Victoria, 2009.
- [90] R. Brun and F. Rademakers. ROOT - An Object Oriented Data Analysis Framework. *Nucl. Inst. & Meth. in Phys. Res. A*, 389:81–86, 1997.
- [91] R. Brun *et al.* GEANT, version 3.2114.
- [92] F. James. Fitting tracks in wire chambers using the Chebyshev norm instead of least squares. *Nucl. Instrum. Methods Phys. Res.*, 211(1):145 – 152, 1983.
- [93] R. Veenhof. Garfield - simulation of gaseous detectors. CERN Program Library W5050.
- [94] C. Gagliardi, Texas A&M University, Texas, USA. Private communication.
- [95] P. Depommier. TN49: Muon polarisation in electromagnetic fields. Technical report, TWIST collaboration, TRIUMF, 2001.
- [96] R. Openshaw, TRIUMF, Vancouver, Canada. Private communication.
- [97] R. Armenta. TWIST Magnet: Field Map Study (TN68). Technical report, TWIST collaboration, TRIUMF, 2002.
- [98] A. Olin. T0 Wire Distortion. Internal TWIST report, July 2009.
- [99] G. Marshall. OPERA map corrections from Hall and NMR maps at 2.0 T. Internal TWIST report, April 2009.

- [100] R. Bayes. *Measurement of  $\rho$  (in preparation)*. PhD thesis, University of Victoria, 2009.
- [101] H. Yukawa. On the Interaction of Elementary Particles. *I, Proc. Phys.-Math. Soc. Jpn.*, 17:48, 1935.
- [102] C.D. Anderson and S.H. Neddermeyer. Cloud Chamber Observations of Cosmic Rays at 4300 Meters Elevation and Near Sea-Level. *Phys. Rev.*, 50:263–271, 1936.
- [103] S.H. Neddermeyer and C.D. Anderson. Cosmic-Ray Particles of Intermediate Mass. *Phys. Rev.*, 54:88–89, 1938.
- [104] S.H. Neddermeyer and C.D. Anderson. Nature of Cosmic-Ray Particles. *Rev. Mod. Phys.*, 11:191–207, 1939.
- [105] M. Riordan. *The Hunting of the Quark*. Sage Publications, 1987.
- [106] M. Conversi, E. Pancini and O. Piccioni. On the Disintegration of Negative Mesons. *Phys. Rev.*, 71:209–210, 1947.
- [107] E. Fermi, E. Teller and V. Weisskopf. The Decay of Negative Mesotrons in Matter. *Phys. Rev.*, 71:314–315, 1947.
- [108] C.M.G. Lattes, G.P.S. Occhialini and C.F. Powell. Observations on the Tracks of Slow Mesons in Photographic Emulsions Part 1. *Nature*, 160:453–456, 1947.
- [109] C.M.G. Lattes, G.P.S. Occhialini and C.F. Powell. Observations on the Tracks of Slow Mesons in Photographic Emulsions Part 1. *Nature*, 160:486–492, 1947.
- [110] T.D. Lee. A Brief History of the Muon. *Hyperfine Interact.*, 86:439–453, 1994.
- [111] C.S. Wu and V.W. Hughes. *Muon Physics: Introduction and History*. Academic Press Inc., 1977.
- [112] R.A. Millikan. Mesotron as the Name of the New Particle. *Phys. Rev.*, 1:105, December 1938.
- [113] C.D. Anderson and S.H. Neddermeyer. Mesotron (Intermediate Particle) as a Name for the New Particles of Intermediate Mass. *Nature*, 142:878, November 1938.
- [114] H. Lyle. Anderson, Carl. Interview by Harriett Lyle. Oral History Project, California Institute of Technology. Retrieved April 2008 from the World Wide Web: [http://resolver.caltech.edu/CaltechOH:OH\\_Anderson\\_C](http://resolver.caltech.edu/CaltechOH:OH_Anderson_C), 1979.

- [115] A.H. Compton. Foreword: Symposium on Cosmic Rays. *Rev. Mod. Phys.*, 11:122, 1939.
- [116] H.J. Bhabha. The Fundamental Length Introduced by the Theory of the Mesotron (Meson). *Nature*, 143:276–277, February 1939.
- [117] J. L. Beveridge *et al.* A spin rotator for surface  $\mu^+$  beams on the new M20 muon channel at TRIUMF. *Nucl. Instrum. Methods Phys. Res., Sect. A*, 240:316–322, 1985.
- [118] Triumf CMMS. Helios superconducting solenoid. Website: <http://cmms.triumf.ca/equip/helios.html>.
- [119] G. Morris, TRIUMF, Vancouver, Canada. Private communication.
- [120] S.R. Dunsiger *et al.* Magnetic field dependence of muon spin relaxation in geometrically frustrated  $\text{Gd}_2\text{Ti}_2\text{O}_7$ . *Phys. Rev. B*, 73(172418), 2006.
- [121] F. James. MINUIT – Function Minimization and Error Analysis, CERN Program Library Entry D 506.
- [122] J.F. Ziegler. The stopping and range of ions in matter. <http://www.srim.org/>.
- [123] TRIUMF CS. TRIUMF Computing Services description of SRIM. <http://it-services.triumf.ca/scientific-computing/software/detector-engineering/srim-1>.
- [124] D.M. Garner. *Application of the muonium spin rotation technique to a study of the gas phase chemical kinetic of muonium reactions with the halogens and hydrogen halides.* PhD thesis, University of British Columbia, June 1979.
- [125] J. Doornbos, TRIUMF, Vancouver, Canada. Private communication.

# Appendix B

## History of the muon

In 1935, Yukawa postulated the existence of a new field to explain the binding between nucleons[101], with the force mediated by a heavy quantum. The electromagnetic field was already known to mediate force with its own light quantum, namely the photon. Yukawa predicted the nuclear force quantum would have unit charge, mass “ $2 \times 10^2$  times as large as the electron”, and substantial interactions with matter. The new field would be very strong, but only over a small range due to the quantum’s mass.

In 1936, Anderson and Neddermeyer published cloud chamber observations of cosmic rays[102], and noted “About one percent of the exposures ... reveal the presence of strongly ionizing particles which in most cases seem to be protons ... and usually arise from a type of nuclear disintegration not heretofore observed.” In the years following this publication, the authors and other independent experimenters published new results on these particles, with the mass “ranging from 120 to about 400 electron masses”[103], “about 240 electron-masses”[103] and eventually “in the neighbourhood of 200 electron masses”[104]. Many people believed that Yukawa’s postulated particle had been discovered.

World War II interrupted pure physics research. Shortly after the war, physicists were keen to understand the muon better, and identify whether it was really the Yukawa particle. The particle appeared to have the correct charge and mass, but Yukawa had predicted a particle that interacted strongly with matter, with “its flight halting abruptly the very moment it passed an atomic nucleus”[105]. In 1946, Conversi, Pancini and Piccioni demonstrated that positive and negative muons stopping in graphite produced a similar number of decay electrons[106], in contrast to the theoretical prediction that negative muons should produce far less decay electrons due to nuclear capture. Fermi, Teller and Weisskopf subsequently concluded “the interaction of mesotrons with nucleons according to the conventional schemes is many orders of magnitude weaker than usually assumed”[107]. The muon no longer appeared to be the Yukawa particle.

The issue was resolved when Powell’s collaboration discovered the real Yukawa particle, the pion[108, 109]. They observed “two types of mesons exist, of different mass, which we refer to as  $\pi^-$  and  $\mu^-$  mesons”[109]. The pion was short lived and therefore had been harder to detect. The discovery of the pion meant the muon was not predicted at all, leading the

theorist I.I. Rabi to allegedly exclaim "Who ordered that?" [110]. The mass of the muon is now determined as 105.7 MeV (211 electron masses), and the charged pions have mass 139.6 MeV (280 electron masses). The true carriers of the strong force are also identified as the gluons, not the pion.

The interested reader can find more detailed accounts of the muon's history in Refs. [4, 105, 110, 111].

# Appendix C

## Naming of the muon

Historically the muon has also gone by the name “mesotron” and “mu-meson”. The occurrence of the various names in abstracts of the American Physics Society journals is shown in Fig. C.1. The history of the particle’s name has involved several Nobel prize winning Physicists, and will now be summarised using first hand evidence wherever possible.

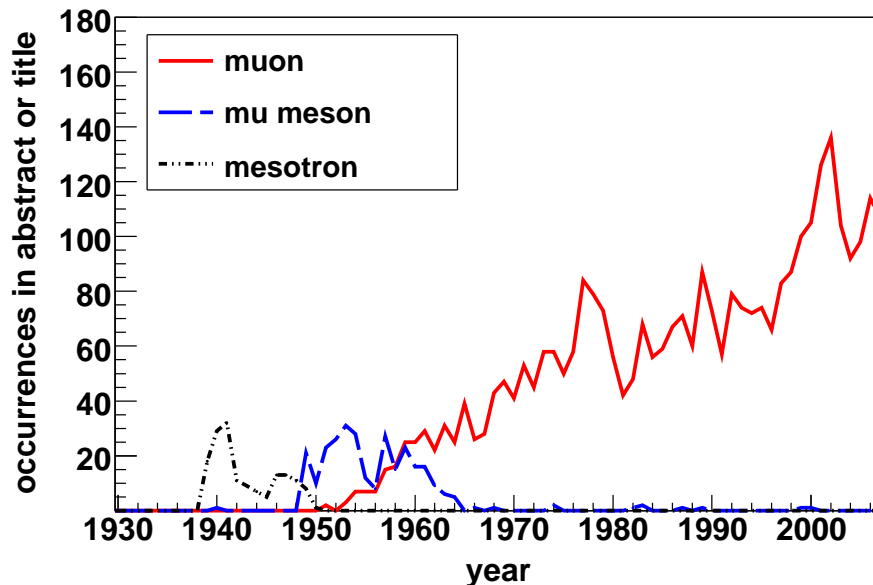


Figure C.1: Frequency of “muon”, “mu-meson” or “mesotron” in the American Physical Society abstracts.

The initial name suggested by N. Bohr<sup>46</sup> was “yucon”[112], since it was initially believed to be the strong force particle predicted by Yukawa in 1935. The name “mesotron” was first suggested in a 1938 Nature article by C.D. Anderson and S.H. Neddermeyer[113]. Prior to this article, the particle was known by a variety of names such as “Yukon for Yukawa ... X-particle ... heavy electron ... baryon”[114], and additionally “dynatron, penetron, barytron”[113].

<sup>46</sup>N. Bohr was awarded the 1922 Nobel Prize for Physics “for his services in the investigation of the structure of atoms and of the radiation emanating from them”.

The Nature article itself has a colourful history, revealed in a 1979 interview[114] with C. Anderson:

“So Seth and I – Millikan was away – wrote a little note, one paragraph, to Nature suggesting that the name of it be mesoton – “meso” meaning intermediate, like mezzanine in a building ... When Millikan<sup>47</sup> came back, I told him about this and showed him the letter, and he hit the ceiling. He said “That’s not a good word. It should be mesotron. There should be an “r” in there.” And he said, “Look, there’s electron, there’s a neutron. And I said, “There’s proton.” Well, the end and issue of it was that Seth and I cabled that “r” to Nature, and it came out mesotron, a word which I didn’t like – nobody liked it”

The Nature article argues that “it does appear quite certain that the mass, whether unique or not, is greater than that of an electron and less than that of a proton”, and hence the particle was given a name indicating its mass was in between the two well established particles. Amusingly, the Nature articles finishes with, “It appears quite likely that the appropriateness of this name will not be lost, whatever new facts concerning these particles may be learned in the future”.

A month later, R.A. Millikan wrote a short note in Physical Review, where he quotes a letter from Bohr:

“I take pleasure in telling you that every one at a small conference on cosmic-ray problems, including Auger, Blackett, Fermi<sup>48</sup>, Heisenberg<sup>49</sup>, and Rossi ... was in complete agreement with Anderson’s proposal of the name ‘mesotron’ for the penetrating cosmic-ray particles.”

C. Anderson’s Nature article and R. Millikan’s Physical Review article apparently failed to win popular consensus, as made apparent in a foreword by A.H. Compton<sup>50</sup> for a 1939 “Symposium on Cosmic Rays” [115]:

“An editorial problem has arisen with regard to the designation of the particle of mass intermediate between the electron and the proton ... A vote indicated

---

<sup>47</sup>C. Anderson was supervised by R.A. Millikan, who was awarded the 1923 Nobel Prize for Physics for his measurement of the electron’s charge.

<sup>48</sup>E. Fermi was awarded the 1938 Nobel Prize in Physics for “his demonstrations of the existence of new radioactive elements by neutron irradiation, and for his related discovery of nuclear reactions brought about by slow neutrinos”.

<sup>49</sup>W.K. Heisenberg was awarded the 1932 Nobel Prize in Physics for “the creation of quantum mechanics”.

<sup>50</sup>A.H. Compton was awarded the 1927 Nobel Prize in Physics for his work on the change in X-ray wavelengths upon scattering.

about equal choice between *meson* and *mesotron* with no considerable support for *mesoton*, *barytron*, *yukon* or *heavy electron*. Except where the authors have indicated a distinct preference to the contrary, we have chosen to use the term *mesotron*.”

The transition from “mesotron” to “meson” appears to have been initiated by a footnote in a 1939 Nature article[116] by H.J. Bhabha:

“It is felt that the ‘tr’ in this word is redundant, since it does not belong to the Greek root ‘meso’ for middle; the ‘tr’ in neutron and electron belong, of course, to the roots “neutr” and “electra” ... It would therefore be more logical and also shorter to call the new particle a meson instead of a mesotron.”

C. Anderson described other objections to the term “mesotron”, since “tron” is usually reserved for instruments, such as “audiotron or cyclotron or synchrotron”[114].

The pion was discovered in 1947 by C.F. Powell. According to Ref. [105], Powell named the new heavier particles “pi-mesons” and the older particles “mu-mesons”. Additionally, C. Anderson credits Powell with the use of greek letters: “And (Powell) used, I guess for his own bookkeeping, Greek letters – pi and mu”. Lee[58] suggests that Powell “introduced the symbol  $\pi$  which stands for ‘primary’”, but credits Fermi as being the first to use the symbol  $\mu$ .

# Appendix D

## Magnetic field mapping and simulation

Prior to data acquisition, the magnetic field was measured at  $B = 1.96$  T,  $B = 2.00$  T and  $B = 2.04$  T using the custom built apparatus shown in Figs. D.1. and D.2. Hall probes were placed along an arm at intervals of 4.13 cm, and the apparatus was rotated by  $15^\circ$  increments and moved in steps of 5 cm or 2.5 cm longitudinally<sup>51</sup> ( $z$ ). The Hall probes only measured the longitudinal component of the field, and were calibrated using an NMR that measured the total field. The Hall probe measurements had a precision of 0.1 mT. In 2002 measurements were taken of the tracking region using seven probes on the rotating arm. In 2003 measurements of the fringe field and the upstream part of the tracking region were taken. For the 2003 measurements only five Hall probes were used since the assembly needed to pass through the hole in the doors.

A simulation was required to smooth out the field and generate the  $x$  and  $y$  components. The OPERA software package was used for this purpose[83]. The measurements taken with the Hall probe mapper were not given to OPERA. Instead the pieces shown in Fig. D.3 were modelled, and their properties<sup>52</sup> were adjusted to minimise the differences between OPERA and the measurements. The agreement was better than 0.2 mT within the 2 T region. Further upstream, the match becomes worse as demonstrated in Fig. D.4.

---

<sup>51</sup>The smaller steps were taken at the edges of the tracking region.

<sup>52</sup>Specifically, the coil position, current density, coil radii, material B-H curves and door position were adjusted.

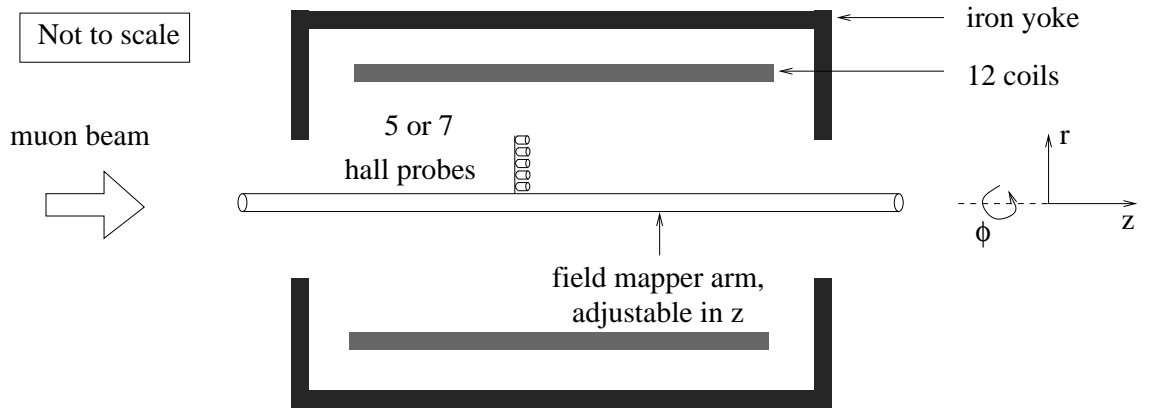


Figure D.1: Schematic of the field mapper device. Hall probes were attached at radial intervals of 4.13 cm, and the arm was rotated in  $15^\circ$  increments. The whole assembly was inserted from the downstream end.

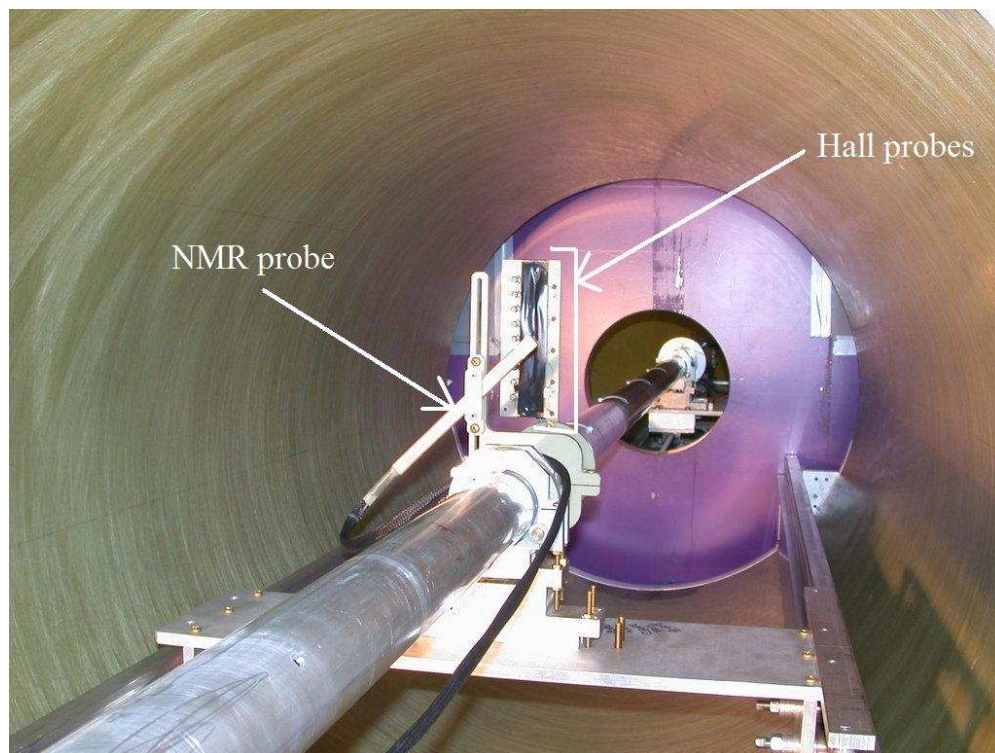


Figure D.2: Photograph of the field mapper, taken from inside the solenoid. The bore of the magnet has 1 m diameter. The device is constructed from non-magnetic materials (aluminium, brass).

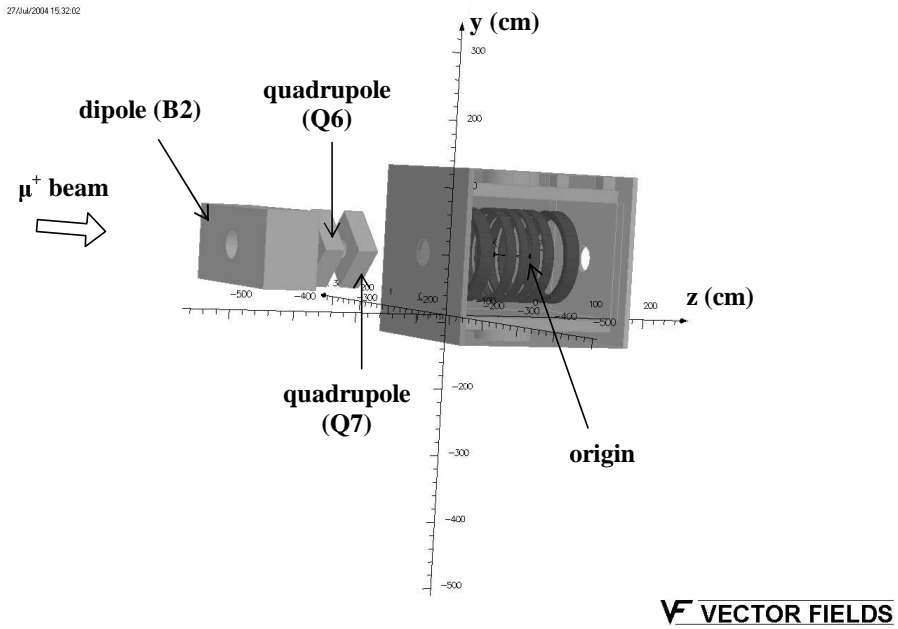


Figure D.3: Components included in the OPERA simulation of the magnetic field.

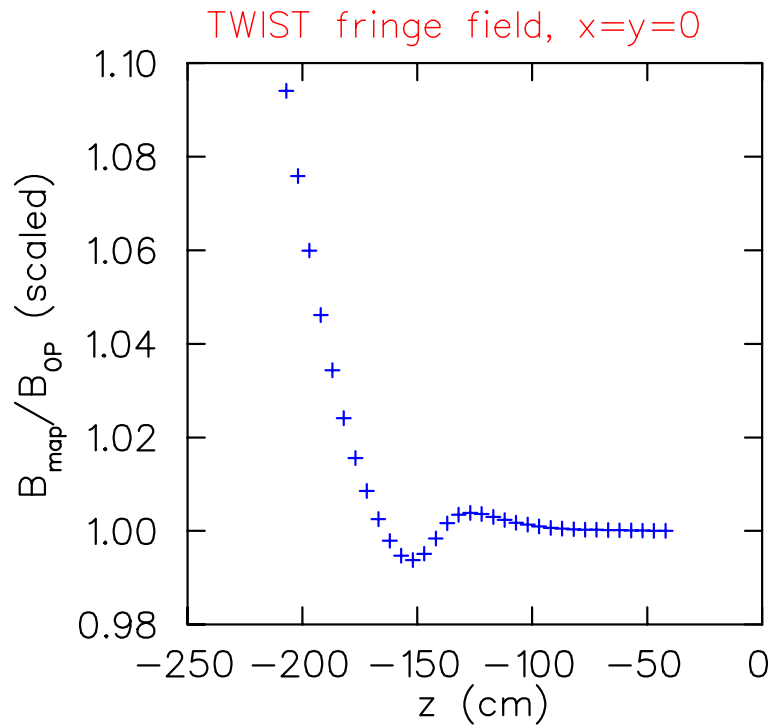


Figure D.4: For  $x = y = 0$ , the ratio of the measured field map to the OPERA model[84].

# Appendix E

## New downstream trigger

The determination of the wire timing offsets required a reliable downstream trigger, even when the experiment's magnetic field was switched on (see Section 3.2.1). The author's first project was to help in the design and construction of such a trigger. The final design is photographed in Fig. E.1, where two scintillators of thickness 0.318 cm, separated by 0.318 cm, are read out by light guides that are matched to long ( $\sim 2$  m) light pipes. These transported the collected light to photomultiplier tubes located in a relatively weak field region. The front of the arrangement is shown in Fig. E.2, where light guides are connected to the top and bottom of each scintillator, resulting in a four-fold coincidence that gives a reliable timing measurement.

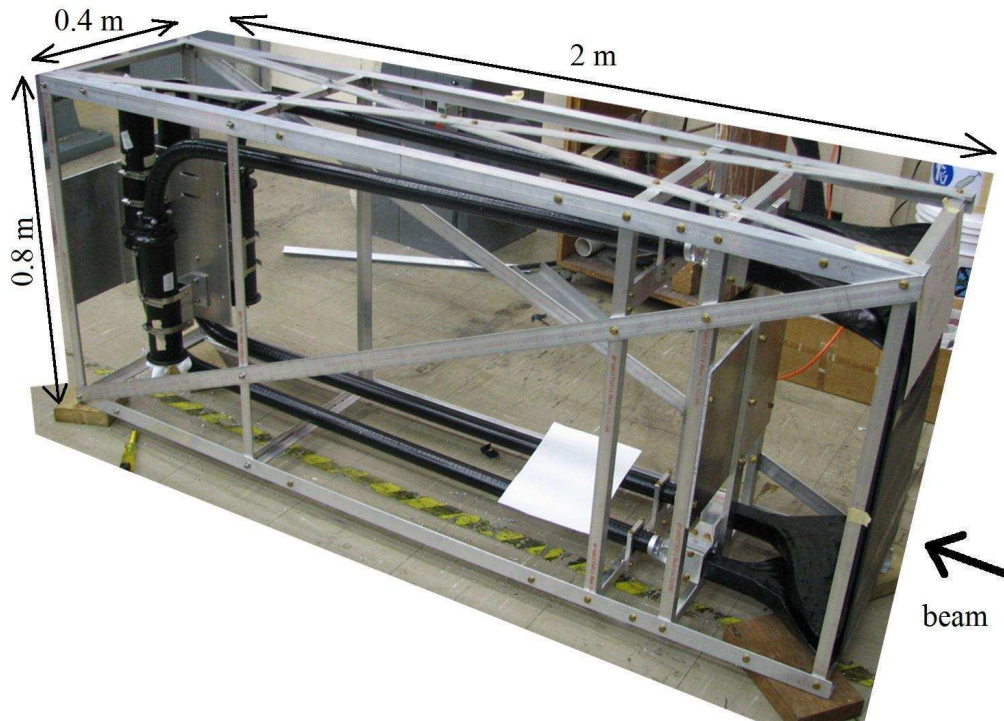


Figure E.1: Downstream trigger: photograph of completed frame, light guides, photomultiplier tubes and scintillators.

Appendix E. New downstream trigger

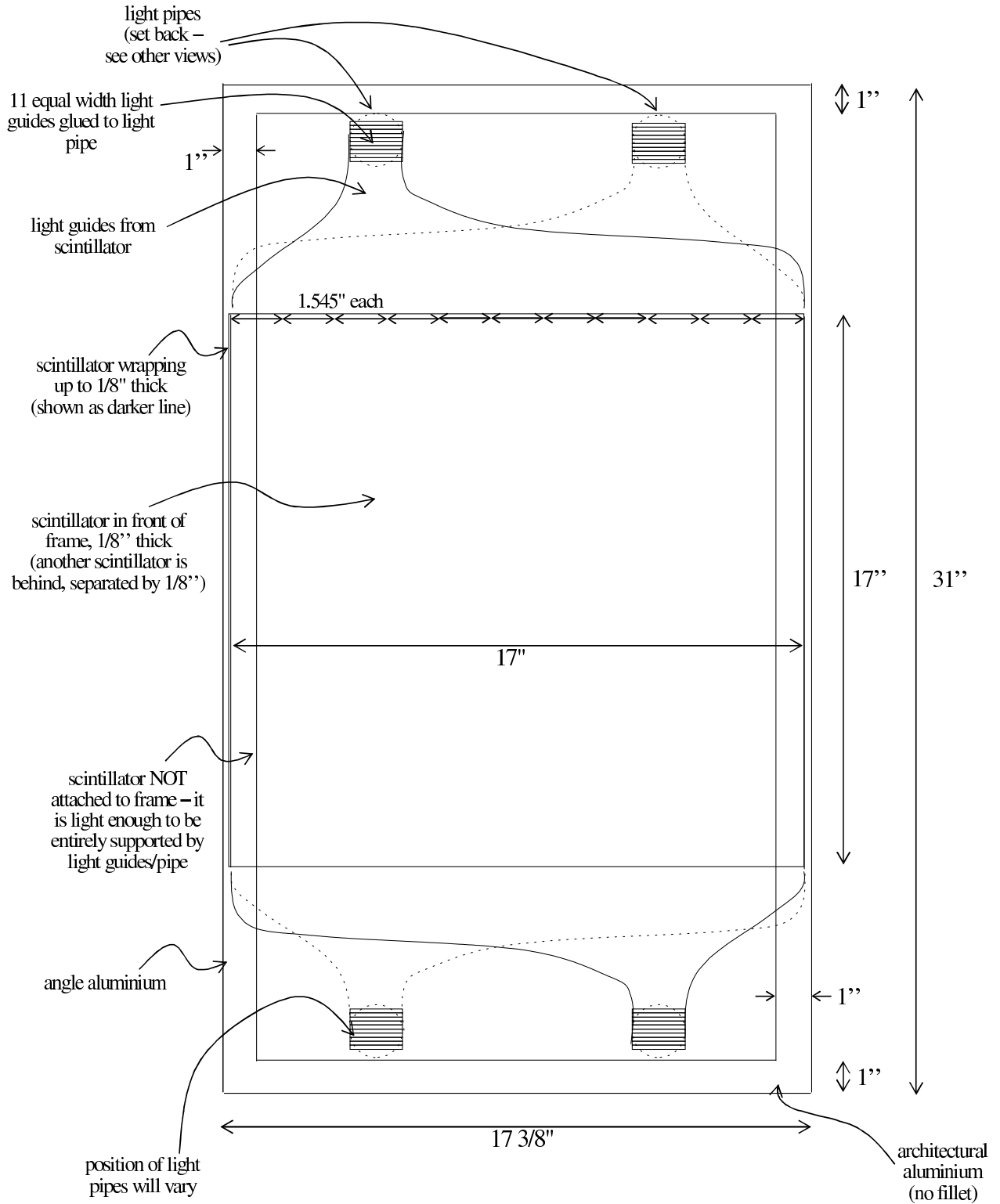


Figure E.2: Front view (looking downstream) of new downstream trigger. Measurements are in inches.

# Appendix F

## Bias in $P_\mu^\pi \xi$ extraction technique

The  $P_\mu^\pi \xi$  result is quoted at the time of muon production, but the data and simulation spectra are constructed with  $P_\mu$  at the time of decay, after all depolarisation processes have taken place. Algebraically, the difference in the product  $P_\mu \xi$  between the data and simulation spectra can be written as

$$\Delta [P_\mu \xi] = P_\mu^{D,data} \xi^{data} - P_\mu^{D,sim} \xi^{sim}, \quad (\text{F.1})$$

where the superscript  $D$  in  $P_\mu^D$  implies that  $P_\mu$  is at the time of decay, and *sim* refers to the simulation's values.  $\Delta [P_\mu \xi]$  is the quantity to which the uncertainties are assigned. When the experiment reveals the hidden value of  $\xi$  used in the simulation, the result is then stated as,

$$P_\mu^{\pi,data} \xi^{data} = P_\mu^{\pi,sim} \xi^{sim} + \Delta [P_\mu \xi]. \quad (\text{F.2})$$

where the superscript  $\pi$  in  $P_\mu^\pi$  implies that  $P_\mu$  is at the time of muon production. The experiment claims to accurately simulate the depolarisation between production and decay, so that

$$P_\mu^{\pi,data} - P_\mu^{D,data} = P_\mu^{\pi,sim} - P_\mu^{D,sim}. \quad (\text{F.3})$$

Equations (F.1) and (F.3) can be re-arranged to yield

$$\begin{aligned} \Delta [P_\mu \xi] &= P_\mu^{\pi,data} \xi^{data} - P_\mu^{\pi,sim} \xi^{sim} \\ &\quad + (P_\mu^{D,sim} - P_\mu^{\pi,sim}) (\xi^{data} - \xi^{sim}). \end{aligned} \quad (\text{F.4})$$

Now  $(P_\mu^{D,sim} - P_\mu^{\pi,sim})$  is the amount of depolarisation in the simulation, which is of order  $10^{-3}$ . The term  $(\xi^{data} - \xi^{sim})$  depends on the tolerance of the hidden values, which is at most  $10^{-2}$ . Therefore this term is of order  $10^{-5}$ , and can be safely neglected. In other words, even though spectra at the time of decay are being compared, the result for  $P_\mu^\pi \xi$  at the time of muon production can be extracted with sufficient accuracy for this measurement.

# Appendix G

## Time expansion chambers analysis

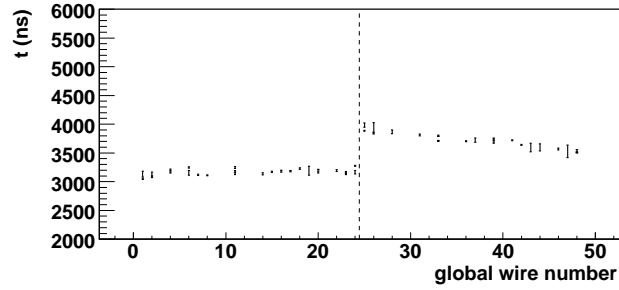
### G.1 Introduction

An accurate measurement of the muon beam was critical in determining the muons' polarisation at the time of decay. This was achieved by determining the position and angle of individual muons using the time expansion chambers (TECs) that were described in Section 2.3. The analysis that converted signals from the TEC electronics into an unbiased measurement of the muon beam will be described.

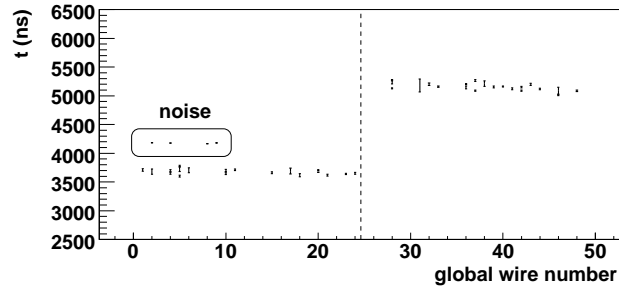
The TEC analysis code was extensively reviewed for this measurement. The track reconstruction software did not limit the precision of the  $P_{\mu}^{\pi} \xi$  measurement; instead the reproducibility of the TEC hardware and noise from the electronics meant that further improvements in the TEC analysis code were unwarranted.

### G.2 Typical raw events

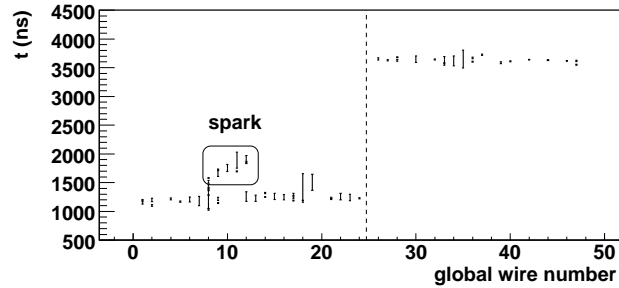
The TECs were in a region of weak magnetic field, so that muon trajectories were well approximated by straight lines. The majority of events were like Fig. G.1(a), with a single clean track through both the  $x$  and  $y$ -module, and most of the wires producing at least one distinct signal pulse (“hit”). Some of the wires had multiple hits due to the break-up of ionisation into clusters, and crosstalk from the electronics, and this prevented a simple straight line fit from being applied to each hit's leading edge. A minority of events suffered from electronics noise, sparks, beam positrons and multiple muons, and examples of these are shown in Figs. G.1(b) to G.1(d).



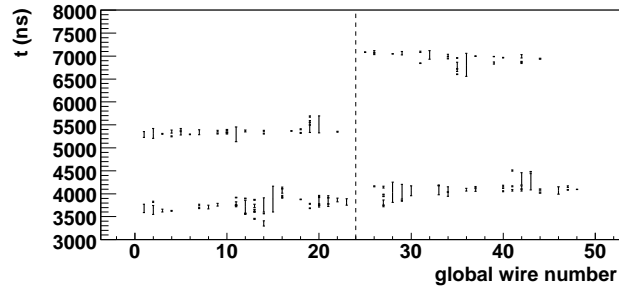
(a) The majority of events had one clean muon track in each module.



(b)  $x$ -module noise that must be removed. This was localised to seven wires of the  $x$ -module.



(c)  $x$ -module sparking.



(d) Multiple muon event. Ordinate scale is changed.

Figure G.1: Examples of TEC events from data. Wires 1 to 24 are the  $x$ -module, and 25 to 48 are the  $y$ -module.

## G.3 Analysis

### G.3.1 Unpacking and wire time offsets

A TEC event was analysed if a particle triggered the muon scintillator, and a positron was then detected more than 700 ns from the trigger time. This corresponded to  $\approx 80\%$  of trigger particles, although including the other 20% was found to introduce no measurable bias. The TEC analysis removed events where the trigger particle was not a surface muon, as determined by the the particle identification from Section 3.3.1.

The leading edge times and hit widths were first “unpacked” from the data files, using the analysis code described in Section 3.2.1. Hits with an error code from the TDC were discarded, and wire time offsets were applied to the good hits.

When the TEC sense planes were new, on average there were 17 out of 24 wires with at least one hit. This was lower than the original design specification, but was adequate for this measurement. The hit efficiency decreased as the TECs aged, requiring the sense planes to be replaced when an average of 10 wires had at least one hit.

Crosstalk and electronics noise produced hits that were all less than 20 ns in width. Unfortunately these could not be removed by a simple pulse width cut, since hits from the muon ionisation could be as narrow as 8 ns. Placing a pulse width cut to remove noise would have removed real muon hits, thus reducing the single hit efficiency and degrading the resolution. The noise was instead removed by improving the pattern recognition, which will be described later.

### G.3.2 Reject multiple trigger events

Events with multiple muons were rejected since they produced two tracks in each TEC module, and these could not be matched up between the modules (see Fig. G.1(d)). If two muons were detected by the spectrometer’s proportional chambers, then the event was removed from the TEC analysis. This is the only place where information from inside the detector was used.

The number of scintillator hits was also available, but was not used by default. Tests confirmed that adding a stricter multiple trigger rejection based on the number of scintillator hits had no measurable effect on the analysis.

### G.3.3 Discriminator amplitude walk

For a discriminator with a fixed threshold, there exists a correlation between signal amplitude and leading edge time. At this stage in the analysis, hits with a width less than 120 ns were corrected according to

$$\Delta t = \begin{cases} (100.0A_i) \text{ ns} & (0.0 < t_{\text{width}} < 20.0) \text{ ns} \\ (120.0 \text{ ns} - t_{\text{width}}) A_i & (20.0 < t_{\text{width}} < 120.0) \text{ ns} \end{cases} \quad (\text{G.1})$$

where  $A_i$  (no units) is determined for each wire individually as part of the calibration.

In the previous  $P_{\mu}^{\pi} \xi$  analysis, the calibration of  $A_i$  for each wire was not iterated until convergence. As a result, the  $P_{\mu}^{\pi} \xi$  analysis was sensitive to whether the discriminator amplitude walk correction was made. The current analysis found that disabling the correction altogether had a negligible effect on the muon beam measurement.

### G.3.4 Track candidates

Track candidates were constructed according to the algorithm that is outlined in Fig. G.2, which has the following steps:

1. Select a single hit.
2. Draw a corridor  $\pm 300$  ns from this hit.
3. On each wire, pick up the single hit that is within the corridor, and closest to the hit in (1).
4. If there are more than four hits, then keep this selection as a track candidate.
5. Reject track candidate if the hits span less than 2.7 cm (14 out of 24 wires).
6. Repeat (1) to (4) for every hit.

This algorithm gave every hit a chance of being a good hit, and only allowed one hit per wire. The rejection of track candidates based on their hit span ensured good angular resolution.

The track candidate with the most number of hits ( $n_{\text{max}}$ ) was then found. The other track candidates were only kept if they had enough hits<sup>53</sup>. The leading edge times in the track

---

<sup>53</sup>The criteria was

- For  $n_{\text{max}} > 12$ , require  $n \geq (n_{\text{max}} - 2)$
- For  $8 < n_{\text{max}} \leq 12$ , require  $n \geq (n_{\text{max}} - 1)$ .

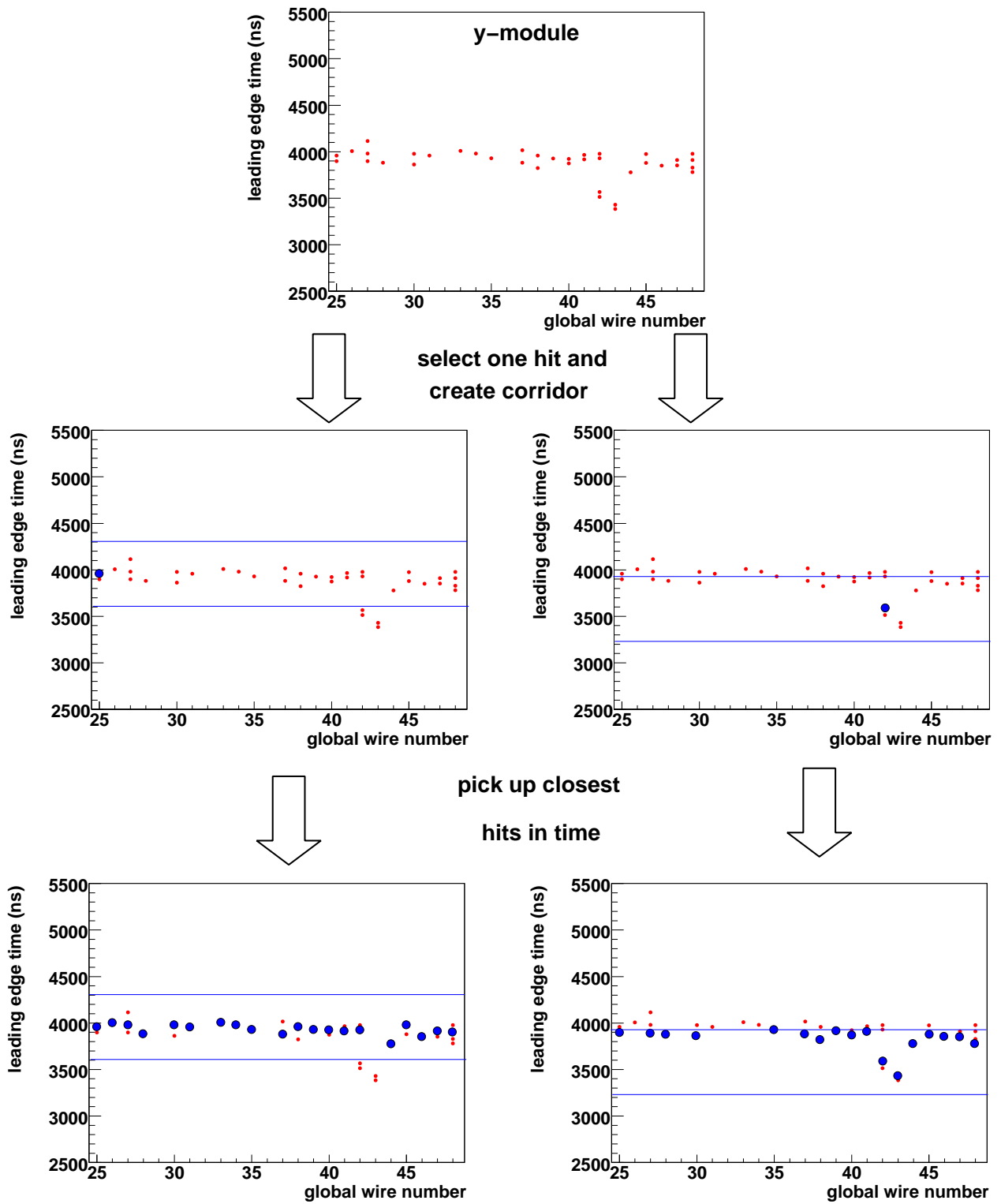


Figure G.2: Construction of two possible track candidates. See the text for more details.

candidates were then converted to distance, using a space-time-relationship (STR) described by a cubic function,

$$s = p_0 + p_1t + p_2t^2 + p_3t^3, \quad (\text{G.2})$$

where  $s$  is  $x$  or  $y$ , depending on the module, and  $p_i$  are determined by a calibration technique that will be described later. A least-squares straight line fit was then carried out to the positions, and the track candidate with the smallest residuals was declared as the successful muon trajectory.

Finally, to avoid a suspected bias towards low angles from the fixed corridor, hits were recovered within 0.15 cm of the fitted muon track and the straight line fit was repeated. This process was iterated until convergence. Unfortunately it was not possible to definitively say whether recovering hits and refitting offered a genuine improvement; this was judged by examining individual event displays. The average position and angle were insensitive to whether an iteration was made, but the RMS (root mean square) of the reconstructed angles changed by about 4 mrad. This introduced a  $P_\mu^\pi \xi$  systematic uncertainty, as described in Section 6.3.2.

### G.3.5 Final multiple track removal

Even though events with two muons were reliably removed using the earlier event classification cut, there is still the possibility of multiple tracks due to noise and sparks (see Figs. G.1(b) and G.1(c)), and beam positrons, which were detected with low efficiency but could produce enough hits to make a track. In a module, if the best-fit track and another track candidate were too close, then the event is rejected.

The separation time was tuned for the current analysis. The old value of 1  $\mu\text{s}$  was conservatively large, and a setting of 0.3  $\mu\text{s}$  was found to be better at rejecting multiple track events, or those confused by noise.

### G.3.6 Other algorithms

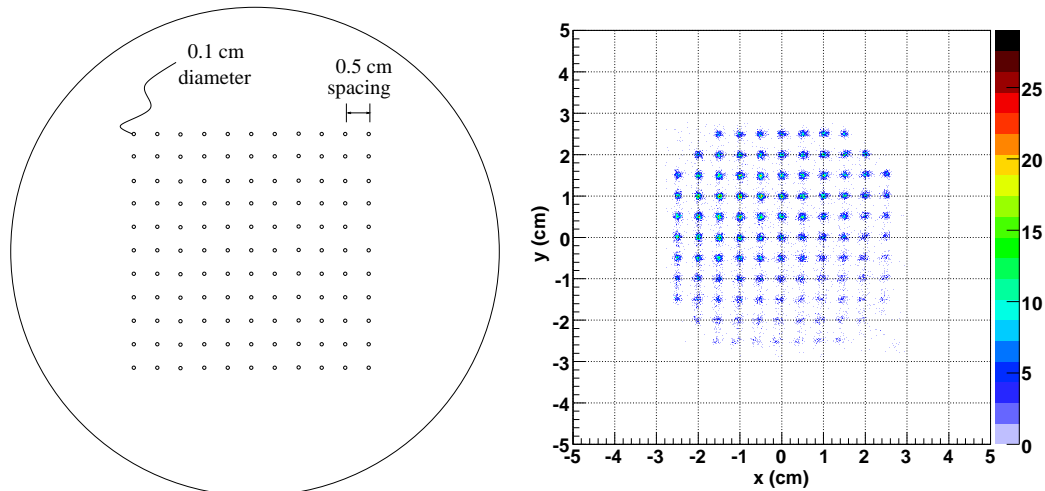
Alternative reconstruction algorithms were tested, such as a Hough Transform, Kalman filter and iterative straight line fitting with outliers rejected at each stage. However they were found to need careful tuning to become robust to the noise in the data, and could not readily determine the RMS of angles better than the algorithm described here.

- 
- For  $n_{\text{max}} \leq 8$ , require  $n = n_{\text{max}}$ .

The selection is necessary to prevent the analysis code selecting junk tracks, such as the “spark” in Fig. G.1(c).

## G.4 Sense plane calibration

Special TEC calibration data were acquired, where each end of the box containing the TECs had an  $(11 \times 11)$  hole collimator attached (see Fig. G.3(a)). The beam line was tuned to



(a) 121 hole collimator.

(b) Reconstructed position of muon tracks, after correcting the STRs.

Figure G.3: TEC drift cell space-time relationships (STRs) were determined by placing a 121 hole collimator on each end of the TEC box.

illuminate the entire collimator, and an angle cut was made in the analysis to select tracks that passed through opposing holes. These tracks allowed determination of the wire time offsets, discriminator amplitude walk correction, and space-time-relationships for each drift cell. The calibration technique and the results from four independent calibrations (labelled 2006H, 2007A, 2007B, 2007C) will be described. Further detail can be found elsewhere[89].

### G.4.1 Wire time offsets

The time of TEC hits were measured with respect to the muon trigger scintillator. An offset had to be determined for each TEC wire due to differences in cable lengths and TDC channels. These were determined by selecting tracks from the central hole of the collimator, and histogramming the times for each wire. The offset required to match-up the peaks of these histograms was then determined. This calibration also found the global time offset of the TEC wires relative to the muon scintillator.

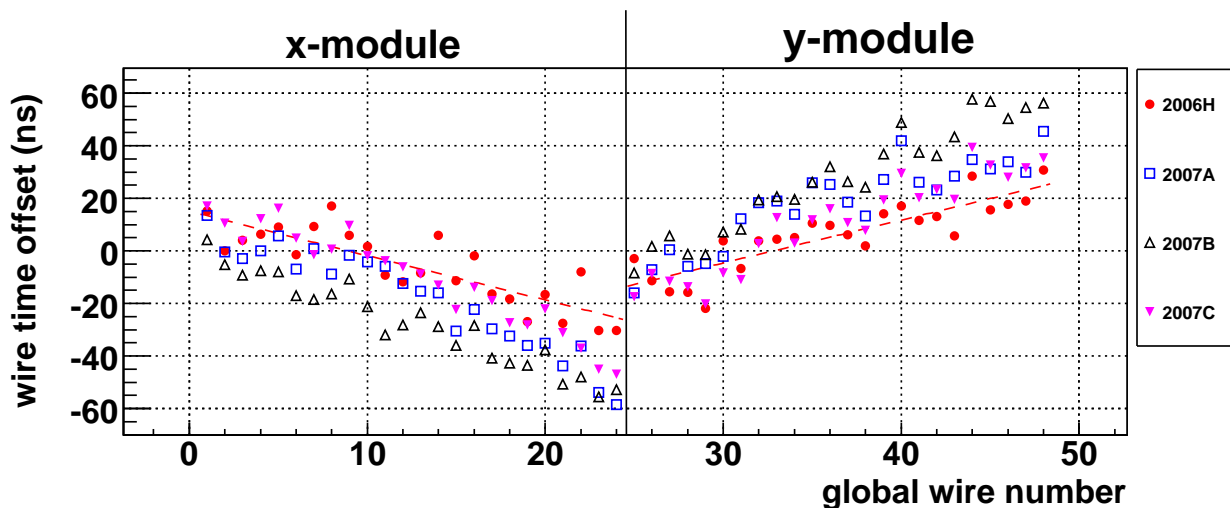


Figure G.4: Wire time offsets for the calibrations in 2006 and 2007. The gradient corresponds to a rotation of the TECs within their box of between 7 – 12 mrad. A fit line is included for 2006H only.

The wire time offsets are compared in Fig. G.4, which shows that there is a slope corresponding to a rotation of 7 – 12 mrad in each module<sup>54</sup>. The collimators were aligned to better than  $500\ \mu\text{m}$ , which corresponded to 3 mrad over their separation distance of 16 cm; therefore the wire time offset calibration compensated for a rotational misalignment of the individual TEC modules, rather than a collimator misalignment. The previous analysis found similar features that suggested a 2 – 4 mrad rotation, but the statistical precision was significantly worse. The possible time variation over a 0.1 cm diameter hole was  $< 1\ \text{ns}$ , so that the remaining features in Fig. G.4 are differences in cable lengths and electronics.

### G.4.2 Discriminator amplitude walk

The parameters characterising the discriminator amplitude walk correction ( $A_i$  in Eq. (G.1)) are compared for each wire in Fig. G.5. There is no evidence of wire-to-wire differences outside of statistics (if differences existed, this would indicate that the thresholds in the electronics were not set to consistent values). The parameters are remarkably consistent between calibrations.

<sup>54</sup>The gradient for the 2006H planes is between  $-1.7\ \text{ns}$  and  $-2.6\ \text{ns}$  per wire in the  $x$ -module, and between  $1.6\ \text{ns}$  and  $2.8\ \text{ns}$  per wire in the  $y$ -module.  $1\ \text{ns}$  is approximately  $9\ \mu\text{m}$ , and the wires are 0.2 cm apart, so that the rotation is 8 – 11 mrad in the  $x$ -module, and 7 – 12 mrad in the  $y$ -module.

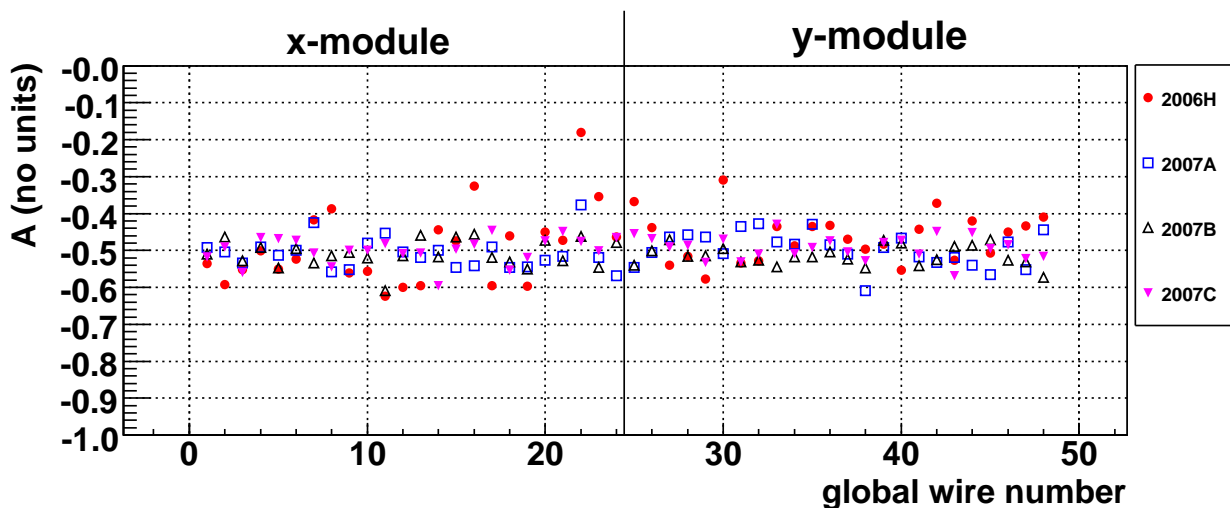


Figure G.5: Discriminator amplitude walk parameters for the calibrations in 2006 and 2007. The correction is independent of wire and sense planes.

### G.4.3 Space-time relationship

The space-time-relationship (STR) for each drift cell was initially generated using the GARFIELD software[93]. This STR is an approximation since only one TEC module was modelled, which neglected the electric field interference between the two TEC modules. In addition, the GARFIELD simulation relied on accurate inputs for the voltage, geometry and gas density. The collimator data were used to adjust the STRs, by altering the parameters in Eq. (G.2) to place the collimator holes at their known positions; Fig. G.3(b) shows an example of the calibration data after the STRs have been corrected.

The gas inside the TECs was held at a constant pressure, so that temperature variations altered the gas density and hence the space-time relationship. A change of  $\pm 3^\circ\text{C}$  altered the mean positions by  $< 500\ \mu\text{m}$ , and the average angles by  $< 0.4\ \text{mrad}$ , which were not significant variations for this analysis. No correction was made due to temperature since each data set had a beam measurement within  $1.5^\circ\text{C}$  of the calibration temperature.

## G.5 Performance

### G.5.1 Resolution

The single hit resolution for each wire was determined as follows:

1. For the track candidate with lowest  $\chi^2$ , re-fit with a wire excluded.
2. For the excluded wire, histogram the residual distance between the hit and the fit.
3. Find the RMS of the residual histogram. This is a measure of the single hit resolution for the wire.

The resolution was between  $275\ \mu\text{m}$  and  $375\ \mu\text{m}$  for all wires, as shown in Fig. G.6, which demonstrates that the resolution did not change significantly as the planes aged. The resolution also depended on the distance from the sense plane; an earlier study determined that it varied between  $150\ \mu\text{m}$  and  $350\ \mu\text{m}$ [76].

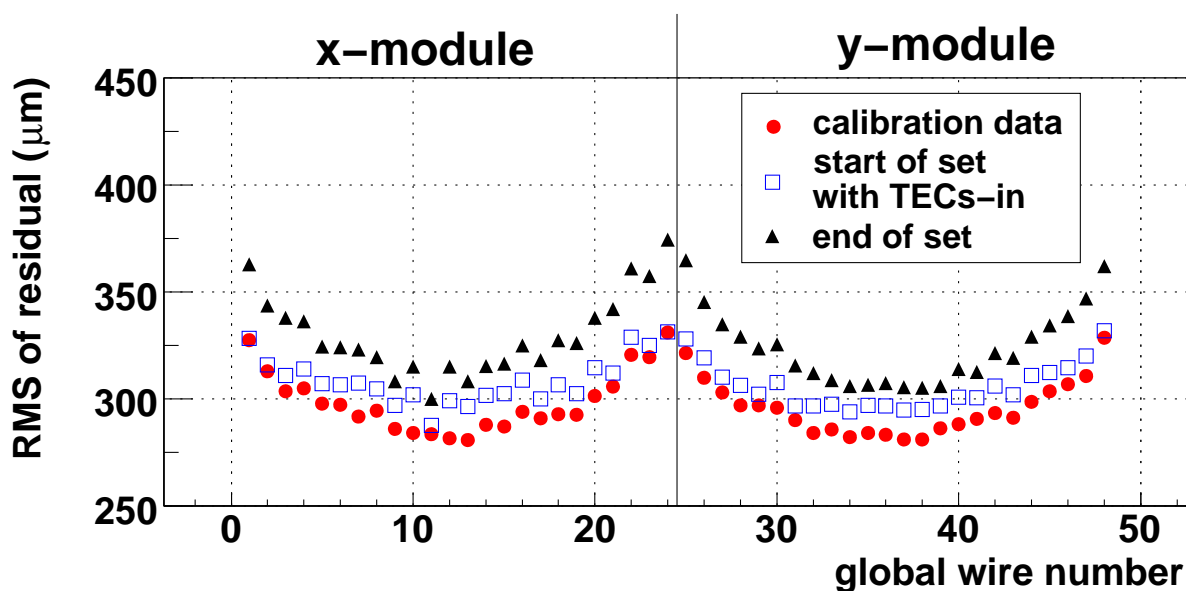


Figure G.6: Resolution (RMS of residual distribution, when wire is excluded from fit). The calibration data corresponds to newly built sense planes. The beginning and end of the set with TECs-in corresponds to a time period of one week, over which the planes aged significantly.

The resolution of the track position and angle could be determined using simulation. With wire inefficiency simulated, and no multiple scattering, the angle resolution for a single track was  $\sim 3\ \text{mrad}$ , and the position resolution was  $\sim 150\ \mu\text{m}$ [57]. However, this is misleading since the resolution in real data will be worse due to the electronics noise and beam positrons.

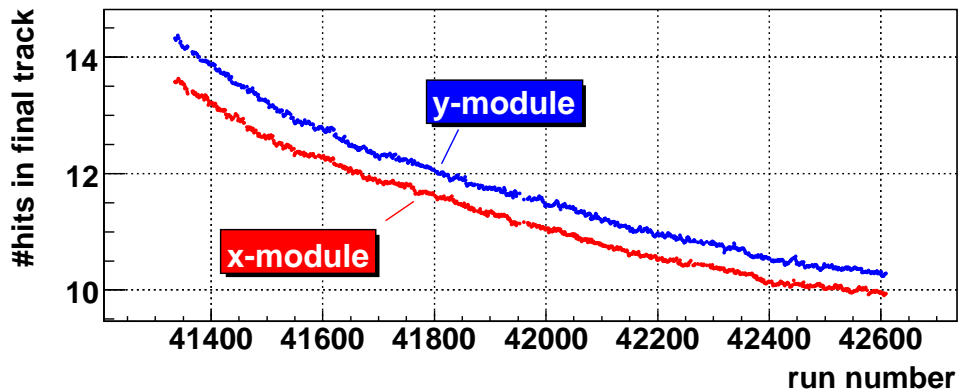
## G.5.2 Number of hits per event

The average number of hits in the final track was about 15. This average depended on the track's distance from the sense plane, since as an ionisation cluster drifts its electrons separate in time, so that a longer drift time resulted in a lower probability of a hit exceeding the electronics threshold. At 2.0 cm (5.0 cm), the average number of hits was 12 (17). There were no asymmetries observed in the beam profile, indicating that even far from the sense plane there were enough hits available.

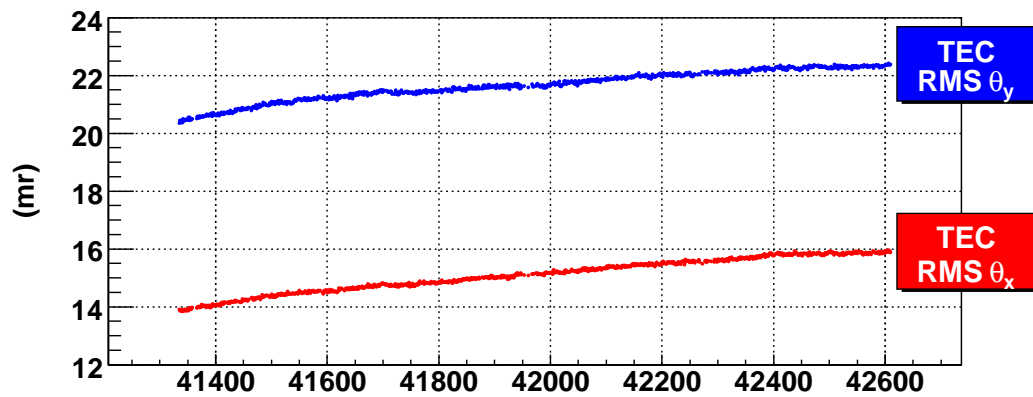
The number of hits per event decreased as the sense planes aged. This was quantified by accumulating an entire set with the TECs in place, and is shown in Fig. G.7(a). The mean positions and angles were highly stable during this set (see Section 5.4.7), but with less hits available the angular resolution decreased, and the RMS of the reconstructed angles therefore increased. Figure G.7 shows this effect, where the RMS is seen to change by 2 mrad in each module. This information is used in Section 6.3.2 to assign a systematic uncertainty to  $P_\mu^\pi \xi$ . There was also a negligible increase in the RMS of the positions over the entire set (0.04 cm).

## G.6 Summary

As a result of the electronics noise and beam positron signals that were present in the data, the TEC analysis code could not determine the RMS of the reconstructed angle distribution to better than 4 mrad. This will be used to establish a systematic uncertainty. The single hit resolution was better than  $375 \mu\text{m}$  for all drift cells, and the available calibrations for wire time offsets, discriminator amplitude walk and space-time relationships are remarkably stable. The aging of the sense planes was measured, and this will be included in a systematic uncertainty estimate.



(a) Number of hits used for the successful track.



(b) RMS of reconstructed angles.

Figure G.7: Sense plane aging, for one data set (approximately one week). The muon beam was stable during this time period. As the number of hits per event decreases, the angle is less well determined, and the RMS of reconstructed angles increases.

# Appendix H

## E1111: Subsidiary $\mu^+$ SR experiment

### H.1 Introduction

In the TWIST experiment, if a muon decayed within  $1.05 \mu\text{s}$  of the trigger time, the resulting positron was not included in the normal analysis since its hits could overlap with the muon ionisation in the drift chambers. A special asymmetry analysis allowed positrons within  $0.46 \mu\text{s}$  of the trigger time to be included, but this was not early enough to rule out a fast time component to the depolarisation within the muon stopping target. A muon spin relaxation ( $\mu^+$ SR) experiment[31] was undertaken to look for relaxation at early times, in collaboration with CMMS<sup>55</sup>.  $\mu^+$ SR can measure asymmetry as early as about 5 ns since it uses fast scintillators to count decay positrons. A lack of additional depolarisation components down to 5 ns would improve confidence in the main experiment's results. At the time of writing, this is probably the shortest time scale that can be experimentally observed, and the author is unaware of any credible models for muon depolarisation within the first 5 ns in metals.

$\mu^+$ SR experiments run at a higher rate (20 – 40 kHz compared to 2 – 5 kHz), which should have allowed a high statistics measurement of the depolarisation rate comparable to the main TWIST experiment. However, this goal was not achieved due to the length of time required to calibrate the apparatus, and the dominant systematic uncertainty due to the fraction of muons stopping in the trigger scintillator, which will be described in detail later. Regardless, this is one of the highest precision experiments ever carried out using a  $\mu^+$ SR apparatus.

### H.2 Theory

Assuming standard model values of the muon decay parameters, and neglecting the electron mass and radiative corrections, Eqs. (1.14)-(1.18) can be used to write the muon differential decay rate as

$$\frac{d^2\Gamma}{dx d\cos\theta} = \frac{G_F^2 m_\mu^5}{192\pi^3} [3 - 2x + P_\mu \cos\theta(2x - 1)] x^2, \quad (\text{H.1})$$

---

<sup>55</sup>TRIUMF Centre for Molecular & Materials Science

where  $\theta$  is the angle between the positron momentum and muon spin,  $P_\mu$  is the degree of muon polarisation, and  $x \equiv E_e/m_\mu$ . If decay positrons are detected for energy ( $p < x < q$ ) with 100% efficiency, then integration of Eq. (H.1) gives

$$\frac{d\Gamma}{d\cos\theta} = \int_p^q dx \frac{d^2\Gamma}{dx d\cos\theta} = \frac{G_F^2 m_\mu^5}{192\pi^3} \left\{ \left[ (q^3 - p^3) - \frac{1}{2}(q^4 - p^4) \right] + P_\mu \cos\theta \left[ \frac{1}{2}(q^4 - p^4) - \frac{1}{3}(q^3 - p^3) \right] \right\}, \quad (\text{H.2})$$

and if the angular fiducial is ( $a < \cos\theta < b$ ), then the normalised number of counts is given by

$$N = \frac{G_F^2 m_\mu^5}{192\pi^3} (b - a) \left[ (q^3 - p^3) - \frac{1}{2}(q^4 - p^4) \right] (1 + AP_\mu), \quad (\text{H.3})$$

$$A = \frac{1}{2} (b + a) \frac{\frac{1}{2}(q^4 - p^4) - \frac{1}{3}(q^3 - p^3)}{(q^3 - p^3) - \frac{1}{2}(q^4 - p^4)}. \quad (\text{H.4})$$

Assuming that there are counters in the forward (defined as the range  $-1 < \cos\theta < 0$ ) and backward ( $0 < \cos\theta < 1$ ) directions, and that each of these counters have their own values of  $\{a, b, p, q\}$  and an associated background, then Eq. (H.3) can be used to show that

$$n_b(t) = b_b + N_0 e^{-t/\tau_\mu} [1 + A_b P_\mu(t)] \quad (\text{H.5})$$

$$n_f(t) = b_f + r N_0 e^{-t/\tau_\mu} [1 + A_f P_\mu(t)], \quad (\text{H.6})$$

where  $n_b$  and  $n_f$  are the number of backward and forward counts,  $b_b$  and  $b_f$  are the backgrounds in each counter,  $\tau_\mu$  is the muon lifetime, and  $N_0$  is the number of muons at  $t = 0$  multiplied by the factors in Eq. (H.3). An additional factor,  $r$ , is introduced to account for differences between the counters' energy and angular acceptance. The values of the empirical asymmetries  $A_b$  and  $A_f$  are expected to depend only on the counter geometry and the material that a positron passes through, and should remain constant if neither counters nor sample are moved, and the thickness of target material is unchanged.

If  $P_\mu = P_\mu(0)f(t)$ , where  $P_\mu(0)$  is the polarisation at  $t = 0$  and  $f(t)$  is the time dependent part, then Eqs. (H.5) and (H.6) cannot separate  $P_\mu(0)$  from the  $A$ 's unless  $r$ ,  $A_b$  and  $A_f$  are known by other means, such as a Monte Carlo simulation. Therefore  $\mu^+$ SR cannot measure  $P_\mu(0)$  with high precision, and should only be used to determine  $f(t)$ , the time dependent part of the polarisation.

## H.3 $\mu^+$ SR Apparatus

### H.3.1 M20 Beam line

Muons were delivered to the stopping target by the M20 beam line, which is a dedicated surface muon source also located at TRIUMF, in the same experimental hall as the main experiment's M13 beam line. The channel has been described elsewhere[117], and is similar to M13, with the addition of a DC separator element, which selects particles by velocity to remove most positrons originating from the production target. This is important for  $\mu$ SR since there is no event information, and a scattered beam positron can trigger the annular forward or backward counters in the same way as a decay positron. The DC separator had the disadvantage of introducing a significant transverse (vertical) polarisation component. M20 had a momentum acceptance that is larger than M13's and was not determined for this experiment. The beam spot was also larger than for M13, making collimation necessary, which will lead to a background from lower momentum slit-scattered particles.

### H.3.2 Detector

The detector is shown schematically in Fig. H.1, where muons entered from the left and could stop in the 99.99% purity silver mask, the sample under investigation, or one of the trigger scintillators. This arrangement allowed the experiment to measure the sample and the silver mask simultaneously. The results for the silver mask were expected to remain constant for the experiment, allowing changes in the running conditions to be detected. Note that the forward and backward counters were approximately 0.6 cm thick. The backward counter was a disc of about 8.0 cm diameter, with a 2.5 cm hole for the muon beam. The target module was placed in the  $\mu$ SR HELIOS superconducting solenoid [118].

The data acquisition system (DAQ) recorded the positron time of arrival (relative to that of the muon) in two positron counter arrays, using 19200 channels of width 0.78125 ns. The experiment had an observable background made up of muon decays in or near the collimator, scattered positrons, and muon decays between the muon detector and the target. The background from muon pile-up (where a second muon enters the sample region during the same data gate as the original muon) was removed by the electronics, within 14  $\mu$ s of either side of the event<sup>56</sup>. For this experiment, the positron gate was open for 1  $\mu$ s *before* the muon trigger, so that events were recorded that could not possibly be caused by decay of the

---

<sup>56</sup>The removal of the background from muon pile-up is not perfect. With sufficiently high statistics, there is expected to be a visible small time dependence to the background.

detected muon. The aim was to fix the background to the average “ $t < 0$ ” value.

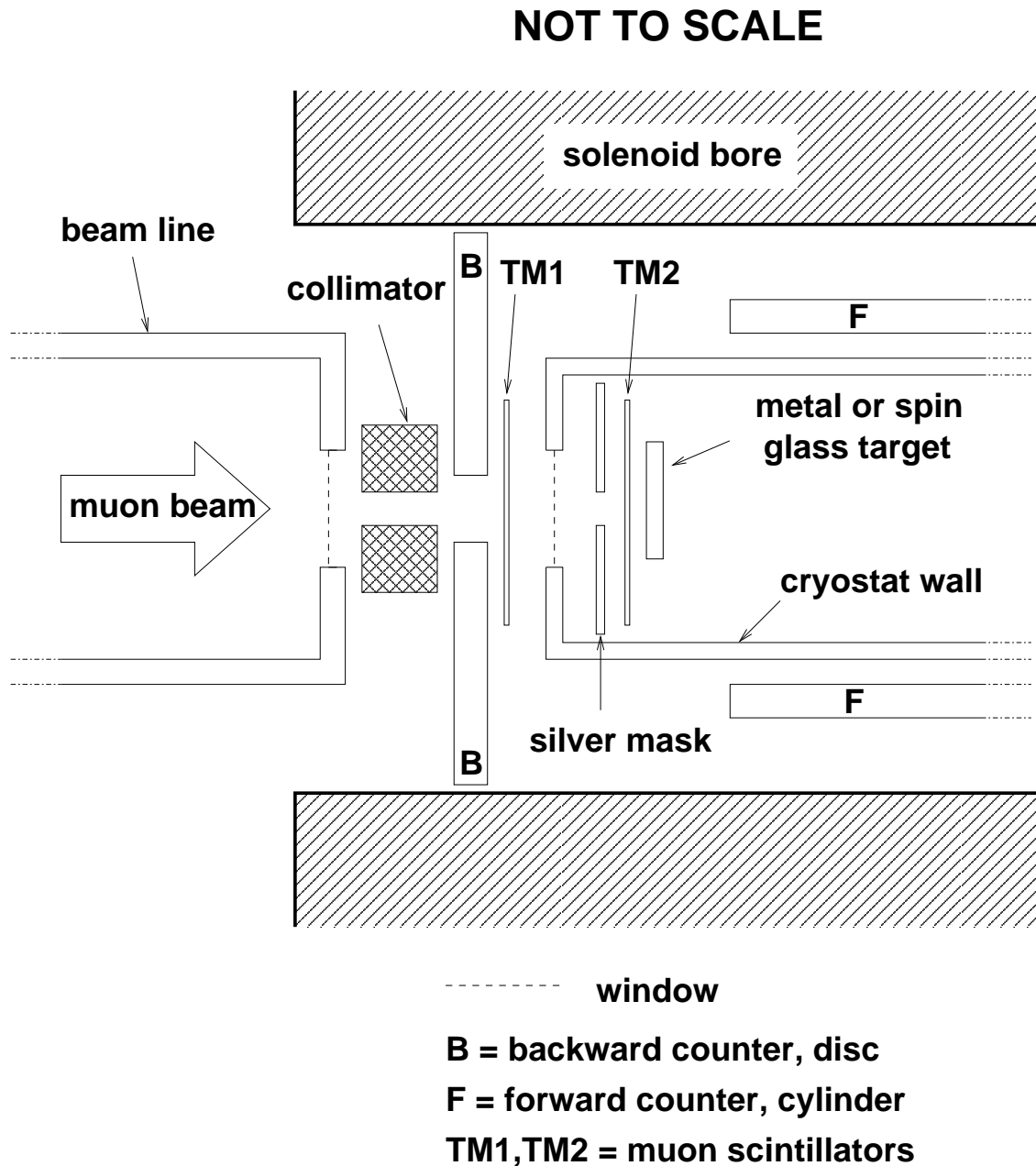


Figure H.1: Schematic for the experimental setup[34, 119]. The muons enter from the left and will trigger an event if they pass through the first scintillator (TM1) and stop in the silver mask, or pass through both scintillators (TM1 and TM2) and stop in the target. The backward positron counter (B) is protected from the muon beam by a collimator. Materials such as the vacuum tubes and light guides are not shown.

### H.3.3 Sample preparation

Muons were stopped in a calibration sample, and then later in aluminium and silver samples. The calibration sample was a spin glass disc<sup>57</sup> of approximately 3.0 cm diameter and mass 4.5 g. The spin glass was known to rapidly and completely depolarise muons within several microseconds with a single exponential form; its analysis allowed the empirical asymmetries of the detectors to be determined. The aluminium and silver samples were extracted from the same foil as the TWIST targets, and they were stacked several layers thick<sup>58</sup>, and clamped together with 3.6  $\mu\text{m}$  thick Mylar. The layers were chosen such that muons had a negligible probability of passing through the foils. Note that there was no grease or glue used.

## H.4 Data

The experiment collected data from 6 December 2006 to 20 December 2006, in runs that lasted between five and fourteen hours each. The conditions of TWIST were matched: the sample was immersed in a longitudinal 2 T magnetic field, and the temperature was not controlled<sup>59</sup>. The experiment started with runs that used a spin glass target. During these initial runs, the beam line was adjusted for rate and beam quality. A few days into the experiment, it was found necessary to keep the amount of material traversed by the decay positrons constant: a target of spin glass and metal foil was used back-to-back, and the target was then reversed to determine the metal depolarisation.

The data have been divided into sets, which are summarised in chronological order in Table H.1. There were unscheduled interruptions during data acquisition; the runs immediately after these interruptions were low rate and have been rejected. The bad runs have already been removed from the totals in the table.

The limited geometry of the decay positron counters (see Fig. H.1) resulted in a total positron rate that was about 10% of the muon rate. Approximately half of the beam time was spent on the nominal sets (E to H). The rate changed between the unscheduled interruptions, which are indicated by horizontal lines in the table. Set D was intended to have only a high DC separator setting, but it was also low rate.

---

<sup>57</sup>The spin glass used in this experiment was a geometrically frustrated antiferromagnet,  $\text{Gd}_2\text{Ti}_2\text{O}_7$ . Condensed matter experimenters have studied the muon depolarisation in this material in order to determine the local magnetic fields [120], but have not undertaken precision tests.

<sup>58</sup>The aluminium target was ten layers thick, and the silver had six layers.

<sup>59</sup>Initially, there was a plan to test the validity of the Korringa relaxation model. This model predicts a relaxation rate,  $\lambda$ , which should be independent of magnetic field, but show an increase with temperature. However, due to the limited beam time this test was abandoned in favour of the primary TWIST aims.

A surface muon edge scan was not carried out, so the exact beam line momentum and resolution were undetermined.

Table H.1: The table shows the division of the data into sets, where a “set” is defined as a sum of individual runs. The horizontal lines indicate when data taking was suspended.

Data set	Target	Description	Duration (hours)	$\mu^+$ rate		$\mu^+$ counts	
				Ag mask (kHz)	sample (kHz)	Ag mask ( $\times 10^9$ )	sample ( $\times 10^9$ )
A	SG <sup>a</sup>	calibration	14.1	24.4	15.2	1.2	0.8
B	Al	nominal Al	8.0	25.0	15.6	0.7	0.5
C	Al	$\frac{1}{2}$ -rate	15.7	12.4	9.6	0.7	0.5
D	Al	DC sep. high	5.7	16.6	10.7	0.3	0.2
E	SG+Al	nominal SG	24.0	19.4	13.3	1.7	1.2
F	Al+SG	nominal Al	40.1	19.9	13.7	2.9	2.0
G	Ag+SG	nominal Ag	32.4	21.8	14.6	2.5	1.7
H	SG+Ag	nominal SG	22.8	21.6	14.5	1.8	1.2
I	SG+Ag	thick scint. <sup>b</sup>	18.0	20.7	14.0	1.3	0.9
J	SG+Ag	thin scint. <sup>c</sup>	22.2	18.3	12.5	1.5	1.0
K	Ag+SG	thin scint.	13.3	20.1	13.8	1.0	0.7

<sup>a</sup> SG = Spin Glass.

<sup>b</sup> The thick scintillator was 508  $\mu\text{m}$ , which is double the nominal thickness.

<sup>c</sup> The thin scintillator was 127  $\mu\text{m}$ , which is half the nominal thickness.

## H.5 Analysis

The aim of the analysis was to fit Eq. (H.5) to the backward counts and Eq. (H.6) to the forward counts simultaneously. The spin glass calibration sample was fit with  $P_\mu(t) = \exp(-\lambda t)$ , which allowed  $A_b$  and  $A_f$  to be determined, and these were fixed for the metal samples. All fitting was carried out using MINUIT[121].

### H.5.1 Rebinning

The fit functions assumed that the background had no time dependence, and the muon beam had no transverse polarisation. In reality, protons arrived at the muon production target in bunches separated by the cyclotron period (43 ns), causing a periodic time dependence to the background. In addition, the transverse polarisation component precessed at the Larmor frequency ( $\omega = g_\mu B = 272 \text{ MHz}$ ). Since these effects were not included in the fit functions, the histograms of counts had to be carefully rebinned to minimise their effect.

The DAQ software performed a Fourier transform that included background subtraction, and found peaks at 23.06 MHz (43.37 ns) and 271.67 MHz (3.68 ns). This suggested that combining 113 channels (bin width 88.28 ns, about 2 cyclotron periods, 24 precession periods) was optimal. In practice, the rebinning was chosen by fitting a spin glass run with between 10 and 500 channels combined, and choosing a stable region. The final choice combined 115 bins (89.84 ns). The spin glass fit parameters were sufficiently robust to the choice of binning; this is demonstrated for the empirical backward asymmetry in Fig. H.2.

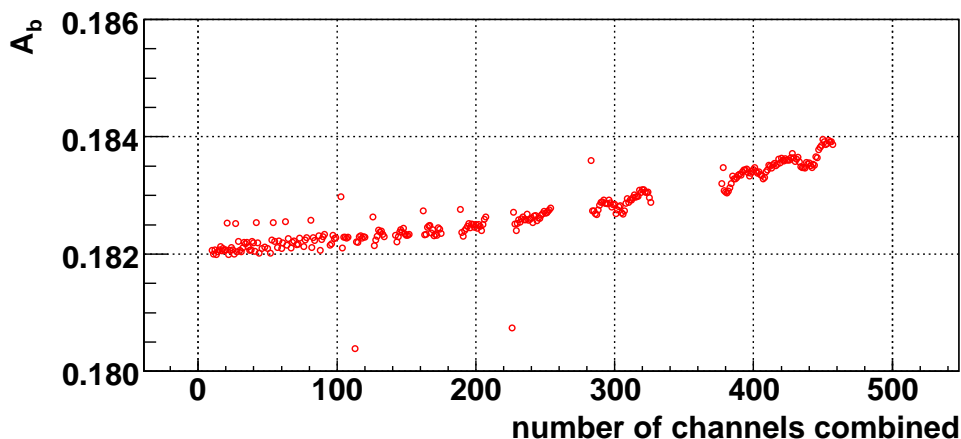


Figure H.2: Backward counter empirical asymmetry,  $A_b$ , from a single spin glass calibration run, with between 10 and 500 channels of width 0.78125 ns combined.

### H.5.2 Calibration using spin glass

The spin glass (SG) data sets were fit assuming an exponential depolarisation,  $P_\mu(t) = P_\mu(0) \exp(-\lambda_{SG}t)$ , and the results are shown in Table H.2. The  $A_b$  and  $A_f$  parameters depended on the target, which confirmed the importance of calibrating with a target of spin glass backed with metal, rather than spin glass alone. The  $r$  parameters varied by significant amounts between sets, but were consistent for the runs within sets. This suggested that the parameter was extremely sensitive to the geometry (*e.g.* target placement), and had to be left free when the metal samples were fit.

The results for a single exponential fit to the double-thickness scintillator were anomalous. In this case, a significant fraction of muons must be stopping and depolarising in the scintillator, and a single exponential model is inappropriate. The fit's confidence level was lower (14%), but not unreasonable, which indicated that the data had poor sensitivity to an extra depolarisation term for the scintillator. The results for the thin scintillator were

consistent with the nominal case, suggesting the fraction of muons stopping in the nominal scintillator was small.

The background in each counter was investigated. When the backgrounds were free fit parameters, the values had a significant statistical discrepancy ( $> 3\sigma$ ) with the result using the  $1\ \mu\text{s}$  of  $t < 0$  counts. Since the backgrounds could be determined using the  $t > 0$  decay data, and had a weak correlation with the other fit parameters, the  $t < 0$  data were subsequently ignored.

Table H.2: Fit parameters for a single exponential fit to the spin glass sets. The bracketed number indicates the statistical uncertainty in the final digits.

Set	A	E	H	I	J
Sample	SG	SG+Al	SG+Ag	SG+Ag	SG+Ag
Scintillator thickness ( $\mu\text{m}$ )	254	254	254	508	127
$\chi^2/\text{ndof}$	316.9/302 = 1.05	285.5/302 = 0.95	268.5/302 = 0.89	328.3/302 = 1.09	316.1/302 = 1.05
Confidence	0.27	0.74	0.92	0.14	0.28
$r$	0.7070 (5)	0.7019 (4)	0.6811 (3)	0.4764 (5)	0.6827 (4)
$A_b$	0.1858 (6)	0.1822 (5)	0.1833 (5)	0.0276 (5)	0.1836 (5)
$A_f$	-0.2409 (6)	-0.2365 (4)	-0.2404 (4)	-0.0522 (7)	-0.2415 (5)
$\lambda_{\text{SG}}(\mu\text{s}^{-1})$	0.878 (5)	0.880 (4)	0.878 (4)	0.55 (2)	0.883 (4)

Alternative models for  $P_\mu(t)$  in the spin glass were tried, even though the reduced  $\chi^2$  values suggested there would be minimal sensitivity. A variable power law,  $P_\mu(t) = \exp(-at^p)$ , found  $p = (1.005 \pm 0.007)$  for set E (SG+Al), with no change in the reduced  $\chi^2$ . A sum of single exponentials was also tried, but the minimisation using MINUIT was unsuccessful for the nominal spin glass sets.

An effort was made to determine the depolarisation within the trigger scintillator, using the set taken with the double thickness (508  $\mu\text{m}$ ) scintillator, where a significant fraction of muons stopped in the trigger. The first approach was iterative:

1. Fit 127  $\mu\text{m}$  set assuming 100% muons stop in the sample, to determine  $\lambda_{\text{SG}}$ .
2. Fit 508  $\mu\text{m}$  set allowing for stops in both the scintillator and sample using

$$P_\mu(t) = \epsilon \exp(-\lambda_{\text{scint}}t) + (1 - \epsilon) \exp(-\lambda_{\text{SG}}t), \quad (\text{H.7})$$

where  $\epsilon$  is the fraction of muons stopping in the trigger scintillator,  $\lambda_{\text{scint}}$  is the relaxation rate in the scintillator, and  $\lambda_{\text{SG}}$  was fixed to the 127  $\mu\text{m}$  value from (1).

3. Fit 127  $\mu\text{m}$  set with Eq. (H.7), with  $\epsilon$  and  $\lambda_{\text{scint}}$  fixed to the values from (2).
4. Iterate (2)-(3) until convergence.

Only two iterations were required, and the results for the 127  $\mu\text{m}$  and 508  $\mu\text{m}$  sets are shown in Table H.3. There was a reduction in  $\chi^2$  when including a second exponential, and the high confidence level suggested that a single exponential model was valid for depolarisation in the scintillator. The addition of a scintillator depolarisation term helped  $r$ ,  $A_b$  and  $A_f$  from Set I become more consistent with the other spin glass results. For the thin scintillator, the  $\chi^2$  was changed minimally, and the fraction of muons stopping in the scintillator was consistent with zero.

Table H.3: Comparison of fit parameters for a single exponential and a sum of exponentials, where the latter allows for separate depolarisation in the spin glass and scintillator. The bracketed number indicates the statistical uncertainty in the final digits.

Set	Set I: SG+Ag, 508 $\mu\text{m}$ scint.		Set J: SG+Ag, 127 $\mu\text{m}$ scint.	
	Single $\lambda$	Converged	Single $\lambda$	Converged
$\chi^2/\text{ndof}$	328.3/302	284.5/301	316.1/302	315.9/301
	= 1.09	= 0.95	= 1.05	= 1.05
Confidence	0.14	0.74	0.28	0.27
$r$	0.4764 (5)	0.648 (1)	0.6827 (4)	0.69 (3)
$A_b$	0.0276 (5)	0.157 (1)	0.1836 (5)	0.19 (2)
$A_f$	-0.0522 (7)	-0.218 (2)	-0.2415 (5)	-0.25 (2)
$\lambda_{\text{SG}} (\mu\text{s}^{-1})$	0.55 (2)	0.886	0.883 (4)	0.886 (8)
$\lambda_{\text{scint}} (\mu\text{s}^{-1})$	-	0.0132 (8)	-	0.00132
$\epsilon$ (%)	-	86.0 (3)	-	4 (9)

The other spin glass sets were fit with an extra scintillator depolarisation term, with  $\lambda_{\text{scint}} = 0.0132 \mu\text{s}$  fixed. The fit to Set A (SG only) would not succeed. For sets E (SG+Al) and H (SG+Ag), the fraction of muons stopping in the scintillator were determined as  $\epsilon = (0 \pm 10)\%$  and  $\epsilon = (8 \pm 8)\%$  respectively. Combined with the 127  $\mu\text{m}$  result of  $\epsilon = (4 \pm 9)\%$ , this suggests that somewhere between 0% and 10% of muons stopped in the nominal (254  $\mu\text{m}$ ) trigger scintillator. The effect of including a scintillator depolarisation term on  $\lambda_{\text{SG}}$ ,  $A_b$  and  $A_f$  is demonstrated in Fig. H.3, where the statistical precision becomes worse, but the central values do not systematically change.

In another approach, a simultaneous fit was made to all sets, with  $\lambda_{\text{SG}}$  and  $\lambda_{\text{scint}}$  as common parameters. The minimiser was able to converge on a solution, but the uncertainties

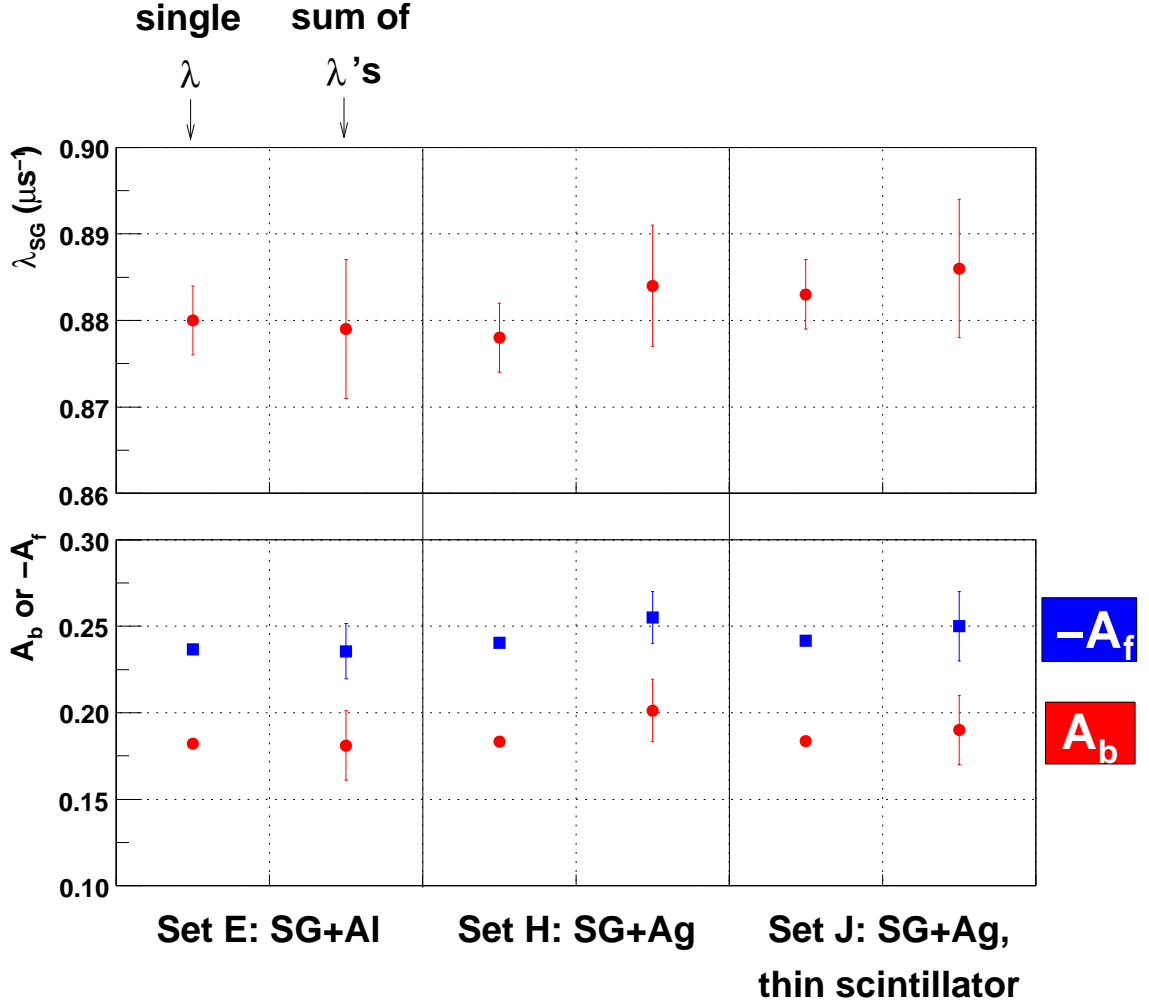


Figure H.3: Effect on  $\lambda_{SG}$ ,  $A_b$  and  $A_f$  when a second exponential scintillator depolarisation with  $\lambda_{scint} = 0.0132 \mu s$  is included.

on the fit parameters could not be reliably determined, and the MINUIT global correlations<sup>60</sup> were close to 1.0. The relaxation rates from this approach were

$$\lambda_{SG} = (0.887 \pm 0.002) \mu s^{-1}, \quad (H.8)$$

$$\lambda_{scint} = (0.0123 \pm 0.0007) \mu s^{-1}, \quad (H.9)$$

which are consistent with the earlier approach. This approach also determined the fraction

<sup>60</sup>The correlation coefficient is a number between  $-1$  and  $+1$  that describes the degree of correlation between the estimate of two fit parameters. The MINUIT *global* correlation for a parameter ( $\alpha$ ) “is a number between zero and one which gives the correlation between parameter  $[\alpha]$  and that linear combination of all other parameters which is most strongly correlated with  $[\alpha]$ ” [121]. A global correlation coefficient close to one indicates there are too many free parameters.

of scintillator stops for the nominal case as somewhere between 0% and 10%.

In summary, the data suggest that about 86% of muons stop in the thick (508  $\mu\text{m}$ ) scintillator, but cannot precisely determine the fraction of muons stopping in the nominal scintillator. Later a simulation will be used to better determine the fraction.

### H.5.3 Metal samples

The silver mask and metal foil data were analysed with the empirical asymmetries fixed<sup>61</sup> to  $A_b = 0.185$  and  $A_f = -0.238$ , under the assumption that no muons stopped in the trigger scintillators. A run-by-run analysis of the silver mask was used as a consistency check, since Fig. H.1 showed that the mask is upstream of the regular target, and should be unaffected by any downstream changes. The  $r$  values and relaxation rates are shown in Fig. H.4, where  $r$  has clear systematic steps whenever the target or running conditions were altered. The relaxation rates are visually inconsistent between runs, and a weighted average of the results finds

$$\lambda = (1.07 \pm 0.07) \text{ ms}^{-1}, \quad (\text{H.10})$$

with a confidence level of just 0.2%. Notably one run from set A is several  $\sigma$  from the average, set D has a negative relaxation rate (but a reasonable fit quality), and there is suggestion that set G has a systematically smaller rate than set H.

The results for the metal samples from TWIST are shown in Fig. H.5. The confidence levels are reasonable except for the last run of set F. For this set, the relaxation rate is still consistent with the other runs, so it was not rejected. The  $r$  parameters show a similar pattern to the silver mask's values in Fig. H.4. However, the relationship was not strong enough to impose a constraint. The relaxation rates for aluminium are statistically consistent for sets B, C, D and F, with a weighted average of

$$\lambda_{\text{Al}} = (1.7 \pm 0.2) \text{ ms}^{-1}, \quad (\text{H.11})$$

under the assumption that all muons stop in the target. Similarly, the relaxation rates for silver are statistically consistent for sets G and K, yielding

$$\lambda_{\text{Ag}} = (1.2 \pm 0.2) \text{ ms}^{-1}. \quad (\text{H.12})$$

A single exponential fit is shown for an aluminium and silver run in Figs. H.6 and H.7.

---

<sup>61</sup>This is an approximation for the silver mask; it will not have the same empirical asymmetry as the metal target due to slightly different geometries.

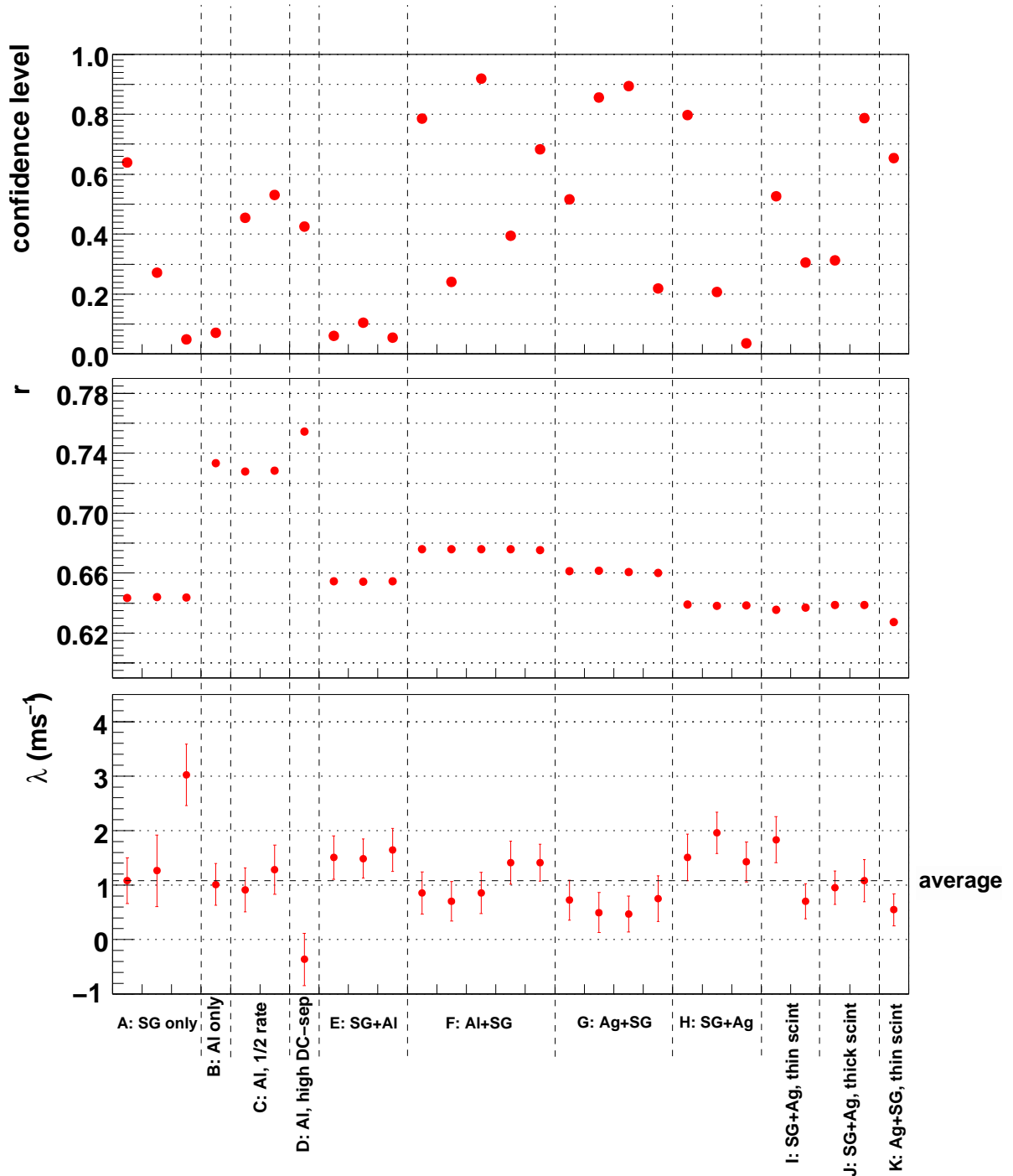


Figure H.4: Silver mask (99.99% purity) fit results. There is evidence that the relaxation values are inconsistent. The weighted average is  $\lambda = (1.07 \pm 0.07) \text{ms}^{-1}$ .

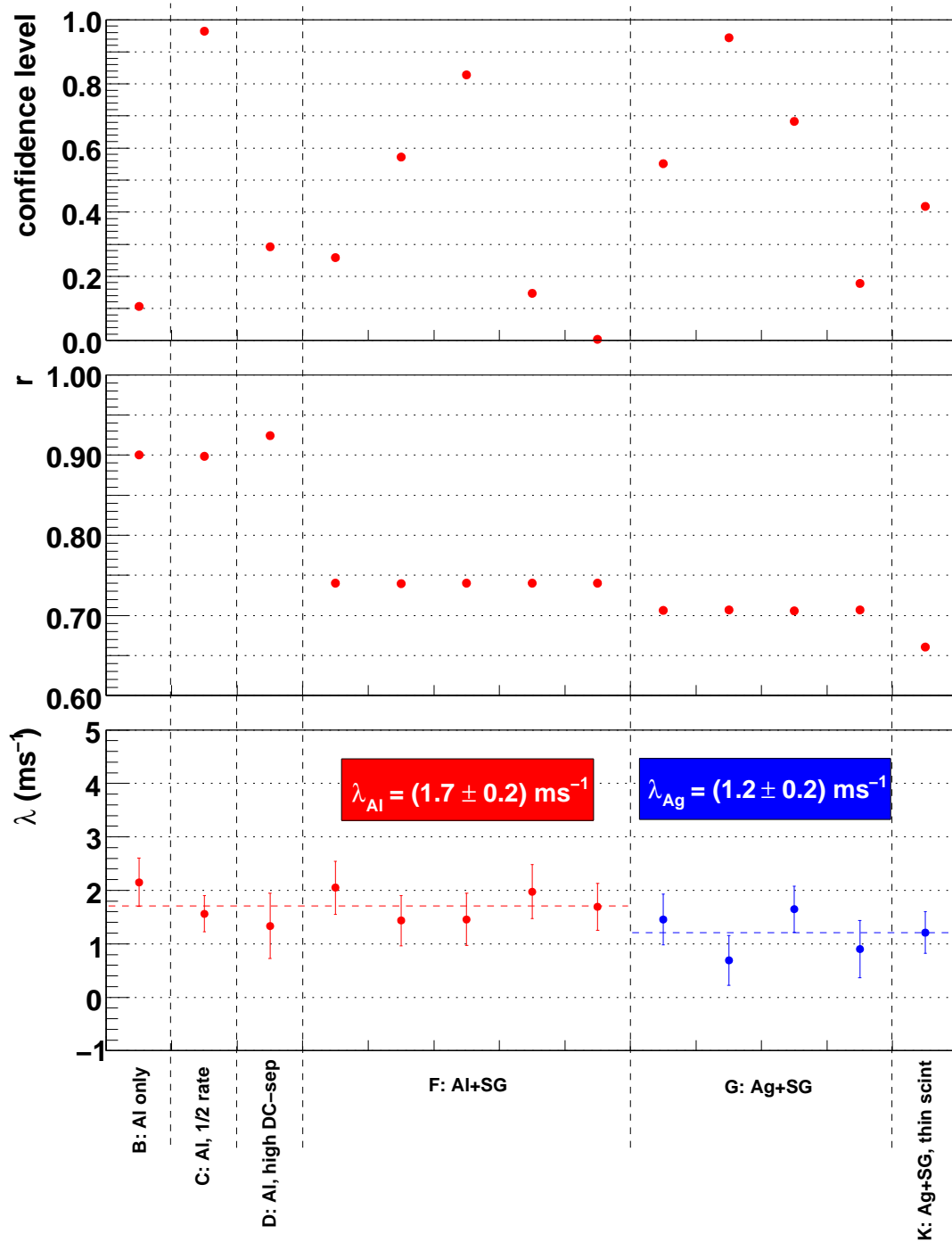
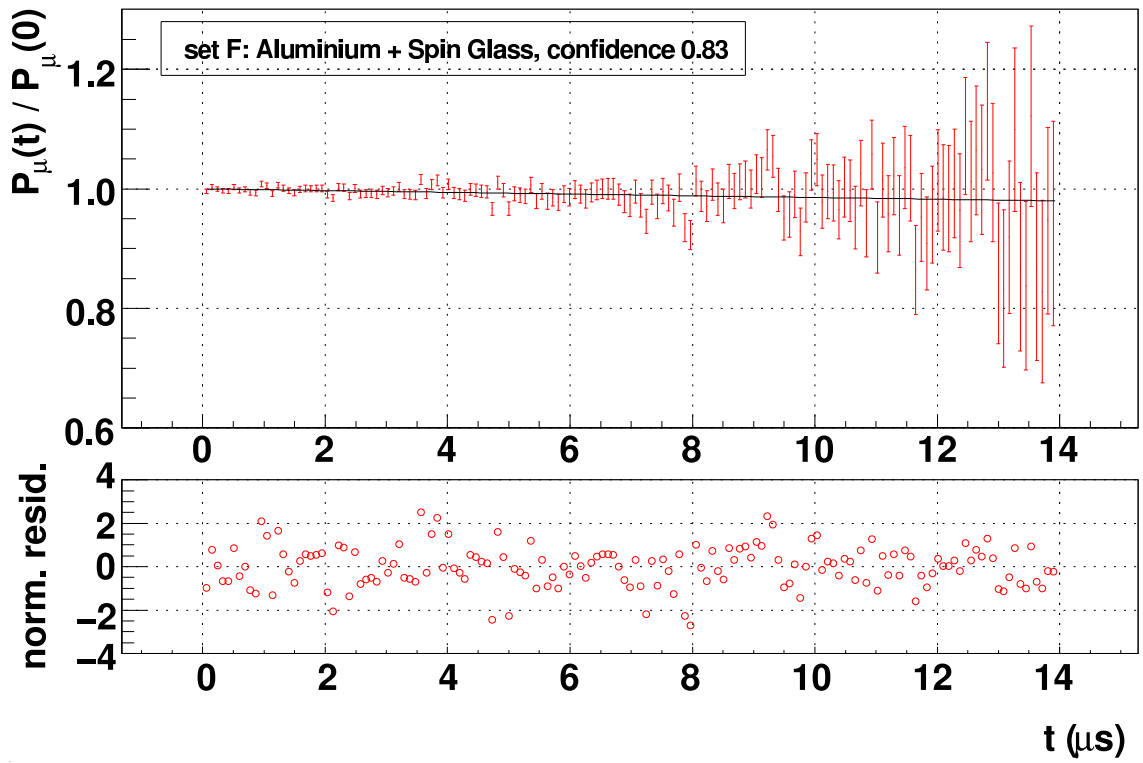
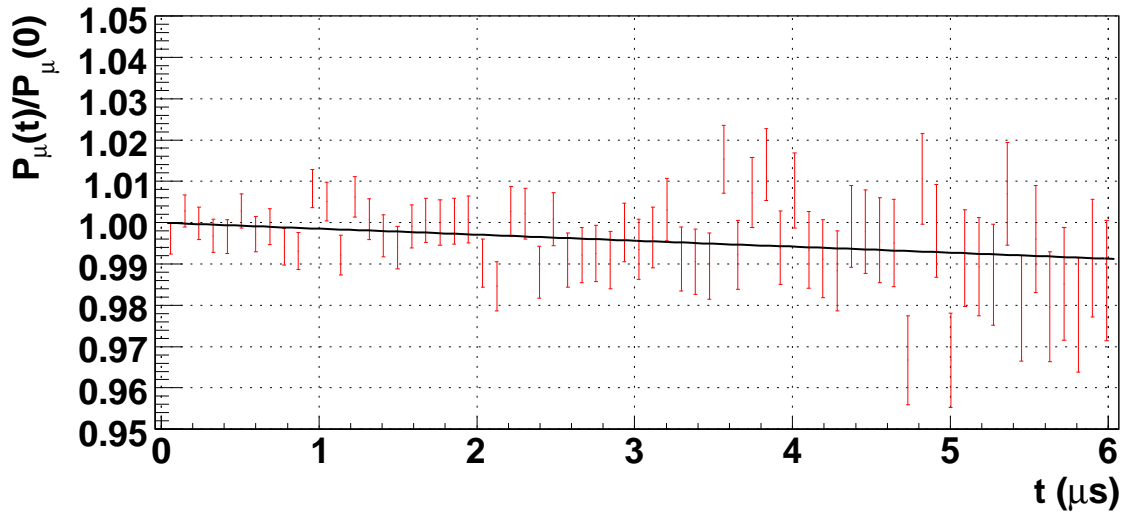


Figure H.5: TWIST metal samples (Al and Ag, both  $> 99.999\%$  purity) fit results. For each foil, the sets taken under different running conditions are statistically consistent.

There is no evidence that anything beyond a single exponential is needed to describe the depolarisation. There is no observable fast depolarisation component below  $1\ \mu\text{s}$ . Note that fits were *not* made to the asymmetry; instead Eqs. (H.5) and (H.6) were used to fit the backward and forward histograms. In fact, the asymmetry figures cannot be constructed unless a model is assumed for  $P_\mu(t)$ .

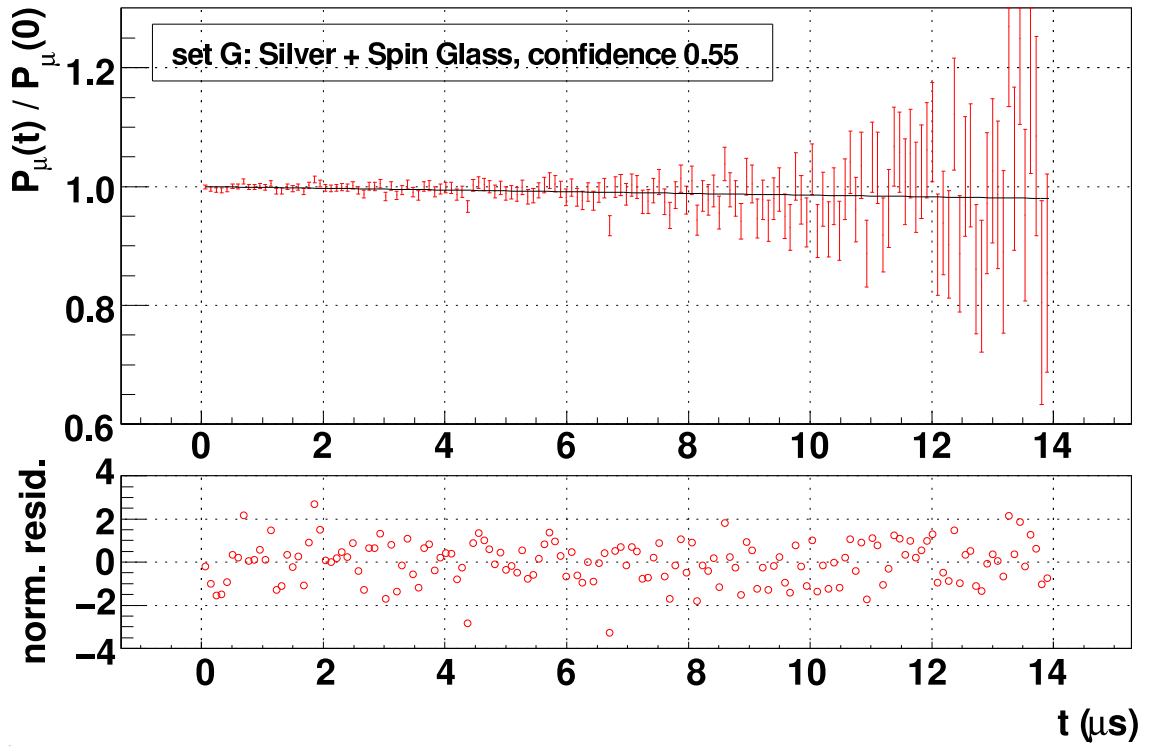


(a) Whole time range.

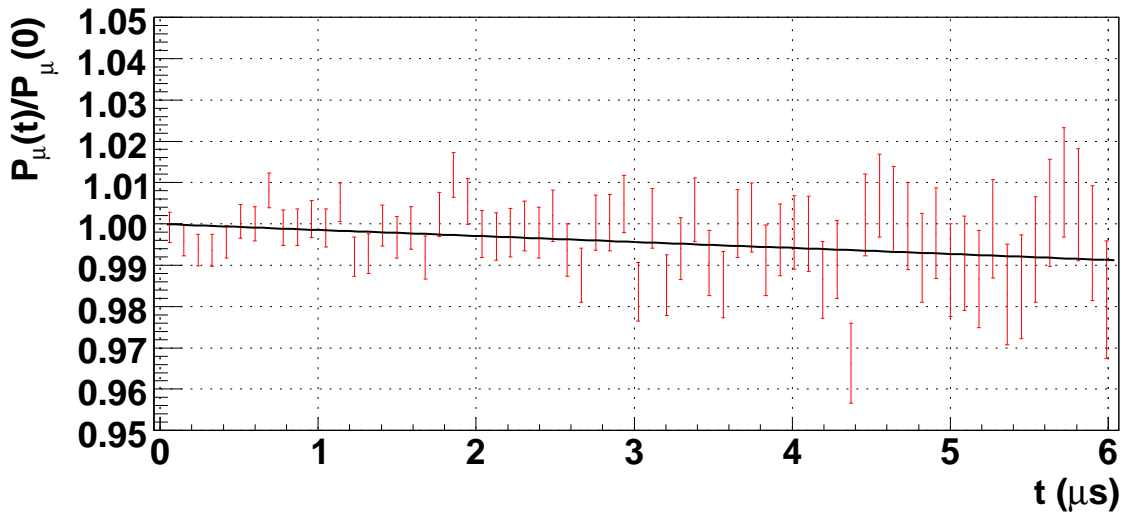


(b) Restricted to early times.

Figure H.6: Aluminium target: one run fit with  $P_\mu(t) = P_\mu(0) \exp(-\lambda t)$ .



(a) Whole time range.



(b) Restricted to early times.

Figure H.7: Silver target: one run fit with  $P_\mu(t) = P_\mu(0) \exp(-\lambda t)$ .

## H.6 Correction due to scintillator stops

The data indicated that between 0% and 10% of muons stopped in the nominal scintillator (see Section H.5.2). This was a problem, since the depolarisation rate in the scintillator was a factor  $\approx 10$  larger than the metal, allowing the possibility that all the depolarisation apparently observed in the metal samples was really due to depolarisation in the scintillator.

The fraction stopping in the scintillator was better determined using a simulation[84]. Software from the SRIM (the **S**topping and **R**ange of **I**ons in **M**atter) group of programs[122] was used, which included full quantum mechanical treatment of ion-atom collisions[123] (in this case the “ion” was the muon). The simulation required the initial momentum to be specified, but this was not measured during the data acquisition period. The M20 channel was set to maximise surface muon intensity, suggesting a minimal part of the momentum distribution lay beyond the kinematic cutoff at 29.79 MeV/c. Therefore simulations were run with a central momentum adjusted to be  $2\sigma$  below the kinematic cutoff, with conservative estimates of the momentum resolution  $\sigma$ . The initial momentum distributions are shown in Fig. H.8(a).

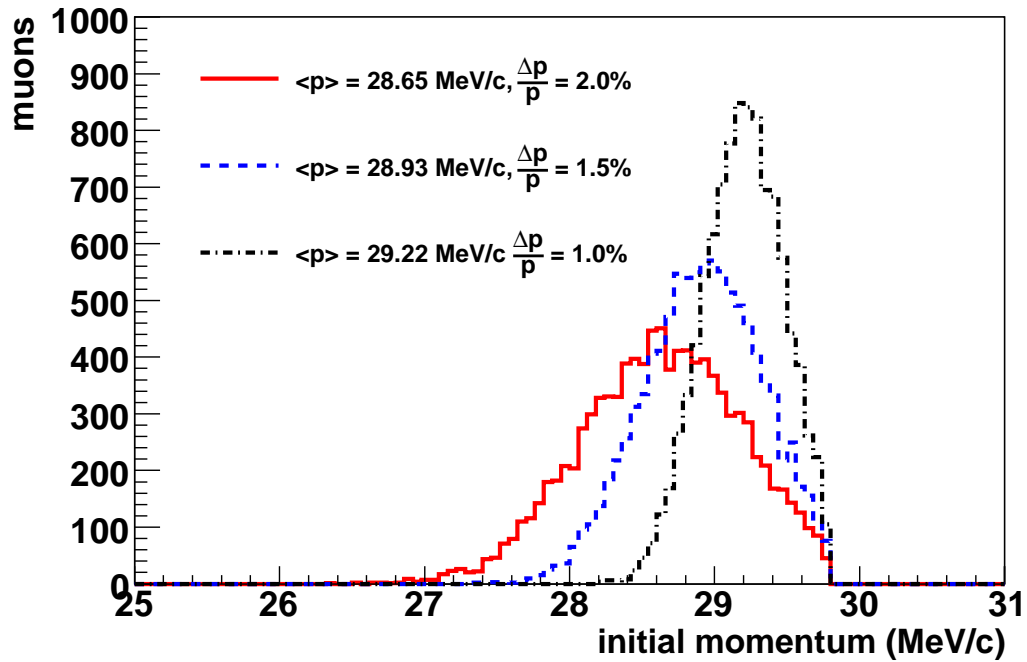
Instead of running separate simulations for each scintillator, a single simulation was run at each momentum, with three pieces of scintillator in place: 127  $\mu\text{m}$ , 127  $\mu\text{m}$  and 254  $\mu\text{m}$ . This allowed the fraction of stops in three thicknesses of scintillator (127  $\mu\text{m}$ , 254  $\mu\text{m}$  and 508  $\mu\text{m}$ ) to be determined simultaneously by integrating the number of stops appropriately. In each simulation, the stopping distribution was adjusted<sup>62</sup> so that the total fraction of scintillator stops was about 86%; this matched the precise result from Table H.3 that 86.0% of muons will stop in 508  $\mu\text{m}$  of scintillator.

The stopping distributions from the simulation are shown in Fig. H.8(b). The number of muons stopping in each scintillator thickness are integrated in Table H.4, which shows that it is possible to obtain anything from 0.5% to 5.9% stopping in the nominal scintillator; this disfavors the data’s suggestion of up to 9%. Clearly the initial momentum distribution is important in such a simulation, and it would have been valuable to make a measurement while acquiring data. In the thin (127  $\mu\text{m}$ ) scintillator, the simulation found that no more than 0.2% of muons stopped in the trigger.

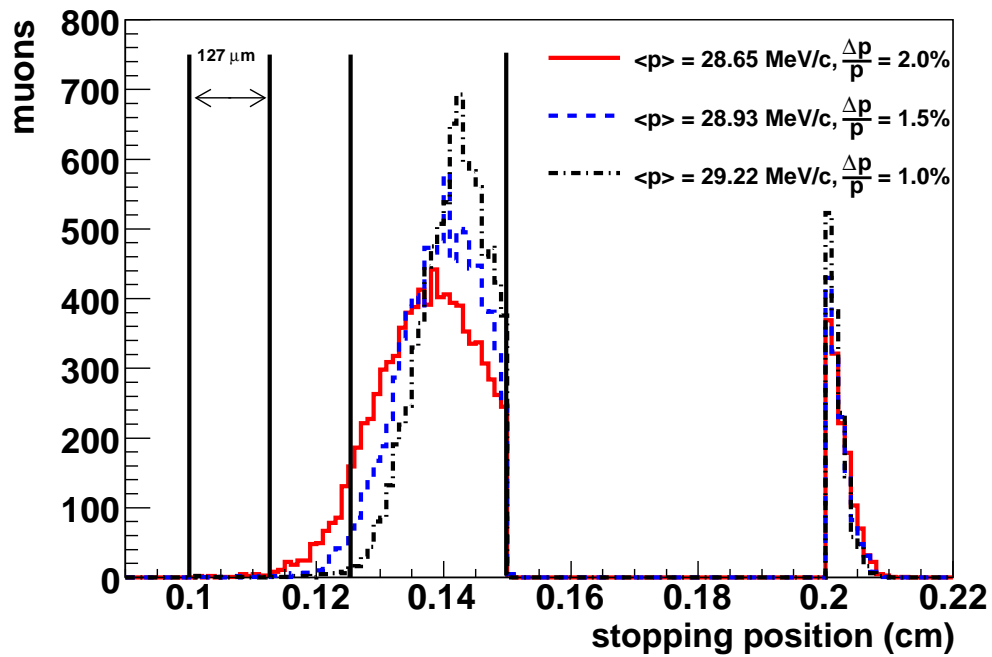
A systematic uncertainty can be estimated by repeating the analysis with a fraction of the muons forced to stop and depolarise in the scintillator. The results for between 0% and 10% of the muons stopping in scintillator are shown in Fig. H.9. If the central value of  $\lambda$  is corrected so that  $\epsilon = 3.5\%$ , with an uncertainty that allows for between 1% and 6%

---

<sup>62</sup>The simulation included a piece of variable thickness Mylar upstream of the trigger scintillators.



(a) Initial momentum used in the simulations.



(b) Stopping distributions for the different initial momenta.

Figure H.8: Initial momentum distributions used in the SRIM simulation, and the resulting stopping distributions.

Table H.4: The fraction of muons stopping in each scintillator, for three different initial momentum distributions.

$\langle p \rangle$ (MeV/c)	$\Delta p/p$ (%)	Fraction of stops (%)		
		thin (127 $\mu\text{m}$ )	nominal (254 $\mu\text{m}$ )	thick (508 $\mu\text{m}$ )
29.22	1.0	$0.07 \pm 0.03$	$0.5 \pm 0.1$	$85.8 \pm 0.9$
28.93	1.5	$0.09 \pm 0.03$	$1.9 \pm 0.1$	$86.8 \pm 0.9$
28.65	2.0	$0.22 \pm 0.05$	$5.9 \pm 0.2$	$86.7 \pm 0.9$

scintillator stops, then the nominal scintillator results become

$$\lambda_{\text{Al}} = (1.3 \pm 0.2 \text{ (stat.)} \pm 0.3 \text{ (syst.)}) \text{ ms}^{-1} \quad (\text{H.13})$$

$$\lambda_{\text{Ag}} = (0.9 \pm 0.2 \text{ (stat.)} \pm 0.2 \text{ (syst.)}) \text{ ms}^{-1}. \quad (\text{H.14})$$

For the single run with the thin (127  $\mu\text{m}$ ) scintillator, the contribution from scintillator stops is negligible, but the statistical uncertainty dominates so that

$$\lambda_{\text{Ag}} = (1.2 \pm 0.4 \text{ (stat.)}) \text{ ms}^{-1}. \quad (\text{H.15})$$

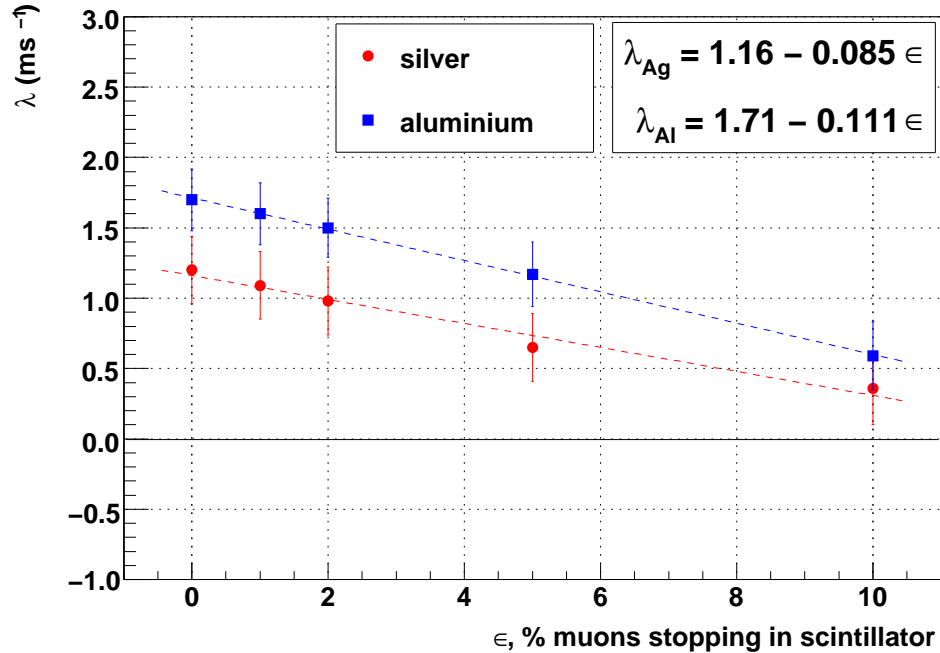


Figure H.9: Exponential depolarisation rate for silver and aluminium, for different fraction of muons stopping in the scintillator. The parameter  $\epsilon$  represents the percentage of muons stopping in the scintillator.

## H.7 Other systematic uncertainties

There is a systematic uncertainty from the fixed  $A_b$  and  $A_f$  values that were used in the metal fits. A 10% change in either of these parameters altered the relaxation rate by at most  $0.12 \text{ ms}^{-1}$ .  $A_b$  and  $A_f$  were determined with statistical precision  $< 0.3\%$ , but were forced to be  $A_b = 0.185$  and  $A_f = -0.238$  for all fits, which meant they were wrong by up to 2% (see Table H.2). An estimate of the systematic uncertainty on the relaxation rate is  $(2/10) \times 0.12 = 0.02 \text{ ms}^{-1}$ . This is negligible compared to the systematic uncertainty from the scintillator stops.

There was no systematic uncertainty assigned due to the background having a time structure. Figure H.5 showed that the confidence levels were reasonable, except for one set, which still produced a consistent relaxation rate. If the confidence levels were lower, or the relaxation rate for the low confidence level run had been anomalous, a systematic uncertainty due to the time structure of the background may have been necessary<sup>63</sup>.

The sets with different muon rates and DC separator settings showed no evidence of an inconsistent relaxation rate (see Fig. H.5). Therefore no systematic uncertainties are assigned for these effects.

## H.8 Conclusions

The  $\mu^+$ SR experiment demonstrated that down to a decay time of 10 ns, a single exponential function is appropriate and sufficient to describe the depolarisation in aluminium and silver. This is an essential contribution to the TWIST result.

The analysis found the following relaxation rates for the TWIST target foils:

$$\lambda_{\text{Al}} = (1.3 \pm 0.2 \text{ (stat.)} \pm 0.3 \text{ (syst.)}) \text{ ms}^{-1} \quad (\text{H.16})$$

$$\lambda_{\text{Ag}} = (0.9 \pm 0.2 \text{ (stat.)} \pm 0.2 \text{ (syst.)}) \text{ ms}^{-1}. \quad (\text{H.17})$$

These are consistent with the results from the TWIST detector, but their uncertainties are not competitive. The dominant systematic uncertainty could not be reduced without accumulating more data.

---

<sup>63</sup>If the background was the leading systematic uncertainty, then a further investigation could revisit the calculations presented in Appendix 3 of Ref. [124], where time dependences due to pile-up are discussed.

## H.9 Future experiments

Several recommendations can be made for a future experimenter. The fraction of muons stopping in the trigger scintillator could have been determined with greater certainty if the beam line had been momentum calibrated. A stopping target of pure scintillator would have provided a clean measurement of the depolarisation rate in the trigger. The thin ( $127\ \mu\text{m}$ ) scintillator provided signals with sufficient amplitude, and could have been used to accumulate all the nominal data.

The fit quality could have been improved by including a time dependence to the background, but this would only be appropriate if more statistics were acquired, which would take far more than two weeks of beam time at TRIUMF. We were unable to find a constraint using the silver mask's fit parameters; for example, the  $r$  parameter from the silver mask and regular metal fits were highly correlated, and it may have been possible to constrain them. A detailed simulation of the apparatus may have allowed such constraints to be investigated.

# Appendix I

## $(g - 2)$ and the M13 beam line

The muons in the simulation are started at the end of the M13 beam line, with their spin and momentum anti-parallel. A small depolarisation takes place through the beam line, since there is a difference in the deflection of the momentum and spin through the magnetic fields of the dipoles. Recall from Eq. (1.37) that the precession frequencies for the momentum ( $\omega_p$ ) and spin ( $\omega_s$ ) differ by

$$\frac{\omega_p - \omega_s}{\omega_p} = a = \frac{g - 2}{2} = 1.17 \times 10^{-3}. \quad (\text{I.1})$$

For an on-axis particle, shown in Fig. I.1, the deviation from the initial momentum direction  $\vec{v}_0$  will be equal in B1 and B2, but with opposite sign in each dipole. The same is true for the spin. Therefore the momentum and spin both have a net deflection of zero, and they remain anti-parallel.

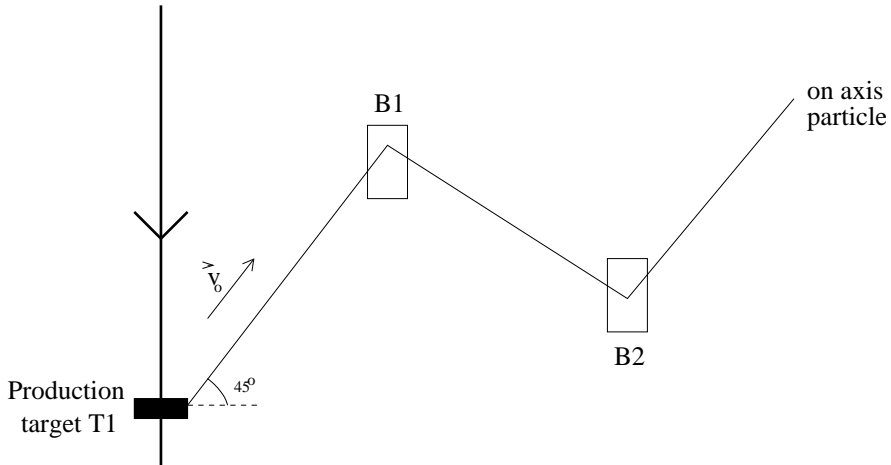


Figure I.1: An on-axis particle passing through M13.

Now consider the two most extreme trajectories that can pass through M13, assuming two different dipole configurations. These are shown in Fig. I.2. The real configuration is the single crossover in Fig. I.2(a)[125]. An upper limit can be set on the total net angular deflection using the emittance at the production target ( $\lesssim 250$  mrad, before focusing by Q1 and Q2) and TECs ( $\lesssim 150$  mrad). Under the configuration in Fig. I.2(a), the largest possible

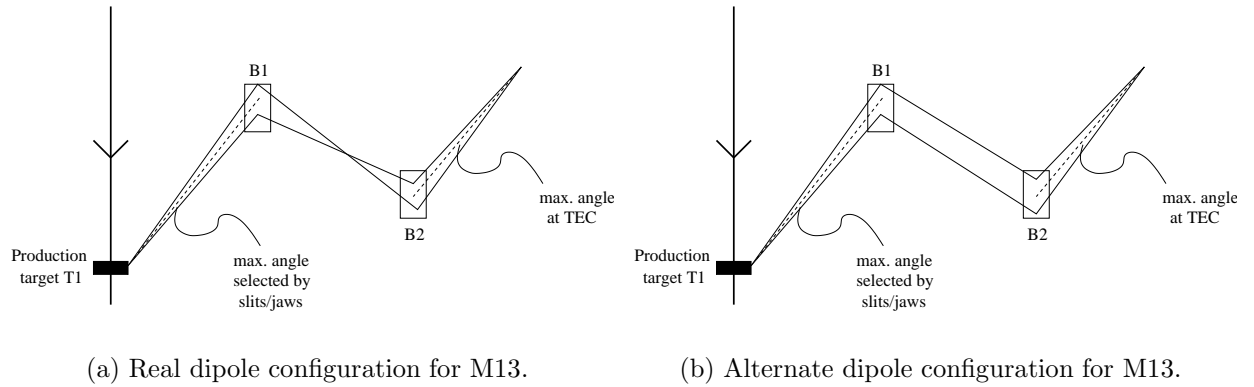


Figure I.2: Most extreme trajectories through M13 beam line, under two configurations.

deflection is  $\sim 100$  mrad, which from Eq. (I.1) changes the angle between the momentum and spin by  $\Delta\theta \sim 1 \times 10^{-4}$ . This contributes a depolarisation  $\sim 1 - \cos \Delta\theta \sim 10^{-8}$ . Even if the beam line were configured according to Fig. I.2(b), the depolarisation would be  $\sim 10^{-7}$ . Both of these depolarisation estimates are completely negligible.

# Appendix J

## Estimating muon stops in PC6 gas

A cut is placed on the muon's pulse width in PC5 and PC6 that removes muons stopping in the PC6 gas. The positions of this cut are shown in Fig. J.1(a); zone 1 is selected for the normal analysis. The cut is imperfect, and allows a small contamination of gas stops into zone 1. The main text uses three numbers to determine the systematic uncertainty from this contamination: the depolarisation in the gas, the fraction of total PC6 stops that are in gas, and the fraction of the gas distribution that leaks across the cut-B line. The method of determining these numbers will now be described.

A special analysis selected zone 3 in order to determine the depolarisation in the chamber gas. The intercept in the asymmetry fits was statistically consistent with zone 1, demonstrating that no measurable gas depolarisation<sup>64</sup> occurs before  $1.05 \mu\text{s}$ . The relaxation rate is  $\lambda_{\text{gas}} = (28 \pm 3) \text{ms}^{-1}$ , which is significantly larger than the metal. Using Eq. (6.7), the average gas depolarisation is then  $\langle P_{\mu} \rangle_{|\text{gas}} = 8.0\%$  ( $\lambda_1 = 0, \lambda_2 = 30.0 \text{ms}^{-1}$ ).

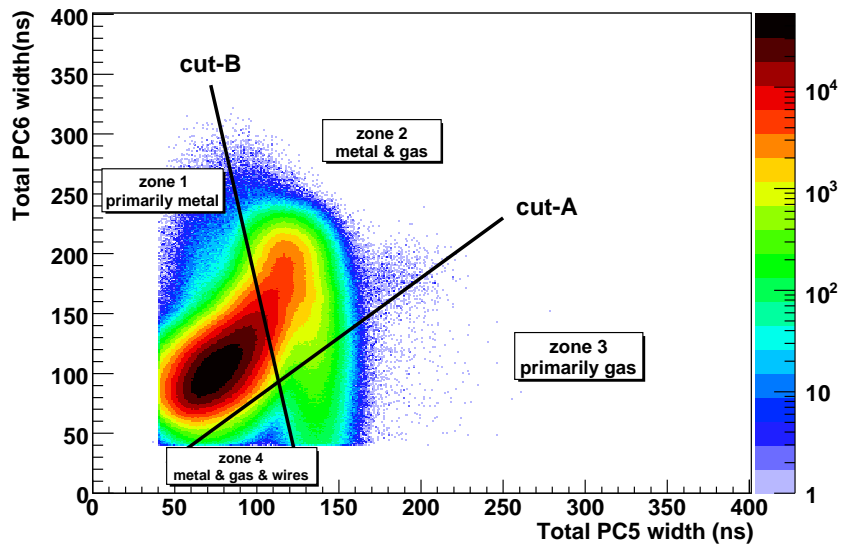
Each data set was re-analysed with *no cut* on the PC5/6 pulse width, and the resulting change in  $P_{\mu}^{\pi} \xi$  is divided by the gas depolarisation (8.0%) to estimate the ratio of gas to metal target stops in PC6. For 2006, between 4% and 5% of the total stops are gas, with the exception of set 68 which has 7% gas stops since the stopping distribution was further upstream. For 2007, between 6.5% and 7.5% of the muons stop in the gas, depending on the set.

The fraction of the gas distribution leaking between zones 1 and 2 is estimated using the contamination of zone 3 into 4 (a clean separation of gas and metal is not possible in zone 2). Figure J.1(b) is a projection of zones 3 and 4, rotated to make the cut-B line vertical. The distribution is fit with the sum of two Gaussian distributions. The fraction of the gas distribution leaking into zone 4 was tuned to be less than 0.5%, to ensure a negligible systematic uncertainty.

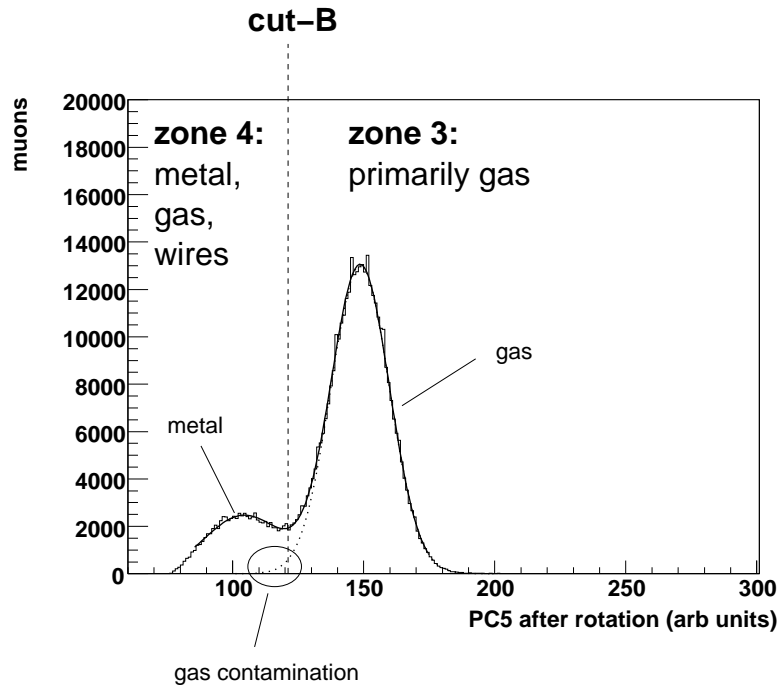
Note that the simulation was unable to estimate the fraction of gas stops in zone 1 since it was not tuned to reproduce the PC chamber response.

---

<sup>64</sup>However, if muons are selected that stop in PC5, PC7 and PC8, a change in the intercept of about 3% is observed, indicating a “fast” depolarisation. The simulation predicts that for these selections, 50% of muons stop in the gas and 50% in the Mylar foil. Since we do not observe a fast depolarisation when pure gas stops are selected in PC6, we conclude that the fast depolarisation is within the Mylar.



(a) Zone definitions for the muon pulse width in PC5 and PC6.



(b) Projection of zones 3 and 4, perpendicular to cut-B. A fit has been made to the sum of two Gaussian distributions.

Figure J.1: Estimation of gas contamination after a cut on the PC5 and PC6 muon pulse width.